New directions for semiconductor nanowires: Demonstrating robust spins and long-lived excitons

DISSERTATION

zur Erlangung des
Doktorgrades der Naturwissenschaften (Dr. rer. nat.)
der Fakultät für Physik der Universität Regensburg

vorgelegt von

Florian Dirnberger
aus Oberviechtach

2019

Das Promotionsgesuch wurde eingereicht am 30. Januar 2019.

Die Arbeit wurde angeleitet von Prof. Dr. Dominique Bougeard.

Prüfungsausschuss:

Vorsitzender:	Prof. Dr. Jaroslav Fabian
Erstgutachter:	Prof. Dr. Dominique Bougeard
Zweitgutachter:	Prof. Dr. Christian Schüller
Weiterer Prüfer:	Prof. Dr. John Schliemann

Contents

1 Introduction

In a historical survey, *Physics Today* highlights the field of condensed-matter physics and its prominent role as physic's largest research community [1]. With the invention of the laser and the transistor in the 1960s, it lead to what was later coined the 'first quantum revolution'. As much as condensed-matter physics was at the forefront then, we are currently witnessing its primary role in the early days of the 'second quantum revolution' [2, 3]. Compared to the 1960s, however, the length scales of the condensed-matter systems involved in state-of-the-art technology have changed significantly. While early lasers and transistors were operating on macroscopic scales, modern quantum technology rapidly approaches the length scales of single atoms and molecules. Hence, nanoscale-sized structures made of metals, semiconductors, insulators and, most often their hetero-structures, lie at the heart of this new technology. Exploring their extraordinary properties is the key challenge to harness the unprecedented technological potential of these new materials. The goal of this thesis is to contribute to this challenge by providing novel insights into the properties of semiconductor nanowires, which are currently emerging as a fundamental building block of modern quantum technology [4–12].

With micron-scale lengths and lateral dimensions on the order of a few tens to a few hundreds of nanometers, semiconductor nanowires are interesting objects in the class of nano-materials. Given their wire-like shape, they represent a natural medium for directional transport at the nanoscale–for light guided along the wires, as much as for electric charges. In the light guiding perspective, nanowires are sub-wavelength waveguides, making their study a prominent subject in the field of nanophotonics, where they recently demonstrated a number of peculiar light-matter interactions [7–9]. In the electronic perspective, the term 'nanowire' has inherited a certain ambiguity. Diameters approaching the micron-scale in some examples, allow us to regard the wires as bulk-like electronic structures. In stark contrast, nanowires with diameters on the order of a few tens of nanometers strongly confine electrons in two spatial directions, reducing their electronic dispersion to the one-dimensional regime.

It is interesting to note in this context, that the rotational symmetry of nanowires gives rise to a single parameter, which determines many of the relevant properties: the wire diameter. With the possibility to freely tune this parameter, the nanowires cross different regimes in both, the electronic and the optical perspective. In this thesis, we thus present our newly developed approach for the synthesis of size-tunable semiconductor nanowires with diameters ranging from a few tens to a few hundreds of nanometers. As much as it challenges the synthesis process, this approach is rewarding our experiments: It allows us to track any measurable observable while tuning the wire diameter and thus paves the way for a number of systematic measurement series.

Hence, our thesis is structured into three objectives:

Firstly, we will prove that tuning the diameter in such a series reveals a shift in the band gap upon reaching the smaller nanowires. As a clear signature for spatial quantum confinement, this evidences the quantum regime in nanowires.
Secondly, spin transport and relaxation, both prominent topics for future information processing schemes, are directly linked to the electronic state of the system. Inducing the electronic transition by tuning the diameter into the quantum regime therefore promises a unique opportunity for the study of spin physics in nanowires. Promising, indeed, since presumptions have been expressed about an exceptional spin coherence of electrons in the quantum-dominated regime [13–16].
Thirdly, to study the aforementioned waveguide nature of nanowires, the advantage of the diameter-controlled approach is eminent. Given their diameters on the order of one hundred nanometers, nanowires are in fact sub-wavelength, one-dimensional waveguides for photons with wavelengths in the visible and infra-red range. If dominant, tuning the diameter in a measurement series should reveal the role of this sub-wavelength waveguide nature in nanowire experiments.

It is particularly attractive that these diverse physical concepts can actually all be studied in experiments by optical spectroscopy. We utilize confocal micro-photoluminescence spectroscopy for the optical excitation of single nanowires with lasers operating either in continuous-wave, or pulsed mode. The near-resonant laser photons excite electron-hole pairs, which subsequently recombine to emit a luminescence photon–the principle observable in these experiments. Beyond the investigation of photonic effects, directly measuring the optical band gap in micro-photoluminescence is an excellent means to probe the effects of quantum confinement in our nanowires. Moreover, involving circularly polarized lasers, it should allow us to first optically generate a non-equilibrium spin ensemble in single wires and then monitor the dynamic depolarization of these spins.

Following this introduction, the thesis is eventually structured into four main parts:

Part I The first part is dedicated to the fundamental concepts of the physics explored in our experiments. We begin this conceptual account with a discussion of

the general properties of the unusual wurtzite crystal phase of GaAs in our nanowires. Following an introduction of the optical processes involved in our experiments, we illustrate the principle of optical spin orientation and the main interactions of spins in a solid-state environment. Chapter 3 introduces the technical aspects of our experimental setup and exemplifies the different measurement configurations applied in the course of this thesis. The following chapter is concerned with the fabrication of GaAs nanowires in molecular beam epitaxy and our strategy to obtain phase pure wurtzite GaAs in our wires.

Part II Perpetuating the discussion of the fabrication process, the second part begins by demonstrating some of the first experimental results. We debate the particular challenges met in the fabrication and ultimately outline our approach to synthesize a diameter-tunable sample series.

Chapter 6 is devoted to a study of the diameter-dependent quantum confinement in our wires, its effects on the photo-carriers and a discussion of the term *one-dimensional*. We further show the confinement effects on the internal properties of the excitons in our nanowires.

Part III Having established the nanowire system conceptually, as well as experimentally, we proceed by presenting our detailed study of spin phenomena in nanowires. Successfully evidencing the optical injection of spins into single, free-standing wires for the first time, we directly unveil their peculiar relaxation dynamics in Chapter 7. Our experimental investigation of the diameter-dependent spin relaxation is followed by a detailed theoretical account of the spin relaxation processes in nanowires. The exceptional spin coherence and other effects in the quantum-dominated wire regime are discussed.

Part IV The last part of this thesis addresses the photonic effects in our sub-wavelength wires. Focusing on the recombination dynamics of free excitons, our study reveals the waveguiding nature inherent to semiconductor nanowires, which allows us to experimentally demonstrate a number of nanophotonic phenomena. Moreover, in Chapter 12 we continue to investigate the peculiar nanoscale interactions as they occur between excitons in nanowires and surface plasmon polaritons in metallic structures.

A last chapter is appended to summarize the work of this thesis and to conclude on the objectives reached. Finally, we review recent literature reports to give an outlook on a possible direction joining spin-related and nanophotonic effects in semiconductor nanowires.

Fundamentals, concepts and experiment

2

Wurtzite GaAs nanowires: From spin physics to nanophotonics

Almost perfectly cylindrical, NWs represent an interesting, wire-like model system to test the laws of solid-state physics at the nanoscale. In particular semiconductor-based NWs are well-suited for this task, since their epitaxy provides a route to practically defect-free crystal lattices–a promising setting for the observation of elaborated physical phenomena. In this thesis, we present two particular aspects of such phenomena: Firstly, we focus on the spin physics involved with optically excited carriers in semiconductor NWs, and secondly, we investigate the peculiar nanophotonic interactions, which occur in this process. In this first part, we introduce the basic concepts behind these physics and present the experimental techniques to study these effects. At the beginning, we will discuss the fundamental material properties of GaAs, a very well-known semiconductor, which, as it happens, adapts a new crystal phase in our NWs.

2.1 Fundamental properties of wurtzite GaAs

As a III-V semiconductor with an optical band gap in the near-infrared part of the electromagnetic spectrum, gallium arsenide (GaAs) evolved into one of the most studied materials in solid-state optics and opto-electronics. From band structure parameters like the effective mass or the Bohr radius, to record high carrier mobilities, its electronic properties in the zincblende (ZB) crystal phase were precisely mapped and well-documented in the past fifty years [17]. With the advancements in nanofabrication techniques, now a new crystal phase of GaAs became accessible in Vapor-Liquid-Solid grown NWs. In this new phase, the Ga and As atoms are arranged in a wurtzite (WZ) crystal lattice, rather than in the bulk-stable zincblende lattice.
At first glance, the two crystal structures are not so different at all. In fact, as schematically illustrated by the colored ball-and-stick models in Fig. 2.1, the tetrahedral bonding of a single atom with its nearest neighbors is identical in both cases and the two structures differ only in the position of the next nearest neighbors. As a direct consequence only the

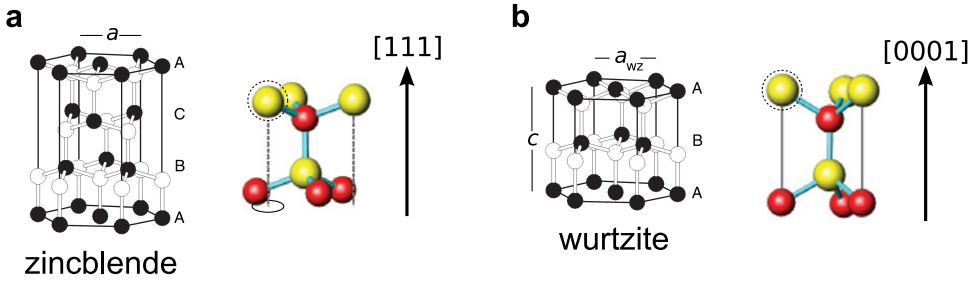

Figure 2.1: Crystal structure and stacking sequence of (a) zincblende and (b) wurtzite phase of GaAs. Italic letters indicate the lattice constants in both unit cells. Pictures on the right-hand side show a zoom in on the environment of the tetrahedral bonding and point out the different distances to the third-nearest neighbor (dashed circle) in wurtzite along [0001] direction and zincblende along [111] direction respectively. Adapted from Ref. [18, 19].

stacking sequence of pairs of group-III and V atomic layers along the ZB [111]-direction, or the WZ [0001]-direction distinguishes the two crystals: the ABCABC sequence of ZB transforms into a ABABAB stacking for WZ, entailing different lattice parameters for the WZ phase; c along the [0001]-direction, respectively called $\hat{c}$-axis, and a_{wz} in the directions perpendicular to this axis. For an ideal wurtzite structure, the lattice constants of the ZB and WZ crystal structure are linked by $a_{wz} = a_{zb}/\sqrt{2}$ and $c = \sqrt{8/3}\, a_{wz}$ [20]. Interestingly, this arrangement of atoms creates a singular axis, the $\hat{c}$-axis, with unique rotational symmetry in the WZ lattice, which has important consequences for the symmetry of the spin-orbit coupling (SOC), as will be discussed Section 2.4.2.
Appearing exclusively in NWs, the fundamental properties of this new phase of GaAs are of course much less known compared to ZB GaAs. According to the more recent reports [21–24], the low-temperature band gap is of the order of ∼1.5 eV and thus comparable to the band gap of bulk ZB GaAs [17]. However, a look at the reduced dispersion $E(k)$ in Fig. 2.2a already shows a prominent difference to the band-structure of ZB GaAs in the bulk: At the top of the valence band, the heavy hole (hh) and light hole (lh) bands are split by an energy $\Delta_{hh/lh}$ with values differing between experimental [23, 25] and theoretical reports [20], but always of the order of 100 meV. This detail of the band structure turns out to be advantageous over bulk ZB GaAs, where hh and lh states are degenerate at $k = 0$. Using the right photon energy, the splitting facilitates the singular excitation of electrons from hh states into the conduction band (cb), which has important consequences for optical spin injection, as outlined in Section 2.4.1.
Only the most rudimentary of the electrons' properties are captured by the simplified schematic shown in Fig. 2.2a. Intricate details of the electronic band-structure, such as the anisotropy of the effective masses, the effective g-factor tensor or complex spin-orbit textures in the electronic dispersion, eventually require sophisticated theoretical treatment. While previous efforts were directed towards calculating the WZ GaAs band-structure, the values of the reported fundamental gap alone, spanning from 1.4 to 1.6 eV [20, 26],

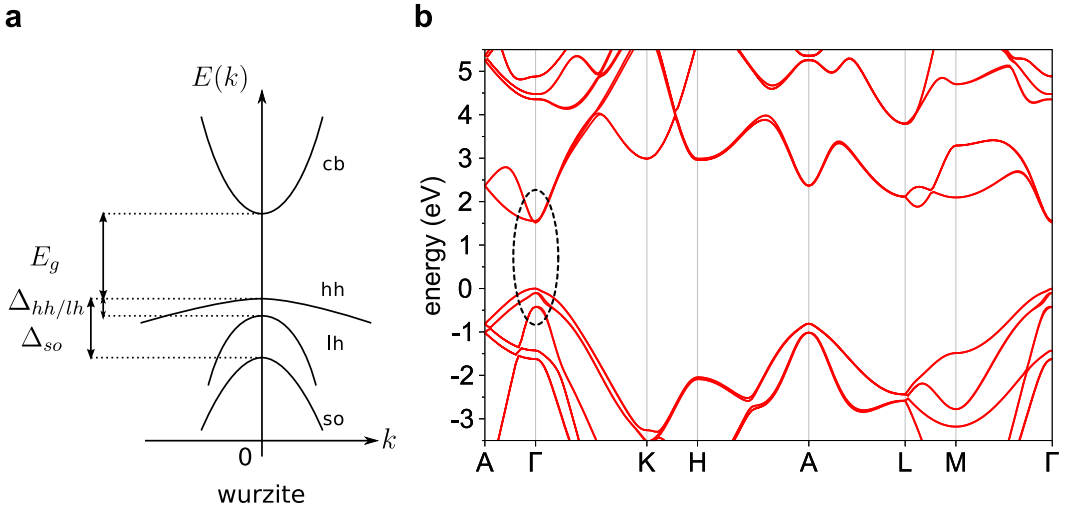

Figure 2.2: (a) Simplified band diagram of WZ GaAs around $k \approx 0$. (b) Preliminary results of the band-structure calculation of WZ GaAs along high symmetry lines of the first Brillouin zone based on a fully ab initio approach. Courtesy of Paulo E. Faria Junior. The dashed ellipse demonstrates the actual band dispersion around $k \approx 0$, contrasting the simplified diagram in (a).

demonstrates the complexity of the task. To estimate the effects of spatial confinement in Section 6.1 of this thesis, we resort to the parameters calculated in Ref. [27], as they show the best agreement so far with our experimental results on the optical band gap of WZ GaAs ($E_{gap} \approx 1.52$ eV).
We note, that combining the values of the optical band gap accessible in our experiments with a sophisticated theoretical approach,[1] efforts lead by Paulo E. Faria Junior to calculate a realistic band-structure of WZ GaAs are currently under way. Figure 2.2b presents a preliminary result of these efforts, illustrating the complexity of the actual band-structure, as opposed to the sketch shown in Fig. 2.2a. Once successfully implemented, such an approach has the potential to reveal the currently unknown effective g-factors of WZ GaAs, the effective masses and even the exchange splitting, sharing interesting perspectives for future joined efforts between theory and experiment.

2.2 Photoluminescence and sub-wavelength nanophotonics

Throughout the history of semiconductor research, observing the response of a semiconductor to an external electromagnetic wave has been a primary source of information. Often enough, the object under study absorbs the electromagnetic wave in a way that its

[1] Ab initio calculations are based on the density functional theory using the screened hybrid functional with the Perdew-Burke-Ernzerhof version for the semilocal generalized gradient approximation functional.

energy releases a bound electron from a deep energy level and excites it into a state, in which it resembles a free electron. After interacting with the crystal lattice in various possible ways, the quasi-free electron recombines with the unoccupied low-energy state it has left behind. In case a photon is emitted in the recombination event, we refer to the process as *photoluminescence*. This photon contains a great deal of information. Properly detecting its energy and polarization state, as well as the dynamic evolution of its intensity (meaning a number of photons, if we repeat the experiment many times), or even the point in space, where it originated from, is very instructive and often allows an inference about the interaction processes between the electron and the crystal afterwards. Of course other processes, such as reflection, or scattering, also take place when electromagnetic radiation is directed onto a semiconductor. The retarded time scale of the luminescence process, however, strictly differentiates it from these (quasi-) instantaneous processes. To obtain a deeper understanding of the fundamentals behind the process of photoluminescence, we provide a more detailed account of the photo-emission in the following.

2.2.1 Spontaneous emission at the nanoscale

Emitters can undergo a transition from an excited state to a lower-in-energy state by spontaneously emitting a photon. Such emitters can be atoms or molecules in an excited state, as well as solid-state excitations like excitons or free electron and hole pairs. In this process, the term *spontaneous* reflects the fact, that the exact moment of the decay cannot be predicted. Thus, to quantify the statistics, the inverse of the excited state lifetime is introduced as a rate to account for the probabilistic nature of the decay. Often, during the long time in which this spontaneous emission process has been studied (for more than a century at least, taking Hertz's work as a cornerstone [28, 29]), this rate of spontaneous emission was believed to be an inherent property of a material. Only until in 1927, when Dirac laid out the foundation of quantum electrodynamics in his newly developed quantum theory of light [30], it was recognized that an emitter radiates its excess energy into discrete photon states, called electromagnetic modes. This process is sketched in

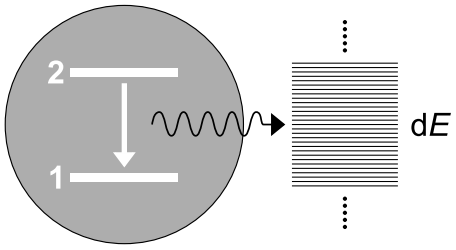

Figure 2.3: A two level system undergoes a transition from an excited state to a lower-in-energy state by spontaneous photon emission. As indicated by the discrete energy levels on the right hand side, this photon is emitted into a discrete set of electromagnetic modes. Sketch adapted from Ref. [28].

Fig. 2.3, illustrating the radiative decay of a two-level system (representing the excited

emitter) into a discrete set of such modes. We emphasize that the quantum description of spontaneous emission entails yet another very fundamental viewpoint: The spontaneous decay of excited atoms is now interpreted as an emission process enforced by the action of the fluctuating quantum vacuum field [31].
Following the approach by Wigner and Weisskopf [32], who soon after Dirac's theory derived the spontaneous emission rate of an isolated emitter in free-space, we analogously find the spontaneous emission rate Γ for an emitter embedded into a dielectric solid-state environment [28, 33]:

$$\Gamma = \frac{2\pi\mu_{12}^2 {E_0}^2}{\hbar^2}\rho(\omega_0)\,. \tag{2.1}$$

Here, $\hbar\omega_0$ is the energy difference between the initial and final states, μ_{12} is the dipole matrix element of the two states and E_0 is the electric field generated by a single photon at the location of the emitter. Most relevant for this thesis, and corresponding to the process sketched in Fig. 2.3, the rate in Eq. (2.1) depends on $\rho(\omega_0)$, the electromagnetic local density of states (LDOS). Highlighting its cornerstone role in general for nanophotonics, and more particularly for the fields of cavity quantum electrodynamics and plasmonics, Pelton [33] paraphrases the physical origin of the LDOS:

> "The spontaneous emission rate is proportional to the electric field that the emitter produces at its own location. This self-generated field, in turn, depends on the polarization that the emitter induces in its environment."

His reasoning already indicates, that a modification of the emitter's dielectric environment may have an effect on the spontaneous emission process.
In fact, already in 1946, Purcell found that this LDOS is easily modified by placing an emitter into a photon cavity [34]–a discovery, which laid the foundation stone for the concepts of photonic crystals developed much later from the seminal work of Hulet [35] and Yablonovich [36]. In such structures, a periodically modulated dielectric environment determines the vacuum modes and thus the spontaneous emission of deterministically placed emitters. Apart from these photonic crystals, the local field enhancements near plasmonic structures have also been used extensively to modify the spontaneous emission rate [33].
Until recently, the considerable modification of spontaneous emission in dielectric nanoparticles has gathered much less attention. To observe an effect on the spontaneous emission rate (cf. Eq. (2.1)) of single emitters embedded in such particles, the nanoparticle size should be of the order of the wavelength of the emitted photons, or smaller, to modify the LDOS. The term *sub-wavelength* usually refers to objects which are smaller than the vacuum wavelength of the interacting light. A model system in this regard are single atoms placed inside nanoscale-sized dielectric spheres [37, 38]. These nanospheres were theoretically predicted to strongly enhance the spontaneous emission of the atoms in the case of resonance, or instead inhibit the spontaneous emission rate substantially in the deep sub-wavelength diameter-regime. Depending on the refractive index of the dielectric material and the exact position of the single emitters inside the nanospheres,

their spontaneous emission lifetime was calculated to vary extensively, over three orders of magnitude [37]. Studying the emission lifetime of single atoms inside dielectric spheres, the predicted effects were investigated in 2002 in a luminescence approach [39]. Unfortunately, a luminescence experiment probes all decay channels, including non-radiative effects; as a consequence the strong inhibition of spontaneous emission could not be observed. Indeed, a luminescence experiment may only unambiguously reveal spontaneous emission lifetimes, if non-radiative effects are not limiting the decay.
Conceptually analogous to the spherical problem is the model of single emitters embedded in an infinitely long dielectric cylinder with sub-wavelength nanoscale diameter. This model is of particular interest for the work in this thesis. Following the argumentation of Ref. [37], the spontaneous emission rate of such a single emitter in a cylinder should behave in a similar fashion compared to the spherical problem, i.e., resonant and sub-wavelength effects on the spontaneous emission rate may occur. In fact, in the electrostatic limit, a straightforward analysis predicts an inhibition of spontaneous emission by $4/[n(n^2+1)^2]$, when the diameter of the dielectric cylinder is much smaller than the vacuum wavelength of the emitted light and n is the refractive index of the cylinder material. For a single emitter embedded in a cylinder made of bulk GaAs with a refractive index $n = 3.45$, this simple model would result in a remarkable reduction of the spontaneous emission rate, by a factor of 144!
Getting to the bottom of these considerations, photoluminescence spectroscopy can be a powerful tool. We will discuss its working principle in the following, before we address the optical excitations involved in the luminescence approach.

2.2.2 The principle of photoluminescence

In a photoluminescence (PL) experiment, the electromagnetic waves used to excite the electrons in a semiconductor, are usually monochromatic and generated from a laser source operating in continuous-wave, or in a pulsed mode. In such a setting, the excitation is non-resonant, when photons with a definite wave vector $\mathbf{k}$ and an energy $h\nu$ exceeding the semiconductor band gap are absorbed. Since the wavelength of the laser photons $\lambda = c/\nu$ is always large compared to the lattice constant a of the solid, the magnitude of the photon wave-vector $|\mathbf{k}| = k$ is small compared to the characteristic dimensions of the Brillouin zone, $2\pi/a$, and we can therefore disregard its effect for the moment.
A most simple picture of the PL process is schematically illustrated in Fig. 2.4a. A laser photon with energy $h\nu'$ excites an electron into the conduction band, leaving behind an unoccupied hole state in the valence band. Due to the non-resonant excitation, an excess energy $h\nu' - E_g$ is imprinted onto the photo-excited electron-hole (e-h) pair; both particles undergo momentum relaxation processes which direct them towards the extrema of the bands. Here, at $k \approx 0$, electron and hole recombine under emission of a luminescence photon. Note that the photon-related transitions in Fig. 2.4a are vertical in k-space, because we neglect the photon momentum.
In reality, such a simplified description of the PL process at best describes a situation in which free electron and hole pairs are the relevant elementary excitations in the crystal.

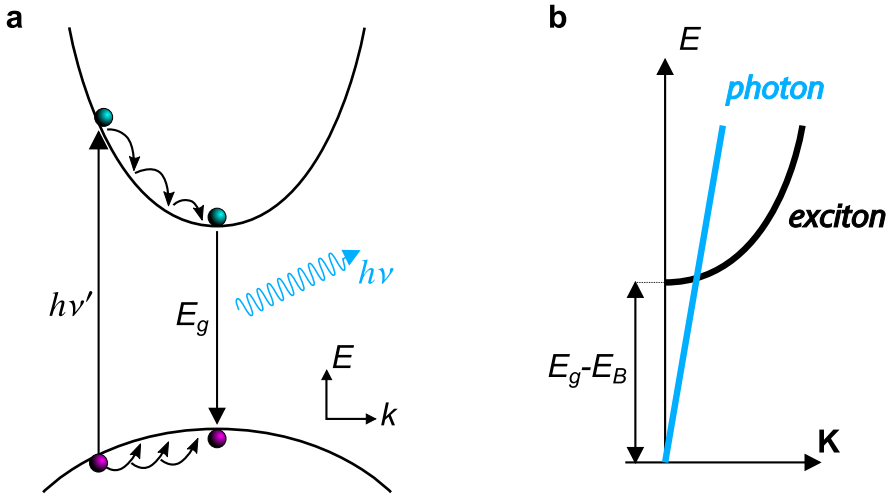

Figure 2.4: (a) A simplified band diagram illustrates the principle of PL spectroscopy: An electron in the lower band absorbs a photon with an energy $h\nu'$ above the band gap E_g and leaves behind a hole. The electron (hole) moves to the minimum (maximum) of the band via momentum relaxation processes, where the radiative recombination annihilates the e-h pair under the simultaneous creation of a photon with energy $h\nu$. However, the physical reality of experiments is generally more accurately represented by the diagram shown in (b). Coulomb interaction binds the e-h pair into an excitonic state, which is characterized by its own dispersion $E_{kin} = \hbar^2 K^2/2m_{exc}$ (black parabola). The photon emission process is liable to the strict energy and momentum conservation rule; its linear dispersion is shown in blue.

In most experimental scenarios, however, this is not the case and the simple picture drastically misrepresents the physical reality. The reason for its failure lies in disregarding the fact, that photo-excited electrons and holes are interacting through attractive Coulomb forces. Indeed, together electron and hole form a bound state called the exciton. Typically two types of excitons are discerned [40]: (i) The *Frenkel* excitons; localized on a length scale comparable to the unit cell of the crystal, these small-radius excitons mostly occur in molecular crystals. (ii) The *Wanner-Mott* excitons; as weakly bound e-h pairs they are spread over many unit cells, but still dominate the optical properties of semiconductors at low temperatures and carrier densities. This type of exciton occurs in III-V semiconductors under optical excitation and, analogous to the description presented in Ref. [40], we will discuss their most important properties in the following.

2.3 Optical excitations in semiconductors

2.3.1 Wannier-Mott excitons in III-V semiconductors

If we consider a single e-h pair in a semiconductor, the two oppositely charged particles are subject to an attractive Coulomb potential

$$U(r) = -\frac{e^2}{4\pi\epsilon_0\epsilon r}, \tag{2.2}$$

where ϵ and ϵ_0 account for the static dielectric constant in the semiconductor and in vacuum, e is the elementary charge and r is the e-h distance. Equation (2.2) illustrates why excitons are often referred to as 'hydrogen-like' states; regarded as point charges with effective masses m_e and m_h, the Coulomb-bound e-h complex can be well-described in the language associated with two oppositely charged particles circulating around each other. The first prominent difference between the hydrogen atom and the Wannier-Mott exciton in this comparison is the lack of a much heavier particle in the latter (the hole mass is typically larger, but both electron and hole effectives masses are still of the same order of magnitude). Another point lacking similarity arises from the dielectric constant of the crystal, which on the one hand hosts the electron and the hole, but on the other hand efficiently screens their mutual electrostatic attraction. Noting the actually much better analogy between an exciton and positronium–a bound state between a light electron and an equally light positron–Keldysh makes a very interesting point [41]. Both of the above mentioned flaws in the analogy decrease the binding energy of the exciton compared to the hydrogen atom and at the same time increase the distance between the two opposite charges, as we will now discuss.
Sticking to the hydrogen picture, we can derive the exciton Bohr radius a_B from the Bohr radius a_B^* of the hydrogen atom [40]:

$$a_B = \frac{\epsilon}{(m_r/m_0)} n^2 a_B^* . \tag{2.3}$$

Here, $n = 1, 2, 3, ...$ is the principal quantum orbit number, $m_r = (m_e m_h)/(m_e + m_h)$ is the reduced exciton mass and m_0 is the free electron mass. The value of a_B typically associated with excitons in this context refers to its ground state with quantum number $n = 1$. For bulk GaAs, the exciton Bohr radius is ~14 nm [42].
In a similar way we get the binding energy of the exciton ground state from the binding-, or ionization energy, $Ry = 13.6\,\text{eV}$, of the hydrogen atom:

$$E_B = \frac{(m_r/m_0)}{\epsilon^2} Ry\,. \tag{2.4}$$

We immediately see from Eq. (2.4), that the effective mass ($m_r/m_0 \approx 0.1$), as well as the dielectric constant significantly reduce the stability of excitons in typical semiconductors ($E_B = 4.2\,\text{meV}$ in bulk GaAs [42]). Multiplying Eqs. (2.3) and (2.4) renders a compact account of the crystal effect on the energy and length scales of the ground state exciton in the hydrogen picture:

$$a_B\, E_B = (a_B^*\, Ry)/\epsilon\,. \tag{2.5}$$

Dissociation of excitons at elevated lattice temperatures ($k_B T \approx 26\,\text{meV}$ at 300 K) is eventually the reason why excitonic effects occur only at low temperatures in conventional bulk III-V semiconductors like GaAs, InP, GaSb. With an exciton binding energy of 28 meV, bulk GaN makes an exception to this rule and allows the observation of excitonic optical features even at room temperature. Keldysh realized early on, that the key to enhancing the exciton binding energies in semiconductors, is to reduce the effect of the dielectric screening in low-dimensional systems [43]. We will encounter this exact effect later in the thesis (cf. Section 6.2) when we address the properties of excitons confined in our NWs.
As a quasiparticle moving through the crystal, free excitons are assigned a wavevector $\mathbf{K}$ ($|\mathbf{K}| = K$), a quasi-momentum $\hbar\mathbf{K}$ and a kinetic energy term $E_{kin} = \hbar^2 K^2/2m_{exc}$. Here $m_{exc} = m_e + m_h$ denotes the total mass of the exciton, which defines the dispersion for excitons in the ground state

$$E(\mathbf{K}) = E_g - E_B + \frac{\hbar^2 K^2}{2m_{exc}}\,. \tag{2.6}$$

This parabolic dispersion is shown in Fig. 2.4b. Interestingly, one apparently rather small detail makes all the difference to the dispersion shown in Fig. 2.4a: in the excitonic picture, as long as we exclude multi-particle processes, excess energy and wave vector cannot be imprinted onto a valence band electron after the recombination; the entire crystal must be in its ground state after the radiative recombination [44].
Indeed, a very strict selection rule governs the radiative decay of free excitons in semiconductors; both energy and momentum of the exciton must exactly match the photon dispersion $E(K) = h\nu = \hbar c K/\sqrt{\epsilon_\infty}$, where ϵ_∞ is the high-frequency dielectric constant. In Fig. 2.4b, this corresponds to the intersection point of photon and exciton dispersions. Since only a small number of the thermally distributed excitons in a semiconductor

around $K \approx 0$ fulfills this selection rule, a large portion of the free excitons in fact do not contribute to the luminescence signal [45, 46]. For completeness we note, that this description still does not consider the polariton-effect on the exciton dispersion [47]. With less than 100 µeV, Van der Poel *et al.* conclude that the polariton splitting-induced oscillations in bulk GaAs occur on a time scale of ~10 ps, long compared to the typical scattering times of free excitons, which prevents the build-up of coherence between photon and exciton-coupled states [45].

2.3.2 The many-body electron-hole plasma

The excitonic picture outlined above per se considers only a single exciton. What happens when a large number of excitons is created in a semiconductor under photo-excitation is as relevant a question as it can be complex to answer. In a luminescence experiment, the excitation power density of a laser can easily generate a high enough number of photo-carriers in a semiconductor so that this question can no longer be ignored [40, 41, 48, 49]. Merely touching the interesting field of many-body physics in optically excited semiconductors, we briefly address the effects most important for our study in the following.

Under increasing laser excitation power, more and more excitons are created and the gas of initially free excitons becomes more densely packed in the semiconductor. The attractive potential of a single e-h pair gets screened by free charge carriers, since some excitons are thermally dissociated even at low temperatures [40]. The potential in Eq. (2.2) becomes

$$U(r) = -\frac{e^2}{4\pi\epsilon_0\epsilon r}\exp(-k_s r), \tag{2.7}$$

where k_s is the screening factor associated with the so-called screening length $\lambda_s = k_s^{-1}$. Upon reaching the Mott density, where λ_s becomes comparable to the exciton Bohr radius a_B, the Coulomb-bound e-h complex is no longer stable and the excitons undergo a many-body phase transition. They transform into an e-h plasma [40].

For bulk GaAs below 10 K, this critical Mott density is $n_M \approx 2\times10^{16}\text{cm}^{-3}$ [48]. It is interesting to note, that the high-density e-h system can in principle transform into many different many-body states; a metallic e-h liquid, Bose-Einstein condensation and, supposedly, even a superconducting phase are possible. We will revisit aspects of this topic in a discussion about the effects of high excitation power in quantum-confined 1D wires in Section 6.4.2.

In the plasma state, electrons and holes are regarded as a perfect gas of free electrons and holes. While this description differs conceptually from a gas of free excitons in many respects, the two phases are not so easily discriminated in optical experiments. Since the exciton gas gradually transforms into the plasma state under increasing e-h pair density, the two different phases are not strictly defined in the transition region. To theoretically describe our NW experiments presented in the course of this thesis, however, it is important to know which carrier description is to apply. We therefore estimate the

optically excited e-h pair density in our NWs in Section 3.2.

2.3.3 Dynamics of the photo-excited electron-hole system

So far we have addressed the static properties of photo-excited excitons and e-h pairs in semiconductors. Now we will discuss their dynamic properties typically observed in time-resolved PL experiments after excitation with a laser pulse that is short compared to the dynamic response.
Of course, spontaneous emission is the process which eventually underlies the radiative e-h recombination and in Section 2.2 we have already introduced its rate for a single emitter embedded in a solid-state environment. Thus we should be able to measure the rate of spontaneous emission given in Eq. (2.1), or vice versa of the radiative free exciton lifetime $\tau_r = 1/\Gamma$, by resolving the luminescence emission in the time domain. Unfortunately, two main obstacles typically inhibit the direct measurement of this radiative free exciton lifetime in time-resolved luminescence experiments.
First of all, non-radiative recombination can significantly affect the lifetime observed in the luminescence decay. To demonstrate this effect, we consider a total density n of excitons generated by a short laser pulse at $t = 0$. In this description, we assume the excitons to be localized emitters in space, which can undergo both radiative and non-radiative decay processes, respectively characterized by the lifetimes τ_r and τ_{nr}. In this case, the time-dependence $\mathrm{d}n/\mathrm{d}t$ of the exciton density can be described as [40]

$$\frac{\mathrm{d}n}{\mathrm{d}t} = -\frac{n}{\tau_r} - \frac{n}{\tau_{nr}} = \frac{n}{\tau_{tot}}\,. \tag{2.8}$$

According to Matthiessen's rule, we have introduced the total emission lifetime τ_{tot} accounting for all radiative- and non-radiative recombination processes. The temporal decay of the luminescence intensity in the experiment is then given by

$$i(t) = i(0)\exp(-t/\tau_{tot})\,, \tag{2.9}$$

with $i(0) = n(0)/\tau_r$ representing the intensity at $t = 0$. Observing the time-dependent decay of the total luminescence signal thus clearly depends on the relative contributions from radiative and non-radiative processes. It is interesting to note that, although observing the decay of a luminescence signal in the experiment, Eq. (2.9) implies that the decay can actually correspond to the non-radiative decay lifetime in the case of $\tau_r^{-1} \ll \tau_{nr}^{-1}$. Of course, the radiative lifetime τ_r must still produce a sufficiently large intensity $i(0) = n(0)/\tau_r$ so that the decay can still be detected in the experiment.
Only in the absence of significant non-radiative recombination, when $\tau_{nr}^{-1} \ll \tau_r^{-1}$, can the luminescence decay be associated with the radiative lifetime τ_r. In Chapter 10 we will discuss this point and argue that non-radiative effects do not significantly contribute to the luminescence decay observed in our NWs. Yet, even in the absence of non-radiative

exciton recombination, differentiating between the radiative lifetime τ_r and the lifetime τ_{pl} observed in our luminescence experiments is very important. This is related to the second of the above mentioned obstacles. In contrast to the assumption used to derive the rate of spontaneous emission in Eq. (2.1), free excitons are not perfect point-like emitters. In fact, created under non-resonant excitation, the exciton ensemble is characterized by a thermally distributed kinetic energy. Thus, only a small fraction of the total number of free excitons can fulfill the strict energy and momentum selection rule dictated by the photon dispersion and participate in the radiative decay [44–46, 50]. In GaAs quantum wells, for example, the lifetimes measured in PL experiments are in the ns-regime, despite the intrinsic 25 ps radiative lifetimes calculated in a straightforward formalism corresponding to the spontaneous emission rate given in Eq. (2.1). This means that the lifetimes measured in PL experiments always include a contribution from the thermal distribution of excitons and possibly also dynamic re-occupation effects of those exciton states, which are close to the center of the Brillouin zone where the radiative recombination occurs. This description is valid as long as the thermalization time of excitons is shorter than the intrinsic radiative lifetime [44].
In summary, the decay of the free exciton emission observed in time-resolved luminescence experiments does not allow for a direct determination of the radiative lifetime, or vice versa the spontaneous emission rate, as it is given in Eq. (2.1). The reason for the discrepancy is the above mentioned thermal distribution of excitons and the wave vector conservation rule.
Correctly interpreted, however, the measured lifetime τ_{pl} still contains important information about the radiative recombination process. An effect that has not only been disregarded in our above discussion, but also in most previous studies of luminescence lifetimes in bulk, or two dimensional III-V based structures [44–46, 50], is the effect of the electromagnetic local density of states (LDOS) on the luminescence lifetime. The reason for that is simple: When we vary the thickness of a GaAs layer, even if it is a quantum well buried between layers of AlGaAs, the LDOS effectively remains constant and does not noticeably affect the luminescence decay, as long as the volume of the sample is large compared to the wavelength of the emitted light. Thus, the particular effect of the LDOS on the luminescence lifetime has so far only been studied in the context of photonic crystals and plasmonic structures. In Chapter 10 of this thesis, we will investigate the effect of the LDOS on the luminescence lifetimes in our nanoscale-sized wires.

2.4 Spin physics in wurtzite GaAs

As outlined in the introductory part, a particular focus of this thesis is the investigation of spin-related phenomena in semiconductor NWs. Generally, we use the absorption of circularly polarized photons in the direct-gap WZ GaAs NWs to create a non-equilibrium spin polarization amongst the photo-excited carriers and then observe their polarized photoluminescence emission to learn about any spin-related processes.

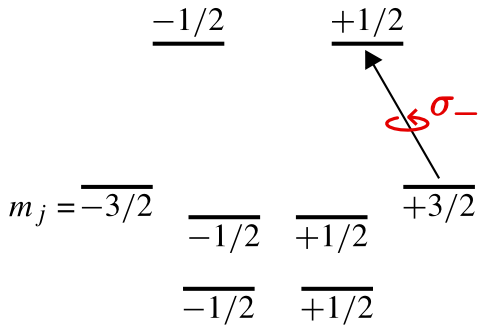

Figure 2.5: Schematic of the states around $k \approx 0$. Only the hh states ($m_j = \pm 3/2$) are involved in the optical spin orientation process for near-resonant laser excitation. Circularly polarized σ_- photons induce the singular transition into a $m_j = +1/2$ cb state.

2.4.1 Optical spin orientation

To excite a spin polarization in our NWs, we make use of a fundamental law of physics–the conservation of angular momentum. Traveling as a plane wave, a circularly polarized photon with helicity $\sigma = \pm 1$ indeed carries an angular momentum, which points either along, or opposite, to the direction of propagation. Assuming it has enough energy to induce an interband transition in the semiconductor, the photon can transfer its angular momentum to the excited e-h pair during the absorption process [51]. This method, called optical orientation, or optical spin injection, is a standard technique for the study of semiconductor spin physics [52, 53].
We will now take a closer look at the optical spin orientation and how it occurs in WZ GaAs. First of all, since optical transitions are involved, we must consider the transition dipole selection rules in the material. Indeed, the symmetry of the WZ lattice dictates a particular set of optical selection rules [54], of which one is important in our context. This rule implies that optical transitions between hh and cb states are only possible, if the polarization of the incoming light is pointing in a direction perpendicular to the WZ $\hat{c}$-axis, i.e., when $E \perp \hat{c}$. Regarding a circularly polarized photon as a superposition of two orthogonal linear polarizations, it is clear that the two components can only be equally absorbed by the crystal, if both polarizations are pointing perpendicular to the $\hat{c}$-axis. Only a photon propagating along the $\hat{c}$-axis can fulfill this selection rule. Hence, we have already identified an important consequence for our experiment: To optically orient the spins in our WZ NWs, the circularly polarized excitation photons must propagate parallel to the $\hat{c} \parallel$ NW-axis. To satisfy this condition, we investigate the NWs in our optical setup as they are free-standing on the growth substrate. As a consequence, the optical spin injection into NWs lying on a substrate is not possible. In the following, we now discuss the transfer of angular momentum in the absorption process when the circularly polarized photons are propagating along the $\hat{c}$-axis and the angular momentum is thus properly absorbed by the crystal.
Having p-type character, the valence band states near the fundamental band gap of the

WZ crystal are states with total angular momentum $J = 3/2$, which may be subdivided into hh and lh states by the projection of J onto the positive z-axis; $m_j = \pm 3/2$ for the hh states and $m_j = \pm 1/2$ for the lh states [51–53]. The $J = 1/2$ valence band states are called split-off (so) states and do not play a role in the physics discussed here. The sketch in Fig. 2.5 provides an overview over the different valence and conduction band states in the vicinity of $k \approx 0$. As addressed above, a circularly polarized photon with helicity $\sigma_\pm$, induces a change $\Delta m_j = \pm 1$ in the absorption process. At this point we benefit from the aforementioned advantage of the WZ phase over bulk ZB crystals: Since the WZ lattice lifts the degeneracy of hh and lh states at $k = 0$, we can use near-resonant circularly polarized laser photons to excite electrons exclusively from one of the two hh states. In this case, all of the photo-excited electrons in the conduction band will have the same spin orientation and the corresponding degree of spin polarization, defined as $P_s = (N_+ - N_-)/(N_+ + N_-)$, reaches 100%. Here, N_+ and N_- denotes the number of electrons with spins pointing along, or opposite to the propagation direction of the photons.
Hence, according to the scenario outlined above, using a near-resonant circularly polarized laser in the experiment, it should be possible to fully spin polarize the photo-excited carriers in our WZ GaAs NWs. However, constituting a non-equilibrium situation, this spin polarization will be depolarized by interactions with the crystal lattice hosting the photo-excited carriers. Particularly in non-centrosymmetric crystals, like WZ, the photo-carriers will be exposed to the consequences of a relativistic effect on the electronic dispersion, which we discuss in the following.

2.4.2 Spin-orbit coupling effects on the electron dispersion

According to special relativity, electrons moving in an electric field experience an effective magnetic field proportional to their velocity and the strength of the electric field. The interaction of the electron spin with the effective magnetic field is called spin-orbit coupling (SOC). This applies for the electric field of a single nucleus, as well as for the periodic lattice potential of a crystal and is accounted for by the spin-orbit term in the Hamilton operator, in general described by [55]

$$\mathbf{H}_{so} = \frac{\hbar}{4\, m_0^2\, c^2}\, \mathbf{p} \cdot (\boldsymbol{\sigma} \times \nabla \mathbf{V}) \,, \tag{2.10}$$

with the free electron mass m_0, the velocity of light c, the reduced Planck constant $\hbar$ and the canonical momentum $\mathbf{p}$. The vector $\boldsymbol{\sigma} = (\sigma_x, \sigma_y, \sigma_z)$ contains the Pauli spin matrices as components and $\mathbf{V}$ denotes the electric potential acting on the spin, which can be a Coloumb potential in the simple case of a hydrogen atom, or a complex periodic potential describing a crystal lattice. Since the periodic potential of the crystal lattice enters in Eq. (2.10), we expect the effect of the SOC on the electronic dispersion to differ depending on the symmetry of the crystal structure.

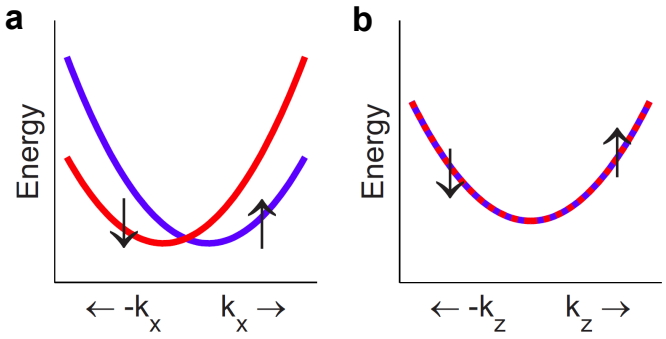

Figure 2.6: Influence of the **k**-linear splitting on the band-structure of wurtzite crystals. Schematic (a) shows the lifted degeneracy of conduction band states along k_x-direction. The second part (b) depicts the spin degenerate parabolic dispersion curve along k_z-direction. Adapted from Ref. [20]

In 1955, Dresselhaus derived the influence of SOC on the electronic band structure of ZB crystals and its effect on conduction band states using perturbation theory and group theoretical selection rules. He found that the spin degeneracy $E_{\mathbf{k}\uparrow} = E_{\mathbf{k}\downarrow}$ is lifted in crystals without inversion symmetry for several directions in the Brillouin zone, whereas the degeneracy $E_{\mathbf{k}\uparrow} = E_{-\mathbf{k}\downarrow}$ from Kramer's theorem still holds. The splitting near the Γ_6 conduction band state was determined to be cubic in **k** multiplied by a material dependent factor γ_D, hence $\Delta E_{Dresselhaus} \sim \gamma_D \cdot \mathbf{k}^3$, in all but the [111] and [100]-directions, in which the degeneracy is conserved [56].
Analogous to Dresselhaus' work on ZB, Rashba introduced in 1959 a set of perturbation operators to derive the symmetry of energy bands including spin splitting of the conduction band states in crystals of WZ structure [57]. In addition to the absence of inversion symmetry, the energy dispersion law in the vicinity of the Γ-point is strongly altered by the high symmetry of the $\hat{c}$-axis and characterized by a **k**-linear spin splitting perpendicular to it. In first order of **k**, the energy dispersion for the conduction band at the Γ-point is

$$E(\mathbf{k}) = \underbrace{ak_\perp^2 + bk_z^2}_{parabolic\ dispersion} \pm \underbrace{\gamma_R \cdot k_\perp}_{correction\ due\ to\ SOC}, \tag{2.11}$$

with γ_R as material specific factor and $k_\perp = \sqrt{k_x^2 + k_y^2}$ describes k-vectors perpendicular to the $\hat{c}$-axis, which results in a shift of conduction band states along $k_{x,y}$-directions, but leaves states in k_z-direction spin degenerate. The linear SOC coefficient was calculated in Ref. [58] for WZ GaAs and found to be $\gamma_R = 0.04\,\text{eVÅ}$. The constants a and b are simple scaling factors of the parabolic curvature.
The schematic in Fig. 2.6 illustrates the effects of SOC on the electronic dispersion law around the conduction band minimum in WZ crystals. In a direction perpendicular to k_z, the initially twofold degenerate parabolic band splits into two fully spin polarized subbands (red and blue parabolas in Fig. 2.6a). A closer look also reveals a small shift

towards negative energies for the conduction band minima of the spin-split states. It can also be observed, that Kramer's degeneracy $E_{\mathbf{k}\uparrow} = E_{-\mathbf{k}\downarrow}$ is still conserved in the dispersion depicted in Fig. 2.6. The spin-orbit fields resulting from spin split states are called *effective* magnetic fields, because in contrary to real magnetic fields, Kramer's degeneracy is not lifted. As the linear spin-splitting does not depend on k_z, the states stay spin degenerate along this direction (cf. Fig. 2.6b).
This coupling between spin and orbital motion has been a focus of solid-state research for years. First the understanding and now the subsequent exploration of SOC effects in semiconductors has led to a fruitful realization of fundamental physical concepts, as reviewed by Manchon *et al.* [59].

2.4.3 Spin relaxation in semiconductors

In the above discussion we concluded that it should be possible to create a non-equilibrium spin polarization among the photo-excited carriers in our NWs. Involving the effects of SOC on the electronic dispersion, various interactions between spin-polarized photo-carriers and the crystal host can destroy the spin polarization to restore the equilibrium state. These are the processes generally understood as spin relaxation.
Since we will evaluate the main mechanisms of spin relaxation with particular focus on their action in our NWs in Section 9.2 of this thesis, we devote our discussion in this section to an understanding of the origin behind the different mechanisms of electron spin relaxation and we thereby focus on the relevant electron spin. For further reading, we recommend the insightful reviews given in Refs. [52, 55, 60].

The Elliott-Yafet mechanism In semiconductors, the electrons in the conduction band–whether they are photo-excited, or introduced from external sources–commonly interact with the crystal lattice through the scattering of charge carriers by phonons or impurities. Even in the absence of magnetic impurities, such scattering can lead to a flip of the electron's spin if SOC is present in the crystal. Introduced by Elliott and Yafet [61, 62], this mechanism is indeed based on the admixture of spin eigenstates in the presence of SOC [52, 55, 60]. Although the admixture is generally very small (justifying the labeling of the eigenstates with 'spin up' and 'spin down'), we acknowledge that momentum scattering of electrons can be a very fast process on the femto- to picosecond time scale, thus allowing many momentum scattering events during the nanosecond lifetime of a typical photo-excited electron in a direct-gap semiconductor [40]. In an extensive theoretical investigation, Jiang and Wu have found, that the Elliot-Yafet mechanism does not significantly contribute to the spin relaxation of electrons in intrinsic bulk GaAs created under photo-excitation [63].

The Dyakonov-Perel mechanism An electron moving through a non-centrosymmetric crystal lattice experiences the conduction band states split by SOC as a momentum-dependent effective magnetic field. The spin of the electron precesses around this effective

field with an average precession frequency $\langle \boldsymbol{\Omega} \rangle$, while every time the electron is scattered and forced to change its momentum direction, the absolute value and direction of the precession around the effective magnetic field changes as well. Hence, whatever the initial orientation of the spin was, after a certain amount of random scattering events it will have lost that information due to precession around the momentum-dependent effective magnetic fields. This mechanism of spin relaxation is named after Dyakonov and Perel (DP), due to their work on spin relaxation of electrons in systems without a center of inversion in 1971 [64].
The schematic in Fig. 2.7 illustrates the initial spin orientation $\boldsymbol{S}$ of an electron (black arrow) precessing around the effective magnetic field $\boldsymbol{\Omega}(\boldsymbol{k}_1)$ (red arrow) until a scattering event occurs and the change of momentum direction ($\boldsymbol{k}_1 \rightarrow \boldsymbol{k}_2$) forces the spin to precess around a different field $\boldsymbol{\Omega}(\boldsymbol{k}_2)$.

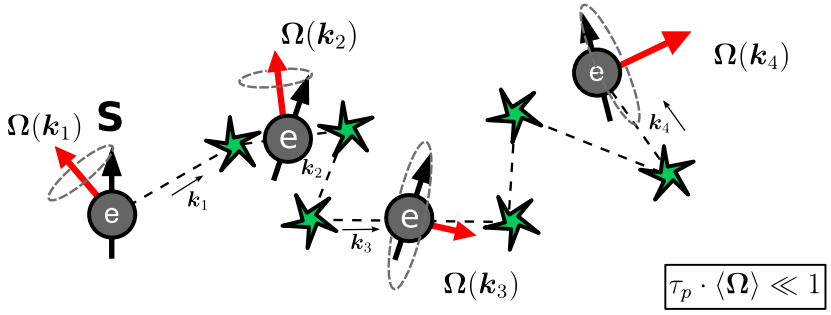

Figure 2.7: The initial spin orientation (black arrow) is forced to precess around an effective magnetic field $\boldsymbol{\Omega}(\boldsymbol{k})$ (red arrow) until a scattering event changes the momentum direction and therefore the magnetic field and the precession.

Within the process of DP spin relaxation, the momentum relaxation time τ_p, which denotes the average time between two scattering events, plays an important role. Between two successive collisions the effective magnetic field $\boldsymbol{\Omega}(\boldsymbol{k})$ is considered to be constant and the precessing motion is centered around the direction of the field. If the collision rate $1/\tau_p$ is small compared to the average precession frequency $\langle \boldsymbol{\Omega} \rangle$, the precession perpendicular to the field will make large angles to the initial orientation before being scattered and forced to precess in another direction. In this case, the angle of precession $\tau_p \cdot \langle \boldsymbol{\Omega} \rangle$ is large and the initial spin orientation will be lost after a few scattering events, so that the spin relaxation time τ_s scales with the momentum scattering, hence $\tau_s \sim \tau_p$. In contrary, if the angle the precession makes to the initial orientation is small ($\tau_p \cdot \langle \boldsymbol{\Omega} \rangle \ll 1$) and hence τ_p is very short, the initial spin direction will be conserved over a large amount of scattering events and the spin relaxation time eventually becomes inversely proportional to the scattering time. Since the momentum relaxation time is very small in most semiconductors, the situation depicted in Fig. 2.7 reflects the most frequently occurring case [53].

The Bir-Aronov-Pikus mechanism Opposed to the attractive Coulomb interaction between the oppositely charged electrons and holes, which leads to the formation of

the excitons in semiconductors (see Section 2.3), the spins of electrons and holes can also couple through the e-h exchange interaction [65]. Usually considered in p-type semiconductors and optically excited systems, a mechanism of spin relaxation based on this e-h exchange interaction was introduced by Bir, Aronov and Pikus [66, 67]. The efficiency of this relaxation process depends strongly on the parameters quantifying the e-h states in a semiconductor, such as the exciton Bohr radius, its velocity and its binding energy. In their fully microscopic approach, Jiang and Wu [63] determine the contribution from both, the DP and the BAP mechanism on the spin relaxation time of photo-excited electrons in intrinsic bulk ZB GaAs. For an e-h pair density of $n_{\mathrm{eh}} = 1 \times 10^{17}\mathrm{cm}^{-3}$ at 5 K, for example, the DP mechanism limits the spin relaxation time to values below 1 ns, and is therefore at least one order of magnitude more efficient than the ~30 ns predicted for the BAP mechanism. Hence, for photo-excited electrons in undoped bulk GaAs, the BAP mechanism does not significantly contribute to the spin relaxation process. Using GaAs/AlGaAs double heterostructures, Wagner *et al.* [68] have outlined a strategy to suppress the BAP mechanism of spin relaxation by spatially separating the photo-excited electrons from the holes in the system.

The hyperfine interaction In a crystal, the spins of the nuclei can interact with both the spin and the orbital angular momenta of the carriers in the system [52, 55, 60]. Owing to their s-wave symmetry, however, this so-called hyperfine (HF) interaction reduces to an interaction between spins for conduction electrons. While the HF interaction is highly relevant for the localized, 0D carriers, the extended states of carriers in higher-dimensional structures averages the fluctuating nuclear field from many nuclei and the relaxation process is thus ineffective [60].

3

Single wire photoluminescence spectroscopy

Having outlined the concepts behind the spin-related and nanophotonic investigations conducted in this theses, we will now address their technical implementation in our NW experiments.

3.1 Optical instrumentation and possible measurement configurations

3.1.1 Micro-photoluminescence setup

All of the luminescence measurements presented in this thesis were conducted in a confocal micro-photoluminescence (μ-PL) setup using both continuous-wave and pulsed operation modes of a laser diode (~1.58 eV, or 785 nm) for the excitation. The pulse width of this laser in the time-domain, i.e., the full width at half maximum, was 70 ps at a repetition rate of 1 MHz. We note that the results shown in Figs. 11.2, 12.2 and 12.3 were obtained under ~3.1 eV, or 405 nm-excitation and that in those cases, the laser diode was operated in a high-current regime to achieve the high power pulses required for the measurement, which broadened the excitation pulse width to about 1 ns. The results in Section 6.3 were partially obtained under continuous-wave excitation from a ~1.8 eV, or 690 nm-laser diode. To study the luminescence properties of our NWs at low temperatures, each sample was mounted inside a continuous-flow He_4 cryostat, resulting in a sample temperature of nominally 4.2 K. Attaching the cryostat to a piezoelectric x-y-z translation stage further enabled a fine mapping of the emitted PL.
As illustrated by the sketch of our μ-PL setup in Fig. 3.1, we use a 100× microscope objective with NA = 0.8 to focus the laser light down to the sample with a spot diameter of around 1 µm for our single wire spectroscopy. The emitted PL is then collected by the same objective and directed towards the detector. Time-integrated μ-PL spectra were

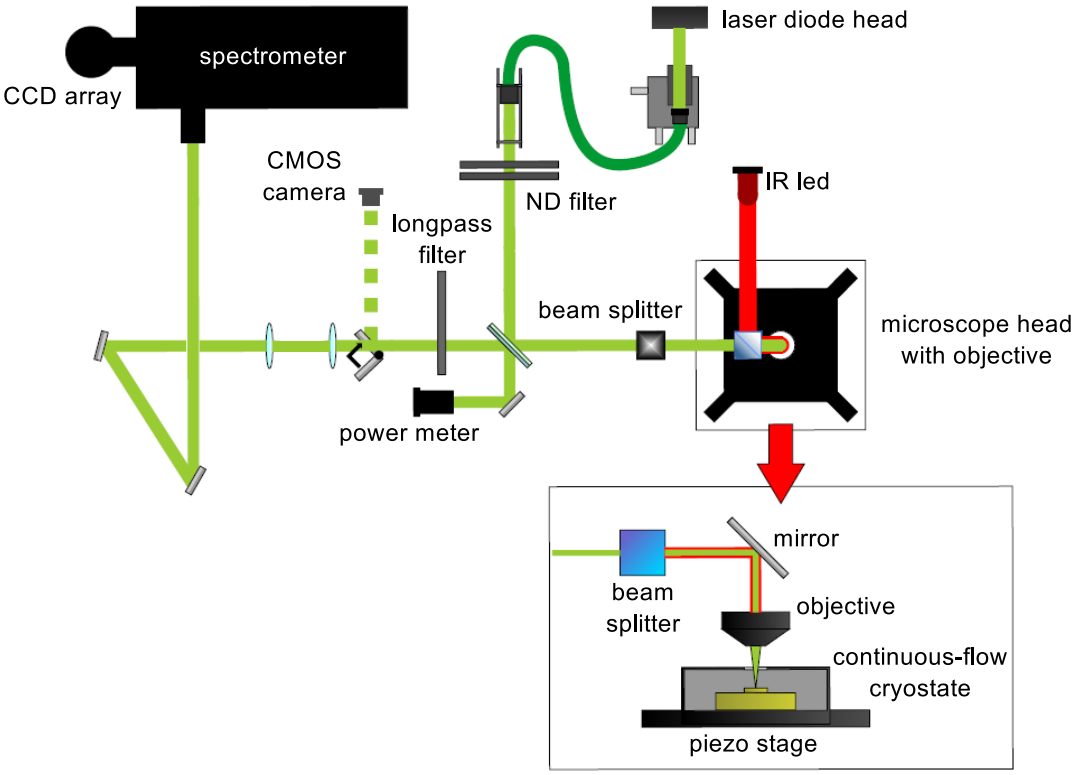

Figure 3.1: Schematic of the μ-PL setup used for the time-integrated experiments. Continuous wave or pulsed laser excitation is focused onto the sample using a 100× microscope objective with NA = 0.8, which provides a laser spot size of around 1 µm, enabling the optical spectroscopy of single wires. Different polarization optics (not shown) facilitate a linear and circular polarization of the incident laser, as well as the respective polarization-resolved detection of the luminescence signal. A piezoelectric x-y-z translation stage is used to spatially map the NW sample. For the time-resolved experiments, the same principal setup is used while the luminescence is detected by the streak camera system. Graphic adapted from Ref. [69].

acquired using a liquid nitrogen cooled charge-coupled device (CCD), while time-resolved photoluminescence signals were detected by a *Hamamatsu* streak camera system (not shown in the sketch) with a time resolution of 50 ps. For the linear polarization-dependent measurements shown Fig. 11.1, a linear polarizer followed by a half-wave plate allowed a continuously adjustable polarization of the exciting laser light, while an additional linear polarizer in the detection path was used to analyze the linear PL polarization properties. For the optical spin orientation experiments, the incident laser excitation was circularly polarized using a quarter wave-plate. Passing the same quarter wave-plate in the detection path, the right (I_+) and left (I_-) circularly polarized components of the luminescence were converted back into two perpendicularly polarized linear components, which could then be detected by analyzing the degree of linear polarization.
The Hanle effect and other magnetic field-dependent µ-PL measurements were performed by mounting the sample between the coils of an electromagnet, where magnetic fields up to 400 mT could be applied in the sample plane perpendicular to the free-standing NWs.
For the space- and time-resolved experiments, NWs were aligned parallel to the entrance slit of the streak camera system.

3.1.2 Possible measurement configurations

A very successful tool in the study of semiconductor nanostructures, μ-PL experiments allow for a broad set of measurement configurations, each providing access to different aspects of the luminescence signal. Since we exploit a number of these measurement configurations to study our NWs, we have summarized the different experiments conducted in this thesis in Fig. 3.2. Note that configurations (a)-(c) are characterized by the time-integrated luminescence detection, while (d)-(f) correspond to a time-resolved detection.

a) Intensity- and energy-resolved measurement: This standard PL experiment allows us to determine the emission energy of a single wire, for example to identify defect-related luminescence peaks, or confinement-induced shifts in the emission energy. This configuration was used to obtain the results shown in Fig. 4.3c, and Chapter 6.

b) Spatially resolved μ-PL mapping: An extension of the standard configuration in **a)**; the piezoelectric translation stage is used raster the point of the laser excitation in real space, generating a two-dimensional map of the luminescence signal. Each pixel of the map contains a single emission spectrum like the one shown in **a)**, corresponding to the excitation and detection at the respective position. This measurement was used to obtain the inset of Fig. 7.2b and, in a modified geometry, the scan in Fig. 4.3b.

c) Real space imaging of the luminescence signal: Using an edgepass filter to remove the backscattered laser light, we obtain a real space microscopic image of

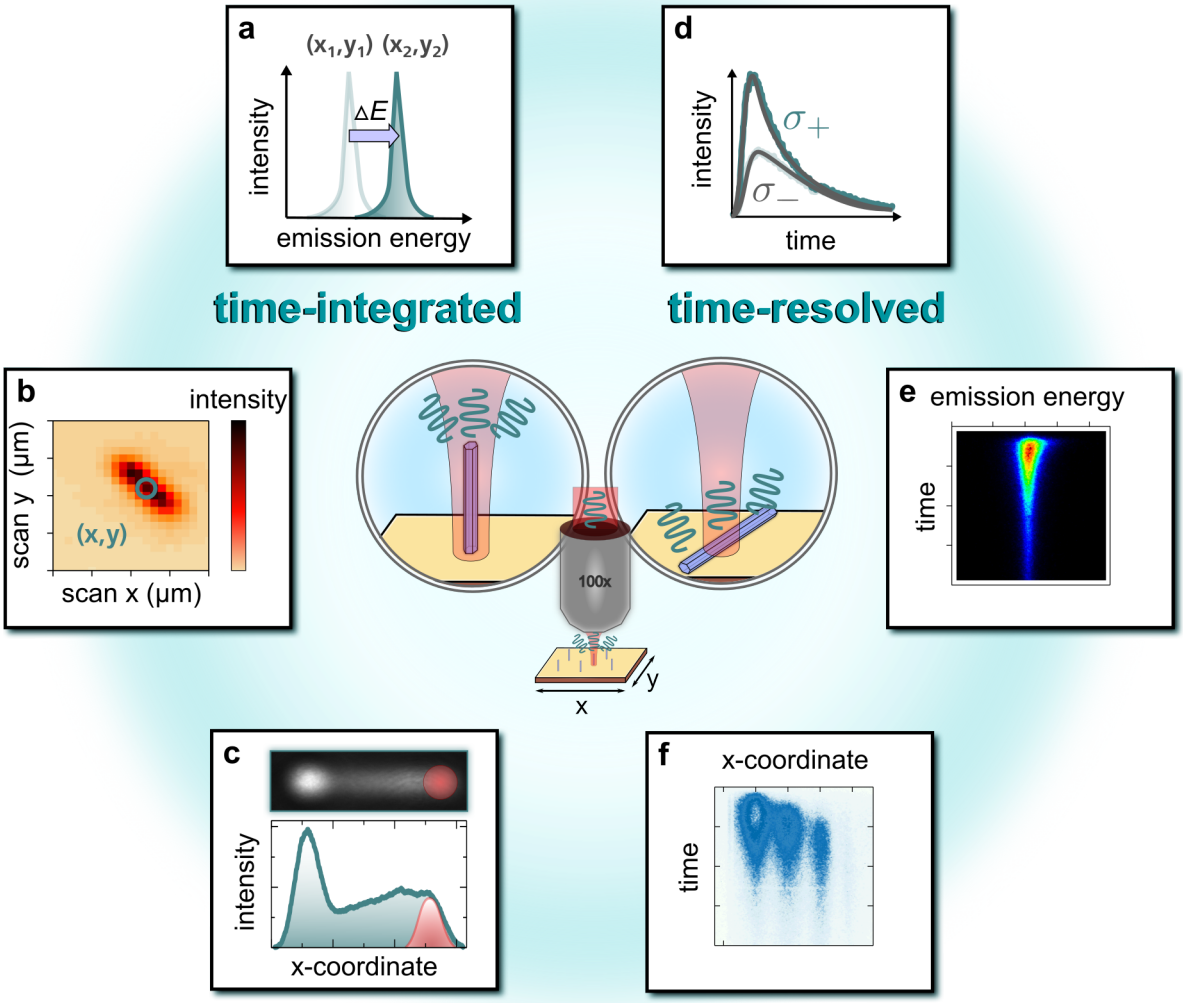

Figure 3.2: Summary of the various measurement configurations in our μ-PL setup used in this thesis. Central part: Confocal microscopy is used to excite single NWs as they are free-standing on the growth substrate, or dispersed onto a new substrate. (a)-(c) correspond to time-integrated measurements, while (d)-(f) are used together with time-resolved luminescence detection. A detailed description of each configuration is given in the text.

the luminescence emission, which contains intensity profiles of the luminescence signal in the sample plane. In contrast to configuration **b)**, we can use this method to locally excite a NW at one end, but image its luminescence intensity along the entire wire (see Fig. 11.2c, Fig. 12.2c and Fig. 12.3a).

d) Time- and polarization-resolved luminescence detection: After excitation with short, circularly polarized laser pulses, free-standing NWs emit partially circularly polarized light. Resolving the polarized emission in the time-domain entails information about the relaxation of spin polarized photo-carriers. The technique was used to evidence optical spin injection into a single free-standing wire in Fig. 7.4, as well as to obtain the main results in Chapter 8 and Chapter 9.

e) Time- and energy-resolved luminescence detection: The standard setting of a streak camera system simultaneously detects the luminescence intensity and its spectral information as a function of the time after the pulsed laser excitation. Apart from the results listed for method **d)**, this measurement configuration was furthermore used to detect the NW emission lifetimes in Fig. 10.2, Fig. 10.3, Fig. 11.2b and Fig. 12.2b. In particular the spectral analysis of the luminescence dynamics shown in Fig. 9.2 is only made possible by this configuration.

f) Time- and space-resolved luminescence detection: Proper real-space alignment of a single NW with respect to the entrance slit of the detector enables the time-resolved detection of the luminescence intensity along the axis of a single wire. This method is used to study space-dependent luminescence dynamics and the diffusion-driven motion of photo-carriers. See Fig. 12.3b and c.

3.2 Estimating the optically excited carrier density in nanowires

In Section 2.3 we discussed the fundamental optical excitations in a semiconductor. At the low temperatures of the experiments, excitons should occur in our NWs under photo-excitation. Yet, as we have also seen in Section 2.3, excitons will transform into an e-h plasma state under high excitation power. Thus, the density of optically excited e-h pairs is an important parameter to characterize our NW system. We first determine the carrier density n_{3D} in our three-dimensional (3D) NWs from the absorbed number of photons

$$n_{3D} = \frac{\bar{P}}{h\nu} {f_{rep}}^{-1} \alpha(h\nu). \tag{3.1}$$

Here $\bar{P} = 1.4\,\mathrm{W/cm^2}$ is the time-averaged output power density $\bar{P}$ of the excitation laser, $h\nu = 1.58\,\mathrm{eV}$ is the energy of the laser photons and $f_{rep} = 1\,\mathrm{MHz}$ is the repetition frequency of the laser pulse. To calculate n_{3D} we further use the value of the absorption coefficient of bulk GaAs $\alpha(h\nu) = 14.8 \times 10^3 \mathrm{cm^{-1}}$ at the excitation energy 1.58 eV [70].

Evaluating Eq. (3.1) under the conditions indicated above results in an optically excited e-h pair density of $n_{3D} = 8 \times 10^{16}\text{cm}^{-3}$ in our larger wires (d = 490–90 nm).
Calculating the carrier density for the 1D wires (see Section 6.1.2) is less straightforward. The nanophotonic nature of the 1D NWs demonstrated in Chapter 10 strongly affects the absorption and emission of light, i.e., in this regime of very thin NWs both processes sensitively depend on the NW diameter [7]. A simple conversion of the carrier density from 3D to 1D based on the absorption coefficient of bulk therefore largely overestimates the actual 1D carrier density. In order to still get a rough estimate of the 1D carrier density, we assume that the probabilities of absorbing and emitting a photon are affected to the same extent in our thinner NWs. The assumption is reasonable, because the excitation is near-resonant, i.e., the absorbed and emitted photons approximately have the same wavelength. In our time-resolved photoluminescence experiment, the reduced emission probability can be measured and is most noticeable for NW diameters in the range d = 20–90 nm (see Fig. 10.3). Here, it produces a large increase in the luminescence lifetime from an averaged recombination time of $\overline{\tau_{pl}} = 1.7$ ns for diameters d = 110–490 nm to $\overline{\tau_{pl}} \approx 75$ ns at d = 20–25 nm. With the above assumption, we estimate that the absorption probability of a photon in the 1D NWs is rescaled by the factor $\frac{1.7\,\text{ns}}{75\,\text{ns}} \approx \frac{1}{50}$. This allows us to reformulate Eq. (3.1) into

$$n_{1D} = \frac{\bar{P}\,A}{h\nu}\,{f_{rep}}^{-1}\,\alpha'(h\nu), \tag{3.2}$$

where $\alpha'(h\nu) = \frac{1}{50}\,\alpha(h\nu)$ for $h\nu = 1.58$ eV, $\bar{P} = 267.0\,\text{W/cm}^2$ and $A = \frac{3\sqrt{3}}{8}d^2$ is the cross-sectional area of the hexagonal NW. Under the above approximation we therefore find a 1D carrier density $n_{1D} \approx 1 \times 10^6\text{cm}^{-1}$ in the NWs with diameters 20–25 nm.
Equation (3.2) takes into account the change in absorption due to the photonic effects of the NWs. Although we believe that this is the dominant effect, we would like to note that it does not account for changes in the absorption coefficient that are related to an alteration of the electronic density of states.
According to our estimate, both of the photo-excited e-h pair densities obtained under pulsed excitation are slightly above the Mott density ($n_M \approx 2 \times 10^{16}\text{cm}^{-3}$ in 3D [48] and $n_M \approx 3 \times 10^5\text{cm}^{-1}$ in 1D [71]). In particular when the dynamic properties of the e-h pairs are discussed and the carrier density becomes time-dependent, the question which picture best describes the photo-carriers in our NWs, a gas of free excitons, or an e-h plasma, is difficult to answer. As many of the dynamic properties determined in Part III were obtained directly after the pulsed laser excitation–a regime in which the e-h pair density is above the critical Mott density–we prefer to speak of *e-h pairs* in Part III.
At the contrary, the luminescence lifetimes discussed in Part IV are for the most part determined over a wide time range after the excitation. As the e-h pair density is initially only slightly above the Mott density, we interpret the luminescence lifetimes observed for long delay times as an excitonic property.

3.3 Optical spin orientation and the spin relaxation time

In the following we provide a detailed account of the fitting procedure developed to extract the spin relaxation time from the polarization- and time-dependent decay traces.
As described in Section 2.4.1, a circularly polarized (σ_+) laser pulse propagating parallel to the axis of the NW creates a non-equilibrium spin polarization among the photo-excited electrons. The dynamical change in the population of spin-up (N_+) and spin-down (N_-) oriented electrons is given by the rate equations

$$\frac{dN_+}{dt} = -\frac{N_+}{\tau_{pl}} - \frac{N_+}{2\tau_s} + \frac{N_-}{2\tau_s} \tag{3.3}$$

$$\frac{dN_-}{dt} = -\frac{N_-}{\tau_{pl}} - \frac{N_-}{2\tau_s} + \frac{N_+}{2\tau_s} \tag{3.4}$$

where τ_{pl} and τ_s are the luminescence lifetime and the electron spin relaxation time [72]. By separately analyzing the time-resolved NW emission of the right $I_+(t)$ and left $I_-(t)$ circularly polarized components, we obtain direct experimental access to the individual decay traces $N_+(t)$ and $N_-(t)$.
The most direct, and also most commonly applied way to obtain the spin relaxation time τ_s from the experimental curves, is by fitting the degree of spin polarization $P_s(t) = (N_+(t) - N_-(t)) \,/\, (N_+(t) + N_-(t))$ to the single exponentially decaying solution

$$P_s(t) = S_0 \, \exp(-t/\tau_s), \tag{3.5}$$

where $S_0 = (N_+^0 - N_-^0)/(N_+^0 + N_-^0)$ is the initial degree of spin polarization at $t = 0$. Another approach to obtain the spin relaxation time τ_s from the experimental $N_+(t)$ and $N_-(t)$ curves is to separately fit the difference and sum signal to the single exponential solutions

$$N_+(t) - N_-(t) = (N_+^0 - N_-^0) \, \exp(-t/\tau) \tag{3.6}$$

$$N_+(t) + N_-(t) = (N_+^0 + N_-^0) \, \exp(-t/\tau_{pl}) \tag{3.7}$$

where we have introduced the decay constant $1/\tau = 1/\tau_{pl} + 1/\tau_s$ in Eq. (3.6). We can see from Eqs. (3.5) to (3.7) that the dynamical changes in the experiment are entirely determined by the spin relaxation time τ_s and the luminescence lifetime τ_{pl}. Although the two approaches (Eq. (3.5), or Eqs. (3.6) and (3.7)) to determine the spin relaxation time are mathematically fully equivalent, we will show that the quality of the fit can differ in the case of a realistic data set. In order to evaluate which of the above described approaches to extract τ_s allows for the most accurate results, we have performed a numerical simulation of the system dynamics. The procedure is as follows: We first calculate a realistic set of decay curves with specific input parameters and then fit these curves to see how accurately the individual fits reproduce the input parameters. We stress the importance of

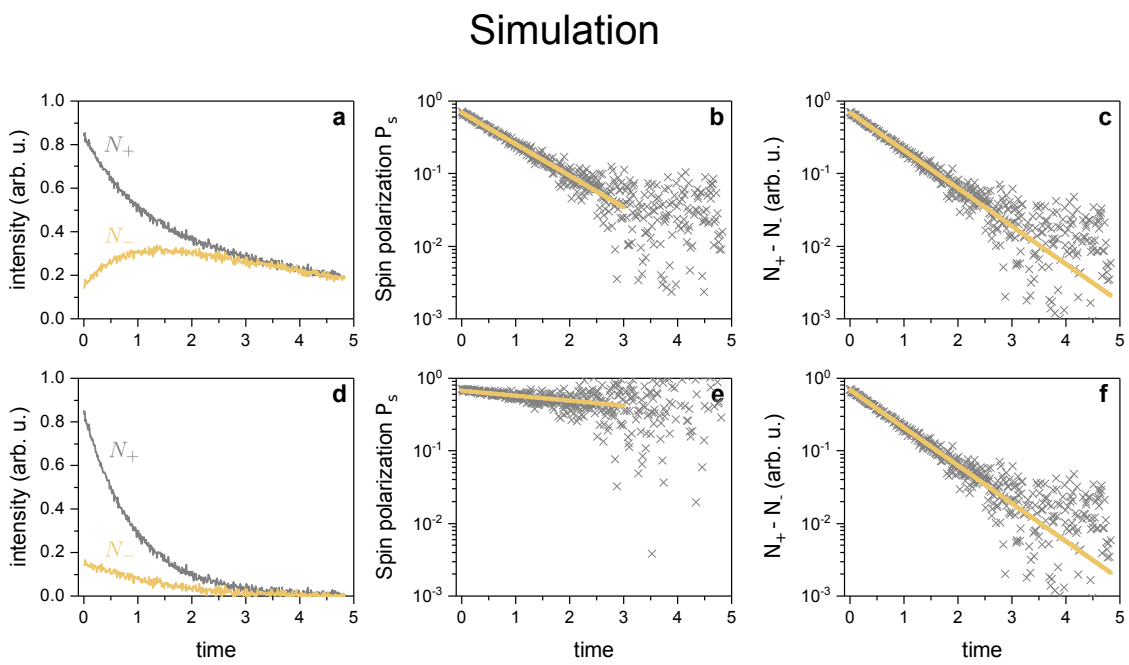

Figure 3.3: Time dependence of the numerically calculated decay curves N_+ and N_-, $P_s(t)$ and $(N_+ - N_-)$. Adding a small statistical error to the N_+ and N_- curves mimicks a realistic set of data. We have calculated two different cases: the upper panel, (a)-(c), represents the decay traces for $\tau_s = 1.0$ and $\tau_{pl} = 5.0$. In the lower panel, (d)-(f), we show the reverse case in which $\tau_s = 5.0$ and $\tau_{pl} = 1.0$. By fitting the different decay traces $P_s(t)$ and $(N_+ - N_-)$, we obtain detailed insight into the accuracy of the individual fits (see text below).

the term *realistic*, as it refers to adding a small level of random noise (signal-to-noise ratio $S/N \approx 100$) to the calculated curves. The results are plotted in Fig. 3.3. The left, middle and right column respectively show the dynamics of the experimentally obtained curves $N_+(t)$ and $N_-(t)$, the calculated spin polarization $P_s(t)$ and the difference signal $(N_+(t) - N_-(t))$ for two limiting cases. The initial degree of spin polarization S_0 was set to 0.7 for all calculations. For the first case (cf. Fig. 3.3a-c), which we would like to discuss, we set $\tau_s = 1.0$ and $\tau_{pl} = 5.0$. This represents a system in which the spin relaxation occurs much faster than the carrier recombination.
In Fig. 3.3a, we observe a time-dependent decrease of the difference between $N_+(t)$ and $N_-(t)$ until the two curves merge at $t \approx 3$. Note that, while the difference has apparently vanished at $t \approx 3$, the total signal intensity has not. This originates from the fact that the luminescence lifetime is larger than the spin relaxation time. We fit the decay of the spin polarization $P_s(t)$ according to Eq. (3.5) as well as the difference signal $(N_+(t) - N_-(t))$ by Eq. (3.6) and find, in both cases, that the fit reproduces the input parameter $\tau_s = 1.0$ with very high accuracy.
As a counterexample, we also calculate the decay traces for a system in which spin relaxation occurs on a much longer timescale than the recombination process of the

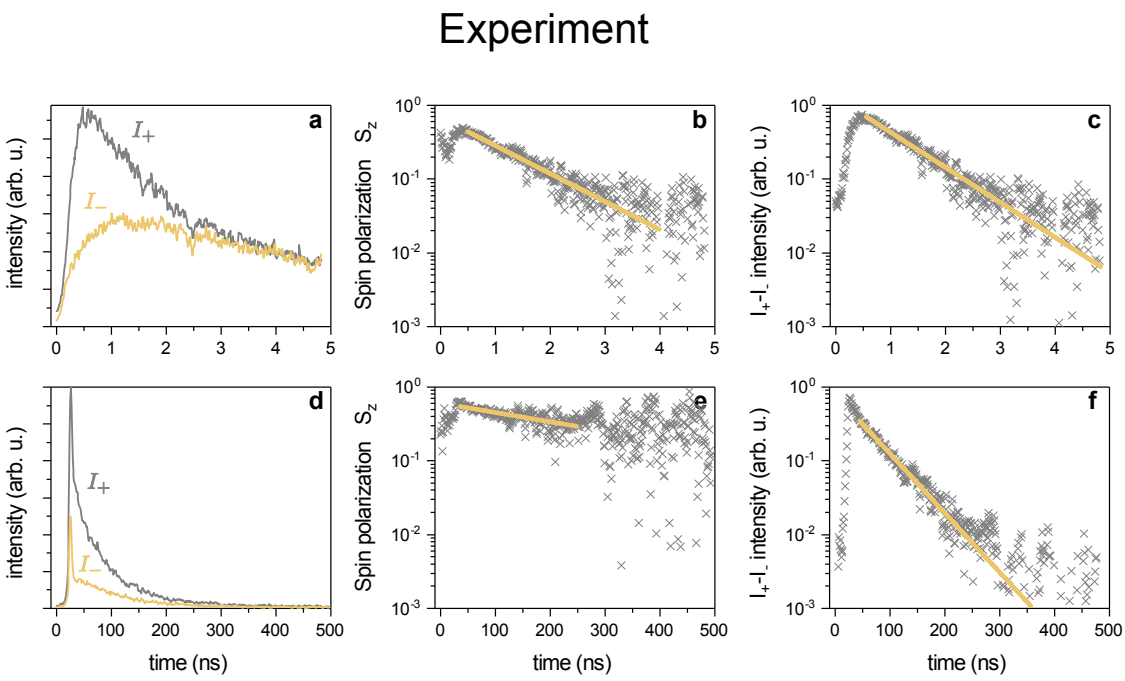

Figure 3.4: Time dependence of the experimentally recorded decay curves I_+ and I_-, $S_z(t)$ and $(I_+ - I_-)$. Upper panel, (a)-(c), shows the emission of a NW with $d = 90$ nm. The luminescence lifetime $\tau_{pl} = 6.7$ ns is determined from a seperate measurement and used as an input parameter for the fit in (c). Both fits in (b) and (c) yield $\tau_s = 1.1$ ns. In (d)-(f), we directly compare these results to the emission from an ultrathin NW with $d = 20$ nm. Although the luminescence lifetime of the NW is very long at $\tau_{pl} = (72.1 \pm 0.4)$ ns, the decay curves of (d) already suggest an even longer spin relaxation time τ_s. The fits in (e) and (f) yield $\tau_s = (344.5 \pm 21.5)$ ns and $\tau_s = (215.7 \pm 10.1)$ ns respectively.

carriers. We therefore set $\tau_s = 5.0$ and $\tau_{pl} = 1.0$ and show the results in Fig. 3.3d-f. Again the difference between $N_+(t)$ and $N_-(t)$ in Fig. 3.3d vanishes at $t \approx 3$, but in contrast to the first case, the total signal amplitude also decreases to zero. In this case, we find that fitting the spin polarization degree $P_s(t)$ shows a much lower accuracy and the fit consequently overestimates the spin relaxation time by $\tau_s = 6.4$. Instead, fitting the difference signal $(N_+(t) - N_-(t))$ provides a much higher accuracy and reproduces the input parameter accurately as $\tau_s = 5.0$. For the values listed above, the statistical fit error of τ_s is smaller than the specified number of valid digits.

By calculating a realistic set of decay traces we obtain important insight into the different approaches to fitting the time-resolved luminescence data. We find that fitting $P_s(t)$, as well as $(N_+(t) - N_-(t))$, both describe the numerical data with very high accuracy, as long as the process of spin relaxation is faster than the carrier recombination. In the reverse case, i.e., if $\tau_s > \tau_{pl}$, our numerical tests suggest that fitting the difference signal $(N_+(t) - N_-(t))$ provides a much better accuracy.

We next apply both fit methods to two complementary sets of experimental data. Unless specified otherwise, the statistical error of the fit is smaller than the number of valid digits. In Fig. 3.4a, we show the experimental decay curves $I_+(t)$ and $I_-(t)$ as recorded from a NW with a diameter $d = 90\,\text{nm}$. While the two curves merge at $t \approx 4\,\text{ns}$, the total signal amplitude is still large compared to the background noise. From a separate measurement we determine the luminescence lifetime $\tau_{pl} = 6.7\,\text{ns}$. In Fig. 3.4b, fitting the spin polarization $P_s(t)$ results in $\tau_s = 1.1\,\text{ns}$. At the same time, we also determine $\tau_s = 1.1\,\text{ns}$ from the $(I_+(t) - I_-(t))$-fit by using τ_{pl} as an input parameter. The experimental decay traces of Fig. 3.4a-c therefore confirm the results of the numerical simulations: For $\tau_{pl} > \tau_s$ both fitting procedures give the same results for the spin relaxation time. In Part III of this thesis, this condition applies for all NWs with diameters in the range from 490 to 90 nm and we use the $P_s(t)$-fit to determine the spin relaxation times τ_s that are plotted Fig. 9.1.
To demonstrate that the opposite case (cf. Fig. 3.3d-f) also occurs in our NW series, we show the decay traces of an ultrathin NW with $d = 20\,\text{nm}$. Note that the initial large peak in Fig. 3.4a stems from the fast decay of the spectrally broad substrate signal and does not belong to the NW emission. In a certain regard, the evolution of $I_+(t)$ and $I_-(t)$ in Fig. 3.4d resembles the decay curves of Fig. 3.3d: The difference between $I_+(t)$ and $I_-(t)$, as well as the total signal intensity both apparently vanish at $t \approx 250\,\text{ns}$. This observation already suggests that $\tau_s > \tau_{pl}$ and that the thinner NWs of our series therefore correspond to a rather peculiar system, in which the process of spin relaxation is slower than the carrier recombination process. From fitting the spin polarization $P_s(t)$, we obtain $\tau_s = (344.5 \pm 21.5)\,\text{ns}$. Instead, the fit of the $(I_+(t) - I_-(t))$-signal determines $\tau_s = (215.7 \pm 10.1)\,\text{ns}$. Again we have determined the luminescence lifetime $\tau_{pl} = (72.1 \pm 0.4)\,\text{ns}$ from a seperate measurement and used as an input parameter for the $(I_+(t) - I_-(t))$-fit. At this point, only the comparison to the results of the numerical simulation allows us to decide which of the two values reflects the real spin relaxation time of the system. We therefore fit all NWs with diameters in the range of 40 to 20 nm to the decay of the $(I_+(t) - I_-(t))$-signal.

4

Synthesis of GaAs nanowires in molecular beam epitaxy

In this chapter, we focus on the fabrication of GaAs NWs in molecular beam epitaxy (MBE) and outline our method to obtain free-standing NWs growing vertically on the growth substrate. Our approach includes the strategy to synthesize the WZ phase of GaAs with extremely high purity, which was developed as a part of the author's Master's thesis [73] and Joachim Hubmann's doctoral thesis [74].

4.1 Principle of the Vapor-Liquid-Solid growth

Introducing our method used to synthesize the NWs in this thesis, we first discuss a general, but intuitive picture of the NW growth in epitaxy, before we elaborate on the formation of the peculiar WZ crystal phase in the next section. We note, that taking full account of the complex thermodynamics involved in the NW growth process demands a more detailed description. For such a microscopic understanding we recommend Ref. [75]. To qualitatively discuss the NW growth mechanism, we instead follow a review by Kimberly A. Dick [76]. We start from a historical survey of one-dimensional crystal growth.

First reported by Wagner and Ellis in 1964, a novel mechanism of one-dimensional crystal growth was observed to originate from small metallic particles [77]. They discovered micrometer-long Silicon (Si) wires (or *whiskers*, as they were called in the original publication) growing epitaxially on gold (Au)-covered Si substrates with small Au particles sitting on top of the wires after the growth. Interestingly, the diameter of these wires often matched the diameter of the hemispherical Au particle, which generated the idea of the crystal growth being catalyzed by the Au particle. They further concluded that the Au-Si system must form a liquid alloy droplet at the elevated temperatures applied during the growth to which the vapor atoms preferentially stick before they supersaturate in the liquid droplet and precipitate at the underlying substrate. Describing the individual phases which the atoms undergo during the growth process, this idea eventually led to the

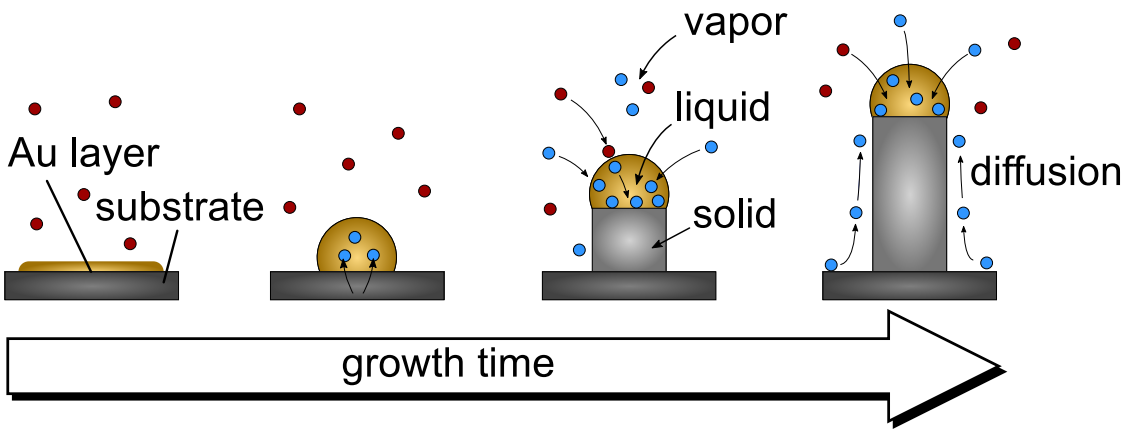

Figure 4.1: Schematic of the VLS growth of NWs on Au-covered GaAs(111) growth substrates. Heating the substrate in the growth chamber in the presence of As vapor leads to the formation of liquid Ga-Au nanodroplets, which serve as preferential adsorption sites for the vapor atoms. Additionally supplying Ga vapor atoms first initiates and then maintains the steady-state growth of the NW beneath the droplet until disrupting the flow of Ga terminates the growth process.

notion of the *Vapor-Liquid-Solid* (VLS) growth.
With the help of Fig. 4.1, we will now discuss the individual steps occurring in the VLS growth of our Au-catalyzed GaAs NWs. To obtain upright standing NWs growing vertically on the substrate, we use GaAs(111)B wafers (the label *B* indicates a As-terminated surface), as a substrate for the NW epitaxy. The growth process is started by heating a thin layer of Au deposited on such a GaAs(111) wafer in the MBE chamber, while supplying a sufficient As background pressure to circumvent the preferential evaporation of As (red atoms) from the GaAs growth substrate [78]. During this heating step, Ga atoms (blue) dissolve from the growth substrate into the developing Au nanodroplets to form the catalyzing liquid Ga-Au alloy (second sketch). This step already indicates that the term *catalyzer* in the classical sense is quite misleading, as it insinuates that the nanodroplet does not take a part in the chemical reaction, while, in reality, a multitude of liquid mixtures exists between Ga and Au, all of which may occur during the growth process [76]. To initiate the next growth step, we evaporate Ga atoms into the growth chamber by heating the Ga effusion cell. Directly hitting the liquid nanodroplet, impinging Ga atoms increase the Ga-content in the droplet until supersaturation at the growth temperature occurs. Limited by the much smaller fraction of As atoms soluble in the liquid alloy, the NW begins to grow epitaxially on the substrate beneath the droplet. As illustrated in the last part of Fig. 4.1, in this growth method the effective ratio of As to Ga atoms differs from the nominally adjusted value due to the much higher diffusion length of Ga atoms compared to As atoms, facilitating the long-range surface transport of Ga atoms towards the nanodroplet. Under the steady flow of Ga and As atoms, the NW continues its growth in a quasi-equilibrium state until the flow of Ga atoms is stopped and the NW wafer is

cooled down, while maintaining the As background pressure.
In literature, the GaAs NWs grown by the VLS method are reported to have lengths of a few to tens of μm with diameters typically ranging from 70 to 150 nm [76].

4.2 Crystal phase formation during growth

Soon after the discovery of the VLS growth mechanism, semiconductor NWs made of III-V compounds became a testbed for materials science, since their synthesis provides access to both, the non-equilibrium WZ crystal phase, as well as the bulk-stable ZB structure. Promising interesting opportunities for band-structure engineering within a single material, merely by controlling its crystal phase and thereby completely eliminating the problem of lattice matching encountered in hetero-epitaxy, the fundamental problem of phase selection in the homo-epitaxial NW growth has attracted considerable attention during the past decade [79–83].

4.2.1 Models for the phase selection in nanowires

Earlier attempts to explain the occurrence of the WZ crystal phase in III-V NWs have inferred the cohesive energy per atomic III-V pair [84, 85]. Although it is 24 meV lower in the ZB as compared to the WZ structure (which is the reason why ZB is stable in the bulk), the increased surface-to-volume ratio was considered to cause a large surface contribution to the total energy in the NW system. It was then argued that the WZ crystal structure occurs in small-diameter NWs having a particularly large surface-to-volume ratio, because it produces a smaller number of dangling bonds at the surface as compared to the ZB phase [85] and thus lowers the total energy of the system. Considering the literature reports, this argumentation is quite problematic. It predicts critical NW diameters, below which the WZ phase is stabilized, far too small to account for the occurrence of the WZ phase in NWs with large diameter [79].
Opposing this conflicting observation, a generally well-accepted model for the WZ formation in III-V NWs was introduced by Glas *et al.* in 2007. Instead of considering the different contributions to the total energy of already fully formed NWs, like previous models, they identified the formation of the nucleus inside the liquid nanodroplet as a key element in the crystal phase selection process. Indeed, they highlight two energetically different positions inside the nanodroplet, both sketched in Fig. 4.2, where a nucleus of sufficient size may be formed to facilitate the layer growth. At the first position, in the middle of the liquid nanodroplet, the nucleus for the NW growth shares three interfaces with the liquid, as shown in the left-hand side of Fig. 4.2. Instead, nucleation at the second position, i.e., at the border between the NW, the liquid droplet and the vapor phase, eliminates one of the three interfaces to the liquid phase and replaces it by an interface with the vapor phase (see white bar in the right-hand side of Fig. 4.2). At this position, the so-called triple phase line, where the nucleus shares interfaces with the vapor, liquid, and solid phases, Glas *et al.* predict the preferential formation of the WZ over the ZB

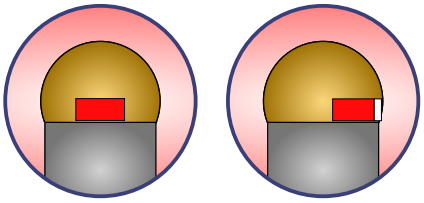

Figure 4.2: Graphical illustration of the two possible, energetically different nucleation sites at the nanodroplet-NW interface. Left image: A nucleus forms in the center of the NW, where it is characterized by three interfaces to the liquid phase. Right image: The nucleus develops at the border between the liquid droplet, the solid NW and the vapor phase–the triple phase line. The newly created interface between the nucleus and the vapor phase is highlighted in white. Glas *et al.* predict the preferential formation of the WZ phase for the nucleation at the triple phase line.

phase, and thus explain the occurrence of the WZ structure in III-V NWs.
Owing to their extensive experimental effort, Jacobsson *et al.* [86] could impressively demonstrate in 2016 that the actual dynamics of the phase selection process during the metal–organic vapour phase epitaxy of NWs are more complex than the effects captured by the model of Glas *et al.* [79]. Growing GaAs NWs directly inside the ultrahigh vacuum chamber of a transmission electron microscope, they could *in situ* observe the reversible switching between WZ and ZB GaAs, layer by layer, as they tuned the As to Ga ratio at a fixed growth temperature. Based on their study, they concluded that the WZ phase forms as a result of an interplay between the shape and the volume of the liquid nanodroplet, as well as the nucleation position. Generating a number of spectacular movies, their real-time imaging method further captured a variety of different NW growth modes, e.g., the dynamic expansion and shrinking of the liquid nanodroplet during growth, or the formation of controllable periodic superlattices between segments of ZB and WZ GaAs.
With this conceptual account for the occurrence of the WZ phase in GaAs NWs, we will now proceed to outline our own strategy developed to synthesize a high-purity WZ phase in our GaAs NWs grown on GaAs(111) substrates in our MBE system.

4.2.2 Wurtzite crystal phase perfection in our GaAs nanowires

The considerations outlined above give us an idea why the WZ phase can appear in the VLS growth mechanism; they do however not provide us with a straightforward strategy to realize this WZ phase with high phase purity in our MBE approach. Developed for the most part by Andreas Rudolph, the more technical aspects of the NW growth in our MBE system, including the sophisticated design of suitable sample holders, the calibration of molecular beam fluxes and a schematic drawing of our MBE growth chamber, can be

found in his doctoral thesis [87]. For the growth concepts developed in this work, these technical details are only of minor importance. In the following, we instead focus on the role of the two most important parameters, which determine the WZ phase purity in our NW MBE growth: the growth temperature and the As_4/Ga-ratio, i.e., the relative number of As_4 molecules and Ga atoms we supply in the vapor phase. Judging from the variety of different approaches reported to tune the crystal phase in NWs [80, 82, 86], it is clear that different parameter regimes must exist in which either the WZ, or the ZB structure becomes the preferential crystal phase.

In order to find the perfect conditions for the formation of the WZ phase in our NW growth approach, which is based on the synthesis from Au-covered GaAs(111) substrates, we have conducted a correlated study, combining our single wire luminescence spectroscopy with the structural characterization of the same wires in transmission electron microscopy in the group of Prof. Josef Zweck. The results of this collaborative effort were reported in *Applied Physics Letters* [88].

In this study we investigated single NWs from a series of wafers, each fabricated under different growth conditions, as discussed below. Before they were examined in the transmission electron microscope, all of the NWs were pre-characterized in our μ-PL setup. In this way, after the entire investigation is completed, we are able to correlate the particular optical emission properties of a single NW with the purity of its crystal structure. To be able to investigate the wires in both TEM and μ-PL, all NWs were *in-situ* passivated by a standard 15 nm-thin AlGaAs shell and after the growth they were removed from the growth substrate and dispersed onto 5 nm thick amorphous Silicon TEM membranes.

To find the perfect growth conditions for the WZ phase in our NWs, we fix the growth temperature at 510 °C and keep the Ga evaporation rate at a constant value of 0.4 Å/s for 120 min, while adjusting the As_4 beam equivalent pressure step-by-step for each wafer. In different growth runs, tuning the As_4 beam equivalent pressure from 3.0×10^{-6} Torr to 1.0×10^{-6} Torr, produced 100 nm-thin NWs with a perfect WZ crystal phase along the entire length of the wire at 1.5×10^{-6} Torr. At this point, it is important to note that our growth approach, based on the heating of a thin Au film, always creates an ensemble of NWs with statistical size distribution (a detailed account of this effect is given in Section 5.1). On the one hand, this is disadvantageous, since for some wires in the ensemble the globally applied growth conditions vary locally and thus prevent the fabrication of a perfectly homogeneous NW ensemble. On the other hand, due to its statistical nature, our approach is much more forgiving in terms of slightly detuned growth parameters; even if the conditions for perfect crystal growth are not met exactly, some wires in the ensemble might still experience the perfect setting for the growth of high purity WZ GaAs. In the end, adjusting the growth conditions to obtain a perfect WZ crystal structure in our NWs in our context means that a high percentage of NWs in the statistical ensemble exhibits a high-purity WZ crystal structure.

In Fig. 4.3 we show the results of our correlated study as they were obtained from a NW with perfect WZ structure: Not a single axial defect was found along the 4.1 µm length of the wire in the TEM. Representative for the entire NW, the high-resolution TEM

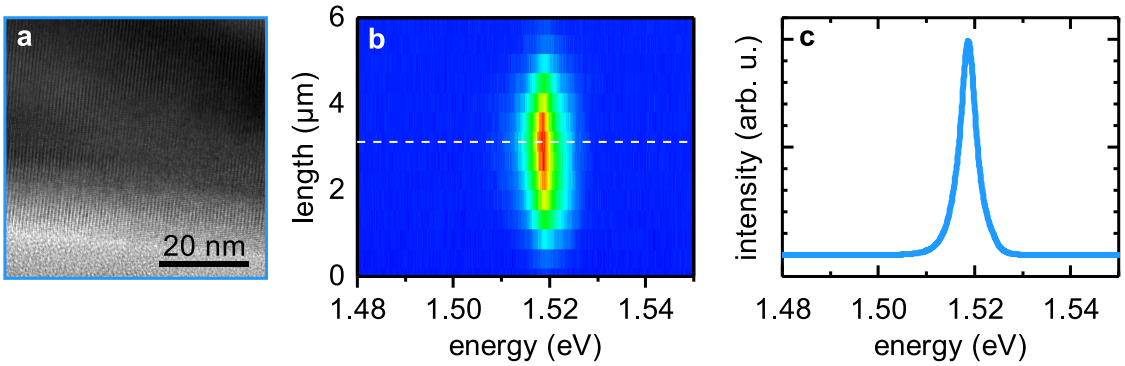

Figure 4.3: (a) High-resolution TEM micrograph showing the defect-free crystal lattice in a short segment of the wire. (b) False-color plot of the spatially resolved μ-PL at 4.2 K as a function of position along the same NW shown in (a). The PL emission extends along its entire length of 4.1 µm. (c) μ-PL spectrum recorded at the position of the dashed line in (b) shows the free-exciton emission line of WZ GaAs NWs. Adapted from Ref. [88]

micrograph in Fig. 4.3a demonstrates the perfect crystal structure in a short segment of this wire. As outlined above, prior to the TEM characterization, the optical properties of the NW were studied in our μ-PL setup to avoid a possible deterioration of the optical emission by the high-energy electron beam in the microscope. Displaying the NW emission along its axis, the false-color plot in Fig. 4.3b demonstrates an important spectroscopic feature of the phase-pure NWs: The emission energy of the luminescence signal does not change along the axis of the wire, as is observed when ZB inclusions or mixed WZ/ZB segments are present in the NW [88]. The dashed horizontal line indicates the position of the luminescence spectrum shown in Fig. 4.3c. With an emission energy of 1.518 eV it clearly identifies the free-exciton emission of GaAs NWs in the WZ phase [24, 88].

Correlating the structural and optical properties of our GaAs NWs, the results of the study presented in this section are essential for the spin-related and nanophotonic effects investigated in the course of this thesis. Knowing the optical emission features of a single NW with perfect WZ crystal structure, enables us to utilize non-invasive μ-PL spectroscopy to easily identify single defect-free WZ GaAs NWs in the as-grown ensemble.

II

Tuning nanowire diameters: Towards one dimension

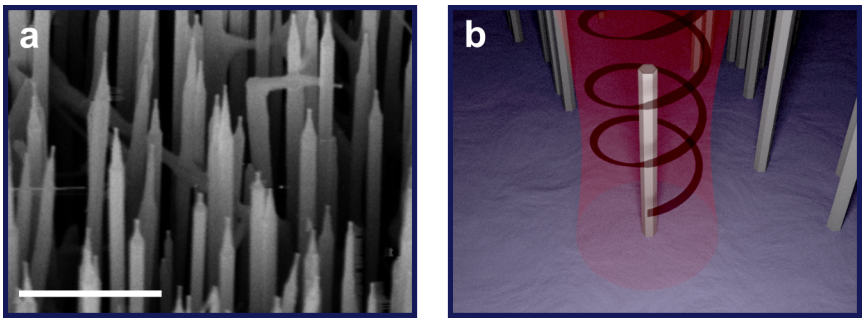

Figure 4.4: (a) Typical as-grown NW ensemble synthesized from a 5 Å Au layer viewed under 35° tilt angle. The wires grow much too densely to excite only a single NW with our 1 µm laser spot, preventing the single wire spectroscopy. The scale bar, indicating 1 µm, serves as a reference for the laser spot. (b) Graphic showing the ideal measurement constellation: large wire-to-wire distances allow the excitation of only one single wire.

To reveal the subtlety of nanophotonic and spin-related effects in semiconductor nanowires (NWs), our experimental strategy should involve the optical spectroscopy of isolated single wires to avoid disguising ensemble effects. With the laser excitation spot in our optical spectroscopy having a lateral size of about 1 µm, this requirement is easily fulfilled when the wires are dispersed on a substrate, because simply diluting the NWs in solution before dropcasting them onto the substrate, reduces the number of deposited NWs per area. In this regard, we are a bit unfortunate since the spin-related experiments presented in Part III demand the optical spectroscopy to be performed on single free-standing wires; a measurement geometry which is rarely encountered in NW experiments. A look at the tilted-view electron micrograph in Fig. 4.4a reveals the reason for this: In a typical sample, the NW ensemble is very dense, creating wire-to-wire distances much smaller than the 1 µm lateral size of a laser spot (cf. scale bar in Fig. 4.4a), which prevents the laser excitation of a single wire. Solving this issue, to realize the ideal starting position for our experiments illustrated in Fig. 4.4b, constitutes a prime motive for the growth improving experiments presented in the following.
A second need, which motivated the growth studies presented in this part, was to extend the realm of NW diameters accessible in our epitaxy approach. The limited range of diameters reported in literature (typically from 70 to 150 nm) not only conceals a number of quantum effects expected to occur for smaller diameters ($d < 70$ nm), but also prohibits a systematic study of any wide-range diameter-dependent effects. We therefore concentrate our efforts to fabricate NWs with diameters in a previously inaccessible range; both in the small diameter-, as well as in the large diameter-regime, while maintaining the previously reported [88] excellent quality of the wurtzite (WZ) crystal phase in all of our wire samples.

5

Controlling the wire diameter during growth

Due to its ability of forming eutectic alloys with many of the well-known semiconductors, the most commonly employed metal for the Vapor-Liquid-Solid (VLS) growth of NWs is gold (Au) [75, 87, 89]. Until now several groups have thus investigated NWs synthesized from Au layers with thicknesses ranging from 1 to 100 Å [87, 90–93]. This includes the report from Gomes *et al.* [91] presenting a particularly thorough study of the correlation between InAs NW growth and the Au layer thickness. We note here, that although a universal correlation between the Au layer thickness, the formation of the alloyed nanodroplets, and the area density and size distribution of the resulting NW ensemble certainly exists, this correlation is not easily identified, since temperature and duration time of the thermal heating step may produce competing effects [87, 90]. To realize the ideal experimental situation shown in Fig. 4.4b, which would facilitate the optical spectroscopy of single free-standing wires, we thus need to understand the formation of the nanodroplets initiating the wire growth in our epitaxy in more detail. Hence, we explore the effect of the Au layer thickness on the NW growth in a new range of very low Au coverage.

5.1 Preparing the nanodroplet catalyzer

For this purpose, we prepare three GaAs(111)B wafers, covered by the nominal Au layer thicknesses 5 Å, 0.5 Å and 0.05 Å, as the growth substrates for a sample series. In three successive growth runs, we heat each of the substrates to a temperature of 600 °C for 15 min before initiating the regular NW growth, thus creating identical conditions for the nanodroplet formation in all three runs. After the growth we investigate the effect of the Au layer thickness on the density of NWs grown per area by scanning electron microscopy. Fig. 5.1a-c shows three top-view micrographs displaying a $(5 \times 5)\mu m^2$ section of the three wafers. The magnification is identical in each micrograph and the scale bars indicate a length of 1 µm.

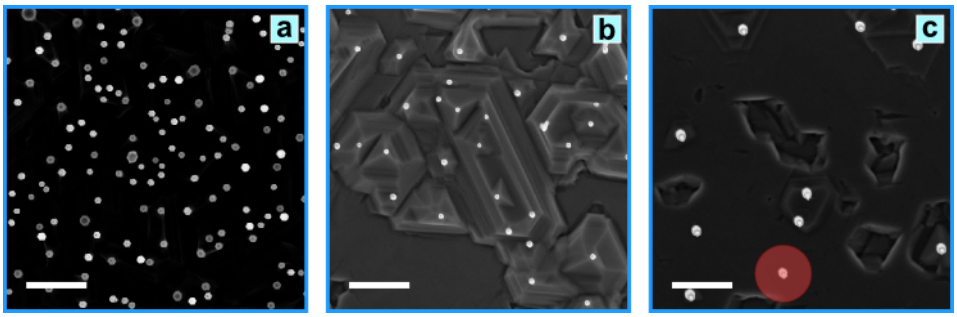

Figure 5.1: Top-view scanning electron micrographs reveal the effect of reducing the Au layer thickness from 5 to 0.05 Å on the growth of our GaAs NWs. (a) About 5 wires per μm^2 grow on a 5 Å Au substrate, showing a broad distribution of small and large NW diameters. (b) A 0.5 Å Au substrate facilitates the growth of a more homogeneous ensemble with 1 wire per μm^2. (c) Reducing the Au layer thickness to only 0.05 Å decreases the number of wires to less than 1 per μm^2, perfectly suiting the requirements of our experiment. The individual micrographs have a size of $(5 \times 5)\mu m^2$ and the scale bars indicate 1 µm.

The micrographs clearly illustrate the observed trend: The number of NWs per area decreases drastically as the Au layer thickness is reduced. The sample, initially covered by 5 Å Au, not only contains a high number of approximately 5 wires per μm^2, but also displays a vast dispersion of small and large NW diameters, as can be seen by the differently sized white spots in Fig. 5.1a. Decreasing the Au layer thickness to 0.5 Å results in a more homogeneous diameter-distribution among the wires and reduces their area density to 1 per μm^2. Yet a comparison with the 1 µm-sized scale bar in Fig. 5.1b shows that the wire-to-wire distance remains mostly below 1 µm, not yet fulfilling the requirement of our optical experiment. However, upon further reducing the nominal Au layer thickness to only 0.05 Å, the NW density is now less than 1 wire per μm^2. The red-shaded circle in Fig. 5.1c indicates that the wire-to-wire distance is now sufficiently large to excite only a single NW in the as-grown ensemble with the optical laser.

5.2 Two-step growth of wires with large diameters

As discussed in the fundamentals of the VLS growth Chapter 4, GaAs NWs often have lengths of few to tens of µm with diameters ranging from 70 to 150 nm. Although larger diameters have been reported for the VLS growth (lateral cavity sizes of 300 nm or more are for example required for GaAs-based nanolaser applications [94, 95]), these wires were not catalyzed by our thin-film heating technique. In one example of large-diameter wires, commercially available Au colloids with 250 nm-diameter were introduced into the growth chamber to initiate the NW growth, resulting in the correspondingly large

NW diameters [94]. In another example, the NW growth is based on a two-step method; developed for the Ga-catalyzed growth, it represents an important step for the integration of comparably large diameters also on Silicon wafers [95]. Following this approach, we have developed a similar two-step growth to achieve large NW diameters with a few hundreds of nanometers based on our thin-film heating technique.
First, we synthesize a low-density ensemble of NWs on 0.05 Å Au substrates under conditions suiting the high-purity WZ crystal phase (see Section 4.2.2), which results in wires with lengths of $\sim 5\,\mu m$ and diameters around 110 nm. These NW cores are subsequently radially overgrown in the second step with an epitaxial GaAs shell. The core, acting as a seed layer, imprints its WZ crystal structure on this additional layer of GaAs. By cooling the wafer from the initial VLS growth temperature of 510 °C to a lower temperature of 460 °C before depositing the additional layer, we can substantially enhance the radial growth rate of this layer (cf. Fig. 5.4) while decreasing the axial growth rate roughly by a factor of two. Here, we emphasize that only the large wire-to-wire distances achieved by the thermal heating of 0.05 Å Au films allows the application of this two-step procedure without encountering major issues from shadowing of the molecular beam by neighboring NWs, or a growing together of NWs in close proximity to each other [96].

5.3 Growth of ultrathin nanowires

Although GaAs NWs have been synthesized for quite some time now, before the beginning of this thesis reports about the effects of spatial carrier confinement in ultrathin VLS-grown NWs have been absent. A new approach to the problem was then reported in 2015 [97], claiming the tunable quantum confinement effect in Ga-catalyzed NWs synthesized on Silicon wafers, as well as the emergence of the expected quantum signatures in optical experiments. This new approach consists in the growth of a regular NW core followed by a subsequent post-growth, high-temperature annealing step. As illustrated in the upper panel of Fig. 5.2, this additional step is introduced to partially decompose the already grown NWs, i.e., ideally the re-evaporation of Ga and As atoms decreases the diameter and it might thus in principle be a route towards arbitrarily thin wires.

5.3.1 Post-growth annealing of nanowires

To investigate the effect of this post-growth annealing step on our Au-catalyzed NWs, we fabricate a series of wafers, each containing nominally identical ensembles of NWs with diameters around 90 to 110 nm. As described in Ref. [97], we stop the supply of arsenic in the growth chamber after the growth of the NW core and subsequently heat the substrate to the target temperature of the annealing step. After the time designated to the annealing we terminate the process by rapidly cooling down the wafer, still in the absence of an arsenic background pressure. The effect of the different annealing conditions (i.e., temperature and duration) on the morphology of the wires is then studied

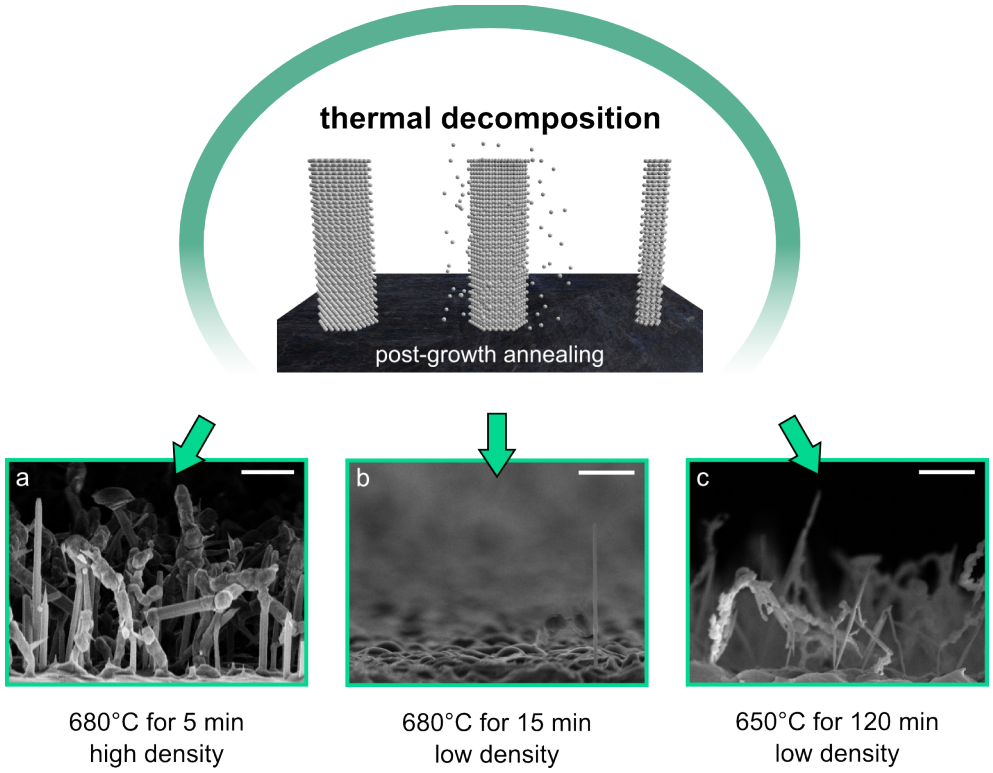

Figure 5.2: The method of post-growth annealing for the fabrication of 1D wires. The sketch in the upper panel illustrates the idealized concept of using the thermal decomposition of regular-sized wires to obtain ultrathin NWs. Adapted from Ref. [98]. Scanning electron micrographs in the lower panel (a)-(c) demonstrate the main problems arising from the high annealing temperatures for Au-catalyzed wires: mergence of neighboring wires, (a) and (c), or complete evaporation of NWs from the wafer surface, (b). Scale bars are 1 µm.

by scanning electron microscopy. The main conclusions can be drawn from the individual micrographs presented in Fig. 5.2a-c.
In the first growth run, we expose a wafer containing a high density of NWs (5 Å Au, i.e., more than 1 wire per μm^2) to the annealing temperatures used in Ref. [97]: 680 °C. Analyzing the micrograph in Fig. 5.2a, it seems that the atomic constituents evaporated from one wire rather re-adsorb on some of the neighboring NWs than to actually completely desorb to the vacuum. Instead of thermally decomposing into ultrathin wires, individual NWs lose their cylindrical form and frequently merge with their neighbors into irregular shapes. Although this wafer was only annealed for 5 min, such a high temperature during the post-growth annealing already completely destroys the morphology of the NWs in a high-density ensemble. In a second growth run, we try to circumvent the re-adsorption of evaporated atoms by preparing a low-density NW ensemble (0.05 Å Au, i.e., less than 1 wire per μm^2, see Section 5.1) with higher lateral distance between neighboring wires for the post-growth annealing. This time exposing

the sample to an annealing temperature of 680 °C for 15 min, entirely evaporates almost all NWs from the wafer surface and only very few wires remain. For these remaining NWs, the concept of post-growth annealing accomplishes at least some results: For the NW observable in the right half of Fig. 5.2b the diameter has decreased to ∼ 50 nm. In an attempt to avoid the evaporation of entire NWs from the wafer, we lowered the annealing temperatures to 650 °C and instead increased the annealing time to 120 min. Although a much larger portion of NWs now remains on the surface (see Fig. 5.2c), the effect on the morphology of the wires is similar to the unsatisfactory results from the first run. We note that even quite a large number of further attempts in finding the right time duration and temperature for the annealing step could not produce the desired effect.
Our study on the post-growth annealing of Au-catalyzed NWs thus indicates that the method presented in Ref. [97] is not suited for a reliable fabrication of ultrathin GaAs wires which would allow us to investigate the properties of spatially confined carriers in a 1D quantum system.
Very recent work also tackles the issue of fabricating ultrathin wires. In their publication, Kim *et al.* propose an innovative 3-step growth method to synthesize ultrathin nanoneedles with diameters down to 20 nm from the Ga droplet residing on the top facet of a regular 150 nm-thin Ga-catalyzed NW [99]. We will, however, show in the next section, that such an additional step in the fabrication process is not required to catalyze wires with equally small diameters in our growth approach.

5.3.2 One-step growth of ultrathin wires

Thermally heating a thin metallic layer on top of a semiconductor substrate often evokes an interesting situation: due to its thermodynamic nature, the resulting nanodroplet formation underlies a statistical size-distribution with diameters possibly spreading over tens of nanometers [91]. At the lower end, this distribution is characterized by a minimum droplet size that cannot be beat. Commonly attributed to the Gibbs-Thomson effect [75, 89, 91, 99], this lower bound for the size of a liquid nanoparticle thus directly constitutes also a lower bound for the diameter of our NWs, which are catalyzed from the nanodroplets. Although for our Au-Ga nanodroplets this lower bound appears to be about 15 nm [100], which would in principle be perfectly suited to fabricate ultrathin wires, it is not self-evident to obtain such small nanodroplets from the thin film annealing technique. For larger Au layer thicknesses (>10 Å), for example, the small nanodroplets disappear due to Ostwald ripening (smaller nanodroplets merge to form larger particles, lowering the energy in the system [91]), preventing the subsequent growth of ultrathin wires [100]. Despite this effect, we will show that we can synthesize ultrathin NWs using regular growth parameters for the VLS growth of Au-catalyzed NWs by utilizing the very low Au coverage of 0.05 Å thin layers on top of GaAs(111)B substrates.
The key to fabricating an ensemble of ultrathin NWs by the Au-assisted VLS technique lies in the preparation of the catalyzing Au-Ga nanodroplets with as small as possible average diameter and a narrow size distribution, a requirement that can actually be fulfilled by the thermal heating of the 0.05 Å Au deposited on the GaAs(111)B growth substrates.

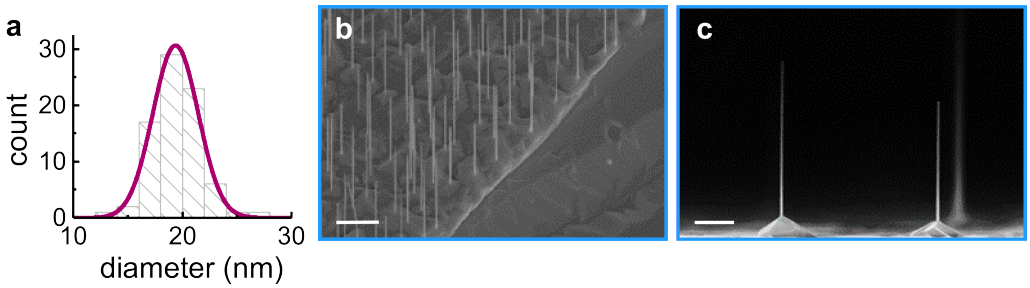

Figure 5.3: (a) After 20 min growth time, the regularly VLS-grown NW ensemble has a mean diameter of 20 nm and a very narrow standard deviation of only ±2 nm. (b) Scanning electron micrograph of a low density NW ensemble close to the wafer edge viewed under 35° tilt angle. Growth was conducted for 60 min resulting in diameters around 40 nm. (c) Side-view image of the same wafer demonstrates the advantage of our approach: single upright standing NWs with ultrathin diameter are well-isolated by µm-distances from their neighbors. Scale bars in the left and right image indicate 1 µm and 500 nm respectively.

As a consequence, growing NWs under otherwise completely regular conditions, for a short time of only 20 min thus results in NWs with a mean diameter of 20 nm and a very narrow standard deviation of only ±2 nm, as can be seen from the histogram shown in Fig. 5.3a. A scanning electron micrograph of such an ensemble of ultrathin wires, grown for 60 min and viewed under 35° tilt angle, is shown in Fig. 5.3b. Note that a closer look at this micrograph reveals a certain blurring of some of the wires. This effect is not a result of low image resolution, but instead attributed to an electron beam-induced oscillation of the ultrathin wires during imaging, that creates the blurring in the micrograph. Viewing the same wafer from the side (cf. Fig. 5.3c) demonstrates the long, untapered, cylinder-like shape of our ultrathin wires with the large distances between two neighboring NWs perfectly suiting the requirements of our optical experiment.
By reducing the Au layer thickness to only 0.05 Å, we avoid the effect of the Ostwald ripening-induced disappearance of the small nanodroplets during the necessary heating step discussed in Chapter 5. Eventually this led us to realize that the regular VLS growth of our wires is actually well-suited to fabricate an ensemble of homogeneous NWs with ultrathin diameters.

5.4 Overview: Tuning the nanowire diameter in a sample series

As mentioned in the introductory part of this chapter, extending the realm of NW diameters accessible in our epitaxy plays a cornerstone role in the systematic investigation of the diameter-dependent effects in our optical spectroscopy. In the end, we require NWs with diameters tunable over a very wide range while the high quality of the WZ crystal phase

is maintained throughout [88]. Using the methods developed in the previous two sections, we fabricated a series of eight individual wafers covering NW diameters in a very large range; from 20 nm, for the smallest, ultrathin wires, to very large wire diameters around 500 nm.
To guarantee a high crystal quality throughout our series, the NW growth for all eight wafers was initiated under identical conditions, namely those suiting the high purity WZ crystal phase of GaAs (see Section 4.2.2). First we discuss the wires grown with the regular one-step method presented in Section 5.3.2. At a constant growth temperature of 510 °C, a step-wise increase in the time during which Ga atoms are supplied from 20 to 125 min results in the growth of NWs with diameters 20, 25, 40, 90 and 110 nm. The light blue hexagons in the upper panel of Fig. 5.4 represent the cross-sections of a few exemplary NW diameters. To graphically demonstrate the wide range of NW diameters covered by our series, the hexagons are drawn to scale. In Fig. 5.4 we plot the dependence of the NW diameter on the growth time, as determined by scanning electron microscopy characterization of a large number of wires. To the left of the dashed line, the graph contains the regular VLS-grown wires, i.e., NWs are grown applying only the first step of the two-step growth presented in Section 5.2.
By fitting the data in Fig. 5.4 with the proper linear function (see light gray line in Fig. 5.4 and description in the figure caption), this growth translates into a radial growth rate of 0.4 nm/min. At the same time, the length of the wires increases from 1 to 5 µm. To obtain the larger wire diameters 160, 235 and 490 nm, we apply the two-step growth method described in Section 5.2. The second step of this method is included to the right of the dashed line in the graph. Due to the reduced substrate temperature of 460 °C the radial growth rate increases to 1.1 nm/min, as determined from the linear fit plotted as a light gray line.
Exemplary for our sample series, we show In Fig. 5.5 three scanning electron micrographs of single as-grown NWs with the respective diameters of (a) 22 nm, (b) 113 nm and (c), grown by the two-step method, 280 nm, as an example for our sample series. Note the different magnification of the micrographs, indicated by the scale bar changing from 50 to 500 nm in (a) and (b), (c). To contrast this scaling of the images required for a full-sized view of the single NWs shown in Figure 5.5a-c, we have also resized the same images to fit a single common scale. Figure 5.5d-f thus only show a short segment of each of the wires. As demonstrated by Fig. 5.5, resizing the micrographs to a common scale avoids the misleading optical impression one might get when trying to estimate the actual NW size from the images shown in (a)-(c). Printed to scale, however, the micrographs provide a realistic impression of the large range of wire diameters covered in our sample series.

Since the dimensionality of photo-excited carriers in a size-variable system like our NWs is not strictly defined by a definite wire diameter, detecting the signatures of spatial quantum confinement in our NWs emerging as a function of their diameter is essential to understand the increasing influence of quantum effects. We thus need to be able to scale the lateral dimension of our NWs during epitaxy in a controllable way. Combining the individual steps presented in Sections 5.1, 5.2 and 5.3.2 allowed us to do exactly so. All

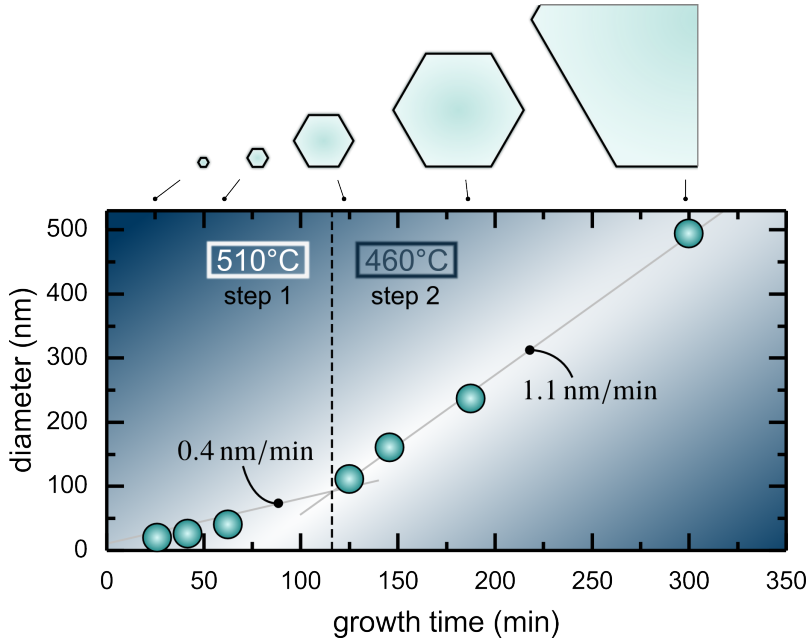

Figure 5.4: Diameter-dependence of the wires synthesized from Au nanodroplets. To demonstrate the large range of diameters covered in our sample series, the light blue hexagons in the upper panel, representing the NW cross-section, are drawn to scale. Increasing the growth time t from 20 to 125 min continuously tunes the NW diameter from 20 to 110 nm with a radial growth rate r of 0.4 nm/min. Larger-diameter NWs are fabricated by overgrowth of a 110 nm-thin core with an additional layer of GaAs at a lowered substrate temperature of 460 °C as discussed in Section 5.2, enhancing the radial growth rate to 1.1 nm/min. The NW diameters are fitted by the linear function $10\,\text{nm} + 2rt$ in the 510 °C region and $110\,\text{nm} + 2r(t - 125\,\text{min})$ in the 460 °C region. The fits are plotted as gray lines.

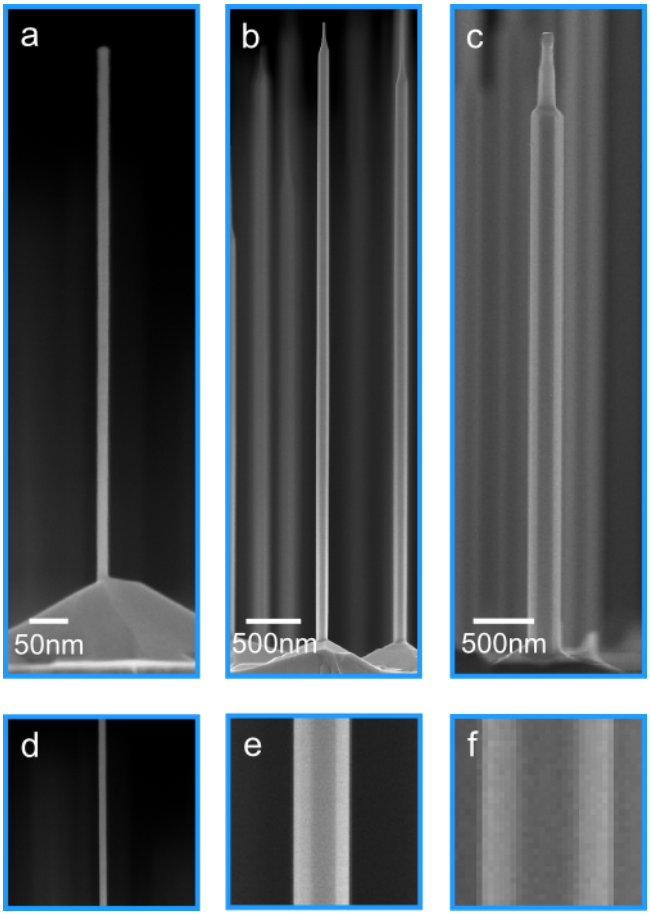

Figure 5.5: Scanning electron micrographs of three single, as-grown NWs with the respective diameters of (a) 22 nm, (b) 113 nm and (c) 280 nm. Note that the magnification of the images changes from (a) to (b) and (c) (cf. scale bar). To illustrate the immense difference in size covered by our sample series, a segment of the identical wires shown in (a)-(c) is magnified to scale in the respective micrographs in (d)-(f).

NWs in our series are grown from 0.05 Å Au substrates and synthesized under identical initial conditions, varying only in the growth time during which the material is deposited and, for the larger diameters, in the rate of this process. We further conclude that such a systematic approach leaves very little room for unforeseen variations in crystal properties like the number of point defects, or any structural inhomogeneities and is thus particularly well-suited to investigate such sensitive properties like the spin relaxation time, or the exciton lifetime.

6

Size-tunable quantum effects in nanowires

When we consider an electron moving through free space, the idea of one dimension seems quite clear: the electron can either go back or forth. As soon as it comes to the implementation of this concept in solid-state devices, however, the definition of one dimensionality is less clear. Particularly distinguishable by the applied experimental method, the various branches of low-dimensional physics thus often employ the attribute *one-dimensional*, and in extension also the expressions *spatial quantum confinement* and *quantum wire*, differently. In nanoscale optics, for example, the occurrence of characteristic quantum confinement features in the optical emission spectra, like an increase in the emission energy, or emission peaks from higher subbands, constitute the right of calling a thin wire a *quantum wire*. These effects are usually considered when the size of an object, i.e., in our context its diameter, becomes comparable to the Fermi wavelength [101], or the exciton Bohr radius in the host material [40]. However, both Fermi wavelength and Bohr radius may depend on external parameters like the carrier density or the system size [102]. Using such a language to express what the term *one-dimensional* (1D) exactly means is therefore not straightforward.
At the contrary, in nanoscale transport, the flow of electrons through the n-th subband of a narrow constriction (e.g., a gate-defined quantum-point contact [103]) is considered one-dimensional as soon as the signatures of quantized conduction are resolved in the experiment. Apart from these employments, the terms *quasi-1D*, or *quantum wire* are occasionally also used to describe narrow semiconductor channels with lateral dimensions on the micron scale, underlining their size-differences against macroscopic objects [104, 105]. In this vast variety of terms and definitions, we follow here in this thesis a more rigorous definition [106, 107]: We refer to a NW as being in the *electronic 1D quantum limit*, when only the lowest 1D subband is occupied by the photo-excited carriers. In the case of zero temperature and elastic scattering, the electrons in our wires are thus bound to move along the wire axis; a situation much alike the above mentioned 1D electron in free space going only back or forth.

6.1 Confinement-induced electronic and optical features

In this section we quantify the definition of 1D for our WZ GaAs NWs and the particular conditions of our experiment, setting a diameter value which we consider as the 1D quantum limit. With the help of a circular potential well model, we shed some light onto the electronic band structure in the wires and estimate the quantum confinement effect on the band dispersion. Joining our experiment with a theoretical estimate, we address the size-dependent signatures of the exciton emission in our NWs to study the impact of the increasing spatial confinement as we tune the wire diameter.
Some of the results, figures and contents presented in this chapter are part of a publication and reported in Ref. [108].

6.1.1 Subband dispersion and the diameter-dependent exciton emission

As illustrated by the sketch in Fig. 6.1, we conduct a μ-PL study on the wafer series presented in Section 5.4 to investigate the diameter-dependent emission energy of single, free-standing wires. A general observation we make in our study is that upon decreasing the NW diameter d below 50 nm, a significant increase in the emission energy occurs. To demonstrate this behavior, we show a series of time-integrated μ-PL spectra in Fig. 6.1a, obtained under cw excitation, for eight single NWs with different diameter, which are each representative for the respective wafer. The averaged emission energy of several single NWs of nominally identical diameter is further summarized in Fig. 6.1b for each of the eight different wafers. While no significant energy shift occurs for NW diameters d in the range of 490 to 90 nm, a clear increase in the emission energy can be observed for $d < 50$ nm. For the larger NWs, we measure an average emission peak energy of $E = 1.521$ eV, which is consistent with earlier reports of the low-temperature PL emission energy in WZ GaAs NWs [24, 88]. Upon decreasing the diameter d below 50 nm, the emission continuously shifts towards higher energies by a total amount of $\Delta E \approx 18$ meV. We attribute this spectral shift to the increasing spatial quantum confinement in the NW core [21].
We estimate the effect of the spatial confinement on the subband energies in our NWs from a circular potential well model with hard wall boundaries

$$E_{n,l} = \frac{\hbar^2 \zeta_{n,l}^2}{2\, m_\perp (d/2)^2}, \tag{6.1}$$

where $E_{n,l}$ are the energy eigenvalues that represent the 1D subbands, $\zeta_{n,l}$ denotes the n-th zero of the Bessel function of the first kind $J_l(\rho)$ and $m_\perp$ is the effective mass along the direction of confinement, i.e., perpendicular to the NW axis [109]. For the diameters of our experiment, we expect the hard wall boundary condition to reliably estimate the

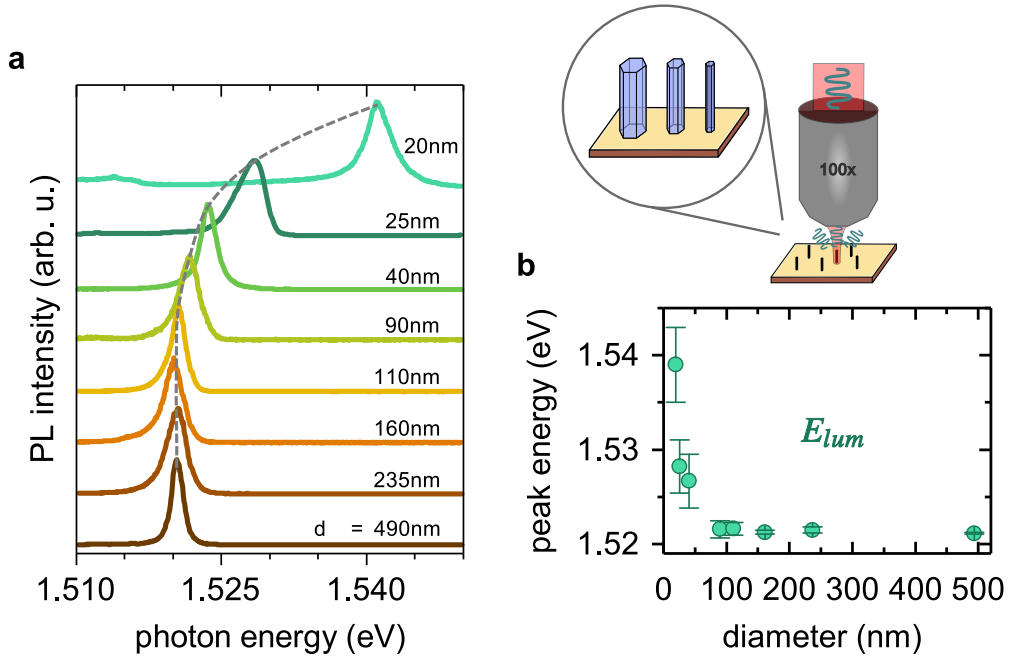

Figure 6.1: Upper right corner: Illustration of free-standing NWs as they are photo-excited in the μ-PL setup. (a) Luminescence emission from NWs with different diameters. Each single NW spectrum represents one of the eight individual wafers produced for our sample series. Spectra were normalized for illustration purposes. The apparent broadening of the luminescence line-width for smaller NW diameters is discussed in Section 6.4.1. (b) The peak energy of the NW emission increases as a consequence of spatial quantum confinement. Each value is obtained by averaging the peak energy from several single NWs. The standard deviation (error bars) increases for smaller NWs, consistent with the statistical diameter distribution of a self-assembled ensemble.

subbands in our wires since the effects of spatial confinement on the single particle energies are small compared to the height of the potential barrier provided by the AlGaAs shell (~300 meV [110, 111]). In Fig. 6.2a we plot the five lowest possible energy states for electrons (red shaded lines) and holes (blue shaded lines) as a function of the NW diameter. To calculate these subband energies, we have used the effective masses given in Ref. [27]: $m_{\perp,e} = 0.075m_0$ and $m_{\perp,h} = 0.12m_0$. Note that the results of Ref. [27] agree well with a recent experimental study on the electronic properties of WZ GaAs NWs [112].
A quantitative comparison between the diameter-dependence of the exciton emission energy in Fig. 6.1b and the diameter-induced change in the calculated transition energy reveals a large discrepancy: at $d = 20$ nm, the potential well model estimates an increase in the emission energy of 47 meV as compared to the largest wires; instead in our experiment, we only observe an increase of 18 meV. This discrepancy will be addressed in more detail in Section 6.2. In a next step, we will focus on the definition of the 1D quantum limit in our NWs.

6.1.2 Defining the 1D quantum regime in nanowires

As already mentioned, in this thesis we stick to the rather rigorous definition of one dimension that is also referred to as the *true 1D regime* [106, 107]: Wires are in this 1D regime when only the lowest subband is occupied by the photo-excited carriers. Assessing a specific diameter value, this definition thus depends on the optically injected carrier density. We note that the 1D limit determined in the following is particularly true for the time-resolved experiments rendering the central results on the spin and exciton lifetimes in Parts III and IV.
After the photo-excitation in our experiment, the carriers relax to the minimum of the conduction or valence band. The 1D limit in our NWs is therefore reached when the thermalized energy distribution of electrons or holes is smaller than the splitting Δ between the lowest two 1D subbands. When we increase the spatial confinement by shrinking the NW diameter in our experiment, the energetic separation between two successive subbands increases correspondingly. Starting from the lowest possible energy, the optically excited carriers fill all available states from $k = 0$ to the Fermi wave vector k_F. At the low temperatures of our experiment (T = 4 K), the highest occupied energy state is then given by the quasi-Fermi level in the conduction or valence band

$$E_F = \hbar^2 k_F^2/(2m_{\parallel}), \tag{6.2}$$

where $k_F = n_{1D}\pi/2$ relates the carrier density n_{1D} to the Fermi wave vector k_F in one dimension [101]. In Eq. (6.2), the energy of the electrons and holes is determined by their effective mass $m_{\parallel}$ along the direction of free motion. We use $m_{\parallel,e} = 0.060m_0$, $m_{\parallel,h} = 0.75m_0$ from Ref. [27] and $n_{1D} \approx 1 \times 10^6 \mathrm{cm}^{-1}$ (see carrier density calculations in Section 3.2) to find that $E_F^e = 16.5$ meV for the electrons, whereas it is only $E_F^h = 1.3$ meV for the holes. In Fig. 6.2b we show the corresponding parabolic dispersion along the

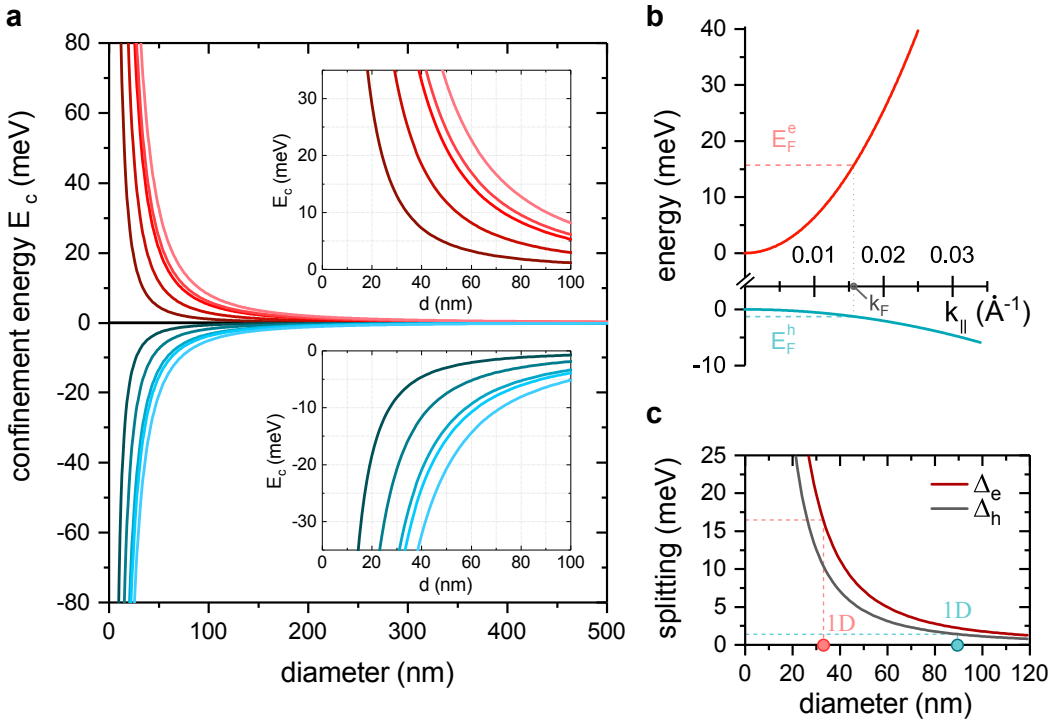

Figure 6.2: One-dimensional band structure in a NW calculated according to Eq. (6.1). (a) shows the diameter-dependence of the five lowest possible energy states as estimated from a circular potential well model for the electrons (red shaded lines), as well as for the heavy holes (blue-shaded lines). The insets show a magnified view of the region of interest. The kinetic energy of the photo-excited carriers is distributed along the direction of free motion. Their parabolic dispersion is plotted in a simple two band scheme in (b) together with the respective quasi-Fermi levels (dashed horizontal lines). Red and blue colors are again associated with conduction and valence bands. The electrons or holes in the NW have reached the 1D limit when the splitting between the two lowest subbands $\Delta_{e,h}$ is larger than the respective quasi-Fermi level $E_F^{e,h}$. The diameter-dependence of $\Delta_{e,h}$ is shown in (c), where the quasi-Fermi levels are depicted as dashed horizontal lines. The two crossing points reflect the 1D limit for electrons (red) and holes (blue).

positive $k_{\|}$-direction in a simplified two-band model. The horizontal dashed lines indicate the position of the quasi-Fermi levels relative to the minimum of the bands, the vertical dashed line marks the Fermi wave vector k_F.
In order to find the 1D limit for the carriers in our NWs, we calculate the diameter-dependent splitting $\Delta_{e,h}$ between the two lowest subbands for the electrons (e) and for the holes (h). The result is plotted in Fig. 6.2c. The horizontal dashed lines again denote the position of the quasi-Fermi levels, whereas their intersection with the $\Delta_{e,h}$-curve (full lines) determines the diameter below which only one single subband is occupied. Due to the highly anisotropic effective mass of the heavy holes, the 1D limit is reached already at larger diameters in the valence band.
Determining the 1D quantum limit for our NWs in this way depends directly on the photo-excited carrier density $n_{1\mathrm{D}}$. For $d < 90\,\mathrm{nm}$ only the lowest subband is populated by the holes in the valence band, while the same condition is fulfilled at diameters $d < 35\,\mathrm{nm}$ for the conduction electrons. We thus conclude that under the given pulsed laser excitation, NWs with diameters below $d < 35\,\mathrm{nm}$ belong to the *true 1D regime* in which electrons occupy only the lowest 1D subband.

6.2 Enhanced Coulomb interaction: Increasing exciton binding energies

From Eq. (6.1) we have calculated the diameter-dependence of the 1D subband energies, i.e., the single particle states available for the photo-excited electrons and holes in our NWs. Since the emission originates from photo-carriers around the Γ-point, the diameter-dependent emission energy we detect in our luminescence experiment should then correspond to a transition between the lowest possible conduction band state, hereafter denoted $E_{e1}(d)$, and the highest possible valence band state, respectively denoted $E_{h1}(d)$.
In order to conduct a quantitative comparison with the experimentally observed emission energies, we plot the sum of the two single particle energies, $E_{e1}(d) + E_{h1}(d)$, as a function of the wire diameter in Fig. 6.3a. This curve quantitatively represents the diameter-dependence of the lowest possible transition energy that is expected to arise from the two lowest single particle states. While the same general trend as in our experiment is observed, the quantitative evaluation of this transition energy reveals a large discrepancy between the calculated single particle energies and the experimentally observed exciton emission energies. The discrepancy is most notable for $d = 20\,\mathrm{nm}$: Here, in the experiment, the exciton emission energy has shifted by $\Delta E \approx 18\,\mathrm{meV}$ compared to the largest wires, whereas the theoretical single particle description predicts a much larger increase of 47 meV, as indicated by the red dot in Fig. 6.3a.
This discrepancy between theory and experiment results from the approximation of non-interacting particles in our rather simple model. Neglecting the opposite charge of the two particles does not cope at all with the physical reality of an attractive Coulomb

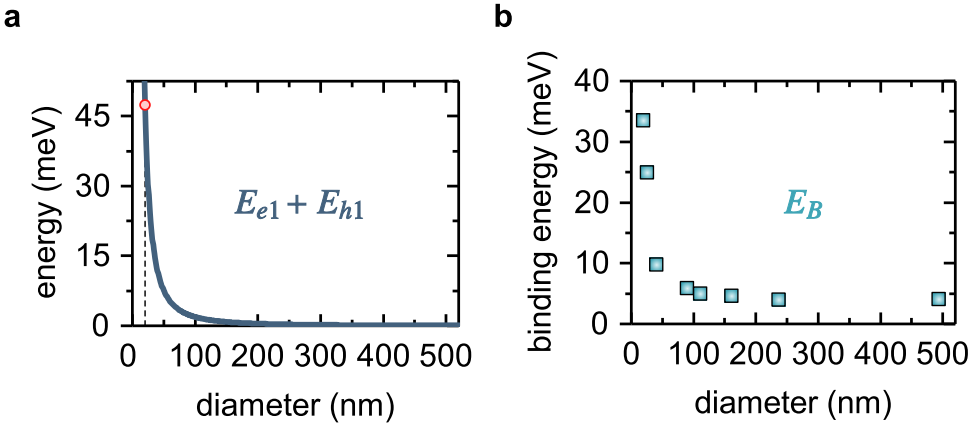

Figure 6.3: (a) Calculated diameter-dependence of the sum of the minimum single particle energies, $E_{e1}(d) + E_{h1}(d)$. (b) As the wire diameter decreases, confinement and dielectric screening affect the exciton states in our wires, substantially enhancing their binding energy E_B. In our experiment, the diameter-dependent binding energies come out as the difference between the theoretically calculated band gap and the experimentally determined emission energies shown in (b).

interaction between them. In particular, this approximation definitely overlooks the confinement-related diameter-dependence of the interaction–a specific feature of the low-dimensional exciton state. Indeed, combining the effects of spatial confinement and efficient dielectric screening of the attractive Coulomb potential, a low-dimensional nanostructure can strongly modify the fundamental properties of excitons in the bulk. The confined exciton is then characterized by a diameter-dependent exciton binding energy and correspondingly also a diameter-dependent effective Bohr radius [42, 102, 113].
To estimate how strongly this binding energy $E_B(d)$ can be enhanced by tuning the NW diameter, we calculate

$$E_B(d) = E_{g,0} + E_{e1}(d) + E_{h1}(d) - E_{lum}(d), \tag{6.3}$$

where we use a low-temperature single-particle band gap of bulk WZ GaAs, $E_{g,0} = 1.525\,\text{eV}$. $E_{e1,h1}(d)$ are the diameter-dependent eigenenergies of the lowest subband in the conduction and valence band as calculated from Eq. (6.1) and $E_{lum}(d)$ is given by the luminescence peak energies of the NW emission. For the largest NWs, the bulk exciton binding energy is $\sim 4\,\text{meV}$ (calculated according to Eq. (2.4)) and thus comparable to the binding energies reported for bulk GaAs [42]. Tying their motion to a single dimension by confining the excitons on increasingly smaller scales in our wires strongly enhances their binding energy. For the 20 nm-thin wires we find the largest enhancement, by a factor of 8, resulting in an exciton binding energy of $\sim 33\,\text{meV}$.
The same physical principles affecting the exciton binding energies in our 1D wires indeed have caused the prominent uprising of two-dimensional layers made from transition metal

dichalcogenides owing to the occurrence of extremely large exciton binding energies with hundreds of meV's in these materials [114]. Before this background, we point out that similarly large binding energies are also predicted for nm-thin semiconductor wires surrounded by a medium with low dielectric screening [113].
By demonstrating the size-tunable binding energy of excitons in 1D wires, our analysis highlights an interesting property of the NW system.

6.3 State-filling-induced emission from higher-order subbands

Owing to the finite recombination lifetimes of excitons relaxed to the bottom of the band, state-filling under high enough laser excitation power facilitates the occupation of higher-order subbands by the photo-excited carriers. According to the optical selection rules in a 1D wire [115], we might expect to find signatures of these occupied higher subbands on the high-energy side of the emission spectra, if we sufficiently increase the laser excitation power. Yet, even under the full-power excitation with our near-resonant 1.58 eV-laser diode such a high-energy peak does not show up in the emission spectrum (light blue curve in Fig. 6.4a). However, when we excite the identical wire with a non-resonant 1.80 eV-laser, a second emission peak indeed appears at the high energy side of the emission spectrum, as demonstrated by the black curve in Fig. 6.4a. We attribute this new peak to the radiative recombination of electrons and holes residing in a higher 1D subband. The experimentally detected difference of 31 meV between the two emission peaks, observed for the 1.80 eV laser excitation, matches the theoretically predicted value of the second lowest transition energy between 1D subbands, i.e., $(E_{e2}-E_{e1})+(E_{h2}-E_{h1})$, for a diameter of $d = 32$ nm. Although this diameter value differs from the average wire diameter measured in the NW ensemble, $d = 25$ nm, it lies well within the statistical diameter distribution of the ensemble (as emphasized by the red bar in the histogram in Fig. 6.4b).
We suggest that the occurrence of the second emission peak is not a matter of the high excitation energy alone, but also related to the higher absorption of the high-energy photons, resulting in larger e-h pair densities in the 1D wire despite the nominally same excitation power.
Using a non-resonant (1.80 eV) laser energy reveals a feature in the NW emission spectrum, which agrees well with our theoretical estimate of the second lowest transition energy in a 1D wire. Hence, this observation further highlights the 1D character of our ultrathin wires.

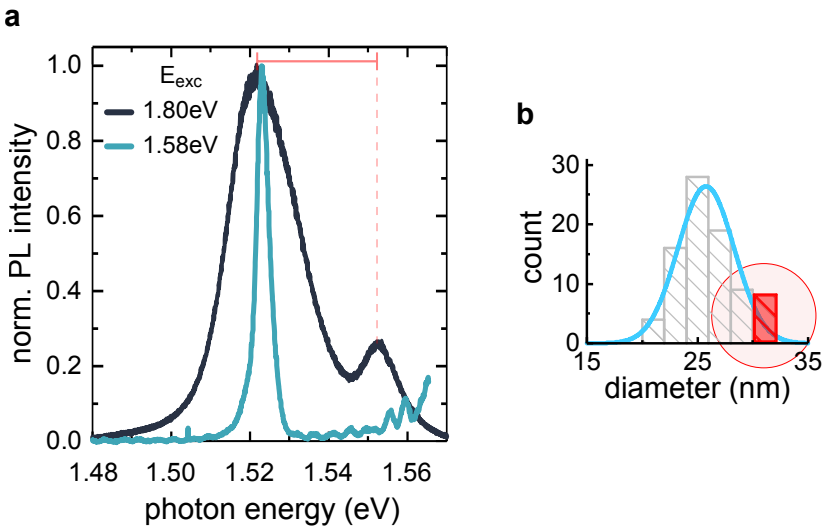

Figure 6.4: (a) The higher laser excitation energy reveals a high-energy peak in the emission spectra from a nominally 25 nm-thin wire, attributed to the radiative e-h recombination from higher subbands. Signals in the range from 1.53 to 1.57 eV of the light blue curve are an artifact of this particular measurement and do not belong to the wire emission. (b) Statistical diameter-distribution of the NW ensemble with nominally 25 nm diameter. The energy difference between the two peaks in (a) agrees well with the theoretically predicted value for a diameter of $d = 32$ nm (red bar) found within the statistical diameter distribution in the wire ensemble.

6.4 Confined to quantum scales: Features of photo-carriers in 1D wires

In addition to the optical emission features related to the subband formation in thin wires, our luminescence experiments uncover further peculiar features in the 1D wire emission spectra.

6.4.1 Trion signatures in the 1D wire emission spectra

In PL experiments, some of the more subtle features in the emission spectra may smear out, or disappear entirely, under elevated excitation powers. To steer clear of overlooking these features, we have investigated our NWs under very low-power excitation and analyzed the diameter dependence of their luminescence. To avoid parasitic PL signal from the substrate and to ensure that the observed luminescence originates exclusively from the NWs, we remove the free-standing wires from the GaAs growth substrate and disperse them onto non-luminescent Si/SiO_2 substrates. Due to small differences in the thermal expansion between GaAs and Si, at low temperatures the substrate strains the deposited NWs and thus slightly lowers the overall band gap as compared to the unstrained, free-standing wires [116].
In Fig. 6.5a-c we show the low-temperature luminescence from three NWs with diameters decreasing from 110 to 25 nm. According to the estimate derived in Section 3.2, the low-power cw excitation creates a carrier density $n_0 \approx 4 \times 10^4 \mathrm{cm}^{-1}$, far below the Mott transition. Such photo-excited carrier densities correspond to an occupation number as low as 4 e-h pairs in the entire wire and the luminescence is thus dominated by excitonic transitions [40, 117]. Hence, the main emission peak observed in Fig. 6.5a-c is attributed to the free exciton recombination in our wires, its smooth line shape reflecting the distribution of free carriers with a full width at half maximum of (1.7 ± 0.2) meV that varies only slightly as the diameter decreases. Importantly, when we decrease the NW diameter, the free-exciton emission retains its overall line shape, confirming the presence of a delocalized 1D wave function [49, 117]. Promoting the high crystal quality of the wire, this observation therefore strongly speaks against structural inhomogeneities, e.g., slight local diameter variations, that would capture and localize excitons, leading to an inhomogeneously broadened NW emission. In the end, the emission spectra shown in Fig. 6.5 highlight the 1D character of excitons in our ultrathin wires.
A closer look at Fig. 6.5 yields another interesting features in the NW emission spectra. Upon decreasing the diameter of our wires from $d = 110$ nm to 25 nm, the low-power cw excitation first reveals a shoulder emerging in the spectrum at the low-energy side of the free exciton emission, which further develops into a clearly distinguishable second peak at $d = 25$ nm (cf. Fig. 6.5a-c). We interpret this lower energy peak to originate from the three-particle trion complex–single excitons bound to residual charge carriers–also observed in two-dimensional structures [118, 119]. Simultaneously, in Fig. 6.5b and c, we note an increase in the energy separation between the peaks such that, at $d = 25$ nm,

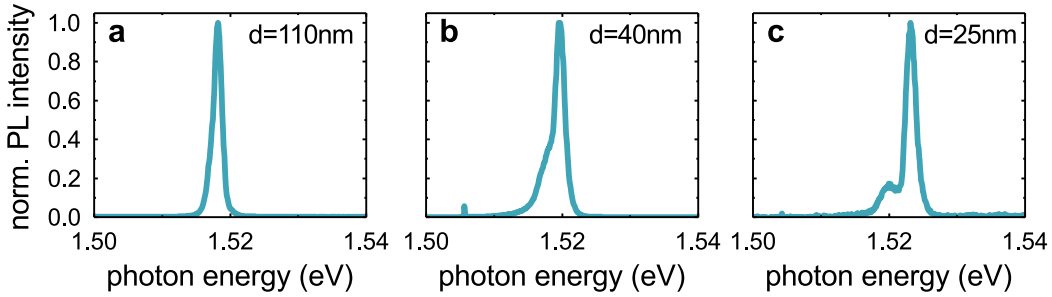

Figure 6.5: (a)-(c) Low-temperature luminescence profiles of three NWs with different diameters. The low-power cw excitation reveals a second peak emerging at the low-energy side of the free exciton emission. Under low-power cw excitation, the 1D carrier density is $n_0 \approx 4 \times 10^4 \mathrm{cm}^{-1}$, corresponding to numbers as low as 4 photo-excited excitons in the entire wire.

the two peaks are clearly distinguishable and separated by a peak-to-peak distance of 3 meV. A priori, the reason for such a shift is not obvious, since it suggests a different diameter-dependence of the binding energy of an exciton and a trion. A detailed theoretical analysis of this problem however indeed explains the increasing energy separation between the exciton and the trion observed in Fig. 6.5 to result from the differences in the dielectric screening predicted for excitons and trions in semiconductor NWs [113] and thus confirms our experimental observation.

6.4.2 Many-body interactions in the 1D e-h system

The optical emission features presented so far have mainly been obtained under relatively low photo-excited carrier densities and were thus governed by excitonic emission. In the following, we analyze the emission from highly excited 1D wires.
Figure 6.6 illustrates how the emission from a 25 nm-thin wire with a length of 1 µm (the same wire as shown in Fig. 6.5c) evolves under increasing e-h pair density. In our experiment, increasing the laser power by two orders of magnitude brings the optically excited carriers into a regime above the Mott transition: instead of 4 excitons, we now excite up to 400 electrons and holes in the 1D wire. In a simple 1D picture of beans on a string, this excitation results in an inter-particle distance of only 1 µm/400 = 2.5 nm. As the carrier density increases, both the luminescence signals from the free exciton and the trion overlap until the two peaks are no longer distinguishable at high carrier densities. According to Ref. [40], the Coulomb screening between the densely packed electrons and holes dissolves the exciton states and the photo-excited carrier ensemble transforms into an e-h plasma. This effect is responsible for the broadening of the line-width observed in Fig. 6.1a [117].
Interestingly, while the line-width of the emission peak broadens under the increasing photo-carrier density, the energy position of the peak is hardly affected, as may be recognized in Fig. 6.6. We attribute this observation to the mutual compensation of two

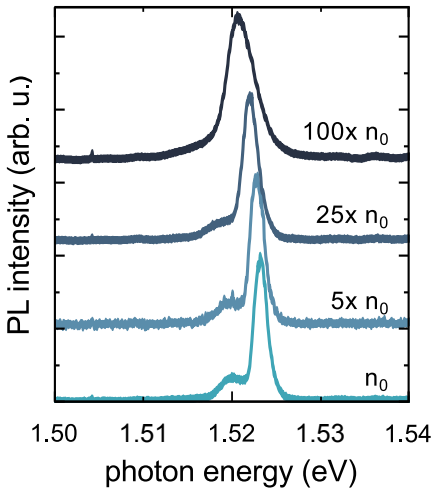

Figure 6.6: Effects of high excitation density on the emission spectra of a 25 nm-thin wire. Increasing the carrier density from $n_0 \approx 4\times10^4\text{cm}^{-1}$ to $100 \times n_0$ dissolves the excitons in the system and merges the two excitonic peaks into a single, broadened emission peak.

counteracting effects in the emerging e-h plasma [40]: On the one hand, the attractive Coulomb potential binding the excitons is increasingly screened by ionized, free electrons and holes, which decreases the exciton binding energy, causing a shift of the emission peak towards higher energies. On the other hand, many-body interactions become more and more pronounced and renormalize the band gap, instead pushing the emission energy into the opposite direction on the energy scale.
Our luminescence experiment therefore clearly supports the occurrence of an e-h plasma under high excitation power in our 1D wires. We would however like to remark that, while the e-h plasma state is commonly observed in GaAs bulk and quantum well structures, its occurrence in a 1D wire is not self-evident. In fact, in 2008, investigating the high-density e-h system in 1D InAs wires, Alén *et al.* demonstrated the transition of free excitons into a very different many-body state called the e-h liquid [120]. Their work is the first to report of such a transition in a direct semiconductor. Under increasing e-h pair density, the occurrence of this peculiar state was evidenced by a new peak emerging on the low-energy side of the exciton emission spectra; a characteristic signature of the e-h liquid phase [41]. We thus note with particular interest the absence of this low-energy emission feature in our 1D GaAs wires in Fig. 6.6.

6.5 Summary and outlook

Owing to the advances in the NW fabrication presented in the last chapter, our wires are diameter-tunable in an unprecedented range, enabling us to monitor a number of confinement-induced electronic and optical effects, which evidence the 1D character of

our wires. The diameter-dependence of the exciton emission energy, for example, clearly reflects the increasing spatial confinement. On the basis of a potential well model, we estimate the subband dispersion in the NWs and eventually determine a diameter below which our wires are in the 1D quantum regime.
Studying the wire luminescence further uncovers a strong diameter-dependence of exciton binding energies in NWs; for the smallest diameter, exciton binding energies reach up to 33 meV, an eight-fold increase as compared to the largest NWs. Moreover, the 1D character of our ultrathin wires unfolds also under high excitation power: A second, higher-in-energy peak emerges in the emission spectrum, which agrees well with our theoretical expectation for the next dipole allowed transition from higher 1D subbands. A detailed examination of the wire emission reveals also the more intricate optical features. Very low power excitation brings forth a low-energy shoulder in the exciton emission spectrum, which originates from the three particle trion complex. Very high power excitation, on the other hand, produces the signatures of excitons dissolved into an e-h plasma; per se surprising, since a recent publication reports the transition of excitons in a 1D wire into a different many-body state called the e-h liquid [120].

II Spin phenomena in semiconductor nanowires

Over the past thirty years, utilizing the spin of an electron as the information carrier has been the central aspect around which the field of spintronics has evolved ever since [59, 121]. In this field, the combined interaction of the spin and the orbital degrees of freedom is of fundamental importance for the development of spintronic device concepts, since it has been shown to directly influence the spin dynamics of mobile charge carriers in the crystal, in particular the spin relaxation [51–53, 55, 64, 122]. Combining optimized SOC and the interesting geometrical form factor, NWs are strong candidates for the realization of spin-field-effect transistor concepts [123], spin–orbit quantum bits [124–127] or the experimental demonstration of Majorana fermion bound states [4, 127, 128]. And yet, compared to their higher-dimensional counterparts, properties like the spin relaxation dynamics were hardly addressed in NW experiments.
Focusing on spin-related phenomena, this part of the thesis will demonstrate that our optical study of spin relaxation in semiconductor NWs substantially contributes to fill this gap; both from an experimental point of view, opening interesting perspectives for spin transport, as well as from a theoretical angle, advancing the understanding of spin relaxation processes in semiconductor wires. Adding on top of that, our experiments on ultrathin NWs allow a glimpse at the peculiar properties of electrons confined to a single dimension.

7

Optical spin injection into a single free-standing wire

In this chapter, starting from the example of single, free-standing wires with typical, regular-sized diameters around $d = 100$ nm, we will introduce a contact-free, non-invasive optical method of spin injection into NWs and use it to uncover a variety of spin phenomena. Although these wires do not show the emission signatures of quantum confinement–and might thus be regarded as small pieces of bulk WZ GaAs–we will show in Chapter 8 that the observed spin dynamics differ strongly from the experimental reports for III–V bulk WZ semiconductors, such as GaN [129–132], already indicating the encounter with new spin-related phenomena in NWs.

Some of the results, figures and contents presented in this Chapter are part of an article reported in *Nature Communications* [133]. The time and magnetic field-dependent measurements were performed in a cooperation together with Prof. Dr. Tobias Korn and Prof. Dr. Christian Schüller. The model introduced in Section 8.2.3 was developed in close collaboration with Dr. Martin Gmitra, Prof. Dr. Jaroslav Fabian and Prof. Dr. Tobias Korn.

7.1 Preparing a nanowire sample for optical spin injection

Owing to our advances in the NW growth process (cf. Section 5.1), wafers with large wire-to-wire distances in the as-grown ensemble are now readily available. We are thus able to optically study spin phenomena in only one single wire at a time, despite the 1 µm lateral size of our laser excitation spot. The first step in this enterprise goes beyond the mere single wire excitation: To unambiguously demonstrate the actual optical injection of spins into a single and upright standing NW involves excluding any structural effects (e.g., NW bending induced by bundling with neighboring wires [134, 135]). For that purpose,

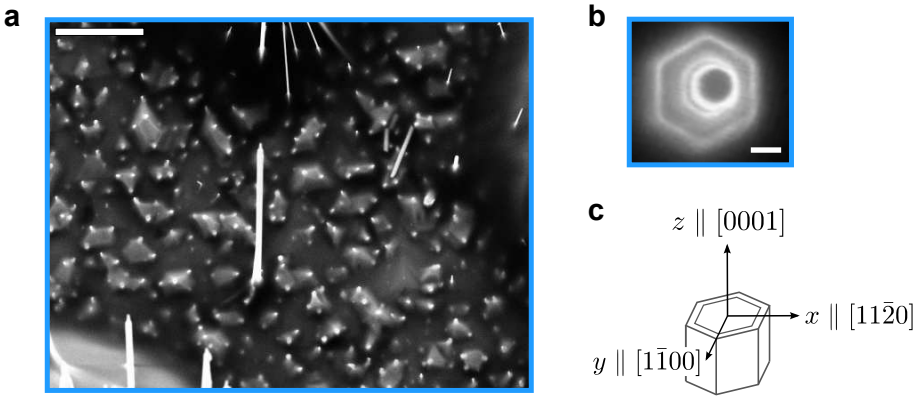

Figure 7.1: Free-standing WZ GaAs/AlGaAs core/shell NWs. (a) Representative scanning electron microscope image of a single, free-standing NW used for optical spin orientation experiments. The scale bar indicates 2 µm. (b) Top-view image of the NW in (a), showing the solidified hemispherical catalyst droplet atop the hexagonal NW. Scale bar, 50 nm. (c) Schematic representation of the core/shell NW and the orientation of the coordinate system with respect to its axis, denoted as the $z \parallel [0001]$ axis.

we want to be able to first identify a single wire with high crystal quality in our optical spectroscopy, then locate its position on the sample and finally relocate the same wire, over the course of weeks, in different setups and measurement configurations. In order to implement these individual steps, we have developed a routine which prepares a NW sample prior to any measurements. The details of this routine are described in Refs. [98, 136]. Here, we summarize the important steps: Dipping the as-grown NW sample into an ultrasonic Isopropanol bath reduces the NW density locally, creating a spatially highly inhomogeneous distribution of standing wires. On the scale of tens of µm, this spatial distribution of still standing wires forms a pattern that is unique and can therefore be repeatedly identified in optical microscopy. Providing any way of large scale orientation on the sample on the hundreds of µm scale (for example by gold structures evaporated onto the sample through the pre-defined holes of a shadow mask, or simply by fine-line scratching using a thin needle), then allows us to relocate the position of the characteristic NW pattern on the sample surface. Eventually the isolated, single NWs existing within these patterns are easily identified, characterized and then relocated in our µ-PL setup. To avoid possible damage by the high-energy electrons, the sample is only mounted into a scanning electron microscope after all optical measurements are completed. In this microscope, the µ-PL-characterized NWs can be identified and investigated with high spatial resolution.
Figure 7.1a shows a representative scanning electron micrograph of such an individual, free-standing wire used for the optical measurements presented in the following sections. As described above, this wire was first identified in µ-PL spectroscopy, fully characterized as outlined in Section 4.2.2 and then located on the sample. After its spin properties were

measured in different experiments, the same identical wire could be located, identified and morphologically studied in the scanning electron microscope. The length of the wire is $l = 5\,\mu m$ and the total diameter is $d = 120\,nm$. Figure 7.1b further displays a top-view of the same wire, revealing its characteristic hexagonal cross section and the solidified hemispherical catalyst droplet at the tip. According to transmission electron microscopy, the six equivalent sidewall facets are oriented along the $\langle 11\bar{2}0\rangle$-directions of the WZ unit cell, as sketched in Fig. 7.1c. We will use the wires from this wafer and their circularly polarized emission to demonstrate the efficient optical injection of spin polarized electrons in the following section.

7.2 Spin signals under continuous excitation and detection

A schematic of our optical approach is depicted in Fig. 7.2a: A free-standing NW is continuously excited with circularly polarized laser light propagating parallel to the NW $\hat{c} \parallel \langle 0001\rangle$ axis. A typical area scan of the integrated PL intensity of a NW is shown in the inset of Fig. 7.2b in false color coding, evidencing the single wire spectroscopy. In Fig. 7.2b , showing the polarization-resolved µ-PL emission of the wire at $T = 4.2\,K$, each of the spectra contains two characteristic peaks. The one at $E = 1.491\,eV$ is also seen when exciting the bare substrate. It stems from excitons bound to single carbon impurities in the GaAs substrate (see Section 2.1, or Refs. [137, 138]). The high intensity luminescence peak at $E = 1.521\,eV$ and its narrow linewidth of $\Delta E = 3\,meV$, however, are characteristic for the free-exciton emission in stacking-fault-free WZ GaAs NWs [24, 88].
The wire is continuously excited under the σ_+ circularly polarized emission of a 1.58 eV, near-resonant laser, estimated to solely induce the heavy hole states-to-conduction band transition in the WZ GaAs core [20, 23, 25, 139–141]. The black curve in Fig. 7.2b shows the spectrum obtained for continuous (i.e., time-integrated) detection of the σ_+ polarization of the resulting emission, while the blue curve shows the spectrum of the σ_- polarization. The corresponding integrated PL intensity I_+ of the WZ free exciton is much stronger than its counter-polarized component I_-, revealing significant circular polarization of the luminescence of the WZ GaAs NW in the absence of an external magnetic field. The degree of circular polarization, defined as $P_C = (I_+ - I_-) / (I_+ + I_-)$, reaches ~54 %. Note, that in contrast, the substrate-related peak shows no significant circular polarization. This large degree of circular polarization of the characteristic NW emission is a strong indication of efficient optical injection of spins into the wire. Yet, as we will see in Chapter 11, static polarization effects in NWs can be induced by structural asymmetries, rendering this particular experiment inconclusive as solid evidence of actual spin injection. We thus require further evidence for the successful optical spin injection into a single wire.

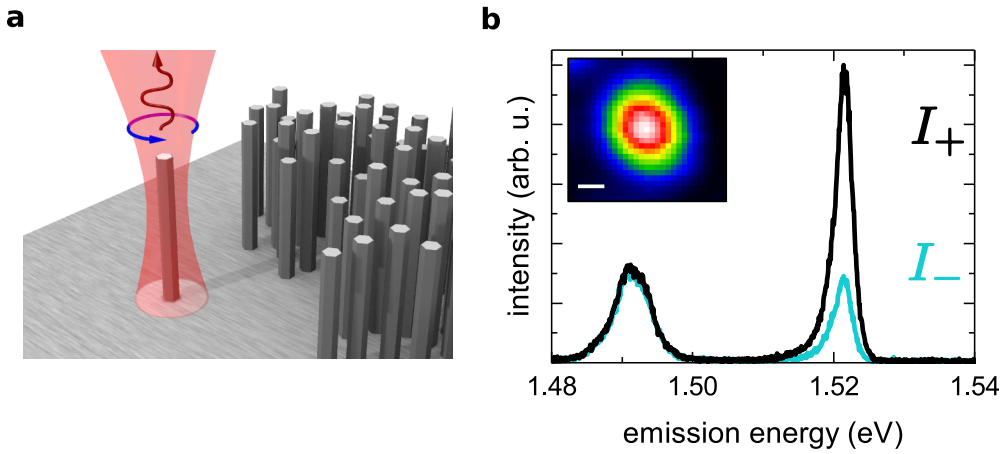

Figure 7.2: Optical spin orientation in single WZ GaAs NWs. (a) Schematic representation of the measurement geometry used for optical orientation measurements in our experiment. An isolated, free-standing NW is individually excited by a tightly focused circularly polarized laser beam propagating parallel to the NW axis. Helicity-resolved PL emission is detected in confocal configuration along the NW axis. (b) Polarization-dependent μ-PL spectra of a single, free-standing WZ GaAs NW at 4.2 K under circularly polarized excitation. While the substrate peak at E = ~1.491 eV holds no significant circular polarization, the NW emission at E = 1.521 eV is highly polarized with a degree of polarization of ~54 %, indicating efficient optical orientation of spins in the wire. Inset shows an area scan of the integrated PL intensity in the vicinity of a NW in false color coding, evidencing single NW spectroscopy. Scale bar, 1 μm.

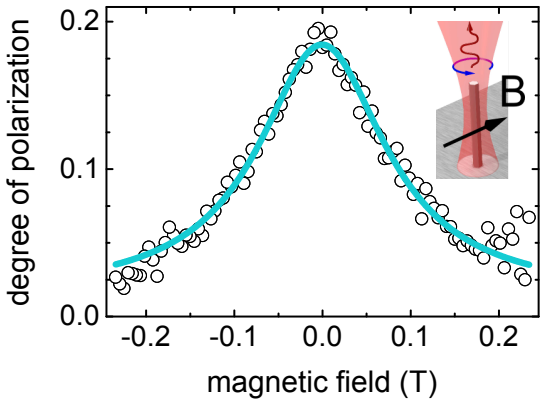

Figure 7.3: Hanle effect measurement for a single WZ GaAs NW. The degree of polarization of the WZ free exciton emission decreases as a function of the transverse magnetic field. The continuous blue line is a Lorentzian fit to the data using equation (7.1). The schematic measurement configuration is superimposed.

Precession in a transverse magnetic field

In the presence of spin relaxation, an optically injected spin ensemble should be depolarized by spin precession in an external transverse magnetic field (Hanle effect [142]), according to [51]

$$P_C(B) = \frac{P_C(0)}{1 + (\omega_L \tau^*)^2}, \qquad \frac{1}{\tau^*} = \frac{1}{\tau_{pl}} + \frac{1}{\tau_s}, \tag{7.1}$$

where $P_C(0)$ is the degree of polarization at zero magnetic field and τ^* is the effective spin lifetime, which is given by the inverse sum of the luminescence lifetime τ_{pl} and the spin relaxation time τ_s. $\omega_L = g^* \mu_B B/\hbar$ is the Larmor spin precession frequency induced by the external magnetic field B, μ_B is the Bohr magneton, g^* is the transverse effective electron g-factor, and $\hbar$ is the reduced Planck constant.
In Fig. 7.3 we thus plot the experimentally determined degree of circular polarization of the WZ free exciton as a function of the magnitude of an external magnetic field applied perpendicularly to the NW axis. In addition, the blue curve represents a fit of the Hanle function to our data. The excellent agreement of data and fit represents clear evidence for the successful optical injection of a spin ensemble into the single NW. However, without knowing the g-factor of WZ GaAs, the time-integrated Hanle measurements cannot be used for a quantitative determination of relaxation times of the spin-polarized electron ensemble in the NW.
With the experiments presented so far, we have outlined a way to identify single, free-standing wires, relocatable in our setup, which show highly polarized emission after circularly polarized laser excitation. In a perpendicular magnetic field, the emission is depolarized in a predictable manner, evidencing the Hanle effect.

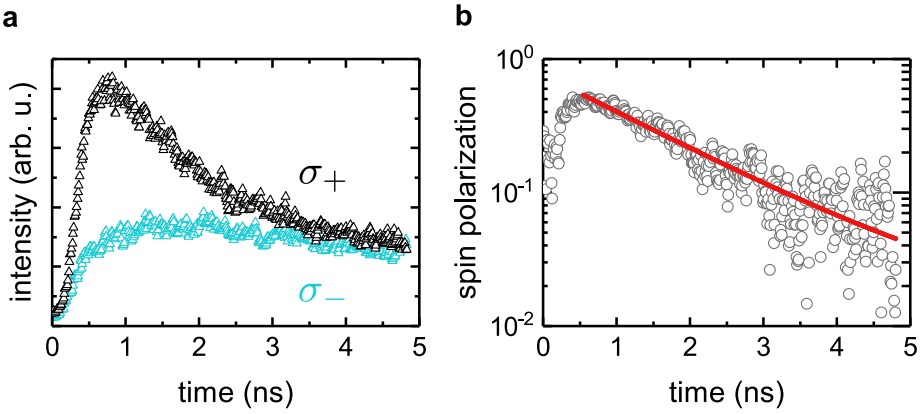

Figure 7.4: Time-resolved emission from a wire excited with short, circularly polarized pulses. (a) The emission is sorted into the two oppositely circularly polarized components labeled as σ_+ and σ_-. The observed intensity difference between the two polarization components, and in particular the dynamic decay of this difference, evidences the optical spin injection and further indicates the time scale for spin relaxation. (b) The temporal evolution of the injected spin polarization is obtained from the curves in (a). The right (σ_+) and left (σ_-) polarized components of the emission render the degree of spin polarization according to $P_s = (\sigma_+ - \sigma_-) / (\sigma_+ + \sigma_-)$. Fitting the spin decay to a single exponential results in a spin relaxation time of $\tau_s = 1.5$ ns for this wire.

7.3 Dynamic detection of spin relaxation

As was mentioned before, detecting the circularly polarized NW emission continuously over time cannot reveal any quantitative information about the dynamic properties of the spins in the system unless the dynamics of e-h pair recombination are precisely known. In NWs, however, as we will see in Part IV, these e-h pair dynamics can vary substantially as a function of the NW diameter, thus obscuring any information on the dynamics of the spins one might otherwise get already from the time-integrated detection of circularly polarized emission. Hence, we detect the luminescence resolving both the dynamics and the polarization of the NW emission after exciting the wires with the 70 ps pulses of the near-resonant laser diode . Figure 7.4a shows one pair of such counter-polarized emission decay curves obtained from a single wire. The labels σ_+ and σ_- again mark the detection of the respective right and left circularly polarized emission. After a rapid increase of the PL signal, the two counter-polarized curves display a significant difference, which decreases over time until at around 3 ns after the excitation, they merge and their difference vanishes in the signal noise. The dynamic change of the two curves, and in particular the time period before they merge, already marks the time scale of spin relaxation. To get to the actual spin signal, we calculate the degree of spin polarization $P_s = (\sigma_+ - \sigma_-) / (\sigma_+ + \sigma_-)$ and plot it on a semilogarithmic scale in Fig. 7.4b. Upon fitting the observed decay with a single exponential decay function, we obtain a spin

relaxation time of $\tau_s = 1.5\,\text{ns}$ for this wire. We discuss the fitting routine for spin signals in detail in Section 3.3. We interpret the observed spin decay as the relaxation of the electron spin polarization, which is evidenced by both, the finite g-factor demonstrated in Section 8.1, as well as our estimate of the short hole spin relaxation time given in Section 9.2.2 and Appendix A.3. Investigating various aspects of the observed electron spin relaxation in this experiment will be the subject of the next chapter. For now, we would like to note that the experiment shown in Fig. 7.4 represents the first optical measurement to monitor the decay of a spin polarization in a NW.

8

Peculiar spin dynamics in regular-sized nanowires

Constituting a prime motive behind the goal to synthesize a diameter-tunable NW system, we will now survey the progressive developments of an idea to suppress spin relaxation in narrow semiconductor channels and present the current state of literature on the topic.
In general, the transport of spins in III-V semiconductor nanostructures is considered an important platform for quantum information transfer [14, 123], although genuinely limited by the process of spin relaxation, which itself, is particularly often dominated by the Dyakonov-Perel (DP) mechanism in III-V materials [53]. Ever since it was speculated that this DP spin relaxation may be strongly suppressed in 1D semiconductor channels [13–16], utilizing the anticipated high spin coherence of mobile charge carriers reflects a long-standing goal in the community. Narrow semiconductor channels made of the technologically important III-V compounds represent a particularly promising platform in this regard. However, these speculations about ultralong spin coherence in 1D could as yet not be tested in experiments. Instead, dating back close to twenty years, Mal'shukov and Chao [14] realized en route that the DP relaxation of a spin polarization can be substantially reduced already in channel widths considerably wider than what is regarded as the 1D regime. Monte Carlo simulations by Kiselev and Kim [15] revealed a similar observation and the effect was eventually experimentally evidenced by Holleitner *et al.* in 2006 probing the spin relaxation in etched InGaAs wires with lateral sizes ranging from 0.4 to 20 µm [104]. While the predicted suppression was indeed observed, it was at the same time also limited by higher-order corrections to the SOC and the spin relaxation times thus effectively only increased from 10 to 30 ps. Accounting for the finite lateral size of the wires by including the appropriate boundary conditions in his analytic approach, these observations were further confirmed by S. Kettemann [143] deriving the suppression of spin relaxation from the weak localization correction to the conductivity of narrow semiconductor wires. Experimentally, much longer spin relaxation times of mobile charge carriers in thin wires were reported only recently for the emergent states of a persistent spin helix [144, 145]. Here, comparably long spin relaxation times of

several nanoseconds were observed for narrowly etched GaAs-based channels. In light of these reports, studying different aspects of the spin relaxation in our very thin NWs (as compared to the afore mentioned etched channels) might uncover an interesting potential of NWs for spin transport.

8.1 Effects of a transverse magnetic field

In other experiments on WZ semiconductors the magnetic field-dependence of spin relaxation could be used to identify the relaxation mechanism: Encoded in the SOC, the crystal structure of bulk GaN, for example, creates a characteristic anisotropy in the DP relaxation mechanism, which uncloaks in a transverse magnetic field [129–132].
Here, we present the results of an analogous approach in our experiment; the complex dynamics of spins under a magnetic field.
These measurements were performed by mounting the sample between the coils of an electromagnet, where magnetic fields up to ~400 mT could be applied in the sample plane perpendicular to the NW axes. We can therefore monitor the dynamics of spins in our wires as we externally apply a transverse magnetic field. Note that all of the results presented exemplarily for one wire in the following were qualitatively confirmed by measurements on several individual NWs from the same wafer.
Figure 8.1a depicts typical time-resolved spin polarization transients of a single, free-standing WZ GaAs wire with a regular-sized diameter of $d = 90$ nm for externally applied transverse magnetic fields B_{ext} from 0 up to 400 mT. According to a single exponential decay fit, the e-h pair emission from the wire decays with a recombination lifetime of $\tau_{pl} = 9.4$ ns (for more details see Part IV). While for $B_{\text{ext}} = 0$ the spin decay is characterized by a single exponential, two main features arise as soon as an external magnetic field is applied perpendicularly to the NW axis. First, we observe a characteristic oscillatory behavior with increasing frequency for increasing B_{ext}, and second, a significantly steeper slope of the envelope compared to the zero field transient.

The effective electron g-factor The oscillations in the spin polarization transients arise from spins precessing around the external magnetic field $\mathbf{B}_{\text{ext}}$ with a frequency corresponding to the Larmor frequency $\omega_{\text{L}} = g^* \mu_{\text{B}} B_{\text{ext}}/\hbar$. According to the optical selection rules, the precession around $\mathbf{B}_{\text{ext}}$ leads to a periodic change between σ_+ and σ_- polarized luminescence and consequently to the oscillations in the spin polarization transients. The corresponding values of ω_{L} are extracted from the fits (see next paragraph) and plotted in Fig. 8.1b as a function of the applied field B_{ext}. From a linear fit to the data we calculate the effective g-factor for the WZ GaAs NW to be $|g^*| = 0.28 \pm 0.02$. This value is different from its zincblende counterpart (i.e., $|g^*| = 0.44$ [146]). Importantly, this experiment finally proves the validity of our initial assumption, stating that optical orientation in our wires is sensitive to the spin relaxation processes of electrons instead of holes: The magnetic field-induced oscillations can be unambiguously attributed to conduction electrons, since the effective g-factor of heavy holes in the WZ crystal is zero

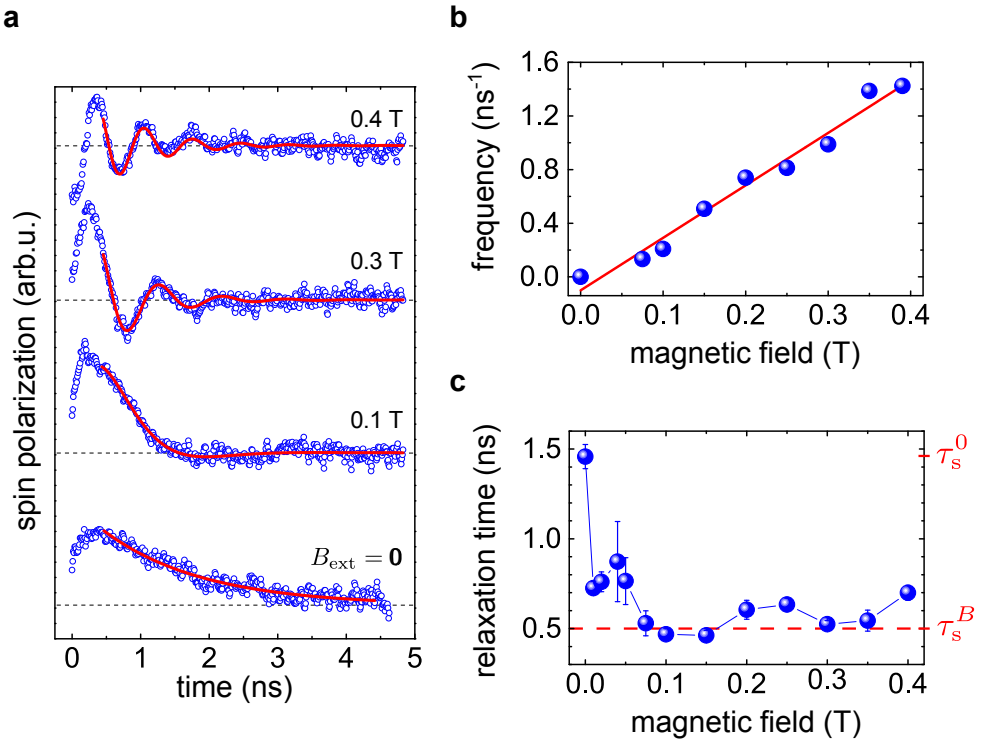

Figure 8.1: Magnetic field effects on the spin dynamics. (a) Typical time-resolved transients of the spin polarization for a single, free-standing WZ GaAs NW at 4.2 K for transverse magnetic fields from 0 to 400 mT. The transients are fitted to a single exponential for $B_{ext} = 0$ and to a damped cosine (continuous red lines) for $B_{ext} > 0$, respectively, accounting for Larmor precession in non-zero magnetic fields. (b) Extracted values of the Larmor precession frequency as a function of the externally applied transverse magnetic field. From a linear fit to the data (continuous red line) we determine the absolute value of the effective electron g-factor in WZ GaAs NWs to be $|g^*| = 0.28 \pm 0.02$. (c) Variation of the spin relaxation time τ_s as a function of the transverse magnetic field. The sudden decrease of τ_s in an external magnetic field reflects an intrinsic spin relaxation anisotropy, with spins pointing along the NW axis relaxing substantially slower than spins perpendicular to the NW axis. The dashed red line marks the drop from the zero-field value τ_s^0 to $\tau_s^B \approx \tau_s^0/3$ in a transverse field. Error bars correspond to the standard error for fitting the spin polarization transients.

in this configuration [112, 147].
We would further like to make a general note about measuring the g-factor in optical orientation experiments. The applicability of the method is limited, mostly by the finite magnetic fields that can be applied in our setup. Depending on the magnitude of this field, the observed number of oscillations determines the quality of the fit. At the same time, setting the time period over which a signal may be observed, the spin relaxation time as well as the carrier recombination time must lie in the appropriate range. In the wire we presented, these requirements were well-balanced ($\omega_L \tau_s \approx 1$) and the measurement was thus successful. For the larger diameter wires presented in the next sections, the luminescence carrier lifetimes were substantially shorter (see Chapter 10), so that less oscillations are visible, decreasing the quality of the fit and eventually the determination of a reliable diameter-dependence of the g-factor.

Unusual spin dynamics in WZ GaAs NWs The second observation we make in our experiment is a significantly faster decay of the spin polarization transients for $B_{\text{ext}} > 0$. Since the temporal decay of the spin polarization transients is directly linked to electron spin relaxation, the considerably slower decay of the zero field trace as compared to the envelope for $B_{\text{ext}} > 0$ reflects a distinct increase of spin relaxation in the presence of a transverse magnetic field. To quantify this effect, we determined the corresponding spin relaxation times τ_s^0 ($B_{\text{ext}} = 0$) and τ_s^B ($B_{\text{ext}} > 0$) by fitting the polarization transients to a single exponential decay $P_s = \exp(-t/\tau_s^0)$ for zero magnetic field and to a damped cosine

$$P_s(t) = \exp(-t/\tau_s^B)\cos(\omega_L t) \quad \text{for } B_{\text{ext}} > 0,$$

respectively. Figure 8.1c exemplarily presents the magnetic field-dependence of τ_s for a single, free-standing NW, from the same wafer as discussed in the previous chapter (cf. also Figs. 7.3 and 7.4), in transverse magnetic fields up to 400 mT. All measured NWs qualitatively show the same behavior: The initially long spin relaxation time $\tau_s^0 \approx 1.5$ ns drops to a substantially reduced value $\tau_s^B \approx 0.5$ ns in the presence of a transverse magnetic field. Clearly observable in Fig. 8.1c, this reduction of the spin relaxation time in an external field reflects an intrinsic spin relaxation anisotropy in WZ GaAs NWs: As discussed in Section 2.4.1, spins point along the NW axis (|| WZ $\hat{c}$-direction) after the excitation; a direction along which they experience a relatively weak relaxation. However, when an external field is applied, spins are forced to rotate in a plane perpendicular to this field, i.e., out of their initial orientation, where they experience a stronger spin relaxation, resulting in a shorter relaxation time.
In order to shed some light onto this unusual behavior of electron spins in a regular-sized wire, we approach the problem in the theory of the DP mechanism [64, 122], which dominates the spin dephasing of free, delocalized electrons in most III-V semiconductor bulk and nano-heterostructure samples [52, 55] and furthermore also in the above mentioned examples of WZ semiconductors [129–132]. In the next section we present a model for the unusual NW spin dynamics developed in the framework of DP spin relaxation, involving the contributions to SOC at the NW sidewall-facet-interfaces.

8.2 Towards a microscopic theory of spin relaxation

The unusual magnetic field dependence shown in Fig. 8.1c is counterintuitive when compared to previously reported experiments on spin dynamics in related bulk WZ GaN structures [129–132]. In these bulk GaN samples, using a similar measurement configuration, an increase, instead of the decrease showing in our experiments, is observed in the spin relaxation time when a transverse magnetic field is applied. In their experiments, accounting for SOC in the form of spin-orbit fields in the framework of the DP mechanism provided a comprehensive understanding of the measured dynamics. Connecting to this description, we start our analysis in the following by elucidating the effect of a transverse magnetic field on the DP mechanism in bulk WZ semiconductors.

8.2.1 Dyakonov-Perel spin relaxation in bulk wurtzite semiconductors

As addressed in Section 2.4.2 and further discussed in Refs. [51–53, 55, 122], the effect of SOC in the DP mechanism on the relaxation time τ_s for a given spin component can be described by

$$\frac{1}{\tau_\mathrm{s}} \sim \langle \mathbf{\Omega}_{\mathbf{k},\perp}^2 \rangle \, \tau_\mathrm{p}^* , \tag{8.1}$$

where $\langle \mathbf{\Omega}_{\mathbf{k},\perp}^2 \rangle$ is the mean square effective magnetic field in the plane perpendicular to the considered spin direction and τ_p^* is the momentum relaxation time for an individual electron. As can be seen from Eq. (8.1), the DP spin relaxation time sensitively depends on the explicit form of the effective, $\mathbf{k}$-dependent magnetic field $\mathbf{\Omega}_\mathbf{k}$. The inversion asymmetry of the bulk WZ crystal structure determines the form of the intrinsic effective magnetic field [56, 129, 130, 132, 148–154]

$$\mathbf{\Omega}_\mathbf{k}^\mathrm{bulk} = \begin{pmatrix} \Omega_{\mathbf{k},x}^\mathrm{bulk} \\ \Omega_{\mathbf{k},y}^\mathrm{bulk} \\ \Omega_{\mathbf{k},z}^\mathrm{bulk} \end{pmatrix} = \beta \begin{pmatrix} k_y \\ -k_x \\ 0 \end{pmatrix}, \tag{8.2}$$

where $z \parallel [0001]$ ($\hat{c}$-axis), $x \parallel [11\bar{2}0]$ and $y \parallel [1\bar{1}00]$ (cf. Fig. 7.1c). The coefficient β is an effective SOC parameter describing the total magnitude of the SO field in bulk WZ (see Appendix A.1). Figure 8.2 shows the orientation of $\mathbf{\Omega}_\mathbf{k}^\mathrm{bulk}$ as blue arrows. In the bulk case, the reported increase in the spin relaxation time when a transverse magnetic field is applied, can be qualitatively understood from the following picture: For $B_\mathrm{ext} = 0$, in Fig. 8.2a, the spin ensemble $\mathbf{S}$ is optically generated along k_z. Since the intrinsic magnetic field $\mathbf{\Omega}_\mathbf{k}^\mathrm{bulk}$–which induces the relaxation of $\mathbf{S}$– contains no k_z-component, the relaxation is maximized. However, if we apply an external magnetic field transversely to the initial z-orientation of the spin ensemble, e.g., $\mathbf{B}_\mathrm{ext} \parallel x$, Larmor precession induced by this external field leads to a rotation of the spin ensemble into the (k_y, k_z)-plane,

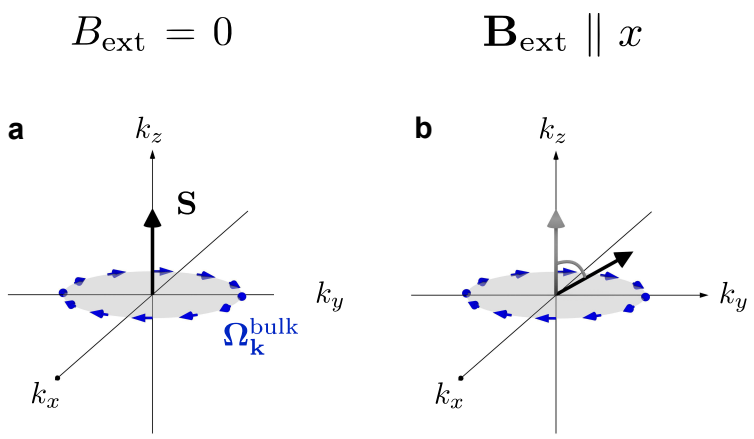

Figure 8.2: Schematic explanation of the spin relaxation anisotropy in bulk WZ crystals: (a) For $B_{\mathrm{ext}} = 0$ the optically generated spin ensemble $\mathbf{S}$ pointing along the $\hat{c}$-axis is susceptible to both the x- and y-component of the SOC field $\mathbf{\Omega}_{\mathbf{k}}^{\mathrm{bulk}}$, while (b) Larmor precession in an external magnetic field $\mathbf{B}_{\mathrm{ext}} \parallel x$ leads to a rotation of $\mathbf{S}$ towards k_y, which is then only subject to the x-component.

as sketched in Fig. 8.2b. Then, $\mathbf{S}$ contains only k_y- and k_z-components. Since $\Omega_{\mathbf{k},y}^{\mathrm{bulk}}$ cannot act on the k_y-component of the spin ensemble and, furthermore, $\Omega_{\mathbf{k},z}^{\mathrm{bulk}} = 0$, the DP mechanism will be less efficient than for the initial situation with $B_{\mathrm{ext}} = 0$. As a consequence, the spin relaxation time τ_{s}^{B} is expected to be longer than τ_{s}^{0}, which has been confirmed experimentally in bulk WZ GaN samples [129–132]. We emphasize that this bulk SOC leads to a magnetic field dependence of the spin relaxation time that is opposite to the results from the NWs and is therefore not capable of explaining the observed spin relaxation in our NWs.
Considering the particular form of a NW–cylinder-like with a large ratio of interface (or surface) area compared to the bulk volume–makes it clear that, even if quantum confinement effects are negligible, a bulk model of DP spin relaxation may not fully account for the NW core/shell heterostructure.
In the following, we thus present a qualitative picture of SOC in our NWs which considers the possible impact of the core/shell interfaces in the DP mechanism.

8.2.2 Qualitative picture of interface-induced spin-orbit coupling

A variety of effects may alter the SOC of electrons in the conduction band of a semiconductor: Space inversion asymmetry of the bulk crystal and external electric fields–whether induced by space charges from doping, or applied through electrostatic gates–are the most prominent reasons encountered in literature [52, 55, 60]. Yet, another contribution to SOC exists [55, 155–165]; it is however less well known, because it usually does not occur in the well-studied bulk or two-dimensional structures: Joining two periodic

crystals in epitaxy breaks the lattice symmetry associated with each crystal on its own at the interface. This entails a non-zero slope of the lattice potential at the interface between two periodic crystals, which gives rise to a strongly localized electric field across the interface and thus contributes to the SOC.
To illustrate the effect, we schematically show in Fig. 8.3 the microscopic details of an interface between two chemically distinct crystals made of materials labeled as A and B. The upper part of the image represents a zoom-in on the microscopic arrangement of the atoms in the vicinity of the epitaxial interface. Each lattice site in the depicted 1D chain hosts two atoms, thus resembling the actual structure of III-V crystals to some extent. Considered as a whole, the sketch represents a single heterointerface between the crystals GaAs and AlAs. The arrangement of the lattice atoms in the depicted 1D chain simplifies the much more complex 3D arrangement in semiconductor heterostructures, but the 1D picture still captures the essential electrostatic effects. We relegate to the fine gray line accompanying the chain of atoms in the background of the picture, which depicts a simplified, almost arbitrarily chosen Coulomb potential profile. The point of this potential is only that it varies for the different atomic specimens in our model. To address the effect of the interface on this potential, let us first consider each material on its own: With wave functions extending over many unit cells, the conduction electrons in a crystal mainly experience the lattice atoms as a material specific potential. However, when we join the two crystals, the total potential becomes a combination of the two different material specific potentials. This total potential Φ is represented by the red line in Fig. 8.3. At the interface, the two material specific potentials must align relative to the vacuum level, causing a non-zero slope of the total potential in the direct vicinity of the interface. This non-zero slope in turn makes the potential space-dependent, i.e., $\nabla_r \Phi \neq 0$, and thus leads to an electric field emerging at the interface, which enhances the SOC for the conduction electrons moving in the system. These interfacial contributions can be on the same scale as those associated with bulk and structure inversion asymmetry, as demonstrated by recent calculations of the SOC parameters of electrons at a single, atomically sharp GaAs/AlGaAs heterointerface [163, 164]. A core/shell NW, sharing six sidewall-facet-interfaces, intrinsically has a large ratio of interface area to bulk volume and any accurate description of the SOC in such a core/shell NW should thus include the interface-SOC effect.
In the following, we discuss the impact of the interface-SOC effect on the spin relaxation in our core/shell NWs, assuming the DP mechanism to dominate the spin relaxation, as was reported to be the case in other III-V WZ semiconductor samples [129–132].

8.2.3 Model of spin relaxation in core/shell nanowires

In addition to the intrinsic SO field $\mathbf{\Omega}_{\mathbf{k}}^{\text{bulk}}$, we now include the contribution to the SOC resulting from the GaAs/AlGaAs core/shell interface. Providing six of these interfaces at each facet and a very high ratio of interface area to volume, the interface-induced effects are expected to be particularly large in our hexagonal core/shell wires. In order to affect the DP spin relaxation process in our NWs, this interface-related SOC effect imposes a

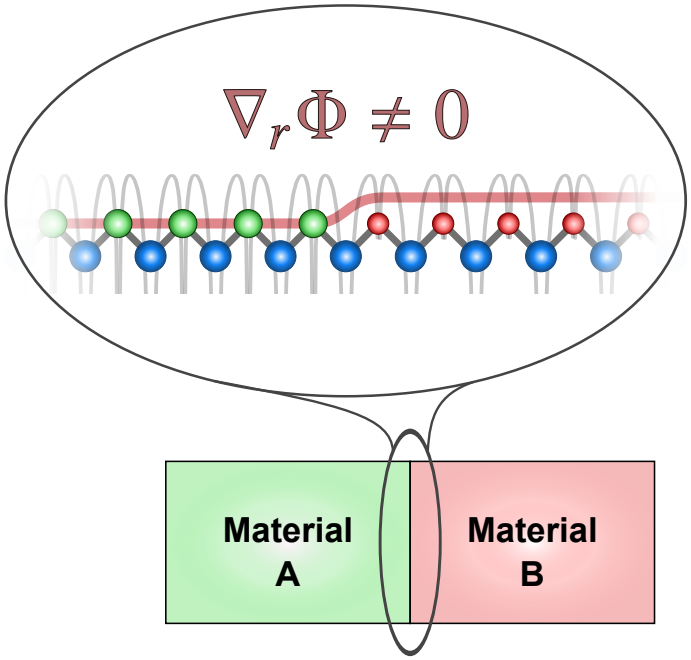

Figure 8.3: Lower panel: Schematic of an epitaxial interface between materials A and B, each a periodic crystal with two atoms in the basis. Upper panel: Zoom-in on the microscopic details at the interface. The particular arrangement of the atoms in the sketch resembles an interface between two III-V semiconductors, e.g., GaAs and AlAs. Blue, green and red spheres may be regarded as As, Ga and Al atoms. The light grey line in the background depicts a simple Coulomb potential varying for the different atomic specimen in the chain of atoms. A conduction electron–its wave function typically spread across many unit cells–mainly experiences the atomic potential as a space-invariant, material specific potential [166]. However, at the epitaxial interface between two chemically distinct semiconductors, the material specific potentials align, leading to a non-zero potential gradient $\nabla_r \Phi$ across the interface. Creating an electric field at the interface, this non-zero slope contributes to the SOC of a conduction electron moving in the system.

requirement on the electron wave function: its transport phase coherence length must be shorter than the NW diameter; then the electrons experience each interface individually, preventing the mirror-symmetric contributions from two opposing interfaces to cancel each other.

The appropriate form of the interface-induced effective magnetic field, $\mathbf{\Omega}_{\mathbf{k}}^{\text{int}}$, depends on the crystallographic orientation at the GaAs/AlGaAs core/shell heterointerfaces. Our WZ GaAs NWs exhibit a typical hexagonal cross section with six equivalent $\{11\bar{2}0\}$ sidewall facets (as discussed in the previous section; cf. Fig. 7.1c). From a symmetry analysis at the respective core/shell interfaces of these facets, we derive that $\mathbf{\Omega}_{\mathbf{k}}^{\text{int}}$ will always lie in the plane of the core/shell interface and is perpendicular to $\mathbf{k}$. In addition, the SOC arising from one interface is of the k-linear Rashba-type. We find this relationship to be equivalent for all six NW sidewall facets. We thus exemplarily discuss the impact of $\mathbf{\Omega}_{\mathbf{k}}^{\text{int}}$ at facet $(11\bar{2}0)$ oriented along the x-direction. A complete evaluation for all facets is given in the Appendix A.2. At this $(11\bar{2}0)$ facet, we obtain $\mathbf{\Omega}_{\mathbf{k}}^{\text{int}} = (0, -\alpha_{\perp} k_z, \alpha_{\parallel} k_y)$. Taking this additional contribution into account, we modify the total effective magnetic field induced by SOC to the expression

$$\mathbf{\Omega}_{\mathbf{k}} = \mathbf{\Omega}_{\mathbf{k}}^{\text{bulk}} + \mathbf{\Omega}_{\mathbf{k}}^{\text{int}} = \beta \begin{pmatrix} k_y \\ -k_x \\ 0 \end{pmatrix} + \begin{pmatrix} 0 \\ -\alpha_{\perp} k_z \\ \alpha_{\parallel} k_y \end{pmatrix}, \tag{8.3}$$

where the coefficients $\alpha_{\parallel}$ and $\alpha_{\perp}$ are effective SOC parameters determining the strength of the interfacial contribution parallel and perpendicular to the WZ $\hat{c}$-axis, respectively. Remarkably, due to the low symmetry $\{11\bar{2}0\}$ NW sidewall facets of the C_s point group, $\alpha_{\parallel}$ and $\alpha_{\perp}$ are linearly independent [167, 168], while the magnitude of the bulk contribution is given by the single parameter β.

The additive action of both SOC-induced fields, $\mathbf{\Omega}_{\mathbf{k}}^{\text{bulk}}$ and $\mathbf{\Omega}_{\mathbf{k}}^{\text{int}}$, is illustrated in Fig. 8.4a and b. An important observation is that the bulk effective field (blue arrows as in Fig. 8.2a, b) lies in the (k_x, k_y)-plane, while the effective field resulting from the heterointerface (red arrows) lies in the (k_y, k_z)-plane, for our example of the facet $(11\bar{2}0)$. Thus, compared to the pure bulk situation sketched in Fig. 8.2, in the NWs the core/shell interface obviously introduces a non-zero k_z-component to the total effective magnetic field. This particular component may now alter the relaxation time of the spin ensemble $\mathbf{S}$. In addition, when $\alpha_{\parallel}$ and $\alpha_{\perp}$ are different, the magnitude of the effective magnetic field components due to interface inversion asymmetry differs for k_y and k_z. This is illustrated through different vector norms of the $\mathbf{\Omega}_{\mathbf{k}}^{\text{int}}$ components in Fig. 8.4a and b, in contrast to the constant vector norms of the contributions from $\mathbf{\Omega}_{\mathbf{k}}^{\text{bulk}}$.

We can now revisit the experimental situation when probing the NW spin dynamics: Let us first consider the case $\alpha_{\parallel} > \alpha_{\perp}$ and $\alpha_{\parallel} > \beta$. As a consequence, the magnitude of the interface-induced effective magnetic field is stronger in k_z- than in k_y-direction. It is also larger than the magnitude of the effective magnetic field due to SOC in bulk. This situation is sketched in Fig. 8.4a and b. For $B_{\text{ext}} = 0$, the spin ensemble $\mathbf{S}$ is optically generated along k_z. Thus, the largest component of $\mathbf{\Omega}_{\mathbf{k}}$ is parallel to $\mathbf{S}$, as shown in

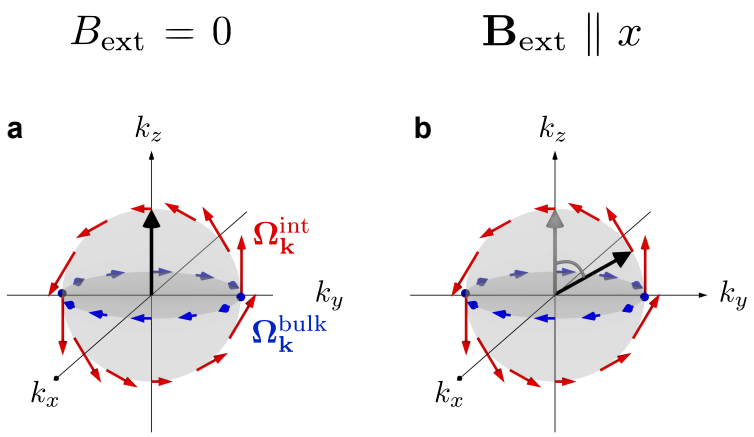

Figure 8.4: Schematic model for the observed spin relaxation in WZ GaAs/AlGaAs core/shell NWs, involving interface-induced SOC at the $(11\bar{2}0)$ sidewall facet: (a) For $B_{\mathrm{ext}} = 0$ the optically generated spin ensemble $\mathbf{S}$ pointing along the $\hat{c}$-axis is not susceptible to the largest component $\Omega_{\mathbf{k},z}^{\mathrm{int}}$ of the SOC fields, while (d) as soon as an external magnetic field $\mathbf{B}_{\mathrm{ext}} \parallel x$ induces spin precession, this large z-component of $\mathbf{\Omega}_{\mathbf{k}}^{\mathrm{int}}$ starts to act on $\mathbf{S}$ and will quickly dominate the relaxation.

Fig. 8.4a, and cannot contribute to the spin relaxation. However, as soon as an external magnetic field induces a precession of the spin ensemble, this large component of $\mathbf{\Omega}_{\mathbf{k}}$ starts to act on $\mathbf{S}$, as illustrated in Fig. 8.4b, and will quickly dominate the relaxation. As a consequence, the spin relaxation time τ_{s}^{B} will then be shorter than τ_{s}^{0}. This precisely describes our experimental findings discussed in Fig. 8.1c. If on the other hand, we then consider all the other possible relations of $\alpha_{\parallel}, \alpha_{\perp}$ and β, they impose $\tau_{\mathrm{s}}^{B} > \tau_{\mathrm{s}}^{0}$. This relation is observed in the bulk WZ material [129–132] and is opposite to the results of our study.

Including the interface-SOC in our core/shell NWs into the framework of DP spin relaxation provides a plausible explanation for the peculiar anisotropy of spin relaxation observed in our experiments.

Furthermore, taking the complete evaluation for all NW sidewall facets into account, our model in fact implies that the interface-induced z-contribution to the effective SO field $\mathbf{\Omega}_{\mathbf{k}}$ is significantly larger than the x-y-contributions from both bulk ($\alpha_{\parallel} > \beta$) and the interfaces ($\alpha_{\parallel} > \alpha_{\perp}$) (see Appendix A.2). We find

$$\frac{\alpha_{\parallel}^{2}}{2\beta^{2} + \alpha_{\perp}^{2}} \approx 4\,. \tag{8.4}$$

In their recently reported $\mathbf{k} \cdot \mathbf{p}$ calculations, Wójcik *et al.* come to a similar conclusion; in core/shell NWs, the contribution from the interfaces to the SOC exceeds the contributions from the bulk [169]. In this matter, we would also like to point out a recent article

suggesting the occurrence of Majorana zero modes in a core/shell NW due to the SOC induced by a radial electric field between a semiconductor core and a superconducting shell [170].

8.2.4 The model under scrutiny: Implications of the emerging spin-orbit fields

By accounting for the interface-SOC in the framework of the DP theory, we obtain a coherent description of the peculiar spin dynamics observed in our NW experiments. Considering the recent reports on this topic [169, 170], the interface-induced SOC seems to represent an important effect in semiconductor NWs.
Although our model coherently describes the experimentally observed spin dynamics in our wires, we must acknowledge that it is based on the assumption of a short transport phase coherence length. Experimentally, this assumption is neither easily verified, nor is it swiftly refuted; however, on the grounds of the large interface area-to-volume ratio and the higher scattering probability of carriers generally associated in the presence of interfaces, the assumption of short coherence lengths seems to be a priori reasonable. Since a direct measurement of the transport phase coherence length itself is not accessible, we instead present the results of two additional, independent experiments; inherently indirect in their design, they might still prove insightful on the validity of our spin relaxation model.

Chemically engineering the interface-SOC The first experiment is based on the chemical engineering of the NW core/shell interface. Tuning the Al content x of the shell, and thus the relative difference between the material specific potentials in the GaAs core and in the $Al_xGa_{1-x}As$ shell, directly scales the strength of the interface SOC. Hence, a measurable change in all interface-related effects on the spin dynamics in our wires is expected. For that purpose, we have fabricated a series of five wafers containing core NWs with identical diameters of $d = 110\,\text{nm}$. Overall the NWs of this sample series differ only in the concentration of Al atoms incorporated into the $Al_xGa_{1-x}As$ shell. By changing the Al portion in the shell, we tune the electric field at the interface arising from the non-zero slope in the potential caused by the relative alignment of the two material specific potentials.
We will qualitatively discuss the effect of the Al content in the shell with the help of the atomic chain sketched in Fig. 8.3. Starting from $x = 100\%$, i.e., a shell made entirely of AlAs, decreasing the Al content in our wafer series corresponds to a progressive replacement of the red spheres in the atomic chain by green spheres. In this case, the material specific potentials on the left and right side of the interface will adjust more and more towards a uniform potential and the non-zero slope will vanish. In our spin relaxation experiment, we thus expect a decreasing contribution of the interface-SOC on the spin dynamics as we reduce the Al content in the shell. As a consequence of Eqs. (8.1) and (8.3), the spin relaxation time is thus expected to increase upon reducing the Al content, since both SOC parameters $\alpha_{\parallel}$ and $\alpha_{\perp}$ are decreasing. In particular, the

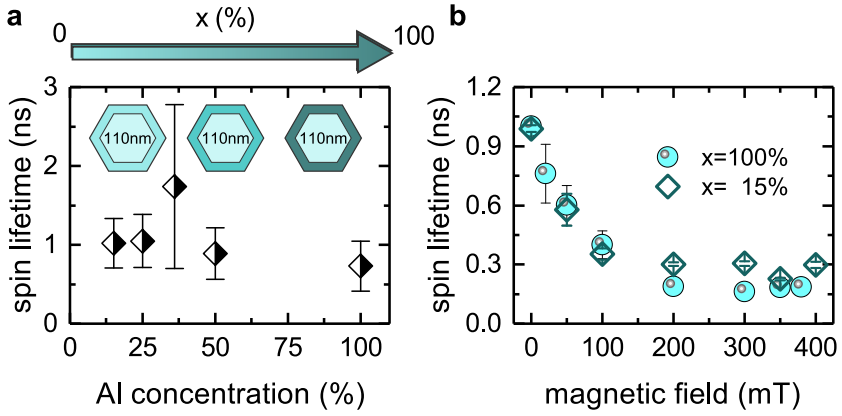

Figure 8.5: Effects of chemically engineering the GaAs/$Al_xGa_{1-x}As$ interface on the spin dynamics. (a) The zero field spin lifetime, averaged over several wires, for different Al concentrations in the range from $x = 15 - 100\%$. The error bars denote the statistical standard deviation. Within the accuracy of our experiment, the zero field lifetimes shows no dependence on the Al concentration. (b) Magnetic field-induced anisotropy of spin relaxation in a wire with $x = 100\%$ (blue spheres) and $x = 15\%$ (green squares) Al concentration in the shell. In contradiction to the expectations from our model, no clear trends can be identified in the anisotropy.

zero field spin relaxation time in Eq. (8.1) should increase as the interface contribution to Eq. (8.3) vanishes.

We have measured this zero field spin relaxation time in the absence of an external magnetic field in a number of NWs from each of the five different wafers varying only in the fraction of Al atoms incorporated into the shell. In Fig. 8.5a we plot the average spin relaxation time (tilted squares) together with the statistical standard deviation (error bars) as a function of the Al concentration x in the $Al_xGa_{1-x}As$ shell surrounding the otherwise nominally identical NW cores. Although numerous single NWs (5 to 10) from each of the wafers with Al concentrations ranging from 15 % to 100 % were investigated, Fig. 8.5a does not identify any sort of dependence of the spin lifetimes on the Al content with statistical significance. The average values merely scatter around a mean spin relaxation time of 1 ns.

Modifying the SOC in the NW by chemically engineering the core/shell interface should have another measurable effect on the observed spin relaxation. In particular, on its anisotropy. The magnetic field-induced anisotropy of spin relaxation observed for our representative NW with 36% Al content (the one discussed previously in Section 8.1; see also Fig. 8.1) implied the ratio $\tau_s^B = \tau_s^0/3$. Relative to this ratio, Eq. (8.3) of our model predicts an increase for any Al content larger than 36%. We thus investigated the magnetic field dependence of spin relaxation in a NW with 100% Al content completely analogous to the experiment presented in Fig. 8.1.

The light blue spheres plotted in Fig. 8.5b demonstrate the effect of a magnetic field

on the spin dynamics for the example of a single NW with $d = 110\,\text{nm}$ and $x = 100\%$. Qualitatively confirmed by measurements of several NWs from the wafers, Fig. 8.5b represents a general observation: At zero magnetic field we measure a spin relaxation time of $\tau_s \sim 1.0\,\text{ns}$, and like in the previous experiments, applying an external magnetic field perpendicularly to the wire axis induces a decrease in the spin relaxation time. In this example, the spin relaxation time is $\tau_s^B = 0.2\,\text{ns}$ for fields larger than 200 mT. Although in absolute numbers this corresponds to a small increase in the anisotropy, i.e., $\tau_s^B = \tau_s^0/5$ in the wire with $x = 100\%$, we note that the analogous experiment performed for a NW with $x = 15\%$ Al content in the shell (see green squares in Fig. 8.5b) does not show the corresponding decrease in the anisotropy expected in turn for an Al content smaller than 36%. Instead, in the $x = 15\%$ wire we measure again $\tau_s^B = \tau_s^0/3$. A number of control experiments performed on other wires with different Al concentrations in the shell shows no signs for a trend that would support the predictions drawn from our model; a conclusion thus in line with the independence of the zero field spin lifetimes on the Al content of the shell demonstrated in Fig. 8.5a.

Diameter-dependence of the anisotropic spin dynamics We examine the puzzling dynamics of the spins in our NWs in a second, independent experiment. Recall the unusual behavior of the spins in our NWs under the incluence of a perpendicular magnetic field: As the field increases, the spins quickly loose their orientation and the associated relaxation time drops. This behavior is entirely opposite to the reports about spin relaxation in other WZ semiconductors such as bulk GaN [129–132]. Since the unusual anisotropy of spin relaxation in our model is attributed to the effect of interface-induced SOC, we require wires with less interface area compared to the bulk volume. In fact, if the diameters of our wires were to approach the limit of bulk WZ GaAs, the anisotropy of spin relaxation should reverse completely. Then, under the influence of a perpendicularly applied magnetic field, spins should maintain their collective orientation for longer time periods, resulting in the increase of the relaxation times reported for bulk GaN [129–132]. In this second approach, we greatly benefit from the advances made in the NW growth (see two-step growth in Section 5.2) which allow us to fabricate NWs with very large diameters.

We have conducted a series of magnetic field dependent measurements on such wires with diameters in the range from $d = 90$ to 490 nm and exemplary show the results from three wires with diameters $d = 110$, 240 and 490 nm in Fig. 8.6a-c. The red dashed lines in each graph indicate the anisotropy $\tau_s^B = \tau_s^0/3$ detected in the previous experiments (cf. Figs. 8.1 and 8.5). The set of measurements presented in Fig. 8.6 confirms what our previously discussed wafer series with different Al concentrations already suggests: The predictions from our model do not show in the experiment. For each of the three different diameters, the magnetic field induced decrease of the spin relaxation time corresponds to the previously observed ratio of $\tau_s^B = \tau_s^0/3$. A reversal of the effect, as expected in the bulk limit of our wires, does certainly not occur.

In summary, chemically engineering the core/shell interface to increase the SOC in our

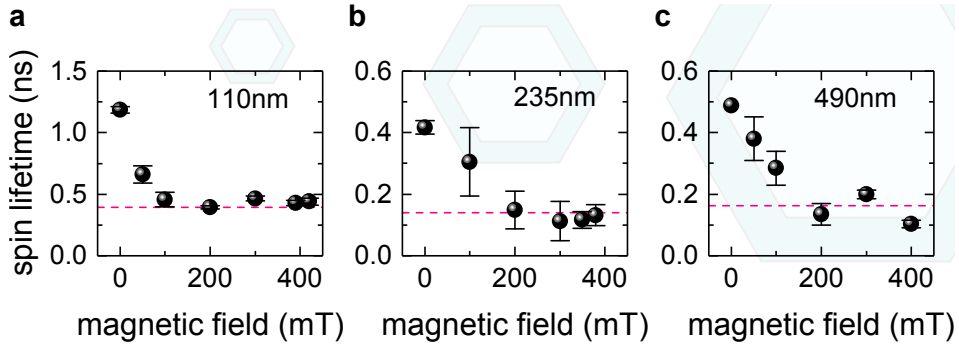

Figure 8.6: Diameter-dependence of the peculiar spin dynamics in our wires. Analogous to the experiment presented in Section 8.1, a magnetic field applied perpendicularly to the NW axis induces a decrease in the spin relaxation time. As a result of this effect, spin relaxation is anisotropic. This anisotropy is quantified by the ratio between the zero field spin lifetime, τ_s^0, and the average lifetime τ_s^B observed for fields larger than 200 mT. The red line indicates the previously observed magnitude of this ratio equal to ≈ 3. The experiment in (a)-(c), conducted on wires with the different diameters 110, 240 and 490 nm, show no indication for a change in this ratio, contradicting the predictions from the model of SOC in core/shell NWs. Demonstrating the large range of wire diameters covered in our experiments, sketches of the hexagonal wire cross sections are drawn to scale and superimposed in the background of each graph. For non-zero fields, all traces are fitted with the effective g-factor $|g^*| = 0.28$ determined in the last section.

wires does not show as a decrease in the zero field spin lifetime, as expected for a higher Al content in the shell. At the same time, the magnetic field does not reveal any of the trends expected from our model either, neither those anticipated for a NW shell containing a high Al content, nor the ones in very large diameter NWs, which should at least to some extent reflect the expectations for a bulk WZ sample.

8.3 Conclusion

In this section, subjecting our NWs to a perpendicular magnetic field has two interesting implications: First, the precession of spins in a transverse field allows us to determine a benchmark for a previously unknown parameter in the WZ phase of GaAs: $|g^*| = 0.28 \pm 0.02$. Importantly, this non-zero effective g-factor confirms the measurement of the electron (instead of hole) spin relaxation in our optical experiment. Second, to explain the strong magnetic field-induced anisotropy observed in our spin relaxation experiments, we develop a model of spin relaxation in core/shell NWs, which, by accounting for an interface-induced SOC effect in the framework of the DP mechanism, coherently explains the observed anisotropy.
Acknowledging that our model is based on the assumption that electrons are incoherently scattered across our NWs (a setting difficult to assess experimentally), we conduct two additional, independent experiments to survey the implications of our model. However, in both independent experiments the anticipated results did not show. This raises the question whether our model based on the DP mechanism fully accounts for the peculiar spin relaxation in our NWs, or if entirely different processes are responsible for the observed relaxation. Getting to the bottom of this problem lies in the focus of the next chapter.

9 Pushing into the 1D quantum regime

By introducing the technique of optically injecting spins into single wires and the experiments showing a variety of their specific, spin-related properties in our NWs, the last two chapters laid out the groundwork to extend our studies to 1D wires. While our experiments provide interesting insights into the dynamics of spins in NWs, they leave a fundamentally important questions unanswered: Which microscopic mechanism drives the spin relaxation observed in our experiments? Attempting to answer this question and, at the same time, motivated by the promise of outstanding spin coherence in 1D wires outlined in the introductory part of Chapter 8, we now focus our efforts to trace the diameter-dependent spin relaxation in our NWs into the 1D quantum regime.

Most of the content presented in this Chapter is the outcome of a close collaboration with Dr. Michael Kammermeier, Dr. Paulo E. Faria Junior, Dr. Tiago Campos, Prof. Dr. Jaroslav Fabian, Prof. Dr. John Schliemann, Prof. Dr. Christian Schüller, Prof. Dr. Tobias Korn and Dr. Paul Wenk and part of an article [108].
Additionally, the results presented in Section 9.2.1 concerning the DP mechanism in WZ wires stem from a collaboration with Prof. Dr. John Schliemann, Dr. Paul Wenk and Dr. Michael Kammermeier and were recently published in the *Physical Review B* [171].

9.1 Diameter-dependent spin relaxation: From 3D to 1D

In the last chapter, probing the dynamics of spin relaxation in a transverse magnetic field has revealed an anisotropy of spin relaxation in our WZ GaAs NWs; unusual compared to the spin dynamics observed in similar experiments on bulk WZ semiconductors, which are fully captured in the framework of DP theory. Despite pairing extensive experimental efforts with a detailed theoretical investigation, we could not obtain a coherent explanation

for the peculiar spin dynamics in the framework of the DP mechanism. Hence, the actual microscopic process behind the spin relaxation in our NWs is still unaccounted for. In this regard, our advances in fabricating WZ GaAs NWs in a wide range of diameters are expected to be highly beneficial: being able to tune the wire diameter from $d = 490$ down to 20 nm allows us to systematically study the spin relaxation as a function of the wire size. The anticipated diameter-dependence of the spin lifetimes could then help to identify the mechanism responsible for the spin relaxation.

We have measured several NWs from each of the eight individual wafers of our diameter series introduced in Section 5.4. In Fig. 9.1a and b, we present two exemplary sets of σ_+ and σ_- counter-polarized decay traces, as obtained directly from the streak camera images. The curves display the temporal evolution of the polarized emission in a spectrally integrated narrow (5 meV) window centered at the peak of the PL emission. Figure 9.1a shows the temporal decay of the circularly polarized emission of a NW with a diameter of $d = 110$ nm on the scale of a few ns. Connecting to the definition in Section 6.1.2, we refer to NWs with $d \geq 110$ nm as 3D wires in the following. As in our previous experiments, we observe a large splitting between the σ_+ and σ_- component, which decreases as a function of time until the two curves merge at ~2.5 ns. This time scale provides a rough measure of the spin relaxation time. From our data analysis (see Section 3.3) we determine a spin relaxation time of 1.0 ns and a luminescence lifetime of 1.7 ns.

Opposed to this 3D case, we find the time scale on which spin relaxation occurs to be very different for the thin NWs. This is demonstrated for a 1D NW ($d = 25$ nm), as shown in Fig. 9.1b. In this case, the splitting between the σ_+ and σ_- curves decays over hundreds of ns with a luminescence luminescence lifetime of 87 ns (see Chapter 10). At $t > 250$ ns, the two curves do not yet appear to be in equilibrium, but their difference vanishes below the noise level. For the 1D NW shown in Fig. 9.1b, we determine a spin relaxation time of $\tau_s = 98$ ns. This strong increase of the spin relaxation time from 1 ns in a wide 3D to 98 ns in a narrow 1D NW already suggests the occurrence of a strong suppression of the dominant spin relaxation mechanism. Here, we emphasize the importance of our fitting routine developed for these experiments, as demonstrated by our exemplary fits in Section 3.3.

To map the evolution of spin relaxation in the transition from 3D to 1D, we have measured and determined the spin relaxation time for the full diameter range from 490 to 20 nm. The statistically averaged spin relaxation times of several (3 to 8) single NWs from each of the eight different wafers are summarized and displayed in Fig. 9.1c.

For the largest NWs of our study ($d = 490$ nm) we find relaxation times of $\tau_s = 0.4$ ns. By reducing the NW diameter in the experiment, we progressively confine the free carrier motion to a movement along the NW axis–a process that gradually induces a fundamental transition in the dimensionality of the electronic band structure. In the range from $d = 235$ to 90 nm we only find a weak increase of the spin relaxation time as the diameter decreases. Interestingly, entering the regime where the transition from 3D to 1D manifests clearly in the NW emission energy (see Fig. 6.1), correlates with a 35-fold increase of the spin relaxation time between NW diameters 90 to 40 nm. When we further reduce the diameter beyond the 1D limit ($d < 35$ nm), this increase becomes very steep,

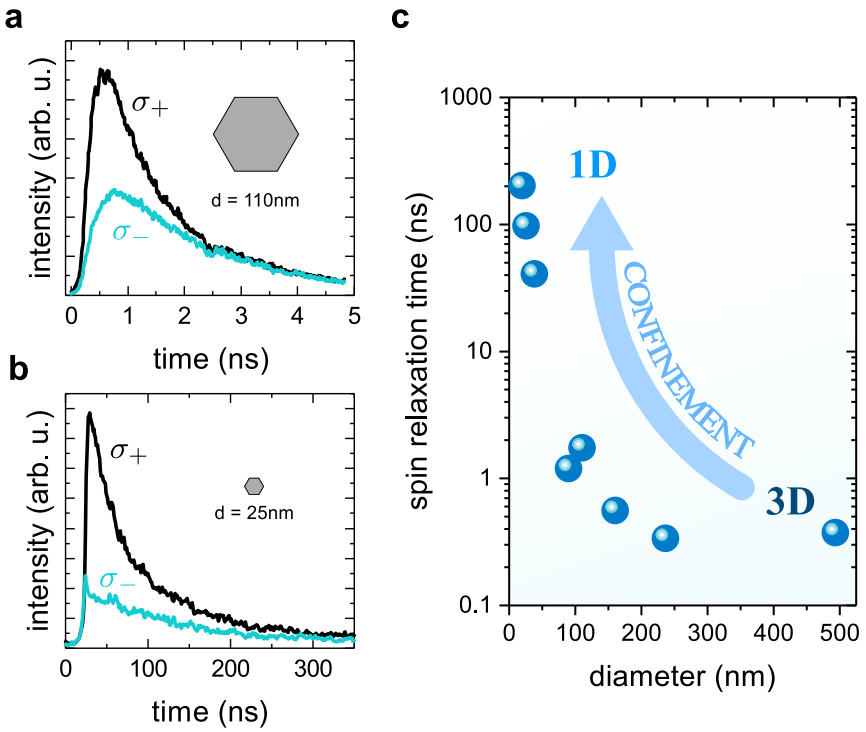

Figure 9.1: Time-resolved decay traces of the σ_+ (black curve) and σ_- (blue curve) circularly polarized emission from two single NWs with the respective diameters (a) $d = 110$ nm and (b) $d = 25$ nm. Note the different time scales in both measurements. The relative size of the two NWs is indicated by the inset. In (a), the difference between the two oppositely polarized traces decays within 2.5 ns after excitation. In (b), even 250 ns after exitation, the two traces do not yet overlap. This already suggests a much longer time scale for spin relaxation in a very thin NW. (c) The spin relaxation time as a function of the NW diameter is displayed on a semilogarithmic scale. Blue symbols represent the statistical average of measurements from several (3 to 8) single NWs. Spin relaxation times increase by more than two orders of magnitude as the NW diameter decreases from $d = 490$ to 20 nm.

culminating in the observation of the spin relaxation time $\tau_s = 202$ ns in the thinnest NWs investigated in our study: An increase by a factor of 500 compared to the 3D NWs.

9.2 A theoretical analysis of spin relaxation in nanowires

Noting the lifetimes in our 1D wires–increasing steeply as the diameter decreases–are still finite, is intriguing, since the most common reason for spin relaxation in III-V semiconductors, the DP mechanism [52, 55, 122], does not contribute to the experimentally observed spin relaxation. Indeed, due to the symmetry of the WZ crystal, the spin splitting in the conduction band is intrinsically zero for electrons moving along the NW || [0001]-axis [57, 58, 172]. By now spatially confining the carriers solely to a motion along this direction for small NW diameters, we completely eliminate the DP spin relaxation in the transition to the 1D NW regime. This means that even if the DP mechanism plays a role for the spin relaxation in our 3D wires, its action must disappear entirely as the wire diameter approaches the 1D limit. Regarding the diameter-dependence of spin relaxation in the DP mechanism, the discussion at the beginning of this part on the suppression of DP spin relaxation in narrow semiconductor channels is highly relevant, since it has already demonstrated that an accurate description of the DP mechanism in finite-sized channels should include a boundary condition for the spin current.

9.2.1 Evaluating different mechanisms

In order to identify the microscopic process responsible for the spin relaxation in our NWs and, in particular the one causing the observed diameter-dependence, we will now evaluate the most prominent mechanisms of spin relaxation.

The Dyakonov-Perel spin relaxation in 3D wires To obtain a coherent understanding of the spin dynamics in our wires, we modified the SOC which enters the DP theory, to account for the particular geometry of our core/shell NWs. Describing the spin relaxation in NWs in an entirely different approach, Wenk and Kettemann showed that the finite lateral size of a narrow wire may be accounted for by an appropriate boundary condition for the spin current. They show that the finite size can have a strong effect on the spin relaxation in narrow semiconductor wires.
In a collaboration with Prof. Dr. John Schliemann, Dr. Paul Wenk and Dr. Michael Kammermeier, we have theoretically investigated this finite-size effect on the DP spin relaxation, particularly focusing on NWs with a WZ crystal symmetry. The results of this collaboration were recently published in the *Physical Review B* [171].
In this analysis, we have investigated the role of the DP mechanism in the 3D diffusive regime of WZ NWs. Regarding our optical experiments, one result of the theoretical work is particularly important: for wire diameters $d \geq L_{so}/2$, where L_{so} denotes the

spin precession length, the DP spin relaxation time τ_s^{DP} becomes comparable to the corresponding bulk value [171]:

$$\tau_s^{\mathrm{DP,bulk}} = L_{so}^2/(8\pi^2 D_e)\,. \tag{9.1}$$

Here, $D_e = \hbar k_F l_e/(3m_e)$ denotes the 3D diffusion constant, $k_F = (3\pi^2 n_{3\mathrm{D}})^{1/3}$ the Fermi wave vector and l_e the mean free path. To estimate the corresponding relaxation time τ_s^{DP} numerically, we use the optically excited carrier density (cf. Section 3.2) in the 3D wires, $n_{3\mathrm{D}} = 8\times10^{16}\mathrm{cm}^{-3}$, and $L_{so} \approx \pi\hbar^2/(m_e\gamma_R)$, where $\gamma_R = 0.04\,\mathrm{eV\AA}$ is the linear spin-orbit coupling coefficient [58] and $m_e = (2m_{\parallel,e} + m_{\perp,e})/3$. This estimate tells us that at a NW diameter $d \approx L_{so}/2 = 460\,\mathrm{nm}$ the spin relaxation time should accordingly be $\tau_s^{\mathrm{DP}} \approx 100\,\mathrm{ps}/(l_e/\mathrm{nm})$. Since the mean free path l_e is typically extracted from magneto-transport measurements, it cannot be directly accessed in our optical experiments. Yet, even if we assume l_e in a large range of values from 10–1000 nm, we find that the respective spin relaxation times $\tau_s^{\mathrm{DP}} \approx 10$–$0.1$ ps are far too small to match our experimentally observed values (see Fig. 9.1c: $\tau_s \approx 0.4\,\mathrm{ns}$ at $d = 490\,\mathrm{nm}$). The inconsistency between our experiment and the theoretical prediction strongly suggests that, even in our NWs with the largest diameters, all prerequisites of the diffusive DP model are not fulfilled. A plausible reason may be that the electrons in our wires are already in the radially ballistic regime, which would be in line with elastic mean free paths of electrons observed in other high-quality III-V NWs [12, 173, 174] and the fact that our NWs are undoped and of high crystalline phase purity. With this numerical assessment, we finally conclude that the DP mechanism does not play a role in the spin relaxation process in any of our NWs. We will thus address other candidates for spin relaxation in the following to evaluate the results of our experiment.

The Elliott-Yafet mechanism in narrow wires Another prominent reason for spin relaxation is the Elliott-Yafet (EY) mechanism [61, 62], based on the admixture of spin eigenstates in the presence of SOC. In literature we find no explicit theory of the EY mechanism for NWs, except a semiclassical description of the EY process in the transition from 3D to 1D predicting a dramatic decrease in the spin relaxation time as the diameter of a NW decreases [175]. This prediction is in striking contradiction to our experiment where we instead observe a clear increase in the spin relaxation time as the NW diameter crosses the 1D limit. Furthermore, a contribution of EY-related mechanisms involving scattering between 1D subbands is excluded in the 1D limit of our NWs, because here only a single subband is occupied at low temperatures, preventing scattering between successive subbands. While a fully quantum-mechanical description may deliver new hints, a dominant contribution of EY to the electron spin relaxation in our experiment thus seems unlikely.

The hyperfine interaction in 1D Particularly in regard of the exceptionally long, but finite spin relaxation times observed in our 1D wires, we briefly address the effects of hyperfine (HF) interaction on the spin relaxation. In the few other solid-state systems

which have been experimentally demonstrated to show comparably long electron spin relaxation times ($\tau_s \geq 100\,\text{ns}$), electrons are bound to quantum dots, or impurities, i.e., 0D localized carriers [176–179]. In these examples, the HF interaction between carrier spins and fluctuating nuclear spins was found to limit the spin relaxation time. Unlike localized states, however, the wave function of carriers in 1D is delocalized which effectively averages the fluctuating HF fields of many nuclei. The spin relaxation due to HF interaction is therefore much weaker in 1D as compared to 0D [180, 181] and is not relevant in our experiment.

9.2.2 Exchange-driven electron spin relaxation in nanowires: The BAP mechanism

In their early work, Bir, Aronov and Pikus (BAP) recognized that the exchange interaction between electrons and holes can lead to efficient relaxation of the electron spin in optical orientation experiments [66, 67]. However, to cause electron spin relaxation this mechanism requires hole spin relaxation times that are short on the time scale of electron spin relaxation. Thus, in order to evaluate the importance of the BAP mechanism for our NWs, we will first discuss whether this requirement is fulfilled for the WZ phase of GaAs.

Hole spin relaxation in WZ GaAs Due to the strong mixing of orbital and spin degrees of freedom in the valence band, the hole spin relaxation time of bulk zincblende (ZB) GaAs is typically very short, $\tau_{s,h}^{\text{ZB}} \approx 110\,\text{fs}$ [182], and thus often referred to as *quasi-instantaneous*. In these samples, the basic requirement for the BAP mechanism of electron spin relaxation is therefore always fulfilled. However, in a bulk WZ crystal, this argumentation is not straightforward, since the symmetry of the WZ lattice strongly modifies the mixing of the valence bands. In order to estimate the spin relaxation time of photo-excited holes in our WZ GaAs NWs, we first analyzed the composition of the heavy hole bands in the bulk and then investigated the effects of spatial quantum confinement on this composition. The results are based on the $\mathbf{k}\cdot\mathbf{p}$ calculations performed by Paulo Eduardo Faria Junior within the scope of our collaboration and presented in the Appendix A.3. Here, we summarize the main result: Although substantially longer than in ZB GaAs, the hole spin relaxation times in WZ GaAs ($\tau_{s,h}^{\text{WZ}} \approx 30 - 140\,\text{ps}$) are nevertheless short compared to the experimentally observed time scale of electron spin relaxation ($\tau_{s,e} = 0.4 - 200\,\text{ns}$) in our experiments. Similar observations, i.e., short hole spin relaxation times in a WZ semiconductor compared to electron spin relaxation times, were also reported for experiments on bulk GaN [183, 184]. The basic requirement for exchange-driven electron spin relaxation through the BAP mechanism is thus fulfilled in our WZ GaAs NWs.

Spectral luminescence analysis of spin relaxation We will now identify BAP as the mechanism responsible for the experimentally observed spin relaxation in our

NWs by analyzing the polarized NW emission in more detail. Opposed to the small number of electronic states around the Fermi level that participate in a typical transport experiment, all of the states occupied by the photo-excited carriers in a luminescence experiment may contribute to the emission spectrum. We use this fact to analyze the spin relaxation times of electrons in different electronic states, distinguishable by their photo-emission energy in our NW luminescence spectroscopy. Ultimately, this analysis results in a relation between the electron's kinetic energy and its spin relaxation time; a characteristic signature of our experiment which we can then compare to the prediction from the BAP theory.

Instead of the standard analysis, in which the spin relaxation time τ_s is determined from a narrow window around the peak of the luminescence, we now determine the spin relaxation time $\tau_s(h\nu)$ as a function of the photo-emission energy. To this end, we exemplary investigate in the following the luminescence emission from a NW with $d = 90\,\text{nm}$ at a photo-excited e-h pair density of $n_{3\text{D}} = 8\times10^{16}\text{cm}^{-3}$. Figure 9.2a shows an emission profile of the σ_+-polarized luminescence recorded 200 ps after the pulsed laser excitation. Now we exploit the fact, that our experiment is both energy- and time-resolved. As indicated by the positions of the blue arrows, a 2 meV-wide integration window is shifted step-by-step from the low-energy to the high-energy side of the luminescence spectrum to determine the spin relaxation time at each of the indicated emission energies. Within the analyzed range, the spin relaxation time $\tau_s(h\nu)$, plotted as blue triangles in Fig. 9.2b, decreases from 1.7 to 0.9 ns with increasing photon energy. In a next step, we relate this emission energy dependence of the spin relaxation time to an internal property of the electrons before the e-h pair recombination–their kinetic energy.

In the simplest picture of the recombination of free e-h pairs at zero temperature, the spectral distribution of the luminescence photons can be understood from $h(\nu - \nu_0) = h\nu' = E_k^e + E_k^h$, where $h\nu_0$ is the photon energy corresponding to the lowest possible energy state, i.e., the (renomalized) electronic band-gap, $h\nu$ is the luminescence photon energy and E_k^e, E_k^h are the kinetic energies of electrons and holes [40]. Since in our case $E_k^e \gg E_k^h$ (cf. Section 6.1.2), we can disregard the contribution from the holes and the spectral distribution of the luminescence is then governed by the kinetic energy of the electrons. The photon energy $h\nu'$, determined by E_k^e, thus allows us to connect the emission-energy dependent spin relaxation time $\tau_s(h\nu)$ to the electron's kinetic energy E_k^e. We can now compare this relation to the prediction from BAP theory.

In the framework of the BAP mechanism, the spin relaxation of electrons by free, non-degenerate holes is given by [66, 67]

$$\frac{1}{\tau_s} = \frac{2}{\tau_0}\,\frac{v_e}{v_B}\,(n_{3\text{D}}a_B^3)|\Psi(0)|^4, \tag{9.2}$$

where $\hbar/\tau_0 = (3\pi/64)\Delta_{exc}{}^2/E_B$ defines a scattering time τ_0, that depends on the exchange parameter Δ_{exc}. $E_B = \hbar/(2m_r a_B^2)$ is the exciton binding energy, $v_B = \hbar/(m_r a_B)$, $m_r^{-1} = m_e^{-1} + m_h^{-1}$ is the reduced mass, and a_B is the exciton Bohr radius. $|\Psi(0)|^2$ is the Sommerfeld factor and v_e is the electron velocity. From Eq. (9.2) and $v_e = (2E_k^e/m_e)^{1/2}$,

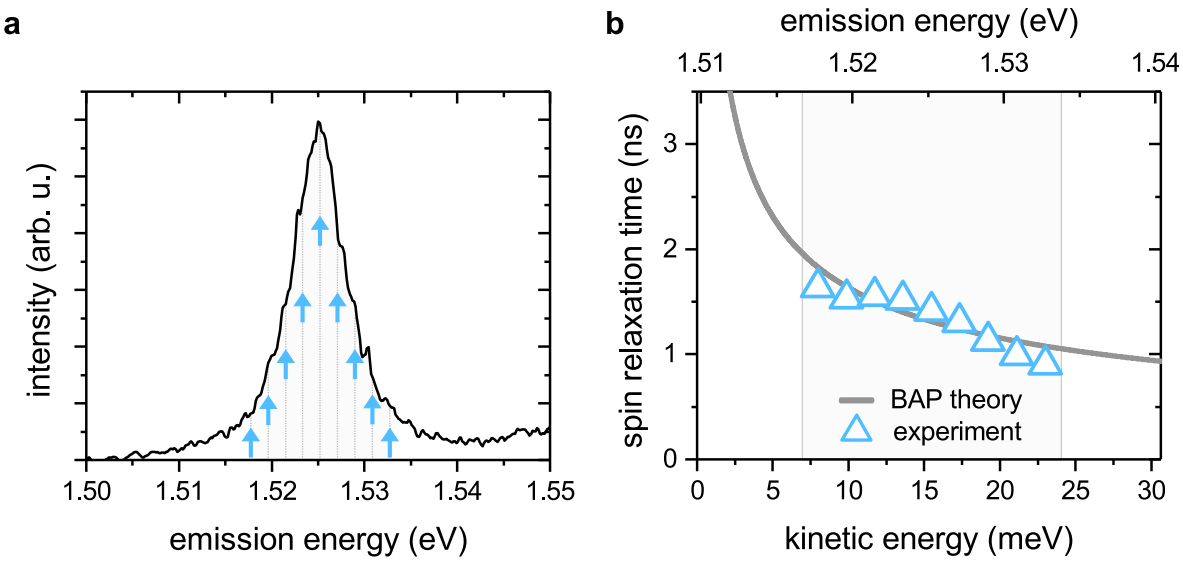

Figure 9.2: A spectral analysis of spin relaxation in a $d = 90\,\text{nm}$ NW. (a) The σ_+-polarized emission, recorded 200 ps after pulsed excitation, is marked with blue arrows to indicate the spectral positions at which the spin relaxation times are determined. (b) Corresponding emission energy dependence of the spin relaxation time. The dark grey line in (b) shows the prediction from BAP theory for the dependence of the spin relaxation time on the electrons' kinetic energy. The x-axis zero was fixed at the onset of the luminescence emission in (a), $h\nu_0 = 1.510\,\text{eV}$, and the parameter $A = 0.16\,\text{ns}$ results from fitting the experimental data. The light-grey shaded areas in (a) and (b) mark the spectral range of the analysis.

we recognize that, in BAP theory, the spin relaxation time is proportional to $(E_k^e)^{-1/2}$, or respectively $(h(\nu - \nu_0))^{-1/2}$. In Fig. 9.2b we thus describe the emission energy-dependent spin relaxation times from our NW with a function of the form $\tau_s(h\nu) = A\,(h(\nu - \nu_0)/\mathrm{eV})^{-1/2}$. For the function plotted as a dark grey line, $h\nu_0 = 1.510\,\mathrm{eV}$ was set as the onset of the luminescence emission at the low-energy side of the spectrum and the parameter A was used as the only fit parameter, rendering $A = 0.16\,\mathrm{ns}$. Considering the approximations of our approach, we conclude that the emission energy dependence of $\tau_s(h\nu)$ observed in our experiment and the kinetic energy dependence of the spin relaxation time predicted by BAP theory are in good agreement.

Diameter-dependence of spin relaxation The spin relaxation in the WZ GaAs NWs observed in our optical experiments is thus driven by the exchange interaction between electrons and holes. However, it is also evident from Fig. 9.1, that the spin relaxation is very efficiently suppressed in our NWs as their diameter decreases. In the following, we will thus investigate how the increasing spatial confinement may disturb the exchange-driven spin relaxation of the electrons in our wires.

As already addressed in our previous discussion on the size-dependent optical properties of our NWs (see Section 6.2), combining the effects of spatial confinement and efficient screening of the attractive Coulomb potential, a 1D nanostructure strongly modifies the fundamental properties of excitons in the bulk. The confined 1D exciton is thus characterized by a diameter-dependent effective Bohr radius [42, 102, 113]. Analyzing Eq. (9.2) reveals that the spin relaxation time in the BAP mechanism depends strongly on such a Bohr radius, i.e., $\tau_s \propto a_B^{-6}$. This effective Bohr radius is determined by the diameter-dependent exciton binding energy [42], which our optical approach allows us to obtain completely independent from the measurement of the spin relaxation time. We determine the binding energy $E_B(d)$ as discussed in Section 6.2 and plot the resulting values again in Fig. 9.3a.

As a consequence of spatial confinement and dielectric screening effects, the binding energy increases with decreasing NW diameter, as expected from theory [42, 102, 113]. For the largest NWs, our analysis renders exciton binding energies of $\sim 4\,\mathrm{meV}$, which increase to $\sim 33\,\mathrm{meV}$ for the thinnest wires. From the relation [102]

$$E_B\, a_B = e^2/(2\epsilon)\,, \tag{9.3}$$

where e is the elementary charge and $\epsilon = 4\pi\epsilon_0\epsilon_r$ with $\epsilon_r = 12.5$ [185], we can thus also directly determine the diameter-dependence of the effective Bohr radius from the exciton binding energies. In Fig. 9.3b this diameter-dependent effective Bohr radius $a_B(d)$ is plotted in units of $a_{B,0} = 14.3\,\mathrm{nm}$. To obtain a function describing the decrease of the effective Bohr radius in our NWs, we numerically approximate the data in Fig. 9.3b finding that the function $a_B(d) = 0.1205 + 0.0560\,(d/\mathrm{nm} - 19.4)^{2/3} - 0.0050\,(d/\mathrm{nm} - 19.4)$, plotted as a grey line, approximates the diameter-dependence of the effective Bohr radius in our NWs well. The same function, converted by the above relation, is also plotted as a grey line in Fig. 9.3a.

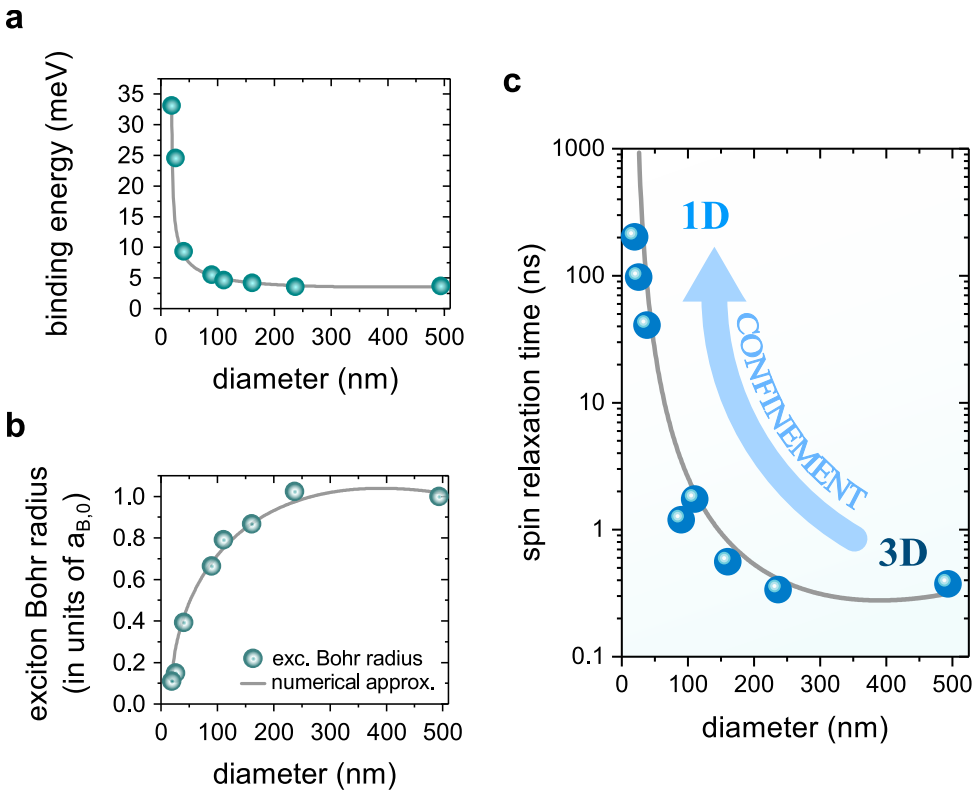

Figure 9.3: Diameter-dependence of the exciton binding energy and the effective Bohr radius in the NWs. (a) Binding energies are determined from Eq. (6.3) as an independent parameter. (b) The decrease in the effective Bohr radius a_B (in units of $a_{B,0} = 14.3\,\text{nm}$) with decreasing NW diameter is calculated from the binding energies in (a). The grey line in (b) is a numerically approximated function describing the diameter-dependence of a_B, or converted to E_B in (a). (c) The spin relaxation time as a function of the NW diameter is displayed on a semilogarithmic scale. Same data as is Fig. 9.1. The diameter-dependence of the spin relaxation time as calculated from an exchange-based model is plotted as a solid grey line. The fit parameter-free model shows excellent agreement with the experimental values.

Finally, we may now also numerically evaluate Eq. (9.2) using the binding energy and effective Bohr radius from Fig. 9.3b. Note, however, that the exchange parameter for WZ GaAs is entirely unknown, except that Ref. [112] provides an upper bound of $\sim 0.5\,\mathrm{meV}$. For $d = 495\,\mathrm{nm}$, the numerical evaluation of the BAP formula provides the relation for the spin relaxation time

$$\tau_s = 0.17\,\mathrm{ns}\,|\Psi(0)|^{-4}(\Delta_{exc}/\mu\mathrm{eV})\,, \tag{9.4}$$

depending on the Sommerfeld factor and the exchange parameter. If we assume for example the exchange parameter of bulk ZB GaAs, $\Delta_{exc} = 47\,\mu\mathrm{eV}$ [67], we find that $|\Psi(0)|^4 = 26.2$ reproduces the experimentally observed spin relaxation time $\tau_s = 0.37\,\mathrm{ns}$ at a NW diameter of $d = 495\,\mathrm{nm}$. Considering the uncertainty of the unknown exchange parameter in this calculation, the value of $|\Psi(0)|^4$ is in reasonable agreement with the values in the range of $|\Psi(0)|^4 = 1 - 20$ given in Ref. [67].
Ultimately, all of these arguments combined lead us to one final conclusion: The strong diameter-dependence of spin relaxation observed in our NW experiments originates from the confinement-induced squeezing of the e-h Bohr radius and its large impact on the BAP mechanism. This diameter-dependence of the spin relaxation time in the BAP mechanism is now plotted as a dark grey line in Fig. 9.3c. It is thus directly determined by the diameter-dependence of the effective Bohr radius: $\tau_s(d) = \tau_{s,0} \cdot a_B(d)^{-6}$, where $\tau_{s,0} = 0.35\,\mathrm{ns}$ is the experimentally determined spin relaxation time of the largest wires ($d > 200\,\mathrm{nm}$).
We emphasize here that the values of $a_B(d)$ were determined completely independently of the spin lifetime experiments and that the solid line in Fig. 9.3c contains no fit parameters. It was only calibrated with $\tau_{s,0}$, the spin relaxation time of the largest NWs. Showing excellent agreement with the experiments, our BAP analysis thus demonstrates that the electron spin relaxation time observed in our experiment throughout the entire transition from 3D to 1D is driven by the exchange-induced interaction between the photo-excited electrons and holes. It even captures the drastic increase of the spin relaxation times in the 1D NW regime, documenting that although the BAP mechanism is only residual in this regime, it is still limiting the spin relaxation.

9.3 Peculiar spin phenomena in 1D wires

The ability to tune the diameter of our NWs in a large range enabled a systematic study of the diameter-dependence of spin relaxation which ultimately identified the microscopic process responsible for the spin dephasing in our experiment. Pushing wires into the 1D quantum regime, we get the chance to investigate a possible impact on the spin-related properties of electrons in 1D.

9.3.1 Ultralong spin lifetimes in 1D wires

We now comment on the observation of spin relaxation times exceeding 200 ns, which is extraordinarily long for GaAs. First of all, let us state here that this observation finally confirms the aforementioned speculations about the robustness of 1D electrons against spin decoherence [13–16] for the first time in an experiment. By revealing the ultralong spin lifetimes of electrons in 1D channels, our experiments enter a new realm of spin coherence for mobile charge carriers and, in some sense, bring the above story of suppressing spin relaxation in narrow semiconductor channels to an end.
Observing such ultralong spin lifetimes is only possible because of the complete suppression of the DP mechanism in III-V 1D NWs, a mechanism which is otherwise known to be highly efficient in most semiconductor structures. Like in our 3D wires, the small, but finite spin relaxation remaining in our 1D NWs is shown to be limited by the BAP mechanism. As the e-h pairs become increasingly confined in the 1D NWs, this mechanism is efficiently suppressed, resulting in more than 500 times longer spin relaxation times than in our larger NWs with a 3D dispersion. We emphasize that the spin relaxation time limited by e-h exchange in our experiment is a consequence of the optical excitation, suggesting even longer spin relaxation times for pure 1D electron systems in NWs.
It is worth noting that in III-V semiconductor structures, electron spin relaxation times of $\tau_s \geq 100$ ns have so far only been observed for localized, 0D electrons [176–179]. In contrast to these 0D systems, in which the HF interaction between carrier spins and fluctuating nuclear spins was found to limit the spin relaxation time, the delocalized wave function of 1D carriers effectively averages the fluctuating HF fields of many nuclei. The spin relaxation due to HF interaction is therefore much weaker in 1D as compared to 0D [180, 181]. Furthermore, the electrons in our NWs are free to move along the 1D channel, making these wires ideal systems for the transport of coherent spin information, e.g., to interconnect spintronic devices on chip or allow coherent spin manipulation. Given this exceptional robustness of electrons in our 1D wires against the major spin relaxation mechanisms, a quantum mechanical theory of spin relaxation in 1D will certainly be essential to harness these advantageous aspects of 1D NWs.

9.3.2 A glimpse at the extraordinary g-factor in 1D wires

Apart from monitoring the spin relaxation, we have also investigated the effect of a transverse magnetic field in our 1D wires.
Triggered by Kitaev's toy model [186] suggesting the occurrence of Majorana bound states in a 1D conductor coupled to a p-wave superconductor, ambitious efforts to detect Majorana fermions in proximity-coupled semiconductor NWs have initiated the recent investigations about g-factors in 1D wires [6, 187–189]. In particular the reports about unusually large g-factors in Majorana wires have puzzled the community, since a number of well-understood studies on 2D systems show a decrease of the g-factor in confined systems [190, 191]. Contradicting these studies only at first glance, recent model

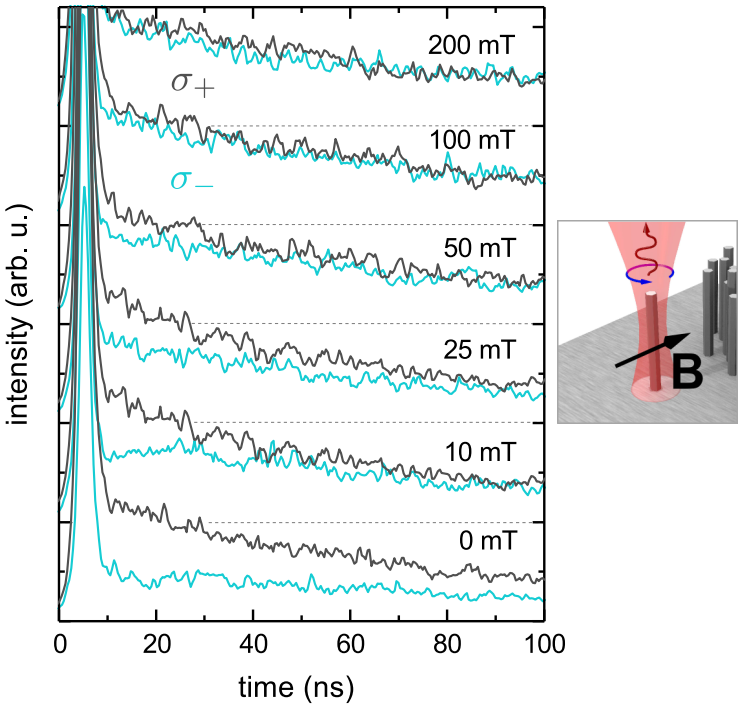

Figure 9.4: Magnetic field effect on the spin dynamics in a 1D wire with $d = 20\,\text{nm}$. For increasing magnetic fields applied perpendicular to the wire, pairs of counter-polarized emission traces are offset by a constant value for illustration purposes. Horizontal dashed lines indicate zero intensity. A large splitting between the σ_+ and the σ_- polarized decay curves observed at zero magnetic field is reduced at small fields (10 to 50 mT) and vanishes completely at larger fields ($> 50\,\text{mT}$). Despite the long time period over which the two signals are split, no magnetic field-induced oscillations occur. The high intensity signal peaking at $\sim 5\,\text{ns}$ stems from the surrounding substrate and does not belong to the NW emission.

calculations now confirm that g-factors in NWs can indeed be enhanced up to an order of magnitude compared to the g-factors in the corresponding bulk material [192]. This effect, related to the angular momentum of electrons in higher 1D subbands contributing to the g-factor in NWs, explains the large values observed in the above mentioned studies on Majorana Fermions in 1D semiconductor wires. While the effect enhances the g-factor in higher subbands, it is absent in the lowest subband having no (or only small [192]) angular momentum. In analogy to 2D systems, the g-factor in the lowest subband of a 1D wire is thus expected to decrease as the confinement increases.

As discussed in Part II, the electrons in our NWs occupy only the lowest subband for $d < 35\,\text{nm}$–the 1D quantum limit of our wires–under the photo-excitation conditions of our experiments. To investigate the g-factor of electrons in the lowest subband of such a 1D wire, we follow the same approach as described in Section 8.1 and apply an external

magnetic field perpendicularly to the NW axis. Notably, the observable range of $|g^*|$ values in this experiment on a 1D wire is quite different as compared to the previous experiments on the 3D wires. This is apparent from the counter-polarized emission curves of the 1D wire. Figure 9.4 shows pairs of σ_+ and σ_- traces, that are offset by a constant value for illustration purposes. In this experiment, two factors play an essential role in determining the g-factor: the time period in which a difference between the σ_+ and σ_- curve is observed and the time period in which the total emission signal is at all detectable. In the 1D wire, both of these factors are substantially enhanced compared to the previously studied 3D wires. This enhancement is indeed caused by the occurrence of the unusually long spin relaxation and luminescence decay times, $\tau_s = 180\,\text{ns}$ and $\tau_{pl} = 79\,\text{ns}$, respectively, in the 1D wire. Combined, these two factors should in principle allow the detection of much smaller g-factors as compared to our previous experiments on 3D wires (cf. Section 8.1). Yet, the pairs of counter-polarized emission curves in Fig. 9.4 show no sign of magnetic field-induced oscillations under the increasing influence of an external field. For comparison, at a magnetic field of 25 mT, the g-factor, $|g^*| = 0.28$, determined for the 3D wire, should induce about 60 oscillatory crossings between the σ_+ and σ_- counter-polarized decay traces during the very long detection time of our experiment. Even a decrease of this $|g^*|$-value by a factor of ten should correspondingly still show at least 6 oscillations. The complete absence of such oscillations in our experiment therefore points to a strongly reduced g-factor in the 1D wires. This conclusion is both in line with the theoretical reports addressed above [190, 192], as well as the calculations by Kiselev *et al.* [191], predicting a decrease of the bulk g-factor particularly in cylindrical GaAs/AlGaAs core/shell wires. In their analytic description, the g-factor indeed decreases gradually as the wire diameter decreases, eventually becoming zero at a wire diameter $d \approx 10\,\text{nm}$.

It is interesting to note that even in the absence of any oscillations, the sets of counter-polarized curves in Fig. 9.4 exhibit a magnetic-field enhanced spin relaxation. The difference between the σ_+ and the σ_- traces clearly decreases already for small magnetic fields of 10 mT and further vanishes completely for fields larger than 50 mT. Quantifying this effect is not easy, since we do not know which mathematical function fits the observed behavior. Yet, if we approximate the decay at 10 mT by a single exponential, we find a magnetic field-induced enhancement of spin relaxation, that is characterized by a decay constant of ~20 ns.

Particularly with regard to the above mentioned theory [192], it would be interesting to repeat the experiments on our 1D wires using a high-power laser. Similarly to the experiments presented in Section 6.3, such a laser could be used to create photo-carriers in higher 1D subbands. As predicted by theory, the g-factors of electrons in those subbands should increase substantially and might thus become detectable in our experiment. Note, however, that this enhancement of the g-factor due to angular momentum unveils only in fields applied along the wire axis, requiring a different magnet in our optical setup. Moreover, in this configuration the direction of the optically injected spins and the external field would coincide, preventing the measurement of the g-factor through Larmor precession. Unfortunately, exploring the g-factor through the Zeeman splitting in the

emission spectrum in turn necessitates larger fields (exceeding 1 T).

9.4 Summary and outlook

We now conclude our insights on spin-related phenomena in semiconductor NWs and summarize the main results. Many of our findings were developed in a collaborative research effort and constitute the subject of three individual manuscripts [108, 133, 171] published in Nature Communications and Physical Review B.
To begin with, we introduce a method of optical spin injection into single free-standing wires by describing the preparation of the as-grown NW samples and the first optical experiments in Chapter 7. Besides unambiguously evidencing the actual optical spin injection, we show that applying a magnetic field induces a precession of the spins in our experiment, which allows us to determine a first value for an effective electron g-factor in WZ GaAs wires ($|g^*| = 0.28$). Intriguingly, the time and polarization-resolved measurements presented in Chapter 8 further reveal an unusual anisotropy of spin relaxation in the NWs: Spins pointing along the wire relax substantially slower than those oriented in a plane perpendicular to the wire axis. Understanding this peculiar behavior of spins in NWs has motivated an inquiry of the different microscopic contributions to the SOC in our core/shell NWs. We thus approach the task by considering a modified SOC in the theoretical framework of DP, a mechanism dominating the spin relaxation in most III-V semiconductor structures (including other WZ semiconductors) [52, 55, 129–132], which coherently explains the observed behavior. Despite its inherent conclusiveness, implications derived from our model of spin relaxation in NWs do not show in two additional, independent experiments. At that point, considering all the different pieces of information presented in Chapter 8 renders quite a puzzling and inconclusive picture of the spin relaxation in NWs.
To get to the bottom of this problem, we then proceed by investigating the spin relaxation as electrons are increasingly confined in our NWs; experiments, which are after all only possible because of the advances in the fabrication of diameter-tunable wires that were presented in Section 5.3.
As highlighted in Section 9.1, probing the diameter dependence of spin relaxation in our wires shows a continuously increasing spin relaxation time as the wire diameter decreases, eventually revealing an exceptional robustness of 1D electrons against spin decoherence. The resulting ultralong spin lifetimes exceed 200 ns in the 1D wires. With this observation, a long history of controlling spin relaxation in narrow semiconductor channels thus peaks in a new realm of spin coherence, promising applications for quantum information transfer and the coherent manipulation of spins. Despite this experimental discovery, the intriguing question which microscopic mechanism causes the observed spin relaxation is, at that point, still unaccounted for. Making an effort to understand the spin relaxation, we present an evaluation of different spin relaxation mechanisms in Section 9.2. Eliminating possible candidates one by one leads to an analysis of exchange-driven spin relaxation. Our evaluation of different mechanisms not only shows, that throughout the

entire transition from 3D to 1D, the BAP mechanism is responsible for the spin relaxation observed in our experiments, but also entails some microscopic insight on the transport coherence of electrons in our NWs: Even in our largest NWs (d = 490 nm), the electron motion is not fully diffusive, and, under the conditions of the optical experiments, we thus consider the electrons in our wires to be in the radially ballistic regime. Finally, we present a fit parameter-free model demonstrating that the decreasing Bohr radius in our NWs describes the experimentally observed spin relaxation with very good agreement. Notably, this Bohr radius is determined completely independently from the spin relaxation measurements.
By addressing the effect of a perpendicular magnetic field on the spins in our 1D wires in Chapter 9, we supplement the efforts to understand an enhancement of the g-factor in 1D semiconductor wires that was recently detected in transport measurements on Majorana wires [6, 187–189]. The absence of a magnetic field-induced spin precession in our optical measurements (as opposed to the experiments on the 3D wires), points to a strongly reduced g-factor in the 1D wires. This observation is actually in line with the predictions from theory for the electrons in the lowest 1D subband. We suggest that the above mentioned enhancement of the g-factor could possibly also be detected in our optical experiments by applying a magnetic field along the wire axis and by using a different laser to populate higher 1D subbands.

To arrive at the conclusions presented in this part, we have conducted an extensive amount of measurements, confirmed and rejected the different theories, alongside dissecting the experimental observations bit by bit. In this way, many of the unresolved issues encountered at the beginning of our study could be conclusively explained and open questions for an outlook scarcely remain. However, one puzzle is still unaccounted for: the origin of the spin relaxation anisotropy we repeatedly encounter in our WZ GaAs NWs. Even in this regard, our experiments at least provide us with a clue. Since this anisotropy neither depends on the wire diameter (see Section 8.2.4), nor on the chemical composition of the shell (see Section 8.2.4), Equation (9.2), which describes the BAP mechanism responsible for the observed (anisotropic) spin relaxation, may point us to the solution. We thus suppose that the anisotropic spin relaxation is a result of (one or more) anisotropic band structure parameters of the WZ GaAs crystal. Due to its hexagonal C_{6v} symmetry, the WZ crystal structure inherently entails the anisotropy of many parameters, including the effective mass [27] or the exchange parameter Δ_{exc} [112]. Ultimately, this hypothesis must be confirmed by a sophisticated calculation of the WZ GaAs band-structure.

IV Photonic engineering at the nanoscale

In the past decade semiconductor NWs have been established as a fundamental building block of nanophotonics in highly efficient light-emitting diodes or solar cells [193, 194], as the active component of nanoscale lasers and THz detectors [94, 195], or as a passive element in novel photo-chemical sensors [196]. The exciton recombination dynamics in such NWs have, up to now, mostly been evaluated by analyzing the role of non-radiative recombination at defects [197, 198] or surfaces [199–201], and electric field-induced band bending effects [202, 203], despite the fact that its approximately cylindric shape inherently equips a NW with particular optical properties. Although diameters of Vapor-Liquid-Solid-grown NWs usually lie in the range of a few tens to hundreds of nanometers–thus in fact representing a waveguide with sub-wavelength diameter for typical band-gap emission energies–the impact of the waveguide and its dielectric surroundings on the dynamics of spontaneous emission has not been considered up to now, besides in lasing studies [9, 94, 95]. In the first chapter of this part of the thesis, we will reveal the dominant role of the sub-wavelength waveguide in the spontaneous emission process of photo-excited excitons in semiconductor wires.

Joining Prof. Dr. Tobias Korn, Prof. Dr. Christian Schüller, Dr. Christoph Lange, Imke Gronwald and Prof. Dr. Rupert Huber in our collaborative endeavor to experimentally study the spontaneous emission in our NWs, Diego Abujetas and Dr. José Sánchez-Gil from the *Instituto de Estructura de la Materia* in Madrid are currently contributing illuminating theoretical input on the matter. While still preliminary, the results of their numerical simulations already confirm the hallmark features of our experiments, on top of deepening our understanding of the physics involved.
Unveiling the spontaneous emission process in semiconductor NWs, the results presented in Chapters 10 and 11 constitute the main body of a manuscript currently under preparation for publication.
We utilize our newly gathered insight into the spontaneous emission process in Chapter 12 to further investigate the interactions between NW excitons and the surface-plasmon-polaritons (SPPs) in metallic structures.

10

Diameter-dependent spontaneous emission in nanowires

To study the possible influence of the waveguide effect on the emission properties of our NWs, we investigate the diameter dependence of the luminescence dynamics. As sketched in the central part of Fig. 10.1, we excite single wires in our confocal μ-PL setup at nominally $T = 4.2\,\mathrm{K}$ using a near-resonant, 1.58 eV laser diode and detect their luminescence dynamics in the streak camera system. Note that, when we speak of a NW diameter in this part of the thesis, we refer to the total diameter of the core/shell NWs instead of the core diameter. Due to very similar refractive indices of the GaAs core and the AlGaAs shell, this is the diameter value most relevant for the optical effects addressed in this part. To maintain a constant photo-carrier density, the time-averaged pulsed excitation power density $\bar{P}$ was $1.4\,\mathrm{W/cm^2}$ in all measurements, except for NWs with $d < 100\,\mathrm{nm}$, where we increase the power density to $267\,\mathrm{W/cm^2}$ to compensate for the reduced absorption. As discussed in Section 3.2, the initially excited carrier density $n_{3\mathrm{D}} = 8 \times 10^{16}\mathrm{cm}^{-3}$, is only slightly above the metal-insulator (or Mott-) transition and the dynamics at later times after the pulsed excitation are governed by excitonic properties. We thus regard the photo-excited carriers in our NWs as a gas of free and mobile excitons.

A 100× microscope objective focuses the laser beam to a spot size of $\sim 1\,\mu\mathrm{m}^2$, allowing us to investigate NWs either directly as-grown, when they are free-standing on the growth substrate [133], or after they were dispersed onto a substrate composed of 300 nm SiO_2 on top of a Silicon wafer (see left and right panels in Fig. 10.1). In analogy to our approach for the optical spin injection (cf. Chapter 7), we preselect NWs showing the defect-free luminescence emission associated with high phase purity, a single emission peak at $E = 1.52\,\mathrm{eV}$ [24, 88, 133]. Thus excluding the exciton capture at defects from the beginning, we are able to study the actual dynamics of the free excitons in our NW experiments. Upon reducing the NW diameter in our series, the increasing spatial quantum confinement successively shifts this peak to a maximum energy of $E = 1.54\,\mathrm{eV}$ (see Chapter 6). The time-resolved luminescence decay is obtained directly from the

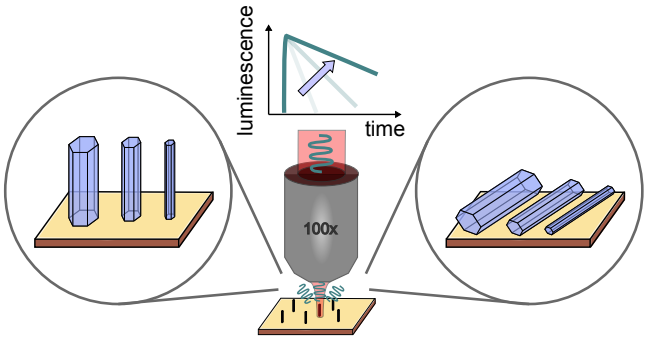

Figure 10.1: Simplified schematic of the setup used to study the exciton dynamics in NWs. A pulsed laser is focused by a 100× microscope objective to excite single wires and record their luminescence dynamics (top). NWs in a large range of diameters are investigated either free-standing (left), or lying on a Si/SiO_2 substrate (right).

streak camera images by spectrally integrating over a 5 meV-wide window centered at the peak of the PL emission.

First, we focus on the exciton dynamics in the free-standing NWs. We have divided representative examples for their diameter dependence into two plots, Fig. 10.2a and b, with different scalings of the time axis. Figure 10.2a compares the normalized decay curves of two of the larger diameters: $d = 540$ nm and 200 nm. Since for both diameters the major part of the luminescence intensity ($> 90\,\%$) can be well characterized by one single exponential decay lifetime (plotted as a solid line in Fig. 10.2a), we denote this value as the lifetime that is used in the upcoming discussion. We note, however, that a small fraction of the total intensity ($< 10\,\%$) does not fit the single exponential decay, rendering the total decay biexponential. While a literature survey provides various explanations for such a biexponential decay, which was also reported in other systems, these explanations do not result in a conclusive picture for our case [204–209]. From the single exponential decay fits plotted as solid lines we find $\tau_{pl} = 2.1$ ns for $d = 540$ nm and $\tau_{pl} = 0.6$ ns for $d = 200$ nm. Hence, the luminescence decays significantly faster in the NW with $d = 200$ nm as compared to the larger NW.

This trend reverses towards smaller diameters. Figure 10.2b shows three NWs with the diameters $d = 120$, 85 and 65 nm for which the traces are now fully described by a single exponential decay. Decreasing the diameter from $d = 200$ to 120 nm we already observe a tenfold increase in the lifetime to $\tau_{pl} = 6$ ns. The recombination times keep increasing for the two smaller diameters, eventually yielding the very long lifetime of $\tau_{pl} = 86$ ns for $d = 65$ nm.

Since non-radiative recombination frequently dominates the exciton dynamics and limits their lifetimes in NWs to a sub-ns range [199, 210], observing lifetimes in the tens-of-ns range in our experiment demonstrates that the surface passivation by the core/shell structure as well as the low measurement temperatures strongly suppress non-radiative recombination [197]. We thus conclude that non-radiative effects [204, 209, 211–213]

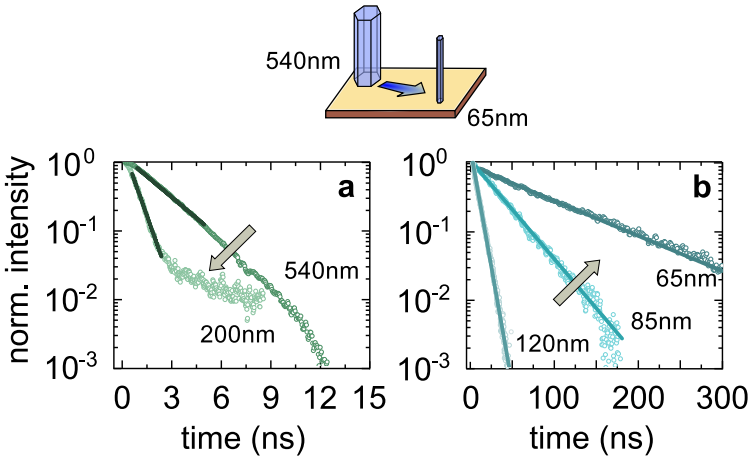

Figure 10.2: Normalized low-temperature luminescence decay curves of single free-standing NWs. (a) and (b) illustrate the remarkable differences of the exciton recombination dynamics in free-standing NWs with diameters ranging from 540 to 65 nm. The fits are plotted as solid lines. Note the different time scales in (a) and (b).

can not account for the observed lifetimes in our NWs. Furthermore, since the excitons are expected to occupy the whole NW volume in less than 200 ps [214], the decay due to diffusion does not contribute to the signal at later time periods ($t > 1$ ns), which we use to fit the curves. As a consequence, we attribute the luminescence decay in our experiment to the purely radiative recombination of excitons.
We have averaged the lifetimes from several single wires (3 to 5) with nominally identical diameter d and summarized the results for diameters ranging from $d = 540$ to 60 nm in Fig. 10.3. The graph confirms the trends observed in Figs. 10.2a,b and reveals two striking features:

(i) a prominent minimum around $d = 200$ nm, where the lifetime drops from a few ns for larger diameters to $\tau_{pl} = 0.8$ ns,

(ii) a dramatic increase in the lifetime for $d \leq 200$ nm, culminating at an average of $\tau_{pl} = 79$ ns for the thinnest NWs ($d = 60$ nm).

Thus, the diameter dependence of the radiative recombination is tremendous: The time over which the absorbed photon energy is stored in the excitons in a NW before being re-emitted can be tuned over two orders of magnitude. Such dramatic changes in the lifetime are unusual for direct-gap semiconductors and their nanostructures. To provide a reference for the lifetime range observed in our NWs, we note that in GaAs quantum wells, upon decreasing the thickness by one order of magnitude, the luminescence lifetimes change by a factor of 4 [50]. In the end, only specifically designed microcavities like photonic crystals or plasmonic structures have been shown to allow such large variations in the radiative lifetimes of single emitters [33, 215–217].

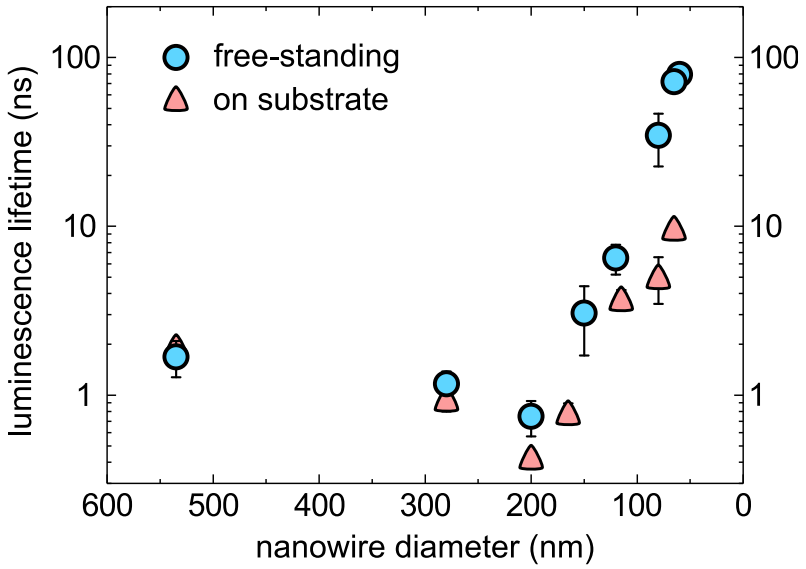

Figure 10.3: Diameter-dependence of the averaged luminescence lifetimes in our NWs. Upon decreasing the NW diameter, the measurements reveal a minimum at $d = 200\,\text{nm}$ followed by dramatically increasing lifetimes. For $d \leq 200\,\text{nm}$, the NWs lying on the Si/SiO_2 substrate show significantly shorter lifetimes. The error bars represent the statistical standard deviation.

Interestingly, considering a NW not only as a direct-gap semiconductor providing a lattice with which the excitons interact (e.g., via lattice vibrations, interfaces, defects), but also as a cavity for the photons it emits, is a rare approach in the current literature. Let us thus regard the photo-excited free excitons in our experiment as an ensemble of emitters, homogeneously distributed within the cavity of a dielectric waveguide–our NWs. In order to spontaneously emit a photon, the excitons will now have to radiate their energy into the electromagnetic local density of states (LDOS) of the cavity, which is given by the photonic waveguide modes. With this waveguide picture in mind, Fig. 10.3 clearly highlights the importance of the NW diameter d with respect to the wavelength λ/n: the relative size of the two quantities practically determines the LDOS in the waveguide, as we discuss in the following. Here, $\lambda = 815\,\text{nm}$ is the wavelength of the emitted light in vacuum and $n = 3.45$ is the refractive index of GaAs [7].
To understand the photonic effects in our wires, we first introduce a qualitative picture of the waveguiding in our free-standing NWs, before presenting the preliminary results of the more complete numerical description from Diego Abujetas and Dr. José Sánchez-Gil.
For the qualitative description, we focus on the fundamental waveguide mode, the HE_{11}-mode, which dominates the emission in our NW diameter range, since all higher-order modes are cut-off below $d \lesssim 250\,\text{nm}$ [7]. Concerning this HE_{11}-mode, three regimes can be distinguished when comparing the NW diameter d to the constant value of λ/n [218]. For these three regimes, the spatial intensity distribution of the HE_{11}-mode with respect to the NW cross-section is sketched in Fig. 10.4 according to the calculations of Tong *et*

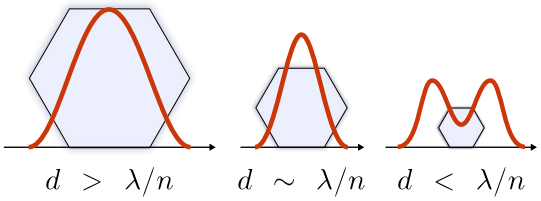

Figure 10.4: Intensity profiles of the fundamental waveguide (HE_{11}) mode sketched according to the calculations of Tong et al. [219]. For $d > \lambda/n$, all available modes, i.e., the fundamental mode and others (not sketched), contribute to the radiative decay. At $d \sim \lambda/n$, the tight confinement of the fundamental mode enhances the emission. Further decreasing the diameter brings the NWs into the regime where d is smaller than λ/n. Here, the major part of the mode intensity gets redistributed to the environment and cannot contribute to the radiative decay.

al. [219].
For $d > \lambda/n$, the fundamental HE_{11}-mode, as well as other, higher-order modes (not sketched), are distributed inside the NW. In this case, the excitons emit their energy into all available modes, resulting in radiative lifetimes, which are comparable to bulk GaAs [7]. For decreasing diameters, however, the emission into the fundamental waveguide mode becomes more and more important, since for $d \sim \lambda/n$, this mode reaches maximal confinement, while all other modes are strongly suppressed. This effect leads to an emission enhancement [34], which we in turn observe as a minimum in the radiative lifetimes in our experiment. For even thinner NWs, a curious effect occurs in the third regime, where d is smaller than λ/n: Far beyond the cut-off diameter for all other modes, the NW begins to expel the fundamental HE_{11}-mode. As the diameter decreases, an increasingly larger fraction of the mode intensity is distributed to the environment outside of the NW [218, 219]. Hence, the overlap of a small-diameter NW ($d < \lambda/n$) with the optical mode is strongly reduced (cf. right-hand side of Fig. 10.4), inducing the experimentally observed dramatic increase in the lifetimes with decreasing NW diameter.
This qualitative picture thus captures both of the striking features (i) and (ii) revealed by Fig. 10.3: A minimum in the radiative lifetime occurs at $d \sim \lambda/n$, and for diameters below the minimum, a strong increase follows from the mode redistribution. Since we exclude non-radiative recombination effects, we thus come to the conclusion that the diameter dependence of the emission lifetime observed in our free-standing NWs is a direct result of their inherent photonic waveguide nature.
By numerically simulating the real-space distribution of the HE_{11}-, and the higher-order modes in COMSOL, our collaborators Diego Abujetas and Dr. José Sánchez-Gil furthermore accomplished a quantitative account of the waveguide effect. Figure 10.5a and b show the simulated intensity distribution of the HE_{11}-mode for two NWs with diameter $d = 250\,\text{nm}$ ($d > \lambda/n$) and $d = 90\,\text{nm}$ ($d < \lambda/n$). Taking the emission into

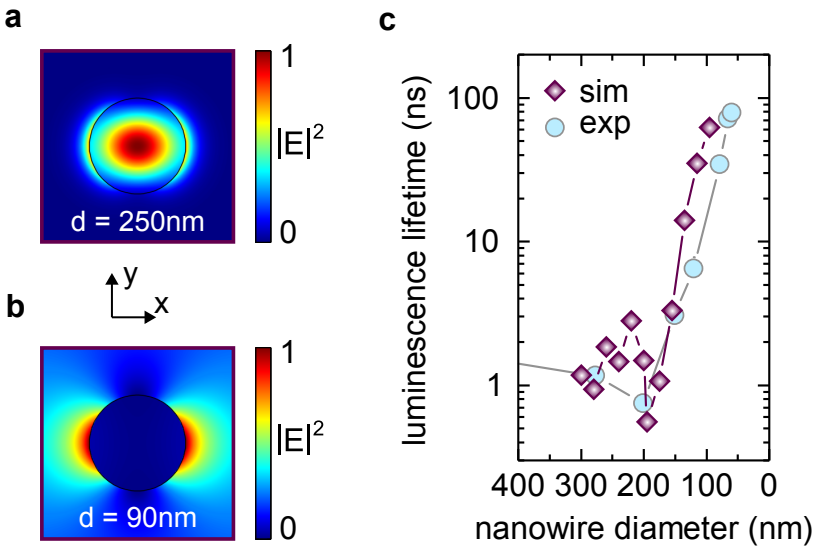

Figure 10.5: Numerical simulation of the normalized HE_{11} intensity distributions for a cylindrical wire with $n = 3.45$ surrounded by vacuum ($n = 1$) and diameter d: (a) 250 nm and (b) 90 nm. (c) While still preliminary, the simulated emission lifetime, considering the HE_{11}-, as well as higher-order modes, shows good agreement with our experimentally determined lifetimes in the free-standing wires. Finite-element-method-based numerical simulations were performed using the commercial software COMSOL Multiphysics v4.3b. Courtesy of Diego Abujetas and Dr. José Sánchez-Gil.

all available modes into account, they calculated the spontaneous emission lifetime of a single dipole emitter centered on the axis of a dielectric cylinder with $n = 3.45$ surrounded by vacuum ($n = 1$). Their results are plotted together with our experimental lifetimes obtained from the free-standing wires in Fig. 10.5c. While still preliminary, the simulated lifetimes already show good agreement with our experiment, particularly since they quantitatively reproduce the two orders of magnitude increase of the luminescence lifetime below $d = 200\,\mathrm{nm}$. Beyond the quantitative agreement, the numerical simulations also provide a very illustrative account of the expelling of the fundamental mode for small NW diameters, as shown in Fig. 10.5b.

Now we return to the experimental results in Fig. 10.3. Transposing this idea of an expelled optical mode to our experiment, we can anticipate a considerable impact on the radiative exciton recombination when we modify the direct environment of our small-diameter NWs, for example, by depositing them onto a dielectric substrate. We indeed clearly observe this impact in Fig. 10.3 when comparing the diameter-dependent emission lifetimes of NWs lying on Si/SiO_2 substrates with the free-standing NWs which are completely surrounded by vacuum in our experiment. As might be expected, the lifetimes of the largest NWs, where the optical modes are confined within the NW, are identical in both configurations. In contrast, approaching the small-diameter regime ($d < \lambda/n$) of our NWs introduces a quantitative difference: For the NWs lying on Si/SiO_2, the substrate constrains the expelling of the mode to the environment [220]. Thus the radiative exciton recombination is enhanced compared to the free-standing NWs, which are completely surrounded by vacuum. As a consequence, the lifetimes of the NWs lying on substrates are clearly shorter: For the thinnest NWs, the lifetime difference between both configurations even reaches up to one order of magnitude. Surprisingly, the excitons in the GaAs core have thus become sensitive to the dielectric environment outside of the NW.

To summarize, our study on radiative exciton recombination in GaAs NWs unveils a dominant role of the photonic waveguide nature that is inherent to semiconductor NWs. This finding is particularly relevant for Vapor-Liquid-Solid-grown NWs, since a Purcell-enhanced minimum ($d \sim \lambda/n$), as well as a drastic increase of the emission lifetime ($d < \lambda/n$) fall in the typical wire diameter range of a few tens to a few hundreds of nanometers. Hence, it provides an indispensable perspective for the understanding of exciton dynamics in semiconductor wires. Furthermore, entering the small-diameter regime ($d < \lambda/n$) introduces a particularly pronounced sensitivity of the radiative exciton recombination on the dielectric surrounding of a NW: We show that bringing a NW in contact with a Si/SiO_2 substrate reduces the lifetimes up to a factor of ten. Our study thus highlights the relevance of the photonic waveguide nature for the analysis and interpretation of NW luminescence experiments.

11 All-dielectric control over spontaneous emission in nanowires

Recognizing that the spontaneous emission of free and mobile excitons in our semiconductor NWs is dominated by the photonic waveguide properties of the NWs opens a route to manipulate the photo-emission, merely by tailoring the dielectric environment of the emitters. In the following we will present two explicit examples for such an all-dielectric control over of the exciton emission.

11.1 Single mode linearly polarized emission from wires with elliptical cross-section

In the past years, quantum emitters embedded in photonic NW waveguides were recognized as an extremely efficient platform for highly directive single photon sources due to their ability to manipulate the spontaneous emission process and to guide the emitted light [7, 221–223]. Contrasting the narrow optical resonances on which similar applications of semiconductor microcavities rely, semiconductor NW waveguides were reported to operate with much higher band widths [7, 221]. It is thus possible to funnel a large fraction of the spontaneous emission from single emitters into the fundamental optical mode of the NW waveguide over a comparably wide range of wavelengths [7]. However, due to the radially symmetric cross-section of most NW waveguides, the fundamental optical mode–the hybrid HE_{11} mode–is always two-fold degenerate; a consequence of the two possible orthogonal linear polarizations in the waveguide. To extract a succession of single photons with definite linear polarization from a photonic waveguide, either the emitter itself must be intrinsically polarized (e.g., through uniaxial strain or an asymmetric confinement potential), or the waveguide geometry must somehow remove the degeneracy of the fundamental optical mode. First investigated by Munsch *et al.* [224] in a top-down fabricated waveguide with elliptical cross-section, this second approach turns out to be very efficient; over a broad range of wavelengths it allows over 90 % of the total emission

intensity to be emitted into a single mode with definite linear polarization.
In the following, we will show that besides the top-down etching technique introduced by Munsch *et al.* [224], the bottom-up growth of core/shell NWs in molecular beam epitaxy is exceptionally suited to realize such a single mode NW waveguide. To that end, we synthesize a core/shell NW wafer adjusting the standard growth parameters described in Section 5.4. Under the conditions of symmetric NW growth, i.e., if the wafer is rotating during growth, such NWs would exhibit a hexagonal cross-section with a core diameter around 80 nm and a total diameter of 120 nm. Here, to obtain wires with radially non-symmetric cross-section, we switch off the continuous rotation of the wafer before the growth. Using characteristic RHEED (reflection high-energy electron diffraction) patterns to identify the orientation of the wafer with respect to the molecular beam sources of Ga and Al, we rotate the wafer such that only one or two of the initially developing six NW facets are facing the molecular beams. Keeping the rotation off, but conducting the growth under otherwise nominally identical conditions, leads to a highly elliptical cross-section of the growing NWs, as demonstrated by the scanning electron micrographs in Fig. 11.1.
A side-view image of several as-grown NWs is depicted in Fig. 11.1a together with a magnified view of the NW tips shown in Fig. 11.1b. These images suggest that, while a very short segment of the NWs growing directly beneath the catalyzer droplet retains a cylindrical shape (cf. Fig. 11.1b), the growth perpendicular to the wire axis occurs primarily due to the direct impingement of gaseous atoms and is eventually responsible for the asymmetric, elliptical cross-section of the NWs. The wire shown in Fig. 11.1c in a top view, for example, exhibits an approximately elliptical cross-section with a short axis of 70 nm and a long axis of 150 nm.
To evaluate whether our epitaxial approach is suited for the fabrication of polarized single mode waveguides, we investigate the emission polarization properties of these free-standing elliptical wires in our μ-PL setup. Figure 11.1d shows the two emission profiles, $I_{\parallel}$ and $I_{\perp}$, obtained from a single NW when the linear polarization of its emission is analyzed parallel to the long axis of the elliptical cross-section (black curve) and perpendicular to it (blue curve). The observed large difference between the two curves indicates a strongly polarized NW emission. Most strikingly this effect is demonstrated by the angular polarization dependence of the NW emission, represented by the blue spheres in Fig. 11.1e. The angular intensity dependence is well described by a cosine-behavior. To quantify this polarization effect, we introduce the fraction of collected photons linearly polarized along the long axis of the ellipse: $I_{\parallel}/(I_{\parallel} + I_{\perp})$. For the NW emission in Fig. 11.1e, we find that about 85 % of the collected photons are linearly polarized along a direction parallel to the long axis. For comparison we have also plotted the result of the same experiment conducted on a regular NW with hexagonal cross-section (red squares). In this case, the emission shows no preferential direction of linear polarization.
The observed angular dependence of the polarized NW emission directly points towards the waveguide-effect reported by Munsch *et al.* [224]. While the exact waveguide geometry should be properly simulated for a quantitative analysis, the effect may be qualitatively understood from the following simplified picture: We consider an ensemble of randomly

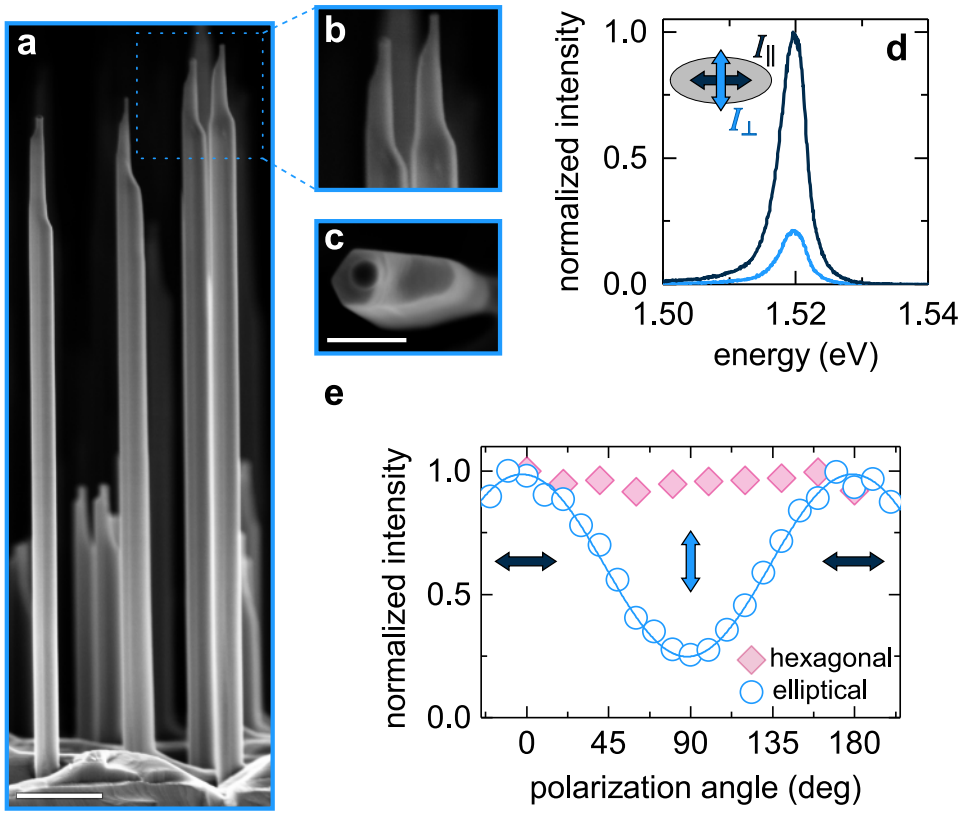

Figure 11.1: Epitaxy of NWs with elliptical cross-section for highly polarized photo-emission. (a) Micrograph showing several as-grown NWs viewed along the short axis of the elliptical cross section. (b) A magnified image of the section marked in (a) demonstrates the generally non-cylindrical shape of the wires, as well as a short cylindrical segment beneath the catalyst droplet at the tip. (c) Top-view of an elliptical NW with a short axis of $d_{\perp} = 70\,\text{nm}$ and a long axis of $d_{\parallel} = 150\,\text{nm}$. Scale bars in (a) and (c) indicate 500 nm and 100 nm. (d) Black and blue curves represent the components of the NW emission polarized parallel ($I_{\parallel}$) and perpendicular ($I_{\perp}$) to the long axis of the elliptical cross-section. The strong difference between the two curves illustrates the high degree of linear polarization emitted from the NW. Spatial directions are indicated in the inset. (e) Normalized emission peak intensity analyzed along different azimuthal directions of a NW with hexagonal (red squares) and elliptical (blue circles) cross-section. The emission of the elliptical wire is strongly polarized along the parallel direction, while the emission of the hexagonal wire is unpolarized.

oriented emitters homogeneously distributed in our NW waveguides (representing the photo-excited free excitons). Emitters polarized along the parallel direction can couple efficiently to a mode which is polarized in this direction. Regarded along this axis, the dimension $d_{\parallel} = 150\,\text{nm}$ of the waveguide is close to the NW diameter where a good coupling to the fundamental waveguide mode, as represented by the Purcell-enhancement at $d = 200\,\text{nm}$ in Fig. 10.3, occurs. Along the perpendicular direction, however, the dimension $d_{\perp} = 70\,\text{nm}$ falls into a regime characterized by a rather poor coupling of the emitters to the fundamental mode and the emission for emitters polarized in this direction is thus suppressed. Hence results the observed strong polarization dependence of the NW emission.
To exclude that the observed polarization dependence is related to an intrinsic polarization of the emitters (e.g., exciton states polarized by an asymmetric confinement potential), we also synthesized a control sample in which the GaAs core (including a 5nm-thin AlGaAs shell) was grown under rotation of the wafer and is thus radially symmetric. Only an additional AlGaAs layer deposited without rotating the wafer eventually forms the overall elliptical cross-section. In this control experiment, we find a comparably strong linearly polarized emission, confirming the dominant role of the NW cross-section shape and thus our waveguide interpretation.
The presented experiments demonstrate the suitability of utilizing molecular beam epitaxy for the fabrication of NW waveguides, which allow the emitters inside of the waveguide to couple efficiently to a single mode of the waveguide with an explicit linear polarization. By simply shaping the cross-section of the NW waveguides, and therefore the dielectric environment of the emitters inside the NWs, we can efficiently couple a large fraction of the total emission into a single mode with definite linear polarization. From this feature arises an important technological advantage for applications in quantum communication [224, 225]: Integrating single quantum emitters into such a waveguide facilitates the repeated directional emission of individual photons with the same linear polarization.

11.2 Spatially tunable spontaneous emission from mobile emitters

The strong dependence of the radiative exciton recombination on the direct environment of a small-diameter NW observed in Fig. 10.3 offers another interesting tuning knob: A local manipulation of the dielectric environment should allow us to tune the emission lifetime along the axis of a single wire.
As a proof of principle, we have fabricated a substrate hosting an array of SiO_2 stripes by electron beam lithography, as sketched in Fig. 11.2a. The gap between two neighboring stripes is $\sim 3\,\mu\text{m}$ and the individual stripes have a height of 450 nm and a width of 3.3 µm. For this experiment, we applied the Ga-assisted growth on Si(111) substrates to synthesize a new batch of GaAs/$Al_{0.36}Ga_{0.64}As$ NWs with predominantly zincblende crystal phase. While maintaining a small diameter of 110 nm, the higher growth temperatures allow

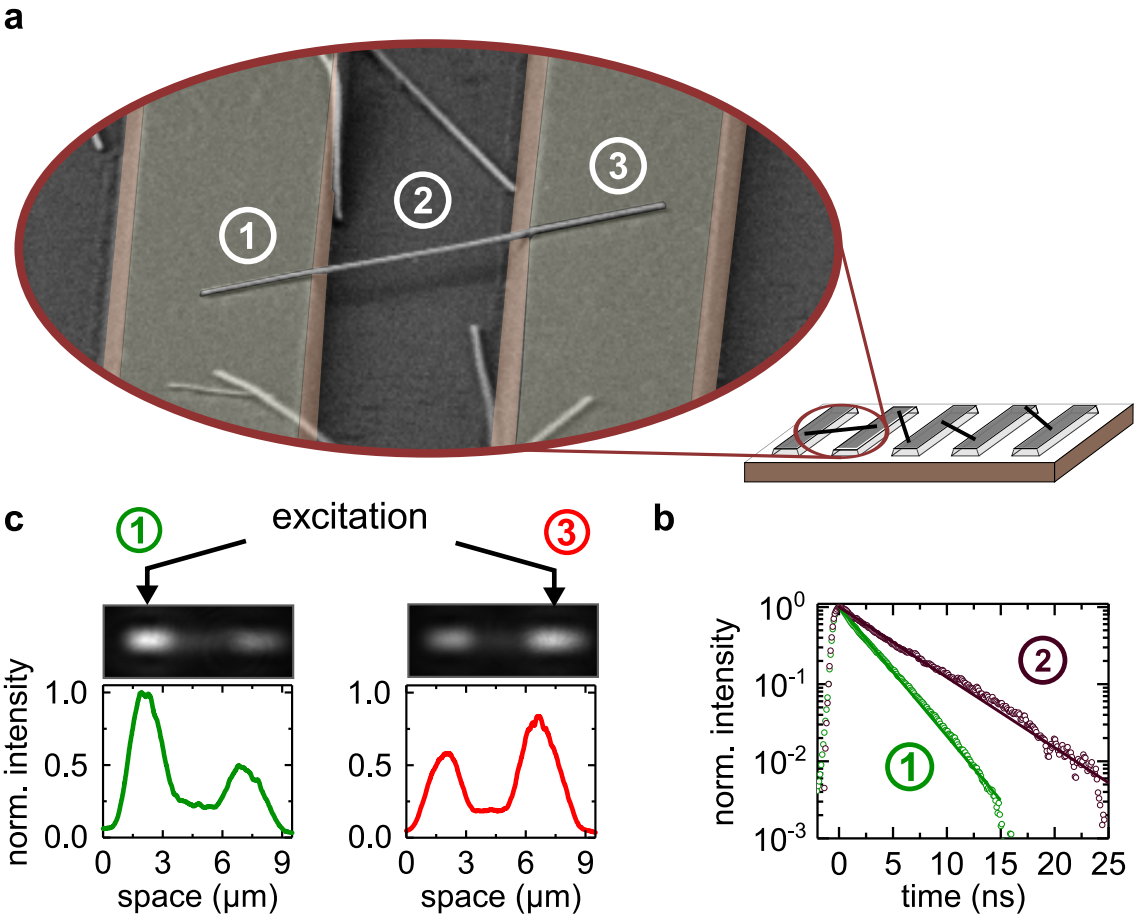

Figure 11.2: (a) Scanning electron micrograph of a NW supported on both ends by a SiO_2 stripe (highlighted by transparent yellow rectangles), while in between a 3 µm-long section of the wire is surrounded by vacuum. (b) The two luminescence decay curves, measured at the positions marked in (a), directly demonstrate the spatially modulated lifetimes. (c) Microscope images of the PL intensity and the corresponding intensity profiles extracted along the axis of the NW. Both profiles are normalized to the maximum intensity in the left panel and the encircled numbers in (a) mark the position of the laser excitation spot. For this experiment, the laser energy was 3.1 eV. Image sizes in (c) are $\sim (10 \times 4)\mu m^2$.

us to grow ~8 µm-long NWs, well suited for the µm-distances between the stripes. The colored scanning electron micrograph in Fig. 11.2a shows a NW suspended between two neighboring stripes with both ends (position ① and ③ in Fig. 11.2a). In between the stripes, however, the NW is surrounded by vacuum (position ②). The corresponding decay curves plotted in Fig. 11.2b unambiguously demonstrate that excitons measured in the vicinity of the SiO_2 stripe (①) show a shorter lifetime of 2.6 ns, while in the part of the NW which is surrounded by vacuum (②) the exciton recombination is more strongly inhibited and they decay with a longer lifetime of 4.8 ns. Probing the decay of the emission therefore confirms our concept of a spatially tunable luminescence lifetime.
This control over the emission lifetimes along a single NW also directly affects the local luminescence intensity along the NW axis. The microscope image in the left panel of Fig. 11.2c displays the spatial distribution of the luminescence upon continuously exciting excitons near the left end of the NW (①). Moving towards the right of the intensity maximum occurring at the excitation spot, the luminescence drops significantly where the NW is surrounded by vacuum (②). Then, a second maximum appears at the right end of the NW (③). Whereas carrier diffusion processes may cause a luminescence intensity that steadily decreases away from the excitation spot for a NW lying on a flat surface (cf. Fig. 12.2c and Ref. [214]), they cannot account for the second local maximum observed at the opposite NW end (③). The luminescence distribution along the NW is thus fully consistent with attributing the shorter lifetimes to an enhanced emission in the vicinity of the SiO_2 stripes. Note that the influence of any structural anisotropies is excluded since exciting the NW at the right end (③) spatially inverts the luminescence profile (see right panel in Fig. 11.2c). Our experiments evidence that the peculiar interaction of sub-wavelength NWs with light enables a locally controlled emission lifetime of excitons along the axis of a single wire.
Demonstrating the all-dielectric manipulation of spontaneous emission both of the examples presented in this section collate semiconductor NWs to a quickly developing branch of nanophotonics, in which sub-wavelength and Mie-resonant effects in dielectric nanoparticles are used to engineer light-matter interaction at the nanoscale [226]. Nanooptics in these all-dielectric nanoparticles is typically associated with low dissipative losses compared to their metallic-based plasmonic counterparts.

12

Metal-semiconductor hybrid devices: Deep sub-wavelength confinement of light

In the last section we have demonstrated the manipulation of spontaneous emission by tailoring the dielectric environment of the light-emitting excitons in our NWs, which allows the implementation of interesting and versatile technological concepts. Particularly for the concepts that rely on the efficient guiding of electromagnetic waves, the all-dielectric nature of our approaches described in the last section certainly entails the advantages of low signal loss at optical frequencies, as well as an easy integration with current semiconductor-based technologies, over lossy, metal-based plasmonic structures [226]. However, the inability of dielectric media to concentrate light into volumes smaller than those set by the diffraction limit restricts the near-field enhancement of electric fields and, in this sense, limits the modification of spontaneous emission. Despite this limitation, high-index dielectric nanostructures can still lead to sub-wavelength confinement of the optical modes [227], but only the local electric field enhancements near metallic surfaces can truly beat the diffraction limit of light [218, 228]. Utilizing these fields might open new ways to manipulate the spontaneous emission of the excitons in our NWs [33].
The diffraction limit of light plays a prominent role in the on-going miniaturization of nanoscale optics; confining electromagnetic waves in ultrasmall volumes is inevitable, for example, for the operation of nanoscale lasers. To meet this technological challenge, a hybrid plasmonic waveguide design was theoretically proposed by Oulton *et al.* in 2008 [229] and its operation was subsequently experimentally demonstrated by the same group in 2009 [9]. Their design relies on a hybrid optical mode developing in the thin dielectric layer sandwiched between a semiconductor NW (CdS, in their experiment), acting as the active component of the laser, and a metallic layer (here, Ag) hosting the surface plasmon polaritons (SPPs). Their experiment demonstrates the lasing operation of hybrid plasmonic waveguides beyond the diffraction limit set by the semiconductor NW. Most relevant for our studies, the authors report a Purcell-enhanced spontaneous emission of excitons resulting from an interaction with the SPPs in the underlying metallic layer, when the NW is optically excited below the lasing threshold. This interaction was

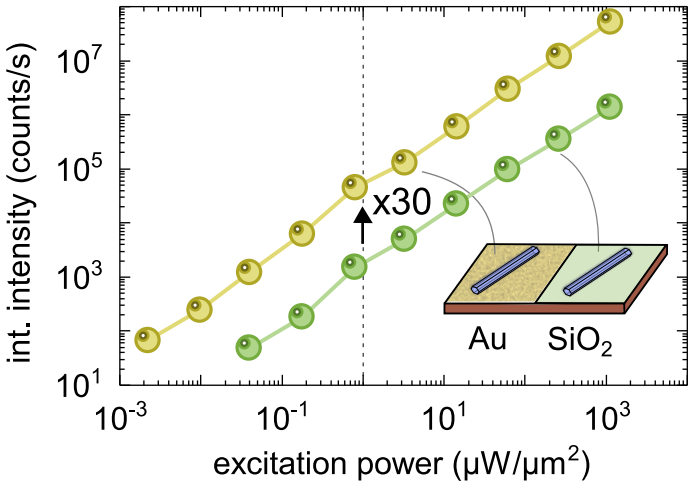

Figure 12.1: Integrated luminescence intensity recorded from a NW on top of a Au-covered substrate (yellow spheres) and a standard Si/SiO_2 substrate at nominally 4.2 K under continuous 1.58 eV laser excitation. The two sub-wavelength wires have a total diameter of 100 nm. Over a wide range of excitation powers, the integrated intensity is 30-fold enhanced for the wire lying on top of the Au-covered substrate. The dashed vertical line indicates a typical excitation power of 1 $\mu W/\mu m^2$ = 100 W/cm^2 used for luminescence experiments.

quantified by a sixfold increase of the emission rate in lifetime measurements.
To investigate the feasibility of such a coupling between the excitons in a semiconductor NW and the SPPs of a metallic layer for our NW system, we fabricate a substrate analogous to the one presented by Oulton *et al.* and conduct a comparative luminescence study. The substrate hosts a 100 nm-thin Au layer on top of an oxidized Silicon wafer (Si/SiO_2), which is capped by a nominally 1 nm-thin Al film. This film is expected to rapidly oxidize under ambient conditions, forming a dielectric layer of Al_2O_3 only a few nm thin. We disperse the wires from a single wafer onto both the Au-covered substrate and a standard Si/SiO_2 substrate serving as a reference. The dispersed core/shell NWs exhibit a total diameter of $d = 100$ nm, thus belonging to the regime where d is smaller than λ/n (see Chapter 10).
On each substrate, we record the low-temperature luminescence intensities of several individual NWs under continuous laser excitation in a wide range of excitation powers. The result of this comparative luminescence study is exemplarily represented by the integrated luminescence intensities of two single wires that are plotted in Fig. 12.1 as yellow (wire on Au) and green (wire on Si/SiO_2) spheres. This straightforward experiment shows a strong enhancement of the luminescence intensity recorded from a NW lying on top of the Au-covered substrate, as compared to the emission detected from a wire dispersed on the Si/SiO_2 reference substrate. Notably, the enhancement is preserved for excitation powers varying over six orders of magnitude. For the wire on the Au-covered

substrate, the average emission intensity increases by a factor of thirty; an observation clearly pointing towards the enhancement of the spontaneous emission process reported by Oulton *et al*.
However simple this experiment might seem at first glance, the possible interactions between the NW and the adjacent metallic layer are manifold, which complicates a straightforward interpretation of the results in terms of quantifying the enhanced spontaneous emission process. First of all, for the wires dispersed on the Au-covered substrate, a change in the rate at which excitons are excited is possible. Considering the near-resonant energy of our laser, 1.58 eV, as compared to the 1.52 eV-energy of the NW emission, it is even likely. Enhancing this excitation rate directly increases the total intensity of the continuously recorded NW emission. Secondly, the presence of a metallic layer in the vicinity of the NW affects the directionality of the emitted light compared to a NW lying on the dielectric reference substrate (consider a light source, uniformly emitting photons into all directions, placed in front of a mirror). This effect might simply scatter more of the emitted photons into a solid angle that is detected by our confocal microscopy setup and thus increase the recorded intensity. Interpreting the observed thirty-fold enhancement of the luminescence intensity as a thirty-fold increase in the spontaneous emission process is therefore not accurate.
To discriminate between these different effects, and to unambiguously demonstrate the feasibility of plasmonic coupling for the modification of spontaneous emission from the excitons in our NWs, we next investigate the effect of a much more localized interaction between a single NW and the SPPs of a metallic nanoantenna.

12.1 Strongly localized interaction with surface plasmon polaritons

In analogy to our previous experiments on single wires suspended between the SiO_2 stripes of a periodically patterned substrate, we also fabricated a substrate hosting periodic arrays of parallel, thin metallic lines on top of an oxidized Silicon wafer to investigate a potential exciton-SPP coupling. These lines made of Au were designed to cover widths ranging from 100 to 1000 nm at a height of 200 nm, with inter-line spacings varying between 2 and 10 µm. Onto this structured substrate, we randomly dispersed the wires from the same wafer that was used in our previous experiments (c.f. Section 11.2), i.e., these NWs are 8 µm long and have a sub-wavelength diameter d of 110 nm. The micrograph in Fig. 12.2a displays a section of the substrate containing two thin Au lines; they are both vertically oriented and each overlaid by a semitransparent yellow line for better illustration. As can be seen, two different single NWs are in direct contact with the Au line in the center of the image. The circular inset in Fig. 12.2 further depicts a magnified view of the upper NW crossing the 100 nm-thin Au line. The area of the actual physical overlap between the two is as small as $(55 \times 100)\,\mathrm{nm}^2$; with $d/2 = 55$ nm being the width of the NW sidewall facet in direct contact with the Au line. Assuming that the

field enhancement quickly decays away from this overlap region, any interaction between the excitons in the NW and the SPPs in the Au line would thus be strongly localized to this area. In fact, the actually interacting segment of the wire makes up only about a hundredths of its entire length; or else we might say that the interaction is localized on a scale about a factor of two smaller than the bulk wavelength of light inside the NW material: λ/n, where $\lambda = 815\,\text{nm}$ is the wavelength of the light in vacuum and $n = 3.45$ is the refractive index of GaAs [7].

To inquire about the potential coupling between a single NW and such thin Au lines, we investigated the luminescence dynamics of the second NW displayed in Fig. 12.2a. Given the fact that our confocal detection may also collect photons emitted from a longer (up to a few microns) segment of the NW in this time- and energy-resolved measurement, the length and positioning of this wire with respect to the Au line is particularly well suited: It allows us to measure the luminescence lifetimes of the wire at two well-separated locations without detecting any signal from the opposite NW end. First we measure at the crossing between wire and Au line (position ①) and then at the opposite end of the 8 µm-long wire (position ②).

First of all, at both positions the luminescence response shows a single exponential decay after pulsed laser excitation (see Fig. 12.2b). The decay at the crossing of the NW and the Au line, however, exhibits a lifetime of only 2.0 ns; short compared to the 3.4 ns-lifetime determined at the opposite end of the wire. This observation thus indicates an enhanced spontaneous emission of those excitons in the wire, which are coupling to the SPPs in the metal line. While a quenching of the luminescence process by non-radiative SPP decay channels in the metal could in principle also be responsible for the observed short lifetime [33], our spatially resolved luminescence experiments presented in the following suggest the opposite. Compared to the experiments of Fig. 12.2b, in which excitation and detection occurred at the same point in space, we now excite the NW locally at one end, but record the entire real-space distribution of its luminescence emission.

Let us however first discuss the emission from a NW that was, by coincidence, placed on the substrate without any contact to the metal lines. Because the wire is hence lying plainly on a dielectric substrate, we can hereafter use its luminescence profile as a reference for the coupled wire. The luminescence profile is plotted as a gray line in the bottom panel of Fig. 12.2c and labeled accordingly. Locally excited at one end, this reference NW nicely shows the diffusion-caused, continuous decrease of the luminescence signal as the distance to the excitation point increases. After a distance of about 5 µm the intensity drops to $1/e$ of its maximum value occurring at the excitation point.

Now, we turn towards the wire shown in the lower part of Fig. 12.2a, which crosses the Au line. We continuously excite this wire at position ② and record its spatial luminescence distribution (see the upper panel in Fig. 12.2c). Surprisingly, despite being located approximately 8 µm away from the excitation spot, we find the brightest part of the NW emission at the crossing with the Au line. As demonstrated by the corresponding intensity profile (green line in Fig. 12.2c) and in analogy to the reference wire, the luminescence intensity initially decreases as the distance to the excitation spot grows. Yet, at the crossing with the Au line, the observed intensity brightens tremendously. With respect

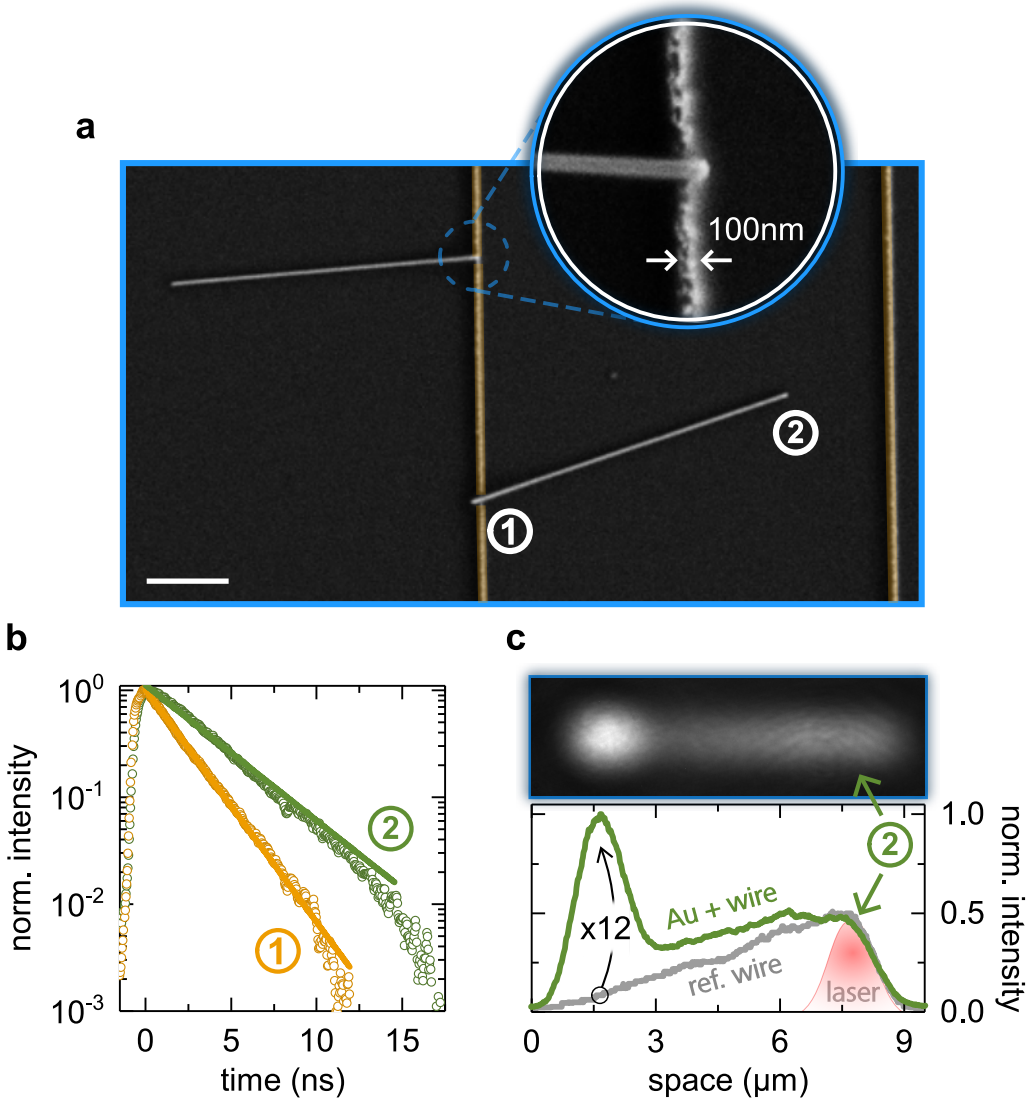

Figure 12.2: (a) Micrograph of two wires dispersed on a patterned substrate hosting periodic arrays of thin Au lines. Scale bar is 2 µm. The inset shows a magnified view of the upper NW crossing the only 100 nm-thin Au line. (b) Luminescence decay traces measured from the NW shown in the lower part of the micrograph. In this experiment the NW was excited and the emission subsequently detected at the same position (indicated in (a)). (c) Upper panel: Real-space distribution of the luminescence intensity emitted from the lower wire in (a). Image size is $\sim (10 \times 3)\mu m^2$. The wire is locally excited away from the thin Au line at position ②. Lower panel: Spatial luminescence profiles from the lower wire in (a) (green line), and a reference wire (image not shown, gray line) lying on the plain substrate. The red bell curve indicates the segment of the NW which is excited by the laser. Note that the laser energy for this experiment was 3.1 eV.

to the reference wire, the emission of our coupled wire at the crossing is enhanced by a factor of 12. Since we solely excite the wire in a small uncoupled segment on top of the Si/SiO_2 substrate, we can now exclude the obscuring effects of a simultaneously enhanced excitation rate, in contrast to our experiments presented in the last section. Furthermore, as far as far-field scattering effects are concerned, even a complete back reflection of the emitted light by the 100 nm-thin Au line would only cause an increase in the spatial luminescence intensity by a factor of 2 and can thus not explain the 12× enhanced luminescence intensity. All the experiments of Fig. 12.2 thus add up to an interpretation fully in line with an enhanced and strongly localized spontaneous emission of excitons in the vicinity of the Au line. Recalling that the width of the Au line is only 100 nm, we note that the emission peak in Fig. 12.2c merely appears to be broadened (half-width of 1.5 µm) due to our detection in the far-field. In fact, although only a short segment making up about 1 % of the entire NW length is in actual physical contact with the Au line, about 40 % of the total integrated emission originates from this short segment.

Before we conclude this section, we would like to comment on the lifetimes determined in Fig. 12.2b. In other examples, a decrease in the lifetimes of single localized emitters in the vicinity of a metallic structure could be translated into a Purcell-factor (or *radiative enhancement factor*, as suggested in Ref. [33]), quantifying the emission enhancement [217, 230]. However, before associating the luminescence lifetime measured at the crossing between the NW and the Au line (position ①) with a Purcell-enhanced radiative lifetime, we should keep in mind that the excitons in our NWs are free and unbound particles. In this regard, the excitons in the uncoupled region of the wire represent a reservoir of mobile particles; they can be transported in real-space to dynamically reoccupy the states in the vicinity of the Au line which are efficiently drained by the locally enhanced recombination. This process will ultimately slow down the decay of the luminescence observed in our experiment and consequently increase the recorded luminescence lifetime. Only the modified lifetimes of single quantum emitters embedded in the NWs (e.g., an axially integrated quantum dot [222]) could truly avoid this effect and reveal the Purcell-factor. On top of that comes the fact, that our far-field detection collects the light at least from a diffraction-limited area corresponding roughly to the size of the spherical inset in Fig. 12.2a. Even if we center this detection area around the crossing of the wire and the Au line, we will additionally collect a part of the emission resulting from a non-coupled segment of the NW. Eventually both of these effects merely inhibit a direct determination of the Purcell-factor, but they do not interfere with our interpretation of enhanced spontaneous emission.

We also note that we have further investigated the emission lifetime and intensity enhancement of wires coupled to Au lines with widths above 100 nm, up to 1 µm. However, neither the observed lifetime, nor the local intensity enhancement show a significant dependence on the Au line width.

To summarize our results so far, we investigated the coupling of excitons in our wires to the SPPs of metallic structures. While the most straightforward approach to this problem–dispersing the wires on a metallic surface and directly comparing their emission

properties to wires placed onto dielectric surfaces–already indicates a strong enhancement of spontaneous emission in our wires, the interpretation is hampered by a variety of non-distinguishable interactions between the NWs and the metal film. We thus fabricated a substrate hosting periodic arrays of thin Au lines on top of a dielectric surface. The experiments conducted on these new samples evidence the coupling of excitons in the NW to the SPPs in the metal, simultaneously producing both indicators for an enhancement of the spontaneous emission process: Shorter lifetimes in the interaction region are accompanied by a strong local increase in the luminescence intensity. Furthermore, we show that the enhancement also occurs when the interaction is extremely localized on a deep sub-wavelength scale of 100 nm. Due to the strong intensity enhancement observed in Fig. 12.2c, we suppose that even much narrower Au lines (well within reach of current electron beam lithography fabrication) would produce a detectable signal, opening the door to a variety of plasmonic resonance effects, which can occur for Au nanoparticles with dimensions below 100 nm.

12.2 Potential of hybrid devices: Diffusion-based light manipulation

The observed interaction of excitons with the SPPs in thin metallic lines entails a number of possible configurations to study the interplay between a dense local gas of excitons, its diffusion-driven expansion through 1D space, and a spatially controlled radiative recombination. Regarding the questions about the coherence of photo-excited electrons in our wires, which were addressed in a previous discussion about the Dyakonov-Perel spin relaxation mechanism (see Sections 8.2 and 9.2), studying the diffusion-driven transport of excitons in an optical experiment might represent an exclusive method to learn about internal parameters, like the transport coherence length, in our NWs. Especially since the standard methods for such an investigation are based on quantum charge transport and thus difficult to implement with undoped semiconductors. In this section, we first present the main diffusion-related effects as they appear in our experiment when a single wire couples to multiple interaction sites and then, in the last part, we elaborate on the aspects of exciton transport.

With lengths of 8 µm, the wires from the wafer used for our previous experiments (Sections 11.2 and 12.1) allow us to spatially resolve and thus separate the luminescence signals from the different interaction sites in our confocal setup.

We will now discuss a variety of phenomena observed from a single wire that was dispersed across four different 1 µm-thin Au lines with a center-to-center distance of 2 µm. For the excitons in the NW, this configuration results in four individual, spatially well-separated interaction sites. As the micrograph in the center of Fig. 12.3 shows, our NW is suspended over all four of the Au lines (labeled ①-④). Continuous excitation of the wire at position ① results in four distinct local maxima in the spatial luminescence distribution, as shown in Fig. 12.3a, each located at the position of an underlying Au line.

Notably, in contrast to the wire coupling to a single interaction site, which was excited at an uncoupled segment (cf. Section 11.1 and Fig. 12.2), we now observe the total maximum of the emission intensity at the point where we excite the wire, since in this example the photo-excited excitons couple directly to the underlying Au line; here they experience the locally enhanced spontaneous emission resulting in the observed intensity maximum. At the same time, however, not all of the photo-excited excitons recombine at this interaction site, they also seem to diffuse away from the interaction region on comparably fast time scales, since we observe a sequence of three more intensity maxima along the wire axis, steadily decreasing in intensity as the distance to the excitation point increases. At interaction site ④, 6 µm away from the excitation spot, the emission intensity has dropped to about 20 % of its maximum intensity, as shown by the luminescence profile in Fig. 12.3a.
To investigate the nature of the exciton diffusion process in our wires, we conduct an experiment in which the wire is locally excited at position ① with short laser pulses, and its emission is subsequently resolved in both time and space domains (see Section 3.1.2). Figure 12.3b shows the resulting streak camera image, displaying the spatial coordinate along the x-axis (parallel to the wire axis) and the temporal evolution of the luminescence along the y-axis. As expected, in this image we can identify four distinct positions along the x-axis at which the luminescence decays as a function of time. Most interestingly, the intensity maxima occurring at ②, ③ and ④ are each delayed with respect to the previous one. This shift of consecutive maxima towards later times is in line with the progressive diffusion of a locally excited exciton gas, dynamically occupying the entire wire volume after the local excitation. If we assume an evenly enhanced spontaneous emission at each interaction site, the observed time delay of the luminescence provides further information on the time scales of the diffusion process. In addition to the diffusion of excitons, the streak camera image in Fig. 12.3b nicely visualizes how the luminescence intensity of our NW can be modulated in both space and time.
To expose the time-space correlation of the diffusing excitons, we integrate the time evolution of the NW emission in a spatially narrow region centered around each interaction site. Hence we obtain the four different time traces plotted in Fig. 12.3c. As already noted, consecutive interaction sites show intensity maxima shifting to later times. Surprisingly, the time difference Δt between two consecutive intensity maxima increases with increasing distance to the excitation spot, as indicated by the increasing time intervals marked on the bottom axis in Fig. 12.3c. From $\Delta t = 0.2$ ns, to 0.4 ns and 0.7 ns, the time delay increases between the sites, suggesting a slow-down of the exciton diffusion process as the distance to the excitation point increases. With a center-to-center distance of 2 µm between two neighboring Au lines, the observed time differences translate into exciton velocities ranging from 1–10 µm/ns (or 10^3–10^4 m/s). This time- and space-resolved experiment could in principle determine the exciton diffusion constant; yet, recent analogous luminescence experiments on the diffusion of excitons in quasi-2D layers of GaAs have unveiled a number of effects, which hamper the direct determination of an exciton diffusion constant from our data shown in Fig. 12.3 [231–233]. Amongst those effects is, for example, a local heating of the exciton gas under non-resonant laser

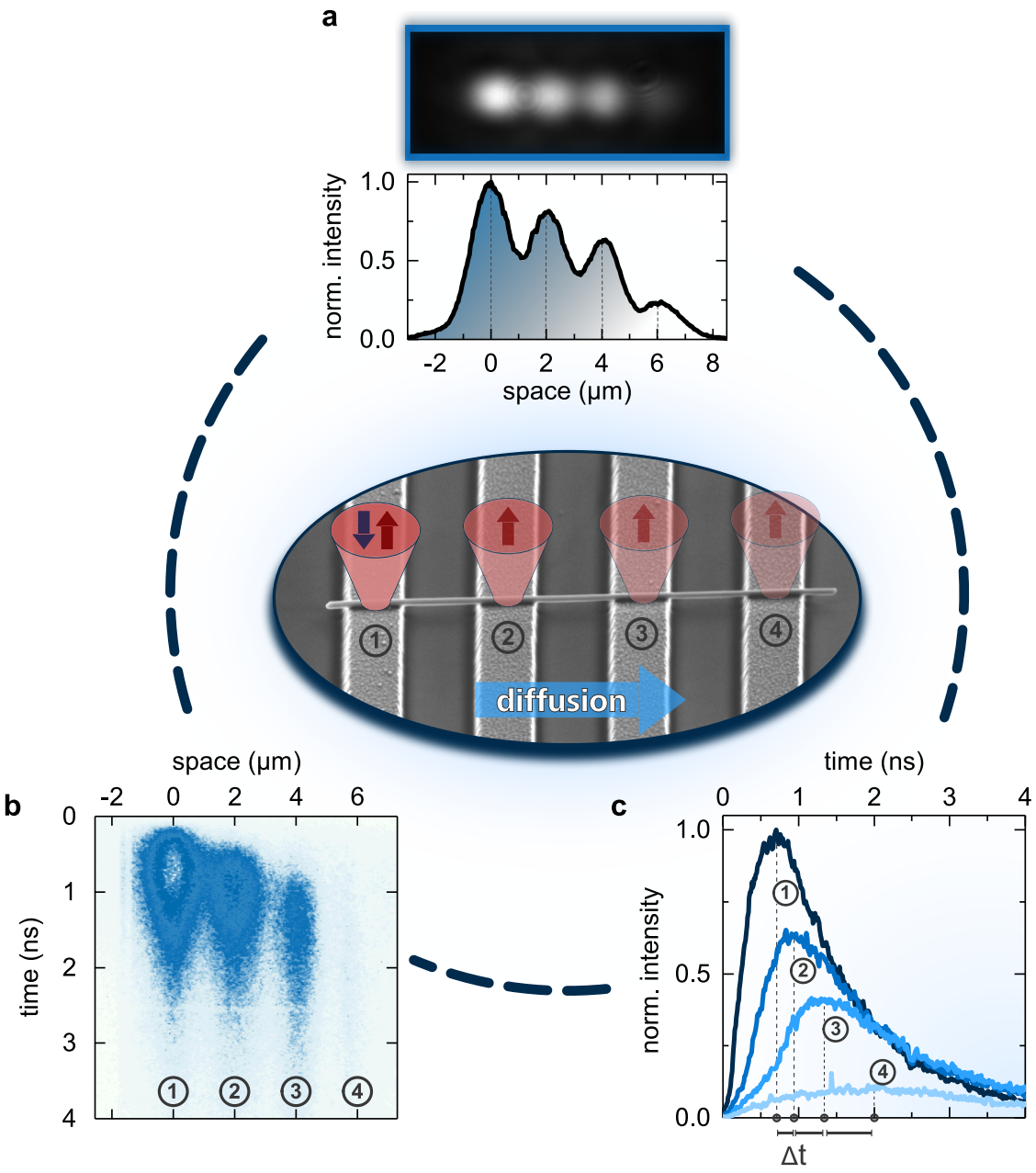

Figure 12.3: Multi-site interaction of excitons in a single NW with the SPPs in different Au lines. Center: Micrograph of a ~8 μm-long wire fully crossing all four individual 1 μm-thin Au lines. (a) Spatial luminescence distribution and the corresponding emission profile of the same wire under continuous local excitation at position ①. The four interaction sites strongly modulate the NW emission in space. (b) Streak camera image displaying the space and time modulated NW emission after pulsed excitation with 3.1 eV at position ①. (c) Maxima of consecutive decay traces, obtained at the different interaction sites, shift towards later times, reflecting the exciton diffusion process. Image size in (a) is $\sim (11 \times 5)\mu m^2$.

excitation, possibly also occurring in our experiment. In Ref. [231] the authors finally conclude that only strictly resonant excitation conditions allow for a reliable determination of the intrinsic exciton diffusion constant. Such an approach is currently realized in a collaborative research effort together with the group of Dr. Alexey Chernikov.
As a final comment we would like to mention an interesting perspective for the exciton transport in the ultrathin wires of the 1D quantum limit. The above shown detection scheme could be applied to monitor the dynamics of a locally excited carrier density (e.g., excitons, or an e-h plasma), as it expands through 1D space–a measurement configuration with the potential to observe fundamentally interesting 1D phenomena, like the many-body localized state [234] or the Tomonaga-Luttinger liquid behavior [235].

13

Summary: Nanowire photonics

Without question, the key finding of the experiments presented in this part of the thesis is the understanding that the free excitons in semiconductor NWs must radiate their energy into the particular set of electromagnetic modes dictated by the sub-wavelength waveguide properties of the wires. Clearly evidencing a variety of nanophotonic effects, our diameter-dependent lifetime studies on free-standing wires reveal both, the Purcell-enhanced minimum in the luminescence lifetime ($d \sim \lambda/n$), as well as the drastic increase of the lifetime ($d < \lambda/n$) predicted by our numerical simulations of the relevant waveguide mode. For small diameters, our experiments on wires dispersed on dielectric substrates further reveal a remarkable sensitivity of the emission lifetime on the dielectric environment of a single wire.

In Chapter 11, this insight into the spontaneous emission process of free excitons allows us to demonstrate in two explicit examples the all-dielectric manipulation of spontaneous emission in NWs: first, we showed in Section 11.1 that the molecular beam epitaxy of NWs is exceptionally suited to fabricate wires with elliptical cross-section, realizing a single mode waveguide emitting photons with definite linear polarization. Second, controlling the dielectric environment of individual NWs enabled us to tune the spontaneous emission of free and mobile excitons along the axis of a single wire (see Section 11.2).

Extending the realm of external control beyond this all-dielectric approach, in Chapter 12 we addressed the potential of hybrid plasmonic-excitonic devices for the tuning of spontaneous emission in NWs. While the emission enhancement from wires dispersed on a flat metallic surface already indicates a strong enhancement of spontaneous emission, the experimental results cannot be unambiguously interpreted. In a next step, we then demonstrated that even a strongly localized interaction between the excitons in a NW and the SPPs in a 100 nm-thin Au line renders large emission enhancements, indicating the tight confinement of light in these hybrid structures to ultrasmall volumes. Indeed, we demonstrate the interaction between this NW and the Au line to be remarkably strong (over 40 % of the total emission originates from the strongly localized interaction region),

stirring future research into interesting directions: Current electron beam lithography techniques allow for a scaling of the interaction region to much smaller length scales. Au line-widths beyond 30 nm at an inter-line spacing of 50 nm are readily accessible and should enable the fabrication of a dense periodic array of localized interaction sites along the axis of a single wire.
Studying a wire subject to multiple interaction sites illustrates the potential of metal-NW hybrid devices for a diffusion-driven manipulation of light emission in space and time. In this context, our experiments presented in Section 12.2 might in principle reveal the exciton diffusion process. However, to investigate the intrinsic diffusion a more sophisticated experiment must involve the strictly resonant excitation of excitons, complicating the above shown measurements.

14

Final conclusion and outlook

In this thesis, we investigate various aspects of direct-gap semiconductor nanowires (NWs) using single wire photoluminescence spectroscopy. Our newly developed approach to synthesize phase-pure GaAs NWs, size-tunable in an unreported diameter-range, forces their previously hidden one-dimensional (1D) quantum nature to emerge in our optical experiments. With such a 1D model system readily to hand, optical spin orientation becomes a suitable means to study the dynamics of electron spins in these NWs. We evidence the optical spin injection into single wires and investigate their spin dynamics. Particularly our experiments in the 1D wire regime complete the previous studies on the suppression of spin relaxation in narrow semiconductor channels and thus accomplish a long-standing goal of the community.
In a second major focus, our thesis addresses several different nanoscale photonic effects. Unexpected, and with impressive diversity, these effects surfaced in our luminescence experiments performed on single wires and unveiled the fascinating sub-wavelength waveguiding nature inherent to our NWs. They shift our perspective towards the realm of nanophotonics, where near-field optical effects and quantum electrodynamics determine the rules of the game. Indeed, the newly gathered insight allows us to directly implement and demonstrate innovative photonic concepts in our NWs.

At the very beginning of this thesis stands the molecular beam epitaxy of a semiconductor NW system, which suits the needs of our luminescence-based approach. The strategy to synthesize direct-gap GaAs NWs with widely tunable diameters, while maintaining a phase-pure wurtzite crystal structure, meets all the requirements in a single series of NW wafers. Furthermore, including the fabrication of ultrathin GaAs NWs, strictly distinguishes our approach in all these points from others reported in literature. Most importantly, our approach allows us to experimentally track any characteristic emission feature as we tune the NW diameter. Since we found a way to synthesize the NWs with a very low areal density in the as-grown ensemble, even free-standing wires can now

be addressed individually in our photoluminescence spectroscopy. In prior experiments, single wire spectroscopy was mostly limited to the study of NWs lying horizontally on a substrate. Regarding the results presented in Parts III and IV, this free-standing configuration turned out to be a key advantage of our approach.
Tuning the diameter from 490 to 20 nm unveiled the characteristic emission signatures, which evidence the role of spatial quantum confinement in our ultrathin wires. In fact, their quantized subband dispersion assigns these wires to the 1D quantum regime, in which only the lowest 1D subband is occupied by the photo-excited electrons. An estimate of the confinement effects further enabled us to quantify a strong enhancement of the exciton binding energy in the thinnest NWs. An important feature, as our analysis in Chapter 9 has shown.

Under circularly polarized excitation, electrons absorb the angular momentum of photons– a concept which is often used for spin orientation in direct-gap semiconductors. For the first time now we applied this concept to optically inject spins into single, free-standing semiconductor NWs and demonstrated its success. Observing a magnetic field-induced characteristic, the Hanle effect, as well as the dynamic depolarization of the spins, thus paved the way for a detailed experimental investigation of spin phenomena in NWs. Our subsequently performed experiments unveiled a rather peculiar behavior of electron spins and, in this way, already foretold the encounter of miscellaneous spin physics in NWs.
Making an effort to understand the unusual spin dynamics observed in our time-resolved luminescence studies, we intensively evaluated the different spin relaxation mechanisms in question. Eliminating possible candidates one by one lead us to an analysis of the exchange-driven spin relaxation process in our NWs. Unexpected at the beginning, it showed that the exchange coupling between photo-excited electrons and holes dominates the spin relaxation in the entire range of NW diameters investigated in our sample series. Fully in line with this conclusion, the exchange-based relaxation mechanism was so strongly affected by the increasing spatial confinement in our NWs, that we witnessed a pronounced weakening of the spin relaxation. This finally culminated in the observation of ultralong spin lifetimes, $\tau_s = 200$ ns, in our thinnest 1D wires. Remarkably, our analysis implies that the electrons in all of our wires are in the radially ballistic regime.
We emphasize that such ultralong spin lifetimes can only occur in our 1D wires because the Dyakonov-Perel mechanism, which is otherwise known to be highly efficient in most semiconductor structures, is completely suppressed in the 1D quantum regime of III-V NWs. We note also that the spin relaxation time limited by electron-hole exchange in our experiment is a consequence of the optical excitation, suggesting even longer spin relaxation times for pure 1D electron systems in NWs.
To assess the technological potential of our findings, it is worth mentioning that in III-V semiconductor structures, electron spin relaxation times of $\tau_s \geq 100$ ns have so far only been observed for localized, 0D electrons [176–179]. The hyperfine interaction, which limits the spin coherence in these 0D systems, is not relevant in 1D. More importantly, the electrons in our NWs are free to move along the 1D channel, making these wires ideal

systems for the transport of coherent spin information, e.g., to interconnect spintronic devices on chip or allow coherent spin manipulation.

In another focus, this thesis addresses the nanophotonic effects, which quite prominently occurred in our luminescence experiments. Without question, the key finding was the understanding that the free excitons in semiconductor NWs must radiate their energy into the particular set of electromagnetic modes dictated by the sub-wavelength waveguide properties of the wires. With exciton dynamics fully dominated by this waveguide-effect, our perspective shifts away from the previously discussed non-radiative chemical effects [197–203] towards the realm of spontaneous emission in nanophotonic structures, in which near-field optical effects and quantum electrodynamics determine the rules of the game.
In our experiment, the diameter-dependence of the free exciton recombination dynamics clearly evidences both, the Purcell-enhanced minimum in the luminescence lifetime, as well as the drastic increase of the lifetime predicted by numerical simulations of the relevant waveguide mode. Distinctively pronounced for small diameters, understanding the waveguide nature allowed us to perceive and promptly demonstrate the local manipulation of the exciton emission dynamics along the axis of a single NW.
From a nanophotonic point of view, our subsequent experiments on the strongly localized photonic interactions between mobile excitons in NWs and the surface-plasmon-polaritons in thin metallic lines, share interesting perspectives for future directions [225, 236]: In general, the commercial success of semiconductor devices is related to the fact that their charge distributions are easily shaped and controlled by external electrostatic gates. Hence, if it were possible to use the thin metallic lines shown in Chapter 12 to affect the excitons not only via the plasmonic near-field interactions already demonstrated in our experiments, but at the same time also through gate-defined electrostatic fields, the obtained virtue would be undeniable. We believe that such an endeavor can indeed be fruitful.

Reviewing the particular spin and nanophotonic properties of our NWs, it would certainly be interesting to explore whether these physics have any aspects in common. According to the recent literature, such common ground may indeed exist. In 2014, Petersen *et al.* demonstrated the so-called 'spin-orbit coupling of light' in nanophotonic waveguides [237], which relies on the very unusual transverse spin angular momentum emerging in confined light fields [238]. In their straightforward experiment, circularly polarized light is directed onto a single gold nanoparticle situated off-axis on top of a waveguide. Without precedence in any prior experiment, adjusting the handedness of the incoming light controlled the propagation direction of the light scattered into the waveguide. Because of its undeniable potential for information transfer, Petersen's seminal work has launched a plethora of novel investigations addressing these 'impossible properties of light' [239–244]. Far beyond the polarization-controlled flow of information, the underlying physics were also demonstrated to have real mechanical impact, for example on floating colloidal particles, pushing them sideways on the surface of water; all controlled by the polarization of a focused light beam [241].

In September 2018, Diego Abujetas and Dr. José Sánchez-Gil reported that this extraordinary transverse spin angular momentum of light not only interacts with off-axis emitters, like in Petersen's experiment. In fact, they predicted that a complex distribution of the orbital and spin momenta exists inside a waveguide within the fundamental HE_{11}-mode– the mode which we experimentally demonstrated in Chapter 10 to dominate the optical properties of our NWs. At this particular point, the NW spin physics and the nanophotonic effects investigated in this thesis may have aspects in common. We imagine the peculiar transverse spin of the HE_{11}-mode to possibly play a role, for example, in the optical spin injection process. Investigating this effect could open unforeseen possibilities for the interplay between excitons, their spins and a polarization-controlled, directional photon emission.

Appendix

A

Spin physics in nanowires

A.1 Spin-orbit coupling in bulk wurtzite crystals

The general conduction band spin splitting in binary bulk wurtzite (WZ) semiconductors arises from two contributions, one being linear in the electron's wave vector k while the other one is proportional to the cube k^3. The cubic k^3-dependent term (called Dresselhaus effect) also describes the spin splitting in semiconductors with zincblende structure and is a consequence of the bulk inversion asymmetry (BIA) of the crystal lattice. The k-linear term (called Rashba effect) occurs in the WZ structure due to the hexagonal $\hat{c}$-axis and reflects an intrinsic wurtzite structure inversion asymmetry (WSIA). The relevant SOC Hamiltonian $H_{\mathrm{SO}}^{\mathrm{bulk}}$ with both BIA and WSIA contribution reads as follows [56, 129, 130, 132, 148–154]:

$$H_{\mathrm{SO}}^{\mathrm{bulk}} = H_{\mathrm{SO}}^{\mathrm{BIA}} + H_{\mathrm{SO}}^{\mathrm{WSIA}} = \boldsymbol{\Omega}_{\mathbf{k}}^{\mathrm{bulk}} \cdot \boldsymbol{\sigma}, \tag{A.1}$$

with

$$\boldsymbol{\Omega}_{\mathbf{k}}^{\mathrm{bulk}} = \left[\gamma_{\mathrm{e}}\left(bk_z^2 - k_\perp^2\right) + \alpha_{\mathrm{e}}\right]\begin{pmatrix} k_y \\ -k_x \\ 0 \end{pmatrix} = \beta\begin{pmatrix} k_y \\ -k_x \\ 0 \end{pmatrix}, \tag{A.2}$$

where $z\|[0001]$ ($\hat{c}$-axis), $x\|[11\bar{2}0]$, $y\|[1\bar{1}00]$, $k_\perp^2 = k_x^2 + k_y^2$, and $\boldsymbol{\sigma}$ is the vector of the Pauli spin matrices σ_i, $i = x, y, z$. The Dresselhaus coefficient γ_{e}, together with the material parameter b, determines the cubic BIA contribution, while the Rashba coefficient α_{e} gives the strength of the k-linear WSIA contribution. The coefficient $\beta = \left[\gamma_{\mathrm{e}}\left(bk_z^2 - k_\perp^2\right) + \alpha_{\mathrm{e}}\right]$ is then an effective SOC parameter describing the total magnitude of the SO field in bulk WZ.

A.2 Evaluation of interface-induced SOC for all nanowire sidewall facets

The investigated WZ GaAs nanowires (NWs) exhibit a hexagonal cross section with six equivalent GaAs/AlGaAs core/shell interfaces ($n = 0, 1, 2, \ldots, 5$), which, according to transmission electron microscopy, are oriented along the $\langle 11\bar{2}0 \rangle$-directions of the WZ unit cell (cf. Fig. 7.1). As outlined in Chapter 8, the interface-induced SO field, $\mathbf{\Omega}_{\mathbf{k}}^{\mathrm{int},n}$, resulting from the particular heterointerface n, has the form

$$\mathbf{\Omega}_{\mathbf{k}}^{\mathrm{int},n} = \begin{pmatrix} \alpha_\perp k_z \sin(n\pi/3) \\ -\alpha_\perp k_z \cos(n\pi/3) \\ \alpha_\parallel \left[k_y \cos(n\pi/3) - k_x \sin(n\pi/3) \right] \end{pmatrix}, \tag{A.3}$$

where the effective SOC parameters $\alpha_\parallel$ and $\alpha_\perp$ determine the strength of the interfacial contribution parallel and perpendicular to the WZ $\hat{c}$-axis, respectively. Here we note again that, due to the low symmetry $\{11\bar{2}0\}$ NW sidewall facets of the C_s point group, $\alpha_\parallel$ and $\alpha_\perp$ are linearly independent [167, 168], while the size of the bulk contribution is given by the single parameter β.

In the absence of external magnetic fields, the dynamics of an electron spin density $\mathbf{S}(t)$, provided that the spin lifetime is longer than the carrier thermalization time, is given by the equation of motion $\dot{S}_i(t) = -\sum_j \Gamma_{ij} S_j(t)$, where Γ_{ij} are components of the spin relaxation rate tensor $\mathbf{\Gamma}$, and $S_{i,j}$ are the average spin components in direction $i, j = x, y, z$. The form of the tensor $\mathbf{\Gamma}$ depends on the spin relaxation mechanism and the symmetry of the system. In a simplified form of the DP spin relaxation theory, Γ_{ij} are determined by the effective magnetic field $\mathbf{\Omega}_\mathbf{k}$ via [51–53, 55, 122]

$$\Gamma_{ij} \sim \left(\delta_{ij} \langle \mathbf{\Omega}_\mathbf{k}^2 \rangle - \langle \Omega_{\mathbf{k},i} \Omega_{\mathbf{k},j} \rangle \right) \tau_\mathrm{p}^* , \tag{A.4}$$

where τ_p^* is the momentum relaxation time for an individual electron, δ_{ij} is the Kronecker delta symbol, the angle brackets denote averaging over the momentum distribution of electrons, and

$$\langle \mathbf{\Omega}_\mathbf{k}^2 \rangle = \sum_i \langle \Omega_{\mathbf{k},i}^2 \rangle . \tag{A.5}$$

Under the assumption that the electron phase coherence length is smaller than the NW diameter, the respective mean square effective magnetic fields with both bulk and interface contributions add to

$$\langle \Omega_{\mathbf{k},i} \Omega_{\mathbf{k},j} \rangle = \langle \Omega_{\mathbf{k},i}^{\mathrm{bulk}} \Omega_{\mathbf{k},j}^{\mathrm{bulk}} \rangle + \frac{1}{6} \sum_{n=0}^{5} \langle \Omega_{\mathbf{k},i}^{\mathrm{int},n} \Omega_{\mathbf{k},j}^{\mathrm{int},n} \rangle . \tag{A.6}$$

Evaluating Eq. (A.4) using Eqs. (A.2), (A.3), (A.5) and (A.6) by averaging over an isotropic angular distribution of $\mathbf{k}$ shows that $\mathbf{\Gamma}$ is a diagonal tensor with nonzero components Γ_{xx},

Γ_{yy}, and Γ_{zz}, where

$$\Gamma_{xx} = \Gamma_{yy} = \left(\frac{1}{2} + \frac{\alpha_{\parallel}^2}{2\beta^2 + \alpha_{\perp}^2}\right)\Gamma_{zz}\,. \tag{A.7}$$

DP spin relaxation in WZ GaAs NWs is therefore anisotropic with respect to the NW axis, which corresponds to the WZ $\hat{c}$-axis, while spin relaxation in the plane perpendicular to the NW axis is isotropic.
In the experiments, the spin component S_z along the $\hat{c}$-axis is detected. In the absence of an external magnetic field ($B_{\text{ext}} = 0$), the exponential decay of S_z corresponds to the zero-field spin lifetime $\tau_s^0 = 1/\Gamma_{zz}$. Applying $\mathbf{B}_{\text{ext}}$ now leads to Larmor precession of the electron spins and an advanced spin dynamics with

$$S_z(t) \propto \mathrm{e}^{-(\Gamma_{yy}+\Gamma_{zz})t/2}\cos\left(\omega_{\text{L}}t\right)\,, \tag{A.8}$$

where $\mathbf{B}_{\text{ext}} \parallel x$. The measured spin lifetime τ_s^B reflects in this case the spin polarization decay with the average decay rate $\Gamma_{\text{eff}} = \left(\Gamma_{yy} + \Gamma_{zz}\right)/2 = 1/\tau_s^B$. Because of Eq. (A.7) an averaged relaxation rate $\Gamma_{\text{eff}} = \left(\frac{3}{4} + \frac{\alpha_{\parallel}^2}{4\beta^2+2\alpha_{\perp}^2}\right)\Gamma_{zz}$ is obtained due to anisotropic DP spin relaxation. Hence the relative relationship between the strengths of the SOC contributions parallel ($\alpha_{\parallel}$) and perpendicular (β and $\alpha_{\perp}$) to the NW axis can be described by

$$\frac{\alpha_{\parallel}^2}{2\beta^2 + \alpha_{\perp}^2} = 2\frac{\tau_s^0}{\tau_s^B} - \frac{3}{2}\,. \tag{A.9}$$

Accordingly, for the experimental values of $\tau_s^0 \approx 1.48\,\text{ns}$ ($B_{\text{ext}} = 0$) and $\tau_s^B \approx 0.52\,\text{ns}$ ($B_{\text{ext}} > 50\,\text{mT}$), respectively, the relative strengths of the varying SOC coefficients are determined via

$$\frac{\alpha_{\parallel}^2}{2\beta^2 + \alpha_{\perp}^2} \approx 4\,, \tag{A.10}$$

which implies that the interface-induced z-contribution to the effective SO field $\mathbf{\Omega_k}$ is significantly larger than the x–y-contributions from both bulk ($\alpha_{\parallel} > \beta$) and the interfaces ($\alpha_{\parallel} > \alpha_{\perp}$).

A.3 Hole spin relaxation in wurtzite GaAs

In their early work, Bir, Aronov and Pikus (BAP) recognized that the exchange interaction between electrons and holes can lead to efficient relaxation of the electron spin in optical orientation experiments [66, 67]. To cause electron spin relaxation this mechanism requires hole spin relaxation times that are short on the time scale of electron spin relaxation. Thus, in order to evaluate the importance of BAP spin relaxation for our NWs, we will first discuss whether this requirement is fulfilled for the WZ phase of GaAs.

Due to the strong mixing of orbital and spin degrees of freedom in the valence band of bulk ZB GaAs, the hole spin relaxation time is typically very short, $\tau_s^{\mathrm{ZB}} \approx 110\,\mathrm{fs}$ [182], and thus often referred to as *quasi-instantaneous*. The basic requirement for the BAP mechanism of electron spin relaxation is therefore always fulfilled. However, in a bulk WZ crystal, this argumentation is not straightforward, since the symmetry of the WZ lattice strongly modifies the mixing of the valence bands. In order to estimate the spin relaxation time of photo-excited holes in our WZ GaAs NWs, we first analyze the composition of the heavy hole (HH) bands and then further investigate the effects of spatial quantum confinement on their composition.

For bulk WZ GaAs we use the 6-band $\mathbf{k}\cdot\mathbf{p}$ model and the parameter set presented in Ref. [27]. We neglect the contribution of the parameter A_7, which is responsible for the spin splittings in the energy bands. The Hamiltonian is ordered by the bulk Bloch functions, in which the states 1 and 4 can be unambiguously identified as HH, while the other basis states (2, 3, 5 and 6) are mixed and give rise to the light hole (LH) and the crystal field split-off hole (CH). More details on the WZ bulk basis set can be found in Refs. [245, 246]. For bulk ZB GaAs, we use the conventional Luttinger-Kohn Hamiltonian and parameters set presented in Ref. [247].

In Fig. A.1a-b, we summarize the HH composition for the bulk case by comparing ZB and WZ GaAs. For ZB, the HH composition is nearly constant at a value of 0.5 in the considered energy range. While the HH composition in WZ is also nearly constant, it is instead very close to 1 and only a zoom-in at the HH composition reveals a non-zero contribution from other states (see inset in Fig. A.1b). By calculating the density of states and integrating in energy, we estimate the bulk Fermi energy for holes with a 3D carrier concentration of $n_{3\mathrm{D}} = 8\times10^{16}\mathrm{cm}^{-3}$ to be $\sim 3\,\mathrm{meV}$. At this energy, the HH composition is ~ 0.9996.

Let us now turn to the HH composition including the quantum confinement in the NWs. To numerically calculate the HH composition in the WZ NWs, we first introduced quantum confinement on the $\mathbf{k}\cdot\mathbf{p}$ description, recognizing that the motion on the xy-plane is now quantized, by making the substitution $k_x \rightarrow -i\frac{\partial}{\partial_x}$ and $k_y \rightarrow -i\frac{\partial}{\partial_y}$, i.e., the in plane momenta are now operators instead of quantum numbers. The total wavefunction is expanded using the envelope function approximation [248], leading to a set of coupled differential equations that need to be solved with suitable numerical methods. We considered cylindrical NWs and used two distinct numerical approaches to solve the 6-band confined Hamiltonian: i) the plane wave expansion (PWE) [172] of the envelope functions, i.e., using plane wave basis; ii) the finite differences method (FDM) to the reduced one-dimensional radial description which arises when considering cylindrical coordinates to describe the xy-derivatives [192, 249]. To achieve numerical convergence, for the PWE approach we have used 20 plane waves, leading to 81×81 grid points in the xy-plane while in the FDM method we used 401 radial points.

In Fig. A.1c, we show the composition of HH states in the highest subbands for cylindrical WZ NWs with diameters of 30 nm and 60 nm using the PWE and FDM approaches. For the 30 nm NWs, using the 1D Fermi wave vector of $k_F \approx 0.015\,\mathrm{\AA}^{-1}$, we can identify

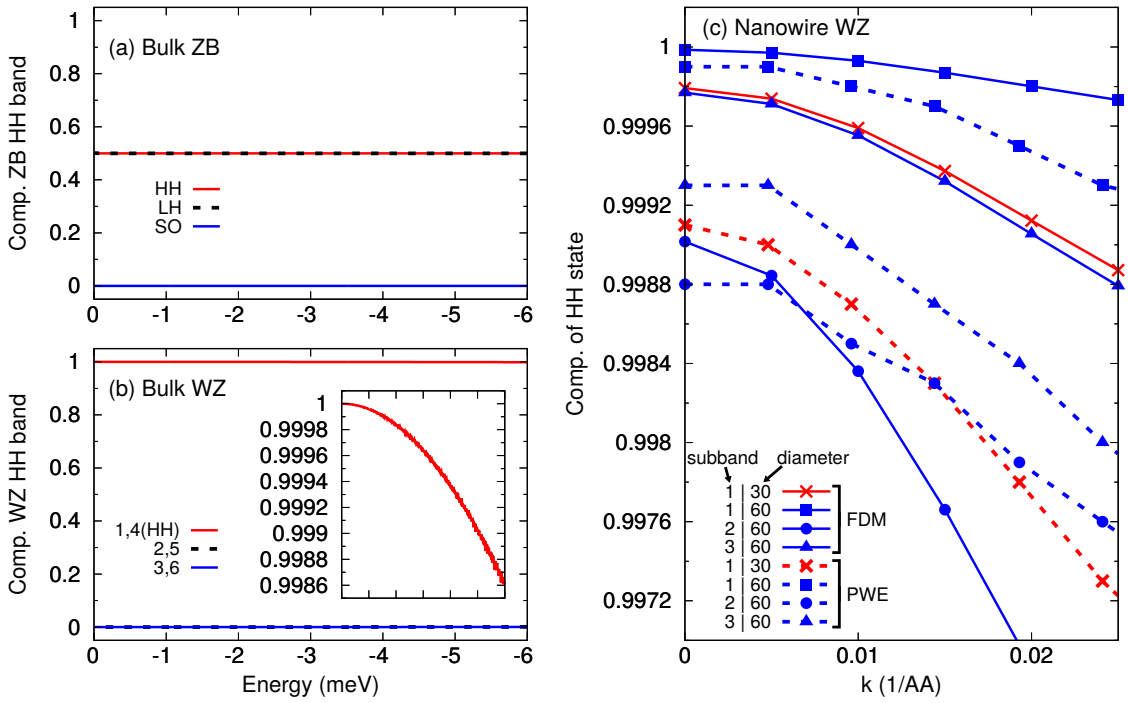

Figure A.1: Composition of the bulk HH band for (a) ZB and (b) WZ GaAs as function of energy, measured from the top of the valence band. The inset in (b) shows a zoom-in at the y-axis of the HH composition, the x-axis remains unchanged. (c) Composition of the HH state for selected subbands of NWs with a diameter of 30 nm and 60 nm. The different numerical techniques are shown with solid lines for the FDM and with dashed lines for the PWE. Courtesy of Paulo E. Faria Junior.

the HH composition to be ~0.9994 for the FDM approach and ~ 0.9984 for the PWE approach. For the 60 nm NWs, as can be seen in Fig. A.1c, the HH composition is comparable to the 30 nm NWs.
Our calculations suggest that the HH composition for the highest subbands does not significantly depend on the diameter and therefore lies in the narrow range from 0.9984 to 0.9996 for all our WZ GaAs NWs. Since spin relaxation of the holes is driven by the Elliott-Yafet mechanism and the relaxation time is thus inversely proportional to the composition of the HH wave function [55, 250], we can estimate the hole spin relaxation time in WZ GaAs by comparison to the HH composition and hole spin relaxation time in ZB GaAs: $\tau_s^{\mathrm{WZ}} = (1-x_{\mathrm{ZB}})/(1-x_{\mathrm{WZ}})\ \tau_s^{\mathrm{ZB}} \approx 30$–$140$ ps, where $x_{\mathrm{WZ}} = 0.9984$ to 0.9996 and $x_{\mathrm{ZB}} = 0.5$ are the compositions of the HH states in WZ and ZB GaAs and $\tau_s^{\mathrm{ZB}} \approx 110$ fs [182]. We thus conclude that, although substantially longer than in ZB GaAs, the hole spin relaxation time in WZ GaAs is nevertheless short compared to the experimentally observed time scale of electron spin relaxation ($\tau_s = 0.4 - 200$ ns). Similar observations, i.e., short hole spin relaxation times in a WZ semiconductor, were also reported for experiments on bulk GaN [183, 184]. The basic requirement for exchange-driven electron spin relaxation in WZ GaAs NWs through the BAP mechanism is thus fulfilled.

Bibliography

[1] J. D. Martin, *When condensed-matter physics became king*, Physics Today **72**, 30–37 (2019).

[2] A. de Touzalin, C. Marcus, F. Heijman, I. Cirac, R. Murray, & T. Calarco, *Quantum Manifesto*, A call upon the European Union to launch a flagship-scale initiative in Quantum Technology., 2016.

[3] T. Durakiewicz, & L. Greene, *Commentary: Enabling a quantum leap*, Physics Today **71**, 10–11 (2018).

[4] V. Mourik, K. Zuo, S. M. Frolov, S. R. Plissard, E. P. A. M. Bakkers, & L. P. Kouwenhoven, *Signatures of Majorana Fermions in Hybrid Superconductor–Semiconductor Nanowire Devices*, Science **336**, 1003–1007 (2012).

[5] P. Krogstrup, N. Ziino, W. Chang, S. Albrecht, M. Madsen, E. Johnson, J. Nygård, C. Marcus, & T. Jespersen, *Epitaxy of semiconductor–superconductor nanowires*, Nature materials **14**, 400 (2015).

[6] S. M. Albrecht, A. P. Higginbotham, M. Madsen, F. Kuemmeth, T. S. Jespersen, J. Nygård, P. Krogstrup, & C. M. Marcus, *Exponential protection of zero modes in Majorana islands*, Nature **531**, (2016).

[7] J. Bleuse, J. Claudon, M. Creasey, N. S. Malik, J.-M. Gérard, I. Maksymov, J.-P. Hugonin, & P. Lalanne, *Inhibition, Enhancement, and Control of Spontaneous Emission in Photonic Nanowires*, Phys. Rev. Lett. **106**, 103601 (2011).

[8] A. V. Akimov, A. Mukherjee, C. L. Yu, D. E. Chang, A. S. Zibrov, P. R. Hemmer, H. Park, & M. D. Lukin, *Generation of single optical plasmons in metallic nanowires coupled to quantum dots*, Nature **450**, 402 (2007).

[9] R. F. Oulton, V. J. Sorger, T. Zentgraf, R.-M. Ma, C. Gladden, L. Dai, G. Bartal, & X. Zhang, *Plasmon lasers at deep subwavelength scale*, Nature **461**, 629 (2009).

[10] E. Garnett, & P. Yang, *Light Trapping in Silicon Nanowire Solar Cells*, Nano Lett. **10**, 1082–1087 (2010).

[11] F. Patolsky, & C. M. Lieber, *Nanowire nanosensors*, Materials Today **8**, 20–28 (2005).

[12] H. Zhang, et al., *Ballistic superconductivity in semiconductor nanowires*, Nat. Commun. **8**, 16025 (2017).

[13] Bournel, A., Dollfus, P., Bruno, P., & Hesto, P., *Gate-induced spin precession in an In0.53Ga0.47As two dimensional electron gas*, Eur. Phys. J. AP **4**, 1–4 (1998).

[14] A. G. Mal'shukov, & K. A. Chao, *Waveguide diffusion modes and slowdown of D'yakonov-Perel' spin relaxation in narrow two-dimensional semiconductor channels*, Phys. Rev. B **61**, R2413–R2416 (2000).

[15] A. A. Kiselev, & K. W. Kim, *Progressive suppression of spin relaxation in two-dimensional channels of finite width*, Phys. Rev. B **61**, 13115–13120 (2000).

[16] T. P. Pareek, & P. Bruno, *Spin coherence in a two-dimensional electron gas with Rashba spin-orbit interaction*, Phys. Rev. B **65**, 241305 (2002).

[17] S. Adachi, *GaAs and related materials: bulk semiconducting and superlattice properties* (World Scientific, 1994).

[18] K. A. Dick, P. Caroff, J. Bolinsson, M. E. Messing, J. Johansson, K. Deppert, L. R. Wallenberg, & L. Samuelson, *Control of III–V nanowire crystal structure by growth parameter tuning*, Semicond. Sci. Technol. **25**, 024009 (2010).

[19] M. I. McMahon, & R. J. Nelmes, *Observation of a Wurtzite Form of Gallium Arsenide*, Phys. Rev. Lett. **95**, 215505 (2005).

[20] A. De, & C. E. Pryor, *Predicted band structures of III–V semiconductors in the wurtzite phase*, Phys. Rev. B **81**, 155210 (2010).

[21] N. Vainorius, S. Lehmann, A. Gustafsson, L. Samuelson, K. A. Dick, & M.-E. Pistol, *Wurtzite GaAs Quantum Wires: One-Dimensional Subband Formation*, Nano Lett. **16**, 2774–2780 (2016).

[22] B. Ketterer, M. Heiss, M. J. Livrozet, A. Rudolph, E. Reiger, & A. Fontcuberta i Morral, *Determination of the band gap and the split-off band in wurtzite GaAs using Raman and photoluminescence excitation spectroscopy*, Phys. Rev. B **83**, 125307 (2011).

[23] B. Ketterer, M. Heiss, E. Uccelli, J. Arbiol, & A. Fontcuberta i Morral, *Untangling the Electronic Band Structure of Wurtzite GaAs Nanowires by Resonant Raman Spectroscopy*, ACS Nano **5**, 7585–7592 (2011).

[24] L. Ahtapodov, J. Todorovic, P. Olk, T. Mjåland, P. Slåttnes, D. L. Dheeraj, A. T. J. van Helvoort, B.-O. Fimland, & H. Weman, *A Story Told by a Single Nanowire: Optical Properties of Wurtzite GaAs*, Nano Lett. **12**, 6090–6095 (2012).

[25] P. Kusch, S. Breuer, M. Ramsteiner, L. Geelhaar, H. Riechert, & S. Reich, *Band gap of wurtzite GaAs: A resonant Raman study*, Phys. Rev. B **86**, 075317 (2012).

[26] F. Bechstedt, & A. Belabbes, *Structure, energetics, and electronic states of III–V compound polytypes*, J. Phys. Condens. Matter **25**, 273201 (2013).

[27] T. Cheiwchanchamnangij, & W. R. L. Lambrecht, *Band structure parameters of wurtzite and zinc-blende GaAs under strain in the GW approximation*, Phys. Rev. B **84**, 035203 (2011).

[28] M. Fox, *Quantum Optics: An Introduction*, Oxford Master Series in Physics (OUP Oxford, 2006).

[29] P. Milonni, *Why spontaneous emission?*, American Journal of Physics **52**, 340–343 (1984).

[30] P. A. M. Dirac, & N. H. D. Bohr, *The quantum theory of the emission and absorption of radiation*, Proceedings of the Royal Society of London. Series A, Containing Papers of a Mathematical and Physical Character **114**, 243–265 (1927).

[31] T. A. Welton, *Some Observable Effects of the Quantum-Mechanical Fluctuations of the Electromagnetic Field*, Phys. Rev. **74**, 1157–1167 (1948).

[32] V. Weisskopf, *Probleme der neueren Quantentheorie des Elektrons*, Naturwissenschaften **23**, 631–637 (1935).

[33] M. Pelton, *Modified spontaneous emission in nanophotonic structures*, Nature Photonics **9**, 427 (2015).

[34] E. M. Purcell, H. C. Torrey, & R. V. Pound, *Resonance Absorption by Nuclear Magnetic Moments in a Solid*, Phys. Rev. **69**, 37–38 (1946).

[35] R. G. Hulet, E. S. Hilfer, & D. Kleppner, *Inhibited Spontaneous Emission by a Rydberg Atom*, Phys. Rev. Lett. **55**, 2137–2140 (1985).

[36] E. Yablonovitch, *Inhibited Spontaneous Emission in Solid-State Physics and Electronics*, Phys. Rev. Lett. **58**, 2059–2062 (1987).

[37] H. Chew, *Radiation and lifetimes of atoms inside dielectric particles*, Phys. Rev. A **38**, 3410–3416 (1988).

[38] K. K. Pukhov, T. T. Basiev, & Y. V. Orlovskii, *Spontaneous emission in dielectric nanoparticles*, JETP letters **88**, 12 (2008).

[39] H. Schniepp, & V. Sandoghdar, *Spontaneous Emission of Europium Ions Embedded in Dielectric Nanospheres*, Phys. Rev. Lett. **89**, 257403 (2002).

[40] I. Pelant, & J. Valenta, *Luminescence Spectroscopy of Semiconductors* (OUP Oxford, 2012).

[41] L. V. Keldysh, *The electron-hole liquid in semiconductors*, Contemporary Physics **27**, 395–428 (1986).

[42] A. Thilagam, *Effect of geometrical shape in the cross section of quantum wires on exciton binding energy*, J. Appl. Phys. **82**, 5753–5757 (1997).

[43] L. Keldysh, *Excitons and polaritons in semiconductor/insulator quantum wells and superlattices*, Superlattices and Microstructures **4**, 637–642 (1988).

[44] L. C. Andreani, F. Tassone, & F. Bassani, *Radiative lifetime of free excitons in quantum wells*, Solid state communications **77**, 641–645 (1991).

[45] W. van der Poel, L. Molenkamp, C. Foxon, et al., *Giant oscillator strength of free excitons in GaAs*, Phys. Rev. B **35**, 8281 (1987).

[46] E. Gross, S. A. Permogorov, & B. Razbirin, *Annihilation of excitons and exciton-phonon interaction*, Soviet Physics Uspekhi **14**, 104 (1971).

[47] J. Hopfield, *Theory of the contribution of excitons to the complex dielectric constant of crystals*, Physical Review **112**, 1555 (1958).

[48] O. Hildebrand, E. O. Goebel, K. M. Romanek, H. Weber, & G. Mahler, *Electron-hole plasma in direct-gap semiconductors with low polar coupling: GaAs, InP, and GaSb*, Phys. Rev. B **17**, 4775–4787 (1978).

[49] M. Yoshita, Y. Hayamizu, H. Akiyama, L. N. Pfeiffer, & K. W. West, *Exciton-plasma crossover with electron-hole density in T-shaped quantum wires studied by the photoluminescence spectrograph method*, Phys. Rev. B **74**, 165332 (2006).

[50] J. Feldmann, G. Peter, E. Göbel, P. Dawson, K. Moore, C. Foxon, & R. Elliott, *Linewidth dependence of radiative exciton lifetimes in quantum wells*, Phys. Rev. Lett. **59**, 2337 (1987).

[51] F. Meier, & B. P. Zakharchenya, eds., *Optical orientation*, Vol. 8, Modern problems in condensed matter sciences (North-Holland, Amsterdam, 1984).

[52] I. Žutić, J. Fabian, & S. Das Sarma, *Spintronics: Fundamentals and applications*, Rev. Mod. Phys. **76**, 323–410 (2004).

[53] M. I. Dyakonov, ed., *Spin Physics in Semiconductors*, Vol. 157, Springer Series in Solid-State Sciences (Springer, Berlin Heidelberg, 2008).

[54] J. L. Birman, *Some Selection Rules for Band–Band Transitions in Wurtzite Structure*, Phys. Rev. **114**, 1490–1492 (1959).

[55] J. Fabian, A. Matos-Abiague, C. Ertler, P. Stano, & I. Žutić, *Semiconductor Spintronics*, Acta Phys. Slovaca **57**, 565–907 (2007).

[56] G. Dresselhaus, *Spin–Orbit Coupling Effects in Zinc Blende Structures*, Phys. Rev. **100**, 580–586 (1955).

[57] E. I. Rashba, & V. I. Sheka, *Symmetry of energy bands in crystals of wurtzite type: II. Symmetry of bands including spin-orbit interaction*, Fiz. Tverd. Tela **2**, 62–76 (1959).

[58] M. Gmitra, & J. Fabian, *First-principles studies of orbital and spin-orbit properties of GaAs, GaSb, InAs, and InSb zinc-blende and wurtzite semiconductors*, Phys. Rev. B **94**, 165202 (2016).

[59] A. Manchon, H. C. Koo, J. Nitta, S. M. Frolov, & R. A. Duine, *New perspectives for Rashba spin–orbit coupling*, Nat. Mater. **14**, 871–882 (2015).

[60] M. Wu, J. Jiang, & M. Weng, *Spin dynamics in semiconductors*, Physics Reports **493**, 61–236 (2010).

[61] R. J. Elliott, *Theory of the Effect of Spin-Orbit Coupling on Magnetic Resonance in Some Semiconductors*, Phys. Rev. **96**, 266–279 (1954).

[62] Y. Yafet, *G factors and spin-lattice relaxation of conduction electrons*, Solid State Physics **14**, edited by F. Seitz, & D. Turnbull, 1–98 (1963).

[63] J. H. Jiang, & M. W. Wu, *Electron-spin relaxation in bulk III-V semiconductors from a fully microscopic kinetic spin Bloch equation approach*, Phys. Rev. B **79**, 125206 (2009).

[64] M. I. Dyakonov, & V. I. Perel, *Spin Orientation of Electrons Associated with the Interband Absorption of Light in Semiconductors*, Sov. Phys. JETP **33**, 1053–1059 (1971).

[65] J.-W. Luo, G. Bester, & A. Zunger, *Long- and short-range electron–hole exchange interaction in different types of quantum dots*, New Journal of Physics **11**, 123024 (2009).

[66] G. L. Bir, A. G. Aronov, & G. E. Pikus, *Spin relaxation of electrons due to scattering by holes*, Zh. Eksp. Teor. Fiz. **69**, 1382–1397 (1975).

[67] A. Aronov, G. Pikus, & A. Titkov, *Spin relaxation of conduction electrons in p-type Ill-V compounds*, JETP **57**, 680 (1983).

[68] J. Wagner, H. Schneider, D. Richards, A. Fischer, & K. Ploog, *Observation of extremely long electron-spin-relaxation times in p-type δ-doped GaAs/AlGaAs double heterostructures*, Phys. Rev. B **47**, 4786–4789 (1993).

[69] A. Bayer, *Optische Spektroskopie an freistehenden GaAs-Nanodrähten*, Diploma Thesis (2013).

[70] M. D. Sturge, *Optical Absorption of Gallium Arsenide between 0.6 and 2.75 eV*, Phys. Rev. **127**, 768–773 (1962).

[71] S. Das Sarma, & D. W. Wang, *Many-Body Renormalization of Semiconductor Quantum Wire Excitons: Absorption, Gain, Binding, and Unbinding*, Phys. Rev. Lett. **84**, 2010–2013 (2000).

[72] R. J. Seymour, & R. R. Alfano, *Time-resolved measurement of the electron-spin relaxation kinetics in GaAs*, Appl. Phys. Lett. **37**, 231–233 (1980).

[73] F. Dirnberger, *Spin Dynamics in Wurtzite GaAs Nanowires*, Master thesis (Universität Regensburg, 2015).

[74] J. Hubmann, et al., *Epitaxial Growth of Room-Temperature Ferromagnetic MnAs Segments on GaAs Nanowires via Sequential Crystallization*, Nano Lett. **16**, 900–905 (2016).

[75] E. Givargizov, *Fundamental aspects of vls growth*, Journal of Crystal Growth **31**, 20–30 (1975).

[76] K. Dick Thelander, *A review of nanowire growth promoted by alloys and non-alloying elements with emphasis on Au-assisted III-V nanowires*, eng, Progress in Crystal Growth and Characterization of Materials **54**, 138–173 (2008).

[77] R. S. Wagner, & W. C. Ellis, *Vapor-Liquid-Solid Mechanism of Single Crystal Growth*, Appl. Phys. Lett. **4**, 89–90 (1964).

[78] M. F. Millea, & D. F. Kyser, *Thermal Decomposition of Gallium Arsenide*, Journal of Applied Physics **36**, 308–313 (1965).

[79] F. Glas, J.-C. Harmand, & G. Patriarche, *Why Does Wurtzite Form in Nanowires of III–V Zinc Blende Semiconductors?*, Phys. Rev. Lett. **99**, 146101 (2007).

[80] P. Caroff, K. A. Dick, J. Johansson, M. E. Messing, K. Deppert, & L. Samuelson, *Controlled polytypic and twin-plane superlattices in III–V nanowires*, Nat. Nanotechnol. **4**, 50–55 (2009).

[81] J. Wallentin, M. Ek, L. R. Wallenberg, L. Samuelson, K. Deppert, & M. T. Borgström, *Changes in contact angle of seed particle correlated with increased zincblende formation in doped InP nanowires*, Nano Lett. **10**, 4807–4812 (2010).

[82] S. Lehmann, J. Wallentin, D. Jacobsson, K. Deppert, & K. A. Dick, *A general approach for sharp crystal phase switching in InAs, GaAs, InP, and GaP nanowires using only group V flow*, Nano Lett. **13**, 4099–4105 (2013).

[83] E. Husanu, D. Ercolani, M. Gemmi, & L. Sorba, *Growth of defect-free GaP nanowires*, Nanotechnology **25**, 205601 (2014).

[84] R. Leitsmann, & F. Bechstedt, *Surface influence on stability and structure of hexagon-shaped III-V semiconductor nanorods*, Journal of Applied Physics **102**, 063528 (2007).

[85] T. Akiyama, K. Sano, K. Nakamura, & T. Ito, *An empirical potential approach to wurtzite–zinc-blende polytypism in group III–V semiconductor nanowires*, Japanese journal of applied physics **45**, L275 (2006).

[86] D. Jacobsson, F. Panciera, J. Tersoff, M. C. Reuter, S. Lehmann, S. Hofmann, K. A. Dick, & F. M. Ross, *Interface dynamics and crystal phase switching in GaAs nanowires*, Nature **531**, 317 (2016).

[87] A. Rudolph, *MBE growth of GaAs nanowires and nanowire heterostructures*, PhD thesis (Universität Regensburg, 2012).

[88] S. Furthmeier, F. Dirnberger, J. Hubmann, B. Bauer, T. Korn, C. Schüller, J. Zweck, E. Reiger, & D. Bougeard, *Long exciton lifetimes in stacking-fault-free wurtzite GaAs nanowires*, Appl. Phys. Lett. **105**, 222109 (2014).

[89] E. K. Mårtensson, A. M. Whiticar, M. de la Mata, R. R. Zamani, J. Johansson, J. Nygård, K. A. Dick, & J. Bolinsson, *Understanding GaAs Nanowire Growth in the Ag–Au Seed Materials System*, Crystal Growth & Design **18**, 6702–6712 (2018).

[90] V. G. Dubrovskii, N. V. Sibirev, Y. Berdnikov, U. P. Gomes, D. Ercolani, V. Zannier, & L. Sorba, *Length distributions of Au-catalyzed and In-catalyzed InAs nanowires*, Nanotechnology **27**, 375602 (2016).

[91] U. P. Gomes, D. Ercolani, V. Zannier, F. Beltram, & L. Sorba, *Controlling the diameter distribution and density of InAs nanowires grown by Au-assisted methods*, Semiconductor Science and Technology **30**, 115012 (2015).

[92] K. Govatsi, A. Chrissanthopoulos, V. Dracopoulos, & S. N. Yannopoulos, *The influence of Au film thickness and annealing conditions on the VLS-assisted growth of ZnO nanostructures*, Nanotechnology **25**, 215601 (2014).

[93] V. Zannier, V. Grillo, & S. Rubini, *Diameter-dependent morphology of vapour-solid-solid grown ZnSe nanowires*, Journal of Physics D: Applied Physics **47**, 394005 (2014).

[94] D. Saxena, S. Mokkapati, P. Parkinson, N. Jiang, Q. Gao, H. H. Tan, & C. Jagadish, *Optically pumped room-temperature GaAs nanowire lasers*, Nature Photonics **7**, 963 (2013).

[95] B. Mayer, et al., *Lasing from individual GaAs-AlGaAs core-shell nanowires up to room temperature*, Nature Communications **4**, 2931 (2013).

[96] D. Jacobsson, F. Yang, K. Hillerich, F. Lenrick, S. Lehmann, D. Kriegner, J. Stangl, L. R. Wallenberg, K. A. Dick, & J. Johansson, *Phase transformation in radially merged wurtzite GaAs nanowires*, Crystal growth & design **15**, 4795–4803 (2015).

[97] B. Loitsch, et al., *Tunable Quantum Confinement in Ultrathin, Optically Active Semiconductor Nanowires Via Reverse-Reaction Growth*, Advanced Materials **27**, 2195–2202 (2015).

[98] M. Forsch, *Interface-induced Spin-Orbit Coupling in GaAs Core-Shell Nanowires*, Master thesis (Universität Regensburg, 2016).

[99] W. Kim, V. G. Dubrovskii, J. Vukajlovic-Plestina, G. Tütüncüoglu, L. Francaviglia, L. Güniat, H. Potts, M. Friedl, J.-B. Leran, & A. Fontcuberta i Morral, *Bistability of Contact Angle and Its Role in Achieving Quantum-Thin Self-Assisted GaAs nanowires*, Nano Lett. **18**, 49–57 (2018).

[100] N. Han, F. Wang, J. J. Hou, S. Yip, H. Lin, M. Fang, F. Xiu, X. Shi, T. Hung, & J. C. Ho, *Manipulated Growth of GaAs Nanowires: Controllable Crystal Quality and Growth Orientations via a Supersaturation-Controlled Engineering Process*, Crystal Growth & Design **12**, 6243–6249 (2012).

[101] J. Davies, *The Physics of Low-dimensional Semiconductors: An Introduction* (Cambridge University Press, 1998).

[102] V. L. Keldysh, *Excitons in Semiconductor-Dielectric Nanostructures*, physica status solidi (a) **164**, 3–12 (1997).

[103] D. J. Reilly, G. R. Facer, A. S. Dzurak, B. Kane, R. Clark, P. Stiles, A. Hamilton, J. L. O'Brien, N. E. Lumpkin, L. N. Pfeiffer, et al., *Many-body spin-related phenomena in ultra low-disorder quantum wires*, Physical Review B **63**, 121311 (2001).

[104] A. W. Holleitner, V. Sih, R. C. Myers, A. C. Gossard, & D. D. Awschalom, *Suppression of Spin Relaxation in Submicron InGaAs Wires*, Phys. Rev. Lett. **97**, 036805 (2006).

[105] P. Wenk, & S. Kettemann, *Dimensional dependence of weak localization corrections and spin relaxation in quantum wires with Rashba spin-orbit coupling*, Phys. Rev. B **81**, 125309 (2010).

[106] T. Giamarchi, *Quantum physics in one dimension*, Vol. 121 (Clarendon press, 2003).

[107] N. Nagaosa, & T. Ogawa, *Electron-hole system in one dimension*, Solid state communications **88**, 295–299 (1993).

[108] F. Dirnberger, et al., *Ultralong spin lifetimes in one-dimensional semiconductor nanowires*, ArXiv e-prints (2018).

[109] R. W. Robinett, *Quantum mechanics of the two-dimensional circular billiard plus baffle system and half-integral angular momentum*, Eur. J. Phys. **24**, 231 (2003).

[110] Y. Wang, F. Zahid, Y. Zhu, L. Liu, J. Wang, & H. Guo, *Band offset of GaAs/Al x Ga1- x As heterojunctions from atomistic first principles*, Appl. Phys. Lett. **102**, 132109 (2013).

[111] M.-E. Pistol, & C. Pryor, *Band structure of core-shell semiconductor nanowires*, Physical Review B **78**, 115319 (2008).

[112] M. De Luca, S. Rubini, M. Felici, A. Meaney, P. C. M. Christianen, F. Martelli, & A. Polimeni, *Addressing the Fundamental Electronic Properties of Wurtzite GaAs Nanowires by High-Field Magneto-Photoluminescence Spectroscopy*, Nano Lett. **17**, 6540 (2017).

[113] A. F. Slachmuylders, B. Partoens, W. Magnus, & F. M. Peeters, *Trions in cylindrical nanowires with a dielectric mismatch*, Phys. Rev. B **76**, 075405 (2007).

[114] A. Chernikov, T. C. Berkelbach, H. M. Hill, A. Rigosi, Y. Li, O. B. Aslan, D. R. Reichman, M. S. Hybertsen, & T. F. Heinz, *Exciton Binding Energy and Nonhydrogenic Rydberg Series in Monolayer WS_2*, Phys. Rev. Lett. **113**, 076802 (2014).

[115] R. Cingolani, H. Lage, L. Tapfer, H. Kalt, D. Heitmann, & K. Ploog, *Quantum confined one-dimensional electron-hole plasma in semiconductor quantum wires*, Phys. Rev. Lett. **67**, 891–894 (1991).

[116] R. Anufriev, N. Chauvin, H. Khmissi, K. Naji, M. Gendry, & C. Bru-Chevallier, *Impact of substrate-induced strain and surface effects on the optical properties of InP nanowires*, Appl. Phys. Lett. **101**, 072101 (2012).

[117] Y. Hayamizu, M. Yoshita, Y. Takahashi, H. Akiyama, C. Z. Ning, L. N. Pfeiffer, & K. W. West, *Biexciton Gain and the Mott Transition in GaAs Quantum Wires*, Phys. Rev. Lett. **99**, 167403 (2007).

[118] A. Esser, E. Runge, R. Zimmermann, & W. Langbein, *Trions in GaAs Quantum Wells: Photoluminescence Lineshape Analysis*, physica status solidi (a) **178**, 489–494 (2000).

[119] G. Plechinger, P. Nagler, J. Kraus, N. Paradiso, C. Strunk, C. SchÃŒller, & T. Korn, *Identification of excitons, trions and biexcitons in single-layer WS2*, physica status solidi (RRL) - Rapid Research Letters **9**, 457–461 (2015).

[120] B. Alén, D. Fuster, G. Muñoz-Matutano, J. Martínez-Pastor, Y. González, J. Canet-Ferrer, & L. González, *Exciton Gas Compression and Metallic Condensation in a Single Semiconductor Quantum Wire*, Phys. Rev. Lett. **101**, 067405 (2008).

[121] D. D. Awschalom, & M. E. Flatté, *Challenges for semiconductor spintronics*, Nature Physics **3**, (2007).

[122] M. I. Dyakonov, & V. I. Perel, *Spin relaxation of conduction electrons in noncentrosymmetric semiconductors*, Sov. Phys. Solid State **13**, 3023–3026 (1972).

[123] J. Schliemann, J. C. Egues, & D. Loss, *Nonballistic Spin-Field-Effect Transistor*, Phys. Rev. Lett. **90**, 146801 (2003).

[124] S. Nadj-Perge, S. M. Frolov, E. P. A. M. Bakkers, & L. P. Kouwenhoven, *Spin–orbit qubit in a semiconductor nanowire*, Nature **468**, 1084–1087 (2010).

[125] S. Nadj-Perge, V. S. Pribiag, J. W. G. van den Berg, K. Zuo, S. R. Plissard, E. P. A. M. Bakkers, S. M. Frolov, & L. P. Kouwenhoven, *Spectroscopy of Spin–Orbit Quantum Bits in Indium Antimonide Nanowires*, Phys. Rev. Lett. **108**, 166801 (2012).

[126] J. W. G. van den Berg, S. Nadj-Perge, V. S. Pribiag, S. R. Plissard, E. P. A. M. Bakkers, S. M. Frolov, & L. P. Kouwenhoven, *Fast Spin–Orbit Qubit in an Indium Antimonide Nanowire*, Phys. Rev. Lett. **110**, 066806 (2013).

[127] S. M. Frolov, S. R. Plissard, S. Nadj-Perge, L. P. Kouwenhoven, & E. P. A. M. Bakkers, *Quantum computing based on semiconductor nanowires*, MRS Bull. **38**, 809–815 (2013).

[128] A. Das, Y. Ronen, Y. Most, Y. Oreg, M. Heiblum, & H. Shtrikman, *Zero-bias peaks and splitting in an Al–InAs nanowire topological superconductor as a signature of Majorana fermions*, Nat. Phys. **8**, 887–895 (2012).

[129] J. H. Buß, J. Rudolph, F. Natali, F. Semond, & D. Hägele, *Anisotropic electron spin relaxation in bulk GaN*, Appl. Phys. Lett. **95**, 192107 (2009).

[130] J. H. Buß, J. Rudolph, F. Natali, F. Semond, & D. Hägele, *Temperature dependence of electron spin relaxation in bulk GaN*, Phys. Rev. B **81**, 155216 (2010).

[131] J. H. Buß, J. Rudolph, S. Starosielec, A. Schaefer, F. Semond, Y. Cordier, A. D. Wieck, & D. Hägele, *Dyakonov-Perel electron spin relaxation in a wurtzite semiconductor: From the nondegenerate to the highly degenerate regime*, Phys. Rev. B **84**, 153202 (2011).

[132] J. Rudolph, J. H. Buß, & D. Hägele, *Electron spin dynamics in GaN*, Phys. Status Solidi B **251**, 1850–1860 (2014).

[133] S. Furthmeier, et al., *Enhanced spin–orbit coupling in core/shell nanowires*, Nat. Commun. **7**, 12413 (2016).

[134] S. Carapezzi, G. Priante, V. Grillo, L. Montès, S. Rubini, & A. Cavallini, *Bundling of GaAs Nanowires: A Case of Adhesion-Induced Self-Assembly of Nanowires*, ACS Nano **8**, 8932–8941 (2014).

[135] J. Liu, S. Lee, K. Lee, Y. H. Ahn, J.-Y. Park, & K. H. Koh, *Bending and bundling of metal-free vertically aligned ZnO nanowires due to electrostatic interaction*, Nanotechnology **19**, 185607 (2008).

[136] J. König, *Driving GaAs nanowires into the quantum regime: A photoluminescence study*, Master thesis (Universität Regensburg, 2017).

[137] H. B. Bebb, & E. W. Williams, "Photoluminescence I: Theory", in *Semiconductors and semimetals*, Vol. 8, edited by R. K. Willardson, & A. C. Beer, (Academic Press, New York, 1972), pp. 181–320.

[138] E. V. K. Rao, F. Alexandre, J. M. Masson, M. Allovon, & L. Goldstein, *Low temperature photoluminescence properties of high-quality GaAs layers grown by molecular-beam epitaxy*, J. Appl. Phys. **57**, 503–508 (1985).

[139] M. Murayama, & T. Nakayama, *Chemical trend of band offsets at wurtzite/zinc-blende heterocrystalline semiconductor interfaces*, Phys. Rev. B **49**, 4710–4724 (1994).

[140] D. C. Kim, D. L. Dheeraj, B. O. Fimland, & H. Weman, *Polarization dependent photocurrent spectroscopy of single wurtzite GaAs/AlGaAs core–shell nanowires*, Appl. Phys. Lett. **102**, 142107 (2013).

[141] G. Signorello, E. Lörtscher, P. A. Khomyakov, S. Karg, D. L. Dheeraj, B. Gotsmann, H. Weman, & H. Riel, *Inducing a direct-to-pseudodirect bandgap transition in wurtzite GaAs nanowires with uniaxial stress*, Nat. Commun. **5**, 3655 (2014).

[142] W. Hanle, *Ueber magnetische Beeinflussung der Polarisation der Resonanzfluoreszenz*, German, Z. Phys. **30**, 93–105 (1924).

[143] S. Kettemann, *Dimensional Control of Antilocalization and Spin Relaxation in Quantum Wires*, Phys. Rev. Lett. **98**, 176808 (2007).

[144] P. Altmann, M. P. Walser, C. Reichl, W. Wegscheider, & G. Salis, *Suppressed decay of a laterally confined persistent spin helix*, Phys. Rev. B **90**, 201306 (2014).

[145] P. Altmann, M. Kohda, C. Reichl, W. Wegscheider, & G. Salis, *Transition of a two-dimensional spin mode to a helical state by lateral confinement*, Phys. Rev. B **92**, 235304 (2015).

[146] C. Weisbuch, & C. Hermann, *Optical detection of conduction-electron spin resonance in* GaAs*,* $Ga_{1-x}In_xAs$*, and* $Ga_{1-x}Al_xAs$, Phys. Rev. B **15**, 816–822 (1977).

[147] I. Broser, & M. Rosenzweig, *Determination of excitonic parameters of the A polariton of CdS from magnetoreflectance spectroscopy*, Phys. Rev. B **22**, 2000–2007 (1980).

[148] E. I. Rashba, *Properties of Semiconductors with an Extremum Loop. 1. Cyclotron and Combinational Resonance in a Magnetic Field Perpendicular to the Plane of the Loop*, Sov. Phys. Solid State **2**, 1109–1122 (1960).

[149] Y. A. Bychkov, & E. I. Rashba, *Properties of a 2D electron gas with lifted spectral degeneracy*, JETP Lett. **39**, 78–81 (1984).

[150] A. D. Margulis, & V. A. Margulis, *Spin relaxation of free carriers in semiconductors with the wurtzite structure*, Sov. Phys. Semicond. **18**, 305–308 (1984).

[151] L. C. Lew Yan Voon, M. Willatzen, M. Cardona, & N. E. Christensen, *Terms linear in k in the band structure of wurtzite-type semiconductors*, Phys. Rev. B **53**, 10703–10714 (1996).

[152] I. Lo, W. T. Wang, M. H. Gau, S. F. Tsay, & J. C. Chiang, *Wurtzite structure effects on spin splitting in GaN/AlN quantum wells*, Phys. Rev. B **72**, 245329 (2005).

[153] W.-T. Wang, et al., *Dresselhaus effect in bulk wurtzite materials*, Appl. Phys. Lett. **91**, 082110 (2007).

[154] J. Y. Fu, & M. W. Wu, *Spin–orbit coupling in bulk ZnO and GaN*, J. Appl. Phys. **104**, 093712 (2008).

[155] R. Lassnig, $\mathbf{k}\cdot\mathbf{p}$ *theory, effective-mass approach, and spin splitting for two-dimensional electrons in GaAs–GaAlAs heterostructures*, Phys. Rev. B **31**, 8076–8086 (1985).

[156] I. L. Aleiner, & E. L. Ivchenko, *Anisotropic exchange splitting in type-II GaAs/AlAs superlattices*, JETP Lett. **55**, 692–695 (1992).

[157] B. Jusserand, D. Richards, G. Allan, C. Priester, & B. Etienne, *Spin orientation at semiconductor heterointerfaces*, Phys. Rev. B **51**, 4707–4710 (1995).

[158] E. L. Ivchenko, A. Y. Kaminski, & U. Rössler, *Heavy-light hole mixing at zinc-blende (001) interfaces under normal incidence*, Phys. Rev. B **54**, 5852–5859 (1996).

[159] P. Pfeffer, *Effect of inversion asymmetry on the conduction subbands in* GaAs–$Ga_{1-x}Al_xAs$ *heterostructures*, Phys. Rev. B **59**, 15902–15909 (1999).

[160] U. Rössler, & J. Kainz, *Microscopic interface asymmetry and spin-splitting of electron subbands in semiconductor quantum structures*, Solid State Commun. **121**, 313–316 (2002).

[161] E. L. Ivchenko, *Optical Spectroscopy of Semiconductor Nanostructures* (Alpha Science International Ltd, 2005).

[162] J. D. Koralek, C. P. Weber, J. Orenstein, B. A. Bernevig, S.-C. Zhang, S. Mack, & D. D. Awschalom, *Emergence of the persistent spin helix in semiconductor quantum wells*, Nature **458**, 610–613 (2009).

[163] Z. A. Devizorova, & V. A. Volkov, *Spin splitting of two-dimensional states in the conduction band of asymmetric heterostructures: Contribution from the atomically sharp interface*, English, JETP Lett. **98**, 101–106 (2013).

[164] Z. A. Devizorova, A. V. Shchepetilnikov, Y. A. Nefyodov, V. A. Volkov, & I. V. Kukushkin, *Interface contributions to the spin–orbit interaction parameters of electrons at the (001) GaAs/AlGaAs interface*, English, JETP Lett. **100**, 102–109 (2014).

[165] Y. Zhou, K. M. Rabe, & D. Vanderbilt, *Surface polarization and edge charges*, Phys. Rev. B **92**, 041102 (2015).

[166] S. Hunklinger, *Festkörperphysik* (Oldenbourg Verlag, 2009), pp. 286–287.

[167] X. Cartoixà, L.-W. Wang, D.-Y. Ting, & Y.-C. Chang, *Higher-order contributions to Rashba and Dresselhaus effects*, Phys. Rev. B **73**, 205341 (2006).

[168] S. A. Tarasenko, *Spin relaxation of conduction electrons in (110)-grown quantum wells: A microscopic theory*, Phys. Rev. B **80**, 165317 (2009).

[169] P. Wójcik, A. Bertoni, & G. Goldoni, *Enhanced Rashba spin-orbit coupling in core-shell nanowires by the interfacial effect*, arXiv preprint (2018).

[170] R. M. Lutchyn, G. W. Winkler, B. Van Heck, T. Karzig, K. Flensberg, L. I. Glazman, & C. Nayak, *Topological superconductivity in full shell proximitized nanowires*, arXiv preprint (2018).

[171] M. Kammermeier, P. Wenk, F. Dirnberger, D. Bougeard, & J. Schliemann, *Spin relaxation in wurtzite nanowires*, Phys. Rev. B **98**, 035407 (2018).

[172] T. Campos, P. E. Faria Junior, M. Gmitra, G. M. Sipahi, & J. Fabian, *Spin-orbit coupling effects in zinc-blende InSb and wurtzite InAs nanowires: realistic calculations with multiband* $\mathbf{k} \cdot \mathbf{p}$ *method*, ArXiv e-prints (2018).

[173] S. Heedt, W. Prost, J. Schubert, D. Grützmacher, & T. Schäpers, *Ballistic Transport and Exchange Interaction in InAs Nanowire Quantum Point Contacts*, Nano Lett. **16**, 3116–3123 (2016).

[174] D. Lucot, F. Jabeen, M. R. Ramdani, G. Patriarche, G. Faini, D. Mailly, & J.-C. Harmand, *Phase coherent transport in gaas/algaas core–shellnanowires*, J. Cryst. Growth **378**, 546–548 (2013).

[175] J. Tsai, & C.-H. Chang, J. Phys.: Condens. Matter **24**, 075801 (2012).

[176] D. D. Awschalom, *Manipulating and storing spin coherence in semiconductors*, Physica E **10**, 1–6 (2001).

[177] R. I. Dzhioev, K. V. Kavokin, V. L. Korenev, M. V. Lazarev, B. Y. Meltser, M. N. Stepanova, B. P. Zakharchenya, D. Gammon, & D. S. Katzer, *Low-temperature spin relaxation in n-type GaAs*, Phys. Rev. B **66**, 245204 (2002).

[178] R. Hanson, B. Witkamp, L. M. K. Vandersypen, L. H. W. van Beveren, J. M. Elzerman, & L. P. Kouwenhoven, *Zeeman Energy and Spin Relaxation in a One-Electron Quantum Dot*, Phys. Rev. Lett. **91**, 196802 (2003).

[179] M. Römer, J. Hübner, & M. Oestreich, *Spin noise spectroscopy in semiconductors*, Review of Scientific Instruments **78**, 103903 (2007).

[180] A. V. Khaetskii, D. Loss, & L. Glazman, *Electron Spin Decoherence in Quantum Dots due to Interaction with Nuclei*, Phys. Rev. Lett. **88**, 186802 (2002).

[181] R. de Sousa, & S. Das Sarma, *Theory of nuclear-induced spectral diffusion: Spin decoherence of phosphorus donors in Si and GaAs quantum dots*, Phys. Rev. B **68**, 115322 (2003).

[182] D. J. Hilton, & C. L. Tang, *Optical Orientation and Femtosecond Relaxation of Spin-Polarized Holes in GaAs*, Phys. Rev. Lett. **89**, 146601 (2002).

[183] C. Y. Hu, K. Morita, H. Sanada, S. Matsuzaka, Y. Ohno, & H. Ohno, *Spin precession of holes in wurtzite GaN studied using the time-resolved Kerr rotation technique*, Phys. Rev. B **72**, 121203 (2005).

[184] C. Brimont, M. Gallart, A. Gadalla, O. Crégut, B. Hönerlage, & P. Gilliot, *Dislocation density and band structure effects on spin dynamics in GaN*, Journal of Applied Physics **105**, 023502 (2009).

[185] A. De, & C. E. Pryor, *Optical dielectric functions of wurtzite III-V semiconductors*, Phys. Rev. B **85**, 125201 (2012).

[186] A. Y. Kitaev, *Unpaired Majorana fermions in quantum wires*, Physics-Uspekhi **44**, 131–136 (2001).

[187] M. D. Schroer, K. D. Petersson, M. Jung, & J. R. Petta, *Field Tuning the g Factor in InAs Nanowire Double Quantum Dots*, Phys. Rev. Lett. **107**, 176811 (2011).

[188] S. Csonka, L. Hofstetter, F. Freitag, S. Oberholzer, C. Schönenberger, T. S. Jespersen, M. Aagesen, & J. Nygård, *Giant Fluctuations and Gate Control of the g-Factor in InAs Nanowire Quantum Dots*, Nano Lett. **8**, 3932–3935 (2008).

[189] I. van Weperen, S. R. Plissard, E. P. A. M. Bakkers, S. M. Frolov, & L. P. Kouwenhoven, *Quantized Conductance in an InSb Nanowire*, Nano Lett. **13**, 387–391 (2013).

[190] I. A. Yugova, A. Greilich, D. R. Yakovlev, A. A. Kiselev, M. Bayer, V. V. Petrov, Y. K. Dolgikh, D. Reuter, & A. D. Wieck, *Universal behavior of the electron g factor in GaAs/AlGaAs quantum wells*, Phys. Rev. B **75**, 245302 (2007).

[191] A. A. Kiselev, E. L. Ivchenko, & U. Rössler, *Electron g factor in one- and zero-dimensional semiconductor nanostructures*, Phys. Rev. B **58**, 16353–16359 (1998).

[192] G. W. Winkler, D. Varjas, R. Skolasinski, A. A. Soluyanov, M. Troyer, & M. Wimmer, *Orbital Contributions to the Electron g Factor in Semiconductor Nanowires*, Phys. Rev. Lett. **119**, 037701 (2017).

[193] F. Qian, S. Gradečak, Y. Li, C.-Y. Wen, & C. M. Lieber, *Core/Multishell Nanowire Heterostructures as Multicolor, High-Efficiency Light-Emitting Diodes*, Nano Lett. **5**, 2287–2291 (2005).

[194] P. Krogstrup, H. I. Jørgensen, M. Heiss, O. Demichel, J. V. Holm, M. Aagesen, J. Nygard, & A. Fontcuberta i Morral, *Single-nanowire solar cells beyond the Shockley–Queisser limit*, Nature Photonics **7**, 306 (2013).

[195] K. Peng, et al., *Single Nanowire Photoconductive Terahertz Detectors*, Nano Lett. **15**, 206–210 (2015).

[196] Y. Su, C. Liu, S. Brittman, J. Tang, A. Fu, N. Kornienko, Q. Kong, & P. Yang, *Single-nanowire photoelectrochemistry*, Nature Nanotechnology **11**, 609 (2016).

[197] P. Parkinson, H. J. Joyce, Q. Gao, H. H. Tan, X. Zhang, J. Zou, C. Jagadish, L. M. Herz, & M. B. Johnston, *Carrier Lifetime and Mobility Enhancement in Nearly Defect-Free Core-Shell Nanowires Measured Using Time-Resolved Terahertz Spectroscopy*, Nano Lett. **9**, 3349–3353 (2009).

[198] F. Wang, Q. Gao, K. Peng, Z. Li, Z. Li, Y. Guo, L. Fu, L. M. Smith, H. H. Tan, & C. Jagadish, *Spatially Resolved Doping Concentration and Nonradiative Lifetime Profiles in Single Si-Doped InP Nanowires Using Photoluminescence Mapping*, Nano Lett. **15**, 3017–3023 (2015).

[199] O. Demichel, M. Heiss, J. Bleuse, H. Mariette, & A. Fontcuberta i Morral, *Impact of surfaces on the optical properties of GaAs nanowires*, Appl. Phys. Lett. **97**, 201907 (2010).

[200] H. P. T. Nguyen, M. Djavid, S. Y. Woo, X. Liu, A. T. Connie, S. Sadaf, Q. Wang, G. A. Botton, I. Shih, & Z. Mi, *Engineering the Carrier Dynamics of InGaN Nanowire White Light-Emitting Diodes by Distributed p-AlGaN Electron Blocking Layers*, Scientific Reports **5**, 7744 (2015).

[201] Y. Dan, K. Seo, K. Takei, J. H. Meza, A. Javey, & K. B. Crozier, *Dramatic Reduction of Surface Recombination by in Situ Surface Passivation of Silicon Nanowires*, Nano Lett. **11**, 2527–2532 (2011).

[202] M. Speckbacher, et al., *Direct Measurements of Fermi Level Pinning at the Surface of Intrinsically n-Type InGaAs Nanowires*, Nano Lett. **16**, 5135–5142 (2016).

[203] C. K. Yong, K. Noori, Q. Gao, H. J. Joyce, H. H. Tan, C. Jagadish, F. Giustino, M. B. Johnston, & L. M. Herz, *Strong Carrier Lifetime Enhancement in GaAs Nanowires Coated with Semiconducting Polymer*, Nano Lett. **12**, 6293–6301 (2012).

[204] L. Wischmeier, T. Voss, I. Rückmann, J. Gutowski, A. C. Mofor, A. Bakin, & A. Waag, *Dynamics of surface-excitonic emission in ZnO nanowires*, Phys. Rev. B **74**, 195333 (2006).

[205] C. Hauswald, T. Flissikowski, T. Gotschke, R. Calarco, L. Geelhaar, H. T. Grahn, & O. Brandt, *Coupling of exciton states as the origin of their biexponential decay dynamics in GaN nanowires*, Phys. Rev. B **88**, 075312 (2013).

[206] A. Kress, F. Hofbauer, N. Reinelt, M. Kaniber, H. J. Krenner, R. Meyer, G. Böhm, & J. J. Finley, *Manipulation of the spontaneous emission dynamics of quantum dots in two-dimensional photonic crystals*, Phys. Rev. B **71**, 241304 (2005).

[207] F. Pagliano, Y. Cho, T. Xia, F. van Otten, R. Johne, & A. Fiore, *Dynamically controlling the emission of single excitons in photonic crystal cavities*, Nature Communications **5**, (2014).

[208] J. Johansen, B. Julsgaard, S. Stobbe, J. M. Hvam, & P. Lodahl, *Probing long-lived dark excitons in self-assembled quantum dots*, Phys. Rev. B **81**, 081304 (2010).

[209] X. Liu, Q. Zhang, G. Xing, Q. Xiong, & T. C. Sum, *Size-Dependent Exciton Recombination Dynamics in Single CdS Nanowires beyond the Quantum Confinement Regime*, The Journal of Physical Chemistry C **117**, 10716–10722 (2013).

[210] J. L. Boland, A. Casadei, G. Tütüncüoglu, F. Matteini, C. L. Davies, F. Jabeen, H. J. Joyce, L. M. Herz, A. Fontcuberta i Morral, & M. B. Johnston, *Increased Photoconductivity Lifetime in GaAs Nanowires by Controlled n-Type and p-Type Doping*, ACS Nano **10**, 4219–4227 (2016).

[211] J. S. Reparaz, F. Güell, M. R. Wagner, A. Hoffmann, A. Cornet, & J. R. Morante, *Size-dependent recombination dynamics in ZnO nanowires*, Appl. Phys. Lett. **96**, 053105 (2010).

[212] J. S. Reparaz, F. Güell, M. R. Wagner, G. Callsen, R. Kirste, S. Claramunt, J. R. Morante, & A. Hoffmann, *Recombination dynamics in ZnO nanowires: Surfaces states versus mode quality factor*, Appl. Phys. Lett. **97**, 133116 (2010).

[213] Q. X. Zhao, L. L. Yang, M. Willander, B. E. Sernelius, & P. O. Holtz, *Surface recombination in ZnO nanorods grown by chemical bath deposition*, Journal of Applied Physics **104**, 073526 (2008).

[214] M. A. Fickenscher, H. E. Jackson, L. M. Smith, J. M. Yarrison-Rice, J. H. Kang, S. Paiman, Q. Gao, H. H. Tan, & C. Jagadish, *Direct imaging of the spatial diffusion of excitons in single semiconductor nanowires*, Appl. Phys. Lett. **99**, 263110 (2011).

[215] S. Noda, M. Fujita, & T. Asano, *Spontaneous-emission control by photonic crystals and nanocavities*, Nature Photonics **1**, 449 (2007).

[216] D. Englund, D. Fattal, E. Waks, G. Solomon, B. Zhang, T. Nakaoka, Y. Arakawa, Y. Yamamoto, & J. Vučković, *Controlling the Spontaneous Emission Rate of Single Quantum Dots in a Two-Dimensional Photonic Crystal*, Phys. Rev. Lett. **95**, 013904 (2005).

[217] G. M. Akselrod, C. Argyropoulos, T. B. Hoang, C. Ciracì, C. Fang, J. Huang, D. R. Smith, & M. H. Mikkelsen, *Probing the mechanisms of large Purcell enhancement in plasmonic nanoantennas*, Nature Photonics **8**, 835 (2014).

[218] D. K. Gramotnev, & S. I. Bozhevolnyi, *Plasmonics beyond the diffraction limit*, Nature Photonics **4**, 83 (2010).

[219] L. Tong, J. Lou, & E. Mazur, *Single-mode guiding properties of subwavelength-diameter silica and silicon wire waveguides*, Opt. Express **12**, 1025–1035 (2004).

[220] M. D. Birowosuto, G. Zhang, A. Yokoo, M. Takiguchi, & M. Notomi, *Spontaneous emission inhibition of telecom-band quantum disks inside single nanowire on different substrates*, Opt. Express **22**, 11713–11726 (2014).

[221] I. Friedler, C. Sauvan, J. P. Hugonin, P. Lalanne, J. Claudon, & J. M. Gérard, *Solid-state single photon sources: the nanowire antenna*, Opt. Express **17**, 2095–2110 (2009).

[222] M. E. Reimer, G. Bulgarini, N. Akopian, M. Hocevar, M. B. Bavinck, M. A. Verheijen, E. P. A. M. Bakkers, L. P. Kouwenhoven, & V. Zwiller, *Bright single-photon sources in bottom-up tailored nanowires*, Nature Communications **3**, (2012).

[223] R. Fons, A. D. Osterkryger, P. Stepanov, E. Gautier, J. Bleuse, J.-M. Gérard, N. Gregersen, & J. Claudon, *All-Optical Mapping of the Position of Quantum Dots Embedded in a Nanowire Antenna*, Nano Lett. **18**, 6434–6440 (2018).

[224] M. Munsch, J. Claudon, J. Bleuse, N. S. Malik, E. Dupuy, J.-M. Gérard, Y. Chen, N. Gregersen, & J. Mørk, *Linearly Polarized, Single-Mode Spontaneous Emission in a Photonic Nanowire*, Phys. Rev. Lett. **108**, 077405 (2012).

[225] P. Lodahl, S. Mahmoodian, & S. Stobbe, *Interfacing single photons and single quantum dots with photonic nanostructures*, Rev. Mod. Phys. **87**, 347–400 (2015).

[226] A. I. Kuznetsov, A. E. Miroshnichenko, M. L. Brongersma, Y. S. Kivshar, & B. Luk'yanchuk, *Optically resonant dielectric nanostructures*, Science **354** (2016).

[227] V. R. Almeida, Q. Xu, C. A. Barrios, & M. Lipson, *Guiding and confining light in void nanostructure*, Opt. Lett. **29**, 1209–1211 (2004).

[228] M. S. Tame, K. R. McEnery, Ş. K. Özdemir, J. Lee, S. A. Maier, & M. S. Kim, *Quantum plasmonics*, Nature Physics **9**, (2013).

[229] R. F. Oulton, V. J. Sorger, D. A. Genov, D. F. P. Pile, & X. Zhang, *A hybrid plasmonic waveguide for subwavelength confinement and long-range propagation*, Nature Photonics **2**, (2008).

[230] A. Rose, T. B. Hoang, F. McGuire, J. J. Mock, C. Ciraci, D. R. Smith, & M. H. Mikkelsen, *Control of Radiative Processes Using Tunable Plasmonic Nanopatch Antennas*, Nano Lett. **14**, 4797–4802 (2014).

[231] S. Bieker, T. Kiessling, W. Ossau, & L. W. Molenkamp, *Correct determination of low-temperature free-exciton diffusion profiles in GaAs*, Phys. Rev. B **92**, 121201 (2015).

[232] S. Bieker, R. Stühler, T. Kiessling, W. Ossau, & L. W. Molenkamp, *Dimensional crossover of free exciton diffusion in etched GaAs wire structures*, Appl. Phys. Lett. **107**, 122106 (2015).

[233] S. Bieker, T. Henn, T. Kiessling, W. Ossau, & L. W. Molenkamp, *Spatially Resolved Thermodynamics of the Partially Ionized Exciton Gas in GaAs*, Phys. Rev. Lett. **114**, 227402 (2015).

[234] M. Schreiber, S. S. Hodgman, P. Bordia, H. P. Lüschen, M. H. Fischer, R. Vosk, E. Altman, U. Schneider, & I. Bloch, *Observation of many-body localization of interacting fermions in a quasirandom optical lattice*, Science **349**, 842–845 (2015).

[235] V. V. Deshpande, M. Bockrath, L. I. Glazman, & A. Yacoby, *Electron liquids and solids in one dimension*, Nature **464**, 209 (2010).

[236] D. Chang, J. Douglas, A. González-Tudela, C.-L. Hung, & H. Kimble, *Colloquium: Quantum matter built from nanoscopic lattices of atoms and photons*, Reviews of Modern Physics **90**, 031002 (2018).

[237] J. Petersen, J. Volz, & A. Rauschenbeutel, *Chiral nanophotonic waveguide interface based on spin-orbit interaction of light*, Science **346**, 67–71 (2014).

[238] K. Y. Bliokh, A. Y. Bekshaev, & F. Nori, *Extraordinary momentum and spin in evanescent waves*, Nature communications **5**, 3300 (2014).

[239] B. Le Feber, N. Rotenberg, & L. Kuipers, *Nanophotonic control of circular dipole emission*, Nature communications **6**, 6695 (2015).

[240] M. Alizadeh, & B. M. Reinhard, *Emergence of transverse spin in optical modes of semiconductor nanowires*, Optics express **24**, 8471–8479 (2016).

[241] S. Sukhov, V. Kajorndejnukul, R. R. Naraghi, & A. Dogariu, *Dynamic consequences of optical spin–orbit interaction*, Nature Photonics **9**, 809 (2015).

[242] A. Hayat, J. P. B. Mueller, & F. Capasso, *Lateral chirality-sorting optical forces*, Proceedings of the National Academy of Sciences **112**, 13190–13194 (2015).

[243] A. Javadi, D. Ding, M. H. Appel, S. Mahmoodian, M. C. Löbl, I. Söllner, R. Schott, C. Papon, T. Pregnolato, S. Stobbe, et al., *Spin–photon interface and spin-controlled photon switching in a nanobeam waveguide*, Nature nanotechnology **13**, 398 (2018).

[244] M. F. Picardi, A. V. Zayats, & F. J. Rodríguez-Fortuño, *Janus and huygens dipoles: near-field directionality beyond spin-momentum locking*, Phys. Rev. Lett. **120**, 117402 (2018).

[245] S. L. Chuang, & C. S. Chang, *k·p method for strained wurtzite semiconductors*, Phys. Rev. B **54**, 2491–2504 (1996).

[246] P. E. Faria Junior, T. Campos, C. M. O. Bastos, M. Gmitra, J. Fabian, & G. M. Sipahi, *Realistic multiband k·p approach from ab initio and spin-orbit coupling effects of InAs and InP in wurtzite phase*, Phys. Rev. B **93**, 235204 (2016).

[247] I. Vurgaftman, J. R. Meyer, & L. R. Ram-Mohan, *Band parameters for III-V compound semiconductors and their alloys*, Journal of Applied Physics **89**, 5815–5875 (2001).

[248] G. Bastard, *Superlattice band structure in the envelope-function approximation*, Phys. Rev. B **24**, 5693–5697 (1981).

[249] L. C. Lew Yan Voon, C. Galeriu, B. Lassen, M. Willatzen, & R. Melnik, *Electronic structure of wurtzite quantum dots with cylindrical symmetry*, Appl. Phys. Lett. **87**, 041906 (2005).

[250] R. Ferreira, & G. Bastard, *"Spin"-flip scattering of holes in semiconductor quantum wells*, Phys. Rev. B **43**, 9687–9691 (1991).

List of publications

8. "Ultralong spin lifetimes in one-dimensional semiconductor nanowires," **Florian Dirnberger**, Michael Kammermeier, Jan König, Moritz Forsch, Paulo E. Faria Junior, Tiago Campos, Jaroslav Fabian, John Schliemann, Christian Schüller, Tobias Korn, Paul Wenk, and Dominique Bougeard, Submitted to Applied Physics Letters (2019)

7. "All-dielectric tuning of exciton emission in semiconductor nanowire waveguides," **Florian Dirnberger**, Jan König, Moritz Forsch, Thomas Koller, Imke Gronwald, Christoph Lange, Rupert Huber, Christian Schüller, Tobias Korn, Diego Abujetas, José Sánchez-Gil and Dominique Bougeard, In preparation (2019)

6. "Magnetic force sensing using a self-assembled nanowire," Nicola Rossi, Boris Gross, **Florian Dirnberger**, Dominique Bougeard, and Martino Poggio, Nano Lett., **19** (2), 930 (2019)

5. "Spin relaxation in wurtzite nanowires," Michael Kammermeier, Paul Wenk, **Florian Dirnberger**, Dominique Bougeard, and John Schliemann, Phys. Rev. B **98**, 035407 (2018)

4. "Origin and manipulation of stable vortex ground states in permalloy nanotubes," Michael Zimmermann, Thomas Norbert, Gerhard Meier, **Florian Dirnberger**, Attila Kákay, Martin Decker, Sebastian Wintz, Simone Finizio, Elisabeth Josten, Jörg Raabe, Matthias Kronseder, Dominique Bougeard, Jürgen Lindner, and Christian H. Back, Nano Lett. **18** (5), 2828 (2018)

3. "Enhanced spin–orbit coupling in core/shell nanowires," Stephan Furthmeier*, **Florian Dirnberger***, Martin Gmitra, Andreas Bayer, Moritz Forsch, Joachim Hubmann, Christian Schüller, Elisabeth Reiger, Jaroslav Fabian, Tobias Korn, and Dominique Bougeard, Nature Communications **7**, 12413 (2016), *contributed equally

2. "Epitaxial growth of room-temperature ferromagnetic MnAs segments," Joachim Hubmann, Benedikt Bauer, Helmut S. Körner, Stephan Furthmeier, Martin Buchner, Günther Bayreuther, **Florian Dirnberger**, Dieter Schuh, Christian H. Back, Josef Zweck, Elisabeth Reiger, and Dominique Bougeard, Nano Lett. **16** (2), 900 (2016)

1. "Long exciton lifetimes in stacking-fault-free wurtzite GaAs nanowires," Stephan Furthmeier, **Florian Dirnberger**, Joachim Hubmann, Benedikt Bauer, Tobias Korn, Christian Schüller, Josef Zweck, Elisabeth Reiger, and Dominique Bougeard, Appl. Phys. Lett. **105**, 222109 (2014)

Danksagung

Zurückblickend auf glückliche Jahre möchte ich denjenigen danken, die meine Zeit während der Promotion bereichert und ihren Beitrag zur Fertigstellung dieser Arbeit geleistet haben.

Mein größter Dank gilt dabei **Prof. Dr. Dominique Bougeard** für die exzellente Betreuung während meiner gesamten Promotion, das Vertrauen, das er mir entgegen gebracht hat, sowie für unsere gemeinsamen Reisen. Darüber hinaus für den von ihm geschaffenen Rahmen, der es mir ermöglicht hat, eigene wissenschaftlichen Interessen zu entwickeln und zu verfolgen.

Bedanken möchte ich mich auch bei **Prof. Dr. Tobias Korn** für seine freundliche und kompetente Art mich Wissenschaft zu lehren und seine stets prompte Unterstützung bei technischen Problemen im Labor.

Dank gebührt ebenso **Prof. Dr. Christian Schüller**, **Prof. Dr. Jaroslav Fabian**, **Prof. Dr. John Schliemann**, **Prof. Dr. Rupert Huber** und **Prof. Dr. Josef Zweck** für ihr Interesse an der Zusammenarbeit im Rahmen dieser Doktorarbeit und die daraus entstandenen Diskussionen.

Mein besonderer Dank gilt **Dr. Martin Gmitra** und **Dr. Paul Wenk** für die Stunden, in denen sie mit mir Fragen diskutiert und Probleme gelöst haben, sowie für den Teil meiner wissenschaftlichen Ausbildung, den ich nur ihnen verdanke.

Ich bedanke mich auch bei **Dr. Paulo Eduardo de Faria Junior** und **Dr. Michael Kammermeier** für ihren Beitrag, den sie zu dieser Doktorarbeit geleistet haben und die freundschaftliche Zusammenarbeit.

Ebenso danke ich **Diego Abujetas** and **Dr. José Sánchez-Gil** vom *Instituto de Estructura de la Materia* in Madrid für die Zusammenarbeit und die freundliche Bereitstellung ihrer Ergebnisse.

Für anregende Diskussionen bedanke ich mich bei **Dr. Christoph Lange**. **Dr. Matthias Kronseder** danke ich für die Herstellung der Wachstumssubstrate und seine willkommene Gesellschaft im MBE Labor. Besonderer Dank gilt auch **Dr. Alexey Chernikov** für die Zusammenarbeit und seine weiterführende Unterstützung.

Bei **Dr. Dieter Schuh** und **Andreas Schützenmeier** bedanke ich mich für die fachkundige Betreuung des MBE Labors und die zahlreichen Hilfestellungen. **Imke Gronwald** danke ich für die Herstellungen der strukturierten Substrate, ihre kompetente Laborarbeit und ihre wundervolle Art.

Den ehemaligen Masterstudenten **Moritz Forsch**, **Jan König** und **Thomas Koller**, die ich während meiner Promotion betreuen durfte, danke ich für ihren Einsatz und unser freundschaftliches Verhältnis.

Dank gebührt darüber hinaus **Michaela Trottmann** und **Maike Halbhuber** für die inhaltlichen Anmerkungen und das Korrekturlesen dieser Arbeit. Bei **Juliane Laurer** bedanke ich mich für ihre Hilfsbereitschaft und die Zurverfügungstellung dieser LaTeX-Vorlage.

Mein Dank gilt außerdem **Floyd Schauer**, **Viola Zeller**, **Andreas Schmidbauer**, **Maike Halbhuber**, **Thomas Meier**, **Michael Prager** und allen anderen, auch ehemaligen, Mitgliedern der AG Bougeard, die die gesamte Zeit meiner Promotion bereicherten.

Michaela Trottmann und **Andreas Bayer** danke ich für eine Zeit, die nicht besser hätte sein können.

Meinen Freunden und meiner Familie danke ich für ihre liebevolle Unterstützung.